

APPROACHES FOR AUTOMATIC URBAN BUILDING EXTRACTION AND  
UPDATING FROM HIGH RESOLUTION SATELLITE IMAGERY

A THESIS SUBMITTED TO  
THE GRADUTAE SCHOOL OF NATURAL AND APPLIED SCIENCES  
OF  
MIDDLE EAST TECHNICAL UNIVERSITY

BY

DİLEK KOÇ SAN

IN PARTIAL FULFILLMENT OF THE REQUIREMENTS  
FOR  
THE DEGREE OF DOCTOR OF PHILOSOPHY  
IN  
GEODETIC AND GEOGRAPHIC INFORMATION TECHNOLOGIES

MARCH 2009

Approval of the thesis:

**APPROACHES FOR AUTOMATIC URBAN BUILDING EXTRACTION  
AND UPDATING FROM HIGH RESOLUTION SATELLITE IMAGERY**

submitted by **DİLEK KOÇ SAN** in partial fulfillment of the requirements for the degree of **Doctor of Philosophy in Geodetic and Geographic Information Technologies Department, Middle East Technical University** by,

Prof. Dr. Canan Özgen  
Dean, Graduate School of **Natural and Applied Sciences** \_\_\_\_\_

Assoc. Prof. Dr. Mahmut Onur Karşlıoğlu  
Head of Department, **Geodetic and Geographic Information Techn.** \_\_\_\_\_

Assoc. Prof. Dr. Mahmut Onur Karşlıoğlu  
Supervisor, **Geodetic and Geographic Information Techn. Dept., METU** \_\_\_\_\_

Assoc. Prof. Dr. Mustafa Türker  
Co-Supervisor, **Geodesy and Photogrammetry Dept., Hacettepe Univ.** \_\_\_\_\_

**Examining Committee Members:**

Prof. Dr. Volkan Atalay  
Computer Engineering Dept., METU \_\_\_\_\_

Assoc. Prof. Dr. Mahmut Onur Karşlıoğlu  
Civil Engineering Dept., METU \_\_\_\_\_

Prof. Dr. Vedat Toprak  
Geological Engineering Dept., METU \_\_\_\_\_

Assist. Prof. Dr. Rahmi Erdem  
City and Regional Planning Dept., Selçuk Univ. \_\_\_\_\_

Assist. Prof. Dr. Yakup S. Özkazanç  
Electrical and Electronics Engineering Dept., Hacettepe Univ. \_\_\_\_\_

**Date:** 03. 03. 2009

**I hereby declare that all information in this document has been obtained and presented in accordance with academic rules and ethical conduct. I also declare that, as required by these rules and conduct, I have fully cited and referenced all material and results that are not original to this work.**

Name, Last name : Dilek KOÇ SAN

Signature :

## **ABSTRACT**

### **APPROACHES FOR AUTOMATIC URBAN BUILDING EXTRACTION AND UPDATING FROM HIGH RESOLUTION SATELLITE IMAGERY**

Koç San, Dilek

Ph.D., Department of Geodetic and Geographic Information Technologies

Supervisor: Assoc. Prof. Dr. Mahmut Onur Karşlıođlu

Co-Supervisor: Assoc. Prof. Dr. Mustafa Türker

March 2009, 228 pages

Approaches were developed for building extraction and updating from high resolution satellite imagery. The developed approaches include two main stages: (i) detecting the building patches and (ii) delineating the building boundaries. The building patches are detected from high resolution satellite imagery using the Support Vector Machines (SVM) classification, which is performed for both the building extraction and updating approaches. In the building extraction part of the study, the previously detected building patches are delineated using the Hough transform and boundary tracing based techniques. In the Hough transform based technique, the boundary delineation is carried out using the processing operations of edge detection, Hough transformation, and perceptual grouping. In the boundary tracing based technique, the detected edges are vectorized using the boundary tracing algorithm. The results are then refined through line simplification and vector filters. In the building updating part of the study, the destroyed buildings are determined through analyzing the existing building boundaries and the previously detected



building patches. The new buildings are delineated using the developed model based approach, in which the building models are selected from an existing building database by utilizing the shape parameters.

The developed approaches were tested in the Batikent district of Ankara, Turkey, using the IKONOS panchromatic and pan-sharpened stereo images (2002) and existing vector database (1999). The results indicate that the proposed approaches are quite satisfactory with the accuracies computed in the range from 68.60% to 98.26% for building extraction, and from 82.44% to 88.95% for building updating.

**Keywords:** Building Extraction, Building Updating, Support Vector Machines Classification, Hough Transformation, Model Based Approach.

## ÖZ

### KENTSEL BİNALARIN YÜKSEK ÇÖZÜNÜRLÜKLÜ UYDU GÖRÜNTÜLERİNDEN OTOMATİK ÇIKARILMASI VE GÜNCELLENMESİ İÇİN YAKLAŞIMLAR

Koç San, Dilek

Doktora, Jeodezi ve Coğrafi Bilgi Teknolojileri Bölümü

Tez Yöneticisi: Doç. Dr. Mahmut Onur Karşlıoğlu

Ortak Tez Yöneticisi: Doç. Dr. Mustafa Türker

Mart 2009, 228 sayfa

Yüksek çözünürlüklü uydu görüntülerinden bina çıkarımı ve güncellenmesi için yaklaşımlar geliştirilmiştir. Geliştirilen yaklaşımlar iki ana aşama içermektedir: (i) bina alanlarının bulunması ve bina sınırlarının bina belirlenmesi. Bina alanları yüksek çözünürlüklü uydu görüntülerinden, hem bina çıkarımı hem de güncellenmesi yaklaşımları için uygulanan, Destek Vektör Makineleri (DVM) sınıflandırması kullanılarak bulunmaktadır. Çalışmanın bina çıkarımı kısmında, önceden bulunan bina alanlarının sınırları geliştirilen Hough dönüşümüne ve sınır izlemeye dayalı teknikler kullanılarak belirlenmektedir. Hough dönüşümüne dayalı teknikte, bina sınırları kenar belirleme, Hough dönüşümü ve algısal gruplama işlemleri kullanılarak belirlenmektedir. Sınır izlemeye dayalı teknikte, elde edilen kenarlar sınır izleme algoritması kullanılarak vektör forma dönüştürülmektedir. Sonuçlar çizgi basitleştirme algoritması ve vektör filtreleri kullanılarak iyileştirilmektedir. Çalışmanın binaların güncellenmesi kısmında, yıkılmış binalar mevcut bina veritabanı ile bulunan bina alanları analiz edilerek belirlenmiştir. Yeni bina sınırları,

bina modellerinin mevcut bina veritabanından Őekil parametreleri kullanılarak belirlendiĐi, geliŐtirilen modele dayalı yaklaŐım kullanılarak belirlenmiŐtir.

YaklaŐımlar TŒrkiye’de Ankara’nın Batıkent bölgesinde, IKONOS pankromatik ve keskinleŐtirilmiŐ renkli uydu gŒrŒntŒleri (2002) ve mevcut vektŒr veritabanı (1999) kullanılarak test edilmiŐtir. Sonuçlar Őnerilen yaklaŐımların, binaların belirlenmesi için %68.60 ile %98.26 aralıĐında ve binaların gŒncellenmesi için %82.44 ile %88.95 aralıĐında hesaplanan doĐruluklarla, oldukça baŐarılı olduĐunu gŒstermektedir.

**Keywords:** Bina Çıkarma, Bina GŒncelleme, Destek VektŒr Makineleri Sınıflandırması, Hough Transformasyonu, Modele Dayalı YaklaŐım.

*To*  
*My Parents*  
*and*  
*My Husband*

## ACKNOWLEDGEMENTS

I would like to express my deepest gratitude to Assoc. Prof. Dr. Mustafa Türker, who was my supervisor and has become my co-supervisor in the last three years of my PhD research, for his support, advice, and guidance throughout this research and thesis writing process.

I am indebted to Assoc. Prof. Dr. Mahmut Onur Karşlıođlu, who has become my supervisor in the last three years of my PhD research. I always felt his support in all issues about the academic life.

I am grateful to Prof. Dr. Volkan Atalay for his valuable comments and contributions during the thesis supervising committees. In addition, I would like to thank to the other examining committee members Prof. Dr. Vedat Toprak, Assist. Prof. Dr. Rahmi Erdem, and Assist. Prof. Dr. Yakup S. Özkazanç for their suggestions and comments.

This study was supported by the State Planning Organization (DPT) Grants: BAP-08-11-DPT2002K120510. In addition, I would like to acknowledge Hacettepe University, Geodesy and Photogrammetry department for supplying the GCPs from orthophotos.

I would like to express my sincere thanks to all my professors and instructors in GGIT department. I would like to thank all my friends in GGIT department for their friendship and support, in particular Ali Özgün Ok, Aslı Özdarıcı, Arzu Erener, Reşat Geçen, Tünay Cesur, and Yener Kazım Ölçer for their help in the field study of this thesis, Ali Özgün OK, Serkan Kemeç, Mahmut Arıkan and Özgün Balkanay for

their help especially in technical problems and Pınar Aslantaş Bostan, Kıvanç Ertuğay, Gülcan Sarp, and Balkan Uraz.

I would like to thank Prof. Dr. Armin Grün for his comments and advices about my studies during the six months I spent in Swiss Federal Institute of Technology (ETH). I am also grateful to all of the friends I met in Zurich especially to Sultan Aksakal (Kocaman) and Devrim Akça. Their friendship made the stay in Zurich a pleasant experience.

My deepest gratitude goes to my parents Sevim and Nevzat Koç for their love, endless support, encouragement, and patience. I am very lucky to have parents like them. Additionally, I would like to thank my elder sister Pınar Çalapala, her husband Murat Çalapala, my unique nephew Kemal Onur Çalapala, my brother Uğur Koç and his wife Efsun Koç for their love, understanding, and patience. My sister and my brother always supported me and cheered me up. I am thankful to all of my relatives, especially to my grandparents Fatma and Kemal Koç, who are like second parents for me, and Hatice and Zeki Şahin.

Lastly, but not leastly, I would like to express my special thanks to my husband B. Taner San for his love, support, encouragement, help and understanding. He gave me strength and cheered me up in my difficult times. Without him, this process would be much more difficult for me.

## ABBREVIATIONS

BDP	Building Detection Percentage
BF	Branching Factor
CSG	Constructive Solid Geometry
DEM	Digital Elevation Model
DGPS	Differential Global Positioning System
DSM	Digital Surface Model
DTM	Digital Terrain Model
FN	False Negative
FP	False Positive
GCP	Ground Control Point
GIS	Geographic Information System
ICP	Independent Check Point
MF	Miss Factor
nDSM	Normalized Digital Surface Model
NDVI	Normalized Difference Vegetation Index
PC	Principal Component
PCA	Principal Component Analysis
QP	Quality Percentage
RS	Remote Sensing
RMSE	Root Mean Square Error
SVM	Support Vector Machines
TN	True Negative
TP	True Positive

## TABLE OF CONTENTS

ABSTRACT .....	iv
ÖZ.....	vi
ACKNOWLEDGEMENTS .....	ix
ABBREVIATIONS .....	xi
TABLE OF CONTENTS .....	xii
LIST OF TABLES.....	xvi
LIST OF FIGURES .....	xx
CHAPTER	
1. INTRODUCTION .....	1
1.1. Objectives of the Research .....	3
1.2. The Software Used in the Study.....	4
1.3. Organization of the Thesis.....	5
2. LITERATURE REVIEW.....	7
2.1. Building Extraction .....	7
2.1.1. Building Extraction from Aerial Images.....	8
2.1.2. Building Extraction from Space Imagery .....	12
2.1.3. Building Extraction from Laser/Lidar/DEM Data .....	15
2.1.4. Building Extraction from Multi-Source Data.....	17
2.2. Building Extraction for Map Updating.....	21
3. THE STUDY AREA AND DATA SETS .....	24
3.1. The Study Area .....	24
3.2. Data.....	27
3.2.1. Raster Data .....	27
3.2.2. Vector Data .....	28
4. BUILDING DETECTION THROUGH SUPPORT VECTOR MACHINES CLASSIFICATION .....	34



4.1. The Methodology .....	34
4.2. Test Areas .....	36
4.3. Calculating the Normalized Digital Surface Model .....	36
4.3.1. Calculating the Digital Surface Model .....	37
4.3.2. Calculating the Digital Terrain Model.....	45
4.3.3. nDSM Calculation .....	47
4. 4. Orthorectification .....	49
4. 5. Calculating the Normalized Difference Vegetation Index .....	50
4. 6. Principal Component Analysis.....	52
4. 7. The Support Vector Machines Classification .....	55
4. 8. Determining the Candidate Building Patches .....	67
4. 9. The Accuracy Assessment .....	69
4.9.1. Accuracy Assessment of the SVM Classification .....	69
4.9.2. Accuracy Assessment of Building Detection.....	69
4. 10. The Experimental Results .....	70
4.10.1. The Results of SVM .....	71
4.10.1.1. Sub-Area I .....	71
4.10.1.2. Sub-Area II .....	75
4.10.1.3. Sub-Area III.....	78
4.10.2. The Results of Building Detection .....	82
4.10.2.1. Sub-Area I .....	82
4.10.2.2. Sub-Area II .....	85
4.10.2.3. Sub-Area III.....	88
5. BUILDING DELINEATION BASED ON HOUGH TRANSFORM AND BOUNDARY TRACING TECHNIQUES.....	93
5.1. Building Delineation Based on Hough Transform.....	94
5.1.1. The Methodology .....	95
5.1.2. Delineation of the Rectangular Shape Buildings.....	97
5.1.2.1. Edge Detection.....	97
5.1.2.2. Hough Transform.....	99
5.1.2.3. Perceptual Grouping .....	101
5.1.3. Delineation of the Circular Buildings.....	105

5.1.3.1. Delineating the ‘Circle’ and ‘Ring’ Shape Buildings .....	106
5.1.3.2. Delineating the ‘C’ Shape Buildings .....	110
5.1.3.3. Delineating the ‘S’ Shape Buildings .....	111
5.1.4. The Experimental Results .....	115
5.2. Building Delineation Based on Boundary Tracing .....	124
5.2.1. The Methodology .....	124
5.2.2. Edge Detection .....	125
5.2.3. Boundary Tracing .....	125
5.2.4. Line Simplification .....	126
5.2.5. Vector Filtering .....	126
5.2.6. The Experimental Results .....	127
5.3. Discussions of the Results .....	135
6. UPDATING AN EXISTING BUILDING DATABASE USING A MODEL BASED APPROACH.....	143
6.1. The Methodology .....	143
6.2. Preparing the Existing Building Database .....	146
6.3. Preparing the Building Patches .....	147
6.4. Shape Characterization .....	148
6.5. Selecting the Building Models .....	154
6.6. Testing the Building Model against the Candidate Building Patch .....	155
6.7. The Experimental Results .....	160
6.8. Discussions of the Results .....	163
7. CONCLUSIONS AND RECOMMENDATIONS .....	167
7.1. Building Detection .....	167
7.1.1. SVM Classification.....	167
7.1.2. Building Detection.....	169
7.2. Building Delineation .....	170
7.3. Updating an Existing Building Database.....	173
7.4. The Recommendations .....	175
REFERENCES .....	176
APPENDICES	
A. PHOTOGRAPHS FROM THE STUDY AREA .....	189

B. EVALUATION OF THE DIGITAL SURFACE MODEL .....	196
C. ACCURACY ASSESSMENT RESULTS OF THE SVM CLASSIFICATION .....	200
D. RESULTS OF THE SVM CLASSIFICATION .....	218
E. SOURCE CODE FOR BUILDING MODEL SELECTION .....	224
VITA.....	226

## LIST OF TABLES

### TABLES

Table 2. 1. The previous studies for building extraction from monocular aerial images.....	9
Table 2. 2. The previous studies for building extraction from stereo aerial images.....	9
Table 2. 3. The previous studies for building extraction from multiple aerial images.....	10
Table 2. 4. The past studies for building extraction using the model-based approaches .....	11
Table 2. 5. The past studies for building extraction from satellite images .....	13
Table 2. 6. The past studies for building extraction using Laser/Lidar/DEM data .	15
Table 2. 7. The past studies for building extraction from multi-source data .....	18
Table 2. 8. The past studies conducted for building extraction to update maps and detect changes.....	21
Table 3. 1. The classification of the buildings .....	27
Table 3. 2. The information about the IKONOS stereo image pairs used in the study .....	28
Table 3. 3. The parameters of the Transverse Mercator Projection System .....	29
Table 4. 1. The parameters used in DSM generation.....	41
Table 4. 2. The RMSEs of the DSMs, which were generated using the GCPs collected through DGPS, from orthophotos and maps, and using all GCPs.....	43
Table 4. 3. The Z value errors of the DSMs, which were generated using the GCPs collected using DGPS, from orthophotos and maps, and all GCPs. .	43

Table 4. 4. The Z value errors of the transects of DSMs, which were generated using the GCPs collected using DGPS, from orthophotos and maps, and all GCPs. ....	44
Table 4. 5. The spectral statistics of the IKONOS Pan-sharpened image .....	55
Table 4. 6. The spectral statistics of the principal components.....	55
Table 4. 7. The data sets and their band combinations used in the SVM classification. ....	61
Table 4. 8. The number of training pixels collected for Sub-Area I.....	61
Table 4. 9. The number of training pixels collected for Sub-Area II .....	62
Table 4. 10. The number of training pixels collected for Sub-Area III. ....	62
Table 4. 11. The number of test pixels collected for Sub-Area I .....	63
Table 4. 12. The number of test pixels collected for Sub-Area II .....	63
Table 4. 13. The number of test pixels collected for Sub-Area III.....	63
Table 4. 14. For Sub-Area I, the spectral separability values of the data sets. ....	64
Table 4. 15. For Sub-Area II, the spectral separability values of the data sets .....	65
Table 4. 16. For Sub-Area III, the spectral separability values of the data sets.....	65
Table 4. 17. For Sub-Area I, the Overall Accuracies and Kappa Coefficients .....	71
Table 4. 18. For Sub-Area II, the Overall Accuracies and Kappa Coefficients.....	75
Table 4. 19. For Sub-Area III, the Overall Accuracies and Kappa Coefficients.....	78
Table 4. 20. For Sub-Area I, the quantitative evaluation of SVM classification using 500, 1000, and 2000 training samples.....	82
Table 4. 21. For Sub-Area II, the quantitative evaluation of the SVM classification using 500, 1000, and 2000 training samples .....	85
Table 4. 22. For Sub-Area III, the quantitative evaluation of the SVM classification using 500, 1000, and 2000 training samples .....	88
Table 5. 1. Error matrix of the delineated building boundaries using Hough transform based approach for the detached dwelling types.....	117
Table 5. 2. The quality assessment results of the urban blocks that contain detached buildings using Hough transform based approach. ....	117
Table 5. 3. Error matrix of the delineated building boundaries using Hough transform based approach for the semi-detached dwelling types. ....	119

Table 5. 4. The quality assessment results for urban blocks that contain semi-detached buildings using Hough transform based approach. ....	119
Table 5. 5. Error matrix of the delineated building boundaries using Hough transform based approach for terraced dwelling type. ....	121
Table 5. 6. The results of quality assessment for urban blocks that include the terraced buildings using Hough transform based approach.....	121
Table 5. 7. The average quality assessment results for the rectangular residential buildings using Hough transform based approach. ....	122
Table 5. 8. The quality assessment results for the circular buildings using Hough transform based approach.....	123
Table 5. 9. The quality assessment results for industrial buildings using Hough transform based approach. ....	123
Table 5. 10. Error matrix of the delineated building boundaries using Boundary tracing based approach for detached dwelling type. ....	127
Table 5. 11. The quality assessment results for six urban blocks that contain detached buildings using Boundary tracing based approach. ....	129
Table 5. 12. Error matrix of the delineated building boundaries using Boundary tracing based approach for the semi-detached dwelling type. ....	129
Table 5. 13. The quality assessment results for urban blocks that contain semi-detached buildings using Boundary tracing based approach. ....	131
Table 5. 14. Error matrix of the delineated building boundaries using Boundary tracing based approach for the terraced dwelling type. ....	131
Table 5. 15. The quality assessment results for the urban blocks that contain terraced buildings using Boundary tracing based approach. ....	133
Table 5. 16. The average quality assessment results for the rectangular residential buildings using Boundary tracing based approach.....	133
Table 5. 17. The quality assessment results for circular buildings using Boundary tracing based approach. ....	134
Table 5. 18. The quality assessment results for the industrial buildings using Boundary tracing based approach. ....	135
Table 5. 19. The comparison of the results of the Hough transform and Boundary tracing approaches.....	136

Table 6. 1. The shape parameters computed for the building patches.....	152
Table 6. 2. The shape parameters computed for the existing building boundaries.....	153
Table 6. 3. The fields of the existing building database .....	154
Table 6. 4. The quality assessment results for two urban blocks. ....	163
Table C. 1. For the data-sets (14 in total) of Sub-Area I, the SVM classification accuracies computed using 2000 test pixels. ....	200
Table C. 2. For the data-sets (14 in total) of Sub-Area I, the SVM classification accuracies computed using 4000 test pixels. ....	202
Table C. 3. For the data-sets (14 in total) of Sub-Area I, the SVM classification accuracies computed using 8000 test pixels. ....	204
Table C. 4. For the data-sets (14 in total) of Sub-Area II, the SVM classification accuracies computed using 2000 test pixels. ....	206
Table C. 5. For the data-sets (14 in total) of Sub-Area II, the SVM classification accuracies computed using 4000 test pixels .....	208
Table C. 6. For the data-sets (14 in total) of Sub-Area II, the SVM classification accuracies computed using 8000 test pixels .....	210
Table C. 7. For the data-sets (14 in total) of Sub-Area III, the SVM classification accuracies computed using 2000 test pixels.....	212
Table C. 8. For the data-sets (14 in total) of Sub-Area III, the SVM classification accuracies computed using 4000 test pixels.....	214
Table C. 9. For the data-sets (14 in total) of Sub-Area III, the SVM classification accuracies computed using 8000 test pixels.....	216

## LIST OF FIGURES

### FIGURES

Figure 3. 1. The location of the study area: (a) The Batikent district of Ankara and (b) the false color composite of the IKONOS pan-sharpened image covering the study area. ....	25
Figure 3. 2. The false color composite of IKONOS pan-sharpened image of the circular buildings (a) the circle shape buildings, (b) the “ring” shape building, (c), (d) the “C” shape buildings and (e) the “S” shape buildings. ....	26
Figure 3. 3. The reference building database (a) before and (b) after shifting the existing building boundaries. ....	31
Figure 3. 4. The scanned development plans. ....	32
Figure 3. 5. The false color pan-sharpened IKONOS satellite image with the digitized urban block boundaries overlaid.....	33
Figure 4. 1. The flowchart of the building detection procedure.....	35
Figure 4. 2. The selected sub-areas: (a) Sub-Area I, (b) Sub-Area II, and (c) Sub-Area III. ....	36
Figure 4. 3. The schematic representations of (a) the DTM and DSM, and (b) the nDSM and the applied threshold. ....	37
Figure 4. 4. The locations of the collected GCPs (white points) and ICPs (black points) on the IKONOS panchromatic image. ....	39
Figure 4. 5. The location of a GCP (a) in the panchromatic satellite image (the red arrow indicates the direction of the photograph) and (b) in the field....	39
Figure 4. 6. (a) A building with a bright roof in the IKONOS panchromatic satellite image and (b) the erroneous pixels in the DSM corresponding to this building. The DSM (c) after applying an editing process to remove the erroneous pixels and (d) after filtering the edited DSM.....	42



Figure 4. 7. (a) The DSM after the editing and geocoding operations and (b) a shaded relief of the surface .....	42
Figure 4. 8. (a) A horizontal profile in the panchromatic IKONOS image and (b) the comparison between the generated DSM and the reference DTM along this profile. ....	44
Figure 4. 9. (a) A subset from the contour lines and (b) the generated DTM.....	46
Figure 4. 10. (a) The DTM and (b) the shaded relief of the terrain.....	46
Figure 4. 11. (a) The calculated nDSM and (b) nDSM after applying a threshold. ....	47
Figure 4. 12. For Sub-Area I, (a) the DTM, (b) the DSM, (c) the nDSM, and (d) the thresholded nDSM images .....	48
Figure 4. 13. For Sub-Area II, the (a) the DTM, (b) the DSM, (c) the nDSM, and (d) the thresholded nDSM images .....	48
Figure 4. 14. For Sub-Area III, (a) the DTM, (b) the DSM, (c) the nDSM and (d) the thresholded nDSM images.....	49
Figure 4. 15. The IKONOS pan sharpened image with the vector building boundaries overlaid .....	50
Figure 4. 16. (a) The NDVI image and (b) bitmap after applying a threshold to NDVI image.....	51
Figure 4. 17. The calculated NDVI images for (a) Sub-Area I, (b) Sub-Area II, and (c) Sub-Area III. ....	52
Figure 4. 18. The results of principal component analysis of the IKONOS Pan-Sharpener Image: (a) 1st PC, (b) 2nd PC, (c) 3rd PC and (d) 4th PC .....	53
Figure 4. 19. For three sub-areas, the principal components of the IKONOS Pan-Sharpener Image.....	54
Figure 4. 20. In the linear separable case (a) the possible hyperplanes and (b) the optimum hyperplanes.....	56
Figure 4. 21. The processes of SVM classification (a) The feature vectors of two classes in input space (b) The feature vectors of two classes separated by a hyperplane in feature space (c) The separated two classes in input space. ....	58

Figure 4. 22. For an urban block, the candidate building patches (a) before and (b) after removing the artefacts.....	68
Figure 4. 23. Schematic representation of True Positive (TP), True Negative (TN), False Positive (FP) and False Negative (FN) areas .....	70
Figure 4. 24. For each data set, the overall accuracies computed using 500, 1000 and 2000 training samples in Sub-Area I.....	72
Figure 4. 25. For each data set, the kappa coefficients computed using 500, 1000 and 2000 training samples in Sub-Area I.....	73
Figure 4. 26. For Sub-Area I, the results of SVM classification using 14 Data- Sets and 500 training samples.....	74
Figure 4. 27. For each data set, the overall accuracies computed using 500, 1000, and 2000 training samples in Sub-Area II .....	76
Figure 4. 28. For each data set, the kappa coefficients computed using 500, 1000, and 2000 training samples in Sub-Area II .....	76
Figure 4. 29. For Sub-Area II, the results of SVM classification using 14 Data- Sets and 500 samples.....	76
Figure 4. 30. For each data set, the overall accuracies computed using 500, 1000, and 2000 training samples in Sub-Area III .....	79
Figure 4. 31. For each data set, the kappa coefficients computed using 500, 1000, and 2000 training samples III.....	80
Figure 4. 32. For Sub-Area III, the results of SVM classification using 14 Data- Sets and 500 samples.....	81
Figure 4. 33. For each data set, the BDP and QP measurements computed for the classifications conducted using 500, 1000, and 2000 training samples in Sub-Area I .....	83
Figure 4. 34. The comparison of BDP values using 500, 1000, and 2000 training samples for Sub-Area I.....	84
Figure 4. 35. The comparison of QP values using 500, 1000, and 2000 training samples for Sub-Area I.....	85
Figure 4. 36. For each data set, the BDP and QP measurements computed for the classifications conducted using 500, 1000, and 2000 training samples in Sub-Area II.....	86

Figure 4. 37. The comparison of BDP values using 500, 1000, and 2000 training samples for Sub-Area II.....	87
Figure 4. 38. The comparison of QP values using 500, 1000, and 2000 training samples for Sub-Area II.....	88
Figure 4. 39. For each data set, the BDP and QP measurements computed for the classifications conducted using 500, 1000, and 2000 training samples in Sub-Area III.....	89
Figure 4. 40. The comparison of BDP values using 500, 1000, and 2000 training samples for Sub-Area III .....	90
Figure 4. 41. The comparison of QP values using 500, 1000, and 2000 training samples for Sub-Area III .....	91
Figure 5. 1. The delineation of building boundaries.....	94
Figure 5. 2. The flowchart of Hough transform based approach.....	95
Figure 5. 3. The schematic representation of (a) a binary image that includes separated components and (b) generated label matrix. ....	96
Figure 5. 4. (a) A line in the xy-plane and (b) the corresponding lines to the points in the normal plane.....	99
Figure 5. 5. (a) $r, \theta$ parameterization of lines in the xy-plane and (b) the sinusoidal curves in the $r\theta$ plane. ....	100
Figure 5. 6. The stages of perceptual grouping .....	103
Figure 5. 7. The schematic representation of the algorithm.....	104
Figure 5. 8. The Circular Hough transform parameter space.....	108
Figure 5. 9. A Circular Hough transform (a) in x-y space and (b) in parameter space. ....	108
Figure 5. 10. Reduction in the error area as “Seg_no” increases from an initial value of 4 up to a final value of 32. The error area is calculated dividing the circular area, $\pi*r^2$ , by the inscribed polygon area, $seg\_no*r^2.\sin * (\pi/seg\_no) * \cos(\pi/seg\_no)$ . The error (black area) is getting smaller while the seg_no increases and is almost negligible for seg_no = 32 (Ujaldon et al., 2008).....	109
Figure 5. 11. The steps of the algorithm to delineate the “C” shape buildings. (a) The detected circles with segment number of 24 (b) Semi-circle	

generation by deleting the circle points that have non-building pixels under them (c) Calculating the distances between sequential semi-circle points to determine the start and end points of the semi-circles (d) Detecting the determined start and end points of the outside and inside circles: SOC – EOC & SIC – EIC (e) Overlaying the delineated “C” shape building boundary with the building patch and (f) the final delineated boundary of the “C” shape building. ....	112
Figure 5. 12. The steps of the developed algorithm to delineate “S” shape buildings. (a) The detected circles with segment number of 24. (b) Semi-circle generation by deleting the circle points that have non-building pixels under them. (c) The determined start and end points of the outside and inside circles: S1OC – E1OC & S1IC – E1IC and S2OC – E2OC & S2IC – E2IC. (d) Finding the nearest points of the inside and outside semi-circles (e) The delineated “S” shape building boundary overlaid with building patch. ....	114
Figure 5. 13. The delineated detached building boundaries using Hough transform based approach for urban blocks that contain (a) low-rise, (b - e) middle-rise, and (f) high-rise buildings. ....	116
Figure 5. 14. The delineated semi-detached building boundaries using Hough transform based approach for urban blocks that contain (a - d) middle-rise and (e) high-rise buildings.....	118
Figure 5. 15. The delineated terraced building boundaries using Hough transform based approach for urban blocks that contain (a - d) low-rise and (e - g) middle-rise buildings. ....	120
Figure 5. 16. The delineated circular building boundaries using Hough transform approach: (a) the circle shape buildings, (b) the ring shape buildings, (c) the C shape buildings, and (d) the S shape buildings. ....	122
Figure 5. 17. The delineated rectangular building boundaries using Hough transform based approach for industrial areas; (a) industrial area 1 and (b) industrial area 2.....	123
Figure 5. 18. The flowchart of the Boundary tracing based approach.....	124

Figure 5.19. The first step and the direction parameters used for the Boundary tracing algorithm .....	125
Figure 5. 20. The delineated detached building boundaries using Boundary tracing approach for urban blocks that contain (a) low-rise, (b - e) middle-rise, and (f) high-rise buildings. ....	128
Figure 5. 21. The delineated semi-detached building boundaries using Boundary tracing approach for urban blocks that contain (a - d) middle-rise and (e) high-rise buildings.....	130
Figure 5. 22. The delineated terraced building boundaries using Boundary tracing approach for urban blocks that contain (a - d) low-rise and (e - g) middle-rise buildings. ....	132
Figure 5. 23. The delineated circular building boundaries using Boundary tracing approach: (a) the circle shape buildings, (b) the ring shape buildings, (c) the C shape buildings, and (d) the S shape buildings. ....	134
Figure 5. 24. The delineated rectangular building boundaries using Boundary tracing based approach for industrial areas; (a) industrial area 1 and (b) industrial area 2.....	135
Figure 5. 25. The results of delineating a building using (a) the Hough transform based approach and (b) the Boundary tracing based approach..	137
Figure 5. 26. (a) A detected building patch and the results of delineating the circular buildings using (b) the Hough transform approach and (c) the Boundary tracing approach. ....	138
Figure 5. 27. (a) The small buildings overlaid with the reference building boundaries, (b) the detected building patches, (c) the detected building patches after removing the artefacts. ....	139
Figure 5. 28. An occluded small building overlaid with the reference building boundary. ....	139
Figure 5. 29. The closely located buildings overlaid with the reference building boundaries. ....	140
Figure 5. 30. Buildings with different roof materials illustrating different reflectance values .....	141

Figure 5. 31. Buildings showing different spectral reflectance values and spectral heterogeneity. ....	141
Figure 5. 32. The adjoining buildings that cannot be delineated separately using the developed approaches. ....	142
Figure 5. 33. Buildings having similar reflectance values with the surrounding areas. ....	142
Figure 6. 1. The flowchart of the existing building database update method. ....	145
Figure 6. 2. The boundaries of destroyed and existing buildings are represented in red and blue colors, respectively. ....	147
Figure 6. 3. For a test area, the preparation of new candidate building patches. (a) Panchromatic image, (b) detected building patches, (c) existing building boundaries overlaid with the building patches, (d) the rasterized existing building boundaries overlaid with the candidate building patches, (e) candidate building patches after masking the existing building boundaries, and (f) the candidate building patches after removing the artefacts. ....	149
Figure 6. 4. The candidate building patches. ....	152
Figure 6. 5. The existing buildings. ....	153
Figure 6. 6. (a) An existing building database and (b) a building selected as a model for the first candidate building patch. ....	155
Figure 6. 7. The centroids of building patches of an urban block. ....	156
Figure 6. 8. The centroid of a selected building model. ....	157
Figure 6. 9. The rotation of a building model over a building patch (white area) per (a) 60°, (b) 45°, (c) 30°, (d) 15°, (e) 10° and (f) 5° from 0° to 360°. ....	158
Figure 6. 10. The rotation of a polygon with a specified angle. ....	159
Figure 6. 11. (a) The rotation of a building model over a candidate building patch (white area) and (b) the true orientation of the building model found based on the intersection between the building model and the building patch. ....	160
Figure 6. 12. The updated building boundaries. The blue polygons represent the existing building boundaries, while the red polygons illustrate the updated building boundaries. ....	161

Figure 6. 13. The delineated new buildings and the reference buildings. The blue polygons represent the reference buildings, while the red polygons illustrate the delineated new buildings. ....	162
Figure 6. 14. The buildings in an urban fringe. Existing buildings and the development plan overlaid with the IKONOS false color image. ....	165
Figure 6. 15. The delineated building boundaries. Because of the artefacts on the building patches the delineated building boundaries do not correctly represent the boundaries of the buildings. The blue polygons represent the existing building boundaries, while the red polygons represent the delineated building boundaries. ....	166
Figure 6. 16. The delineated building boundaries. Because of the similar shape parameters the building models can be selected erroneously. ....	166
Figure A. 1. Photographs taken from the study area .....	189
Figure A. 2. Photographs of detached rectangular shaped residential buildings from the study area.....	191
Figure A. 3. Photographs of semi-detached rectangular shaped residential buildings from the study area.....	192
Figure A. 4. Photographs of terraced rectangular shaped residential buildings from the study area.....	193
Figure A. 5. Photographs of “circle”, “C” and “S” shaped residential buildings from the study area.....	194
Figure A. 6. Photographs of rectangular shaped industrial buildings from the study area.....	195
Figure B. 1. The panchromatic IKONOS image and five profiles .....	196
Figure B. 2. The graphic of the vertical profile. ....	197
Figure B. 3. The graphic of the horizontal profile. ....	197
Figure B. 4. The graphic of the horizontal profile 2.....	198
Figure B. 5. The graphic of the diagonal profile. ....	198
Figure B. 6. The graphic of the diagonal profile 2. ....	199
Figure D. 1. For Sub-Area I, the results of SVM classification performed using 14 Data-Sets and 1000 samples .....	218

Figure D. 2. For Sub-Area I, the results of SVM classification performed using 14 Data-Sets and 2000 samples .....	219
Figure D. 3. For Sub-Area II, the results of SVM classification performed using 14 Data-Sets and 1000 samples .....	220
Figure D. 4. For Sub-Area II, the results of SVM classification performed using 14 Data-Sets and 2000 samples .....	221
Figure D. 5. For Sub-Area III, the results of SVM classification performed using 14 Data-Sets and 1000 samples .....	222
Figure D. 6. For Sub-Area III, the results of SVM classification performed using 14 Data-Sets and 2000 samples .....	223



# **CHAPTER 1**

## **INTRODUCTION**

The collection and updating of geographic data in urban areas are very important for urban planning. The stability and maintenance of current land use information effect the success of urban plans. Geographic Information System (GIS) is a very useful tool for urban planning with its capability to store, retrieve, manipulate, analyze, and display huge amount of spatial and attribute data. However, lack of current land use information limits the efficiency of GIS in urban planning and management. Remote Sensing (RS) technologies are very important to extract geographic information and to update spatial databases.

Automatic extraction of buildings is very important for data acquisition and updating GIS databases. Therefore, it is one of the most challenging tasks in digital photogrammetry and computer vision and has been the focus of intensive research for the last decades. Traditionally, the building boundaries are acquired through manual digitization from digital images in stereo view using the photogrammetric stereoplotters. However, this process is a tiresome and time-consuming task and requires qualified people and expensive equipments. For this reason, building extraction using the automatic techniques has a great potential and importance.

High resolution satellite images provide a valuable new data source for geographic data acquisition, mapping applications and the preparation of the urban plans. During the last decade, spaceborne remote sensing experienced with a big technological development. The high resolution satellite images have been and are being used for

building extraction. On the other hand, the existing GIS databases, which include ground plans, are also available for most of the major cities. Therefore, in these cities instead of extracting all buildings, extracting new buildings and updating the GIS databases with the new building information would be more efficient.

In this study, approaches are presented for building extraction and building updating from high resolution satellite imagery. In these approaches, there are basically two main steps, which are building detection and building delineation. The building detection procedure is common for both the extraction and updating parts of the study. In the building detection part, the Support Vector Machines (SVM) classification is used to detect the candidate building patches by incorporating additional bands. In the building delineation part of the study, different approaches are used for building extraction and updating. For building extraction, the delineation from the candidate building patches is performed using two different techniques that are (i) delineation based on Hough transform, and (ii) delineation based on Boundary tracing. To delineate the building boundaries using the Hough transform based approach, initially the edges are detected from the building patch image through an edge detection algorithm. Then, the Hough transform and the perceptual grouping operations are performed. In the Boundary tracing based approach, to delineate the building boundaries, the first step is to apply an edge detection operation. Then, the boundary tracing, line simplification and the vector filtering operations are carried out.

For the building updating part of the study, a model-based approach was developed. In this approach, existing building database is used as ancillary information to facilitate the complex building extraction problem. In the developed approach, initially the destroyed buildings were determined by analyzing the existing building database and detected building patches. Then, the new buildings are delineated using the developed model based approach, which utilizes existing building database to determine the most proper building model for each candidate building patch. Then, the building boundaries are delineated by assigning the selected building model to the detected building patches.

The developed approaches were implemented in the selected study areas from the Batikent district of Ankara, Turkey, and the performances of the proposed building extraction and updating results were measured.

In this thesis, the term “building extraction” means a process that consists of the detection and the delineation steps. “Building detection” means the classification of image pixels into building regions and “building delineation” means the placement of building boundaries of the detected building patches.

### **1.1. Objectives of The Research**

The objectives of this study are as follows:

- To develop approaches for automatic building extraction from high resolution satellite imagery.
- To detect building patches through Support Vector Machines (SVM) classification of the high resolution satellite imagery using additional bands.
- To assess the effect of using the normalized Digital Surface Model (nDSM), Normalized Difference Vegetation Index (NDVI) and Principal Component (PC) images as additional bands in the classification process.
- To develop approaches for delineating rectangular and circular (circle, ring, C, and S) shaped buildings
- To develop a method for automatically updating an existing building database by utilizing the integration of Geographic Information System (GIS) and Remote Sensing (RS).
- To propose an approach that automatically selects building models from an existing building database by analyzing the shape properties.
- To determine the potential of high resolution satellite imagery for building extraction and updating.

## **1.2. The Software Used in the Study**

In this study, different software was used to perform different implementations and processing. Digital image processing and analysis operations were carried out using PCI Geomatica and ENVI software. The Orthoengine Module of the PCI Geomatica software was used for generating the Digital Terrain Model from contour lines, for generating the Digital Surface Model from IKONOS stereo pairs and for the orthorectification of the images. The Focus Module of the PCI Geomatica software was used for generating Normalized Difference Vegetation Index (NDVI), for calculating normalized Digital Surface Model (nDSM) and for performing Principal Component Analysis (PCA). The candidate building patches were detected using the SVM classification of the ENVI software. The preparation of the existing building database and the editing of the vector data were carried out using the ArcGIS and TNTMips software.

The proposed approaches were developed using the MATLAB 7 programming language. Initially, using this programming language, the morphological operations were carried out to remove the artefacts from the building patch image. Programs were also developed for the Hough transform and Boundary tracing based delineation from building patches. In the Hough transform based approach, the edge detection, Hough transform, and consequent perceptual grouping operations were performed. In the Boundary tracing based approach, the edge detection, Boundary tracing and line simplification operations were performed sequentially. In addition, a program was developed using MATLAB 7 programming language for updating the building boundaries. In this program, the shape parameters of the detected building patches and the existing building boundaries were calculated, the optimum building model was selected from the existing building database and this model was assigned to the building patch automatically.

### **1.3. Organization of the Thesis**

This thesis includes seven chapters. In the following chapter (chapter 2), an extensive literature review is given about building extraction and updating from digital images. The past studies are grouped according to the data sources used and the methodologies.

In chapter 3, the study area is described and detailed information about the raster and vector data used in the study are provided.

Chapter 4 provides the description of the building detection procedure using the SVM classification technique. First, the methodology of the proposed building detection is described. Then, the steps followed for the building detection approach are provided in detail. These steps are mainly the calculation of nDSM from high resolution satellite images, orthoimage generation, the calculation of NDVI and PCA analysis, SVM classification, and the determination of candidate building patches. Finally, the experimental results of the classification and building detection are given.

In Chapter 5, the building boundary delineation procedure from candidate building patches is presented. To delineate the building boundaries, two approaches were developed, which are (i) delineation based on Hough transform and (ii) delineation based on Boundary tracing. First, the methodology of the Hough transform approach is described. The delineation of the rectangular and circular shape buildings using this approach are explained in detail. This is followed by giving the experimental results. After the first approach, the methodology developed based on Boundary tracing is given. Next, the steps followed in this approach and the results obtained are presented. Lastly, the results of both approaches are compared and discussed.

In chapter 6, an approach, which was developed based on a model-based concept, is introduced for updating an existing building database from high resolution satellite images using. First, the methodology of the proposed approach is given. Then, the

preparation of the existing building database and the candidate building patches are described. This is followed by the explanation of the selection the building models from existing building database. After that, the steps to assign the building models to the candidate building patches are described. Finally, the experimental results are given and the results are discussed.

The final chapter (Chapter 7) presents the conclusions reached during the study of the developed approaches and recommendations are given for future studies.

## **CHAPTER 2**

### **LITERATURE REVIEW**

In this chapter, the past studies conducted for building extraction from digital images are provided. The chapter contains two main sections that are (i) building extraction and (ii) building updating. In the first section, the past building extraction studies are grouped into four parts. In the first part, the past studies for building extraction, which were conducted using aerial images, are given. In the second part, the building extraction studies conducted using the satellite imagery are summarized. In the third part, the past studies for building extraction from Digital Elevation Models are given. In the last part, the former building extraction studies from multi-source data are presented. In the second section of this chapter, the past building extraction studies conducted for updating and detecting building changes are presented.

#### **2.1. Building Extraction**

Most of the automated building extraction methods are based on aerial photographs or satellite images. However, the recent studies have suggested that using multiple data sources and combining photogrammetric tools with the GIS data in building extraction studies can be advantageous. There are studies that integrate aerial and space images with additional data sources, such as ground plans, maps, GIS data, DSM, Laser/Lidar data or SAR images for building extraction. Recently, a number of techniques based on DEM and Laser/Lidar data have been developed.

Gruen (2000) stated that multi-image approaches, multi-cue algorithms, fusion of various information sources, DSM for detection and reconstruction, derivation of DSMs from laser scanners, generic roof modeling by decomposition into parts, use of a priori knowledge from maps and GIS, and semi automated reconstruction techniques were the current trends in building extraction studies.

In the researches conducted by Mayer (1999), Sowmya and Trinder (2000), Baltsavias (2004), and Brenner (2005) the previous automatic and semi-automatic building extraction approaches were reviewed extensively. Besides, detailed literature review about building extraction from aerial images is provided by Shufelt (1999). On the other hand, the collection of the state-of-the art articles in man-made object extraction are given in the proceedings edited by Gruen et al. (1995), Gruen et al. (1997), and Baltsavias et al. (2001a).

### **2.1.1 Building Extraction from Aerial Images**

A number of research studies to extract building boundaries from aerial imagery have used a single image (Huertas and Nevatia, 1988; Irving and McKeown, 1989; Liow and Pavlidis, 1990; Lin and Nevatia, 1998; Kim and Nevatia, 1999; Bellman and Shortis, 2000; Pal et al., 2001; Peng et al., 2005; Cha et al., 2006; Katartzis and Sahli, 2008), stereo images (Sahar and Krupnik, 1999; Ruether et al., 2002; Avrahami et al., 2007) or multiple images (Henricsson, 1998; Noronha and Nevatia, 2001; Fradkin et al., 2001; Kim and Nevatia, 2004). Table 2.1, table 2.2, and table 2.3 summarize the recent building extraction studies from mono, stereo, and multiple aerial images, respectively. Most of these methods are based on edge, line, corner analysis and grouping operations (Huertas and Nevatia, 1988; Lin and Nevatia, 1998; Kim and Nevatia, 1999; Sahar and Krupnik, 1999; Kim and Nevatia, 2004; Cha et al., 2006; Katartzis and Sahli, 2008).



Table 2. 1. The previous studies for building extraction from monocular aerial images

Previous Research	Data Source	Used Methodology	Results
Huertas & Nevatia (1988)	Monocular Aerial Image	Edge and Corner Detection Boundary Tracing Shadow Information	2D Detection Delineation
Irving & McKeown (1989)	Monocular Aerial Image	Shadow Information	2D Detection Delineation
Liow & Pavlidis (1990)	Monocular Aerial Image	Edge Detection Segmentation (Region Growing) Shadow Information	2D Detection Delineation
Lin & Nevatia (1998)	Monocular Aerial Image	Edge Detection Line Linking and Approximation Method Perceptual Grouping Shadow Information	3D Detection Delineation
Kim & Nevatia (1999)	Monocular Aerial Image	Edge Detection Perceptual Grouping Neural Network Bayesian Approach	3D Detection Delineation
Bellman & Shortis (2000)	Monocular Aerial Image	Wavelet Transform Support Vector Machines	2D Detection
Pal, Swayne, & Frey (2001)	Monocular Aerial Image	Bayesian Networks Segmentation	2D Detection
Peng, Zhang, and Liu (2005)	Monocular Aerial Image	Snake Model	2D Detection Delineation
Cha, Cofer, & Kozaitis (2006)	Monocular Aerial Image	Hough Transform	2D Detection Delineation
Katartzis & Sahli (2008)	Monocular Aerial Image	Contextual Information Perceptual Grouping Bayesian Markov Random Field Model Shadow Information	3D Detection Delineation

Table 2. 2. The previous studies for building extraction from stereo aerial images

Previous Research	Data Source	Used Methodology	Results
Sahar & Krupnik (1999)	Stereo Aerial Images	Edge Detection Shadow Information	2D Detection
Ruether, Martine, and Mtaló (2002)	Stereo Aerial Image	Snake Model	2D Detection Delineation
Avrahami, Raizman, and Doytsher (2007)	Stereo Aerial Images	Region Growing Morphological Operations	3D Detection Delineation

Table 2. 3. The previous studies for building extraction from multiple aerial images.

Previous Research	Data Source	Used Methodology	Results
Henricsson (1998)	Multiple Aerial Images	Color Information Grouping	3D Detection Delineation
Noronha & Nevatia (2001)	Multiple Aerial Images	Perceptual Grouping Matching Shadow Information	3D Detection Delineation
Fradkin, Maitre, and Roux (2001)	Multiple Aerial Images	Image Segmentation Image Matching	3D Detection Delineation
Kim & Nevatia (2004)	Multiple Aerial Images	Edge Detection Perceptual Grouping Bayesian Networks	3D Detection Delineation

Ruether et al. (2002) and Peng et al. (2005) used a snake based approach to extract building boundaries. Bayesian / Neural Network Classification techniques were used in the studies conducted by Kim and Nevatia (1999), Pal et al. (2001), and Kim and Nevatia (2004). On the other hand, Bellman and Shortis (2000) used Support Vector Machines Classification technique and Wavelet Transform to detect building areas.

In a number of studies conducted for delineating the building boundaries the shadow information was utilized (Huertas and Nevatia, 1988; Irving and McKeown, 1989; Liow and Pavlidis, 1990; Lin and Nevatia, 1998; Sahar and Krupnik, 1999; Noronha and Nevatia, 2001; Katartzis and Sahli, 2008).

As another experience, various building models have been introduced to assist and automate the building extraction procedure in the last decade (Table 2.4). Building models are used to determine the building boundaries after building detection. In the model-based approaches, building extraction is achieved by first extracting object properties and then matching them to a model.

Table 2. 4. The past studies for building extraction using the model-based approaches.

Previous Research	Data Source	Used Methodology	Results
Croitoru & Doytsher (2003)	Monocular Aerial Image	Building Models Modified Pose Clustering	2D Detection Delineation
Croitoru & Doytsher (2004)	Monocular Aerial Image	Building Models Hough Transform Corner Detection	2D Detection Delineation
Rau & Chen (2003)	Monocular Aerial Image	Building Model Split-Merge Shape Method	3D Detection Delineation
Tseng & Wang (2003)	Stereo Aerial Images	Constructive Solid Geometry Least Squares Matching	3D Detection Delineation
Khoshelham & Li (2004)	Monocular Aerial Image	Building Models Canny Edge Detection Perceptual Grouping Least Squares Matching	3D Detection Delineation
Peng & Liu (2005)	Monocular Aerial Image	Building Model Shadow Information Snake Model	2D Detection Delineation

Croitoru and Doytsher (2003) described a model-based approach for building location hypothesis generation in regularized urban areas. In a study conducted by Croitoru and Doytsher (2004), the characteristics of the regularized urban areas were utilized to derive geometric constraints of the building model and then, these constraints were used for reducing the number of low-level features. To delineate building boundaries, the edge and corner detection algorithms and the subsequent perceptual grouping operations were used. Rau and Chen (2003) proposed a robust method for reconstructing building models semi-automatically from 3D line segments. In their method, the 3D line segments were manually measured from stereo aerial images and the region of interest areas were also determined manually. The Split and Merge process was used to generate enclosed regions and 3D buildings were reconstructed. In the method developed by Tseng and Wang (2003) a novel building extraction method was presented that uses the concept of fitting Constructive Solid Geometry (CSG) primitives to aerial imagery. Khoshelham and Li (2004) introduced an approach to reconstruct parametric building model from aerial images. The edges were detected from the image and the edge image was converted to line segments, which were then grouped using the perceptual grouping

technique. After that, a model matching process was used to match the building model selected from a library interactively with the grouped lines. Peng and Liu (2005) developed a methodology to extract buildings based on models and context from aerial images. Initially, the images were simplified and segmented as sunshine and shadow parts. Then, the directions of the cast shadows were estimated by a shadow context model. Finally, the extracted building boundaries were refined using a context and modified partial snake model.

However, the model-based approaches have several disadvantages. These approaches are based on the assumption that there is full knowledge of the object structure (Shufelt, 1999). In addition, the detected building patches are enforced to fit the most suitable pre-defined building models. Therefore, the delineation accuracy depends on the success of the building model library. However, determining and defining all possible building models leads to a formidable model library compilation problem (Shufelt, 1999).

### **2.1.2. Building Extraction from Space Imagery**

The high resolution satellite images are valuable data sources for geospatial data acquisition and GIS databases updating. High resolution satellite images can be preferred instead of aerial photographs, because they are cheaper and easier to access. Sunar Erbek et al. (2005) indicated that high resolution satellite images, which are alternative to aerial photography, can be used to produce land-use maps of the current status of the urban environment that can be used as base for the municipal GIS and can be used for updating existing topographic maps. There are researches that use high resolution satellite images to extract buildings. The methodologies and data used are summarized in table 2.5.

Table 2. 5. The past studies for building extraction from satellite images.

Previous Research	Data Source	Used Methodology	Results
Fraser, Baltasvias & Gruen (2002)	IKONOS MS (4m) IKONOS Pan (1m) IKONOS PSM (1m)	Manual Extraction	Delineation
Sohn & Dowman (2001)	IKONOS Pan (1m)	Local Fourier Analysis Binary Space Partitioning	Detection Delineation
Lee, Shan & Bethel (2003)	IKONOS MS (4m) IKONOS Pan (1m)	Classification Building Squaring Approach based on Hough Transform	Detection Delineation
Shackelford & Davis (2003)	IKONOS MS (4m) IKONOS Pan (1m) IKONOS PSM (1m)	Fuzzy Classifier Segmentation (region merging) Object-Based Fuzzy class.	Detection
Benediktsson, Pesaresi & Arnason (2003)	IKONOS Pan (1m) IRS 1C Pan	Morphological Operations Neural Network Classification	Detection
Jin & Davis, 2005	IKONOS MS (4m) IKONOS Pan (1m) IKONOS PSM (1m)	Morphological Operations Structural, Contextual and Spectral Information	Detection
Ünsalan & Boyer (2005)	IKONOS MS (4m)	K-means clustering Morphological Operations	Detection
Mayunga, Coleman and Zhang (2007)	Quickbird Pan (0.61 m)	Snakes Algorithm Radial Casting Algorithm	Detection Delineation

Most of the studies conducted to extract buildings from high resolution satellite images have used spectral values of the images via classification approaches. Lee et al. (2003) proposed a classification based approach to extract building boundaries from IKONOS multispectral and panchromatic images. In their approach, initially the multispectral image was classified using ECHO classifier, which is a region-based supervised classification technique. Then, the classification results were vectorized to define the working windows. After that, the panchromatic image was classified using an unsupervised classification technique to separate building from background. Lastly, the building boundaries were delineated using a building squaring approach which is based on Hough transform. A methodology that uses fuzzy pixel-based and object-based approach for classification of the pan-sharpened IKONOS images, was presented by Shackelford and Davis (2003). In their approach, first a fuzzy pixel-based classifier was performed. Then, the image was segmented and the features were derived from this segmented image. After that, to improve the

classification results, a fuzzy object-based classification, which utilizes the shape, spectral, and neighborhood features was performed using the segmented image. Benediktsson et al (2003) investigated the classification and feature extraction from panchromatic satellite images using the morphological and neural network classification approaches. Similarly, Jin and Davis (2005) presented a method based on differential morphological profile concept to extract buildings from high resolution panchromatic images.

Sohn and Dowman (2001) developed an approach to extract building boundaries from IKONOS panchromatic images. Initially, the line segments were extracted. Then, a local Fourier analysis was used to do an analysis of the dominant orientation angle in a building cluster and the line segments were regularized using this information. Finally, the building boundaries were extracted based on a binary-space partitioning.

Ünsalan and Boyer (2005) presented a novel system for automatic map generation from IKONOS multispectral images. First, multispectral image analyses were performed to detect cultural activity. Then, the images were segmented using K-means clustering algorithm and a binary image, which contains possible street network and houses, was obtained. Next, the segmented images were decomposed using a balloon algorithm based on binary mathematical morphology. Finally, to extract street networks and houses, these decompositions were represented with a weighted graph.

Mayunga et al. (2007) developed a semi-automatic method for extracting informal settlement buildings from QuickBird panchromatic images using the snakes and radial casting algorithms. The extracted buildings were compared with those extracted from aerial images. The results indicate that 15% of the buildings extracted from aerial image cannot be extracted from the QuickBird image. On the other hand, the mean coverage of the extracted buildings from the QuickBird image was calculated as 90.5%.

The studies conducted by Fraser et al. (2002) and Mayunga et al. (2007) indicate that 15% of the buildings extracted from aerial image cannot be extracted from high resolution satellite images.

### 2.1.3. Building Extraction from Laser/Lidar/DEM Data

A number of past studies for extracting building boundaries are based solely on Laser/Lidar data. Recently Laser/Lidar has become an effective technique for extracting accurate surface models and thus offers possibilities for DEM creation and feature extraction. The production of DSM using the Lidar data is a quicker and more automated process, and the high density of point measurements can offer better definition of urban features (Priestnall et al., 2000). Therefore, these aspects are encouraging the feature extraction studies using the Laser/Lidar data. Table 2.6 summarizes some of the building extraction studies in this field.

Table 2. 6. The past studies for building extraction using Laser/Lidar/DEM data

Previous Research	Data Source	Used Methodology	Results
Weidner & Forstner (1995)	DEM	Morphological Operations Thresholding Minimum description Length based approach	3D Detection Delineation
Sampath & Shan (2007)	Raw Lidar Data Sets	Segmentation-Region growing Boundary Tracing Hierarchical Least Squares Solution	2D Detection Delineation
Dash, Steinle, Singh & Baehr (2004)	Laser DEMs	Segmentation Delanuy Triangulation Modified Standard Deviation	3D Detection Delineation
Ma (2005)	Lidar Points Lidar DEM	Segmentation Boundary Regularization	2D Detection Delineation
Forlani, Nardinocchi, Scaioni, Zingaretti (2006)	Lidar Points	Segmentation Rule Based Classification	3D Detection Delineation
Madhavan, Wang, Tanahashi, Hirayu, Niwa, Yamamoto, Tachibana, Sasagawa (2006)	Laser DEMs	Segmentation Edge Detection Hough Transform	3D Detection Delineation
Miliaresis & Kokkas (2007)	Lidar DEMs	Segmentation-Region growing K-Means Classification	2D Detection

There are basically two groups of studies to extract buildings from Laser/Lidar/DEM data. In the first group, the building extraction is performed from the raw point clouds (Ma, 2005; Forlani et al., 2006; Sampath and Shan, 2007), while in the second group the buildings are extracted from the Laser/Lidar DEMs or DEMs generated from stereo image pairs (Dash et al., 2004; Madhavan et al., 2006; Miliareisis and Kokkas, 2007). Generally, the 3D buildings are extracted from the Laser/Lidar data because it provides comparatively more accurate elevation data.

A new method was presented by Ma (2005) to extract ground points for DEM generation, to detect the building points, and to regularize the building boundaries. Forlani et al. (2006) introduced a methodology for the classification of Lidar data, which was followed by the 3D reconstruction of buildings. In their methodology, first, the raw Lidar data were filtered and interpolated over a grid. Then, segmentation was carried out and geometric and topological relationships between the segmented regions were computed and stored in a knowledge base. Finally, a rule based scheme was applied for the classification of the regions and polyhedral building models were reconstructed. The approach proposed by Sampath and Shan (2007) focused on building boundary tracing and regularization from raw Lidar point clouds. Initially, the raw Lidar points were separated as ground and non-ground points and the buildings were segmented using a moving window. Then, a modified convex hull formation algorithm was applied to trace the building boundaries. Finally, the building boundaries were regularized using a hierarchical least squares solution.

To extract building boundaries from Laser/Lidar DEMs or DEMs generated from stereo image pairs, generally the initial step used in the previous studies are segmentation of the DEMs to obtain building patches/blobs. Weidner and Förstner (1995) attempted to extract buildings from high resolution DEMs. In their study, first, a DEM was generated and then, approximation of topographic surface was computed using the morphological operations. Next, the difference image (DEM – approximate topographic surface) was thresholded to detect the building patches and the buildings were reconstructed using the parametric and prismatic building models.



Finally, the extracted polygons were simplified using the Minimum Description Length based approach. Dash et al. (2004) proposed an algorithm to extract the building boundaries from Laser DEMs to be used as an input for disaster management. Their building extraction procedure includes segmentation, triangulation and modified standard deviation algorithms consecutively. In an approach developed by Madhavan et al. (2006), the DSM was robustly segmented into stable planar regions. Then, the edges were determined using the Sobel edge detector and a sequential Hough transformation was applied for extracting the building boundaries. In a recent study conducted by Miliareisis and Kokkas (2007), a segmentation-based method was presented for the extraction of building class from Lidar DEMs.

#### **2.1.4. Building Extraction from Multi-Source Data**

In a number of past studies conducted for building extraction, the integration of multi-source data was used. Combining aerial/space images with other data sources, such as DSMs, GIS data, ground plans/maps, or knowledge may become advantageous in the building extraction and reconstruction applications. Therefore, a large body of research appears to have focused on using additional data, such as ground plans, maps, GIS data, knowledge, etc. In table 2.7 the past studies that use multi-source data in building extraction process are summarized.

In a considerable number of past studies for building extraction, the attempt was to combine aerial and satellite images with DEM data (Haala and Brenner, 1999; Fujii and Arikawa, 2002; Zhou et al. 2004; Khoshelham et al., 2005; Rottensteiner et al., 2005, 2007; Hongjian and Shiqiang, 2006; Sohn and Dowman, 2007; Rottensteiner et al., 2007 and Lee et al., 2008). Of these studies, Haala and Brenner (1999), Rottensteiner et al., (2005, 2007) used classification, while Khoshelham et al. (2005), Lee et al. (2008) used segmentation to detect building patches. Haala and Brenner (1999) presented a method that combines aerial image and Laser altimeter data. They generated a DSM from Laser data and derived a DTM by applying morphological operations to DSM. Then, nDSM was generated by subtracting DTM from DSM.

The nDSM was then used as additional channel in combination with the three spectral bands (CIR aerial image) in the ISODATA unsupervised classification. In the studies conducted by Rottensteiner et al. (2005, 2007), a method was developed for detecting the buildings using the Dempster-Shafer fusion of the airborne Laser data and multispectral aerial images. This fusion technique handles incomplete information. Then each pixel is classified to the determined classes. To remove the small areas that are erroneously classified as building morphological operations were used. Finally, to eliminate spurious initial building regions second Dempster-Shafer fusion process were applied. The results indicate that the proposed classification approach is compatible for building detection.

Table 2. 7. The past studies for building extraction from multi-source data

Previous Research	Data Source	Used Methodology	Results
Haala & Brenner (1998)	DSM Existing Ground Plans	Planar Segmentation Algorithm	3D Detection Delineation
Haala & Brenner (1999)	Multispectral Aerial Images Laser Data 2D Ground Plan	Unsupervised Classification (ISODATA)	3D Detection Delineation
Fujii & Arikawa (2002)	Aerial Images Laser Data	Vertical Geometric Pattern Analysis Object Modeling Texture-Mapping	3D Detection Delineation
Gamba & Houshmand (2002)	SAR, Lidar Aerial Images	Classification	3D Detection Delineation
Zhou, Song, Simmers & Cheng (2004)	Aerial Images Lidar Data	Edge Detection	3D Detection Delineation
Suveg & Vosselman (2004)	Aerial Images Maps	Constructive Solid Geometry Minimum Description Length	3D Delineation
Khoshelham, Li & King (2005)	Color Aerial Images (Stereo) DSM	Watershed Segmentation Split and Merge Technique Robust Regression Method	3D Detection Delineation
Rottensteiner, Trinder, Clode & Kubik (2005 and 2007)	Multi-spectral Aerial Images Lidar Data	Morphological filtering Dempster-Shafer Method	2D Detection
Hongjian & Shiqiang (2006)	Aerial Image Sparse Laser Sample Data	Laplacian Sharpening Threshold Segmentation Line matching	3D Detection Delineation
Sohn & Dowman (2007)	High Resolution Satellite Imagery Lidar Data	Binary Space Partitioning	2D Detection Delineation
Lee, Lee & Lee (2008)	Lidar Data Aerial Images	Segmentation (Mean-Shift) Line Segments Matching Perceptual Grouping	2D Detection Delineation

Khoshelham et al. (2005) introduced a split and merge technique to fuse aerial image and DSM generated from stereo aerial image for building extraction. In their study, initially the gradient magnitude images were computed. Then, these images were segmented into homogenous regions using the Watershed Segmentation. After that, a Split and Merge technique, which uses the height data, was applied to the segmented images of the buildings. Finally, the buildings were reconstructed. Lee et al. (2008) proposed a new algorithm to extract building boundaries by combining Lidar and aerial imagery. First, the building regions were extracted from Lidar points. The vegetation areas were removed using the second order gradient. Next, coarse building regions were detected using the Mean-Shift segmentation procedure. A merging algorithm, which is based on preliminary detected building regions and their heights, were then applied to combine separate segments of a single building. Finally, the precise building boundaries were delineated using line segments matching and perceptual grouping.

Sohn and Dowman (2007) presented a new approach to extract building footprints by fusing pan-sharpened high resolution satellite imagery and Lidar data. The technique is composed of two steps that are building detection, and building description. In the building detection step, the buildings are localized by subsequently removing urban features that are not buildings. In the building description step, the detected buildings are focused on. Then, based on the Binary Space Partitioning tree algorithm, the Building Unit Shape method was proposed for reconstructing building boundaries. An approach was proposed by Hongjian and Shiqiang (2006) for building reconstruction from aerial image and Laser data. To extract the edges from imagery the Laplacian sharpening operator and threshold segmentation were used. Then, pixel connectivity and subsequent bi-direction histogram and line matching were utilized to extract the building boundaries. Fujii and Arikawa (2002) presented a method for 3D reconstruction of the buildings from airborne laser elevation data and aerial images using the vertical geometric analysis of the elevation data and texture mapping of the aerial images.

The existing GIS datasets can be used as additional information to extract building boundaries from images. Since the building outlines are difficult to be located precisely ground plans/maps are often used. Several studies have been performed to reconstruct the building boundaries with the help of building outlines derived from a 2D GIS (Haala and Brenner, 1998; Haala and Brenner, 1999; Suveg and Vosselman, 2004). In this way, the search problem and the building detection problem are eliminated. In a study conducted by Haala and Brenner (1998), an approach was developed that uses DSM and 2D ground plans to reconstruct 3D buildings. They used ground plans to support DSM segmentation and to derive hypotheses on the possible roof shapes. Suveg and Vosselman (2004) described a 3D building reconstruction method that integrates stereo aerial images with the information from 2D GIS databases and domain knowledge. They suggest that map information should be considered imprecise and uncertain when used for image analysis. Therefore, they processed more accurate aerial images and used map data to help image interpretation. First, the buildings were localized in the images based on the information from the ground plans of the buildings contained in the GIS database. Then, a building library that contains building models was generated. Next, the complex buildings were described using the Constructive Solid Geometry (CSG) tree, in which the leaf nodes contain primitive building models. The results indicate that the system is able to reconstruct more than 75% of the buildings and the accuracy of the reconstruction is good enough for mapping purposes.

Several researchers attempted to combine SAR and optical data to extract the buildings. Gamba and Houshmand (2002) used aerial SAR and Lidar data to extract land cover, DTM, and 3D building shape and they discriminate different objects using their 2D and 3D characteristics. Tupin and Roux (2003) proposed a method for extracting rectangular and complicated shapes. In this method, initially partial potential building footprints were extracted from optical images using the previously extracted primitives.

## 2.2. Building Extraction for Map Updating

Fast urbanization necessitates extensive map updating of large urban areas. The extraction of buildings for map updating can be carried out either by extracting all buildings within the study area or by first determining the change areas and then, extracting the new buildings and/or deleting the destroyed ones. Today, most of the cities likely to have digital maps and GIS data sets, which would facilitate the automatic updating systems of the maps and databases. Using the existing data can greatly improve the efficiency of spatial databases updating and reduce the time needed. As Brenner (2005) indicated that instead of targeting at the first time acquisition of the city models, more and more effort must be put into updating and automatic change detection to keep existing models up-to-date at minimum costs. In table 2.8 the former building extraction studies for map updating and change detection are summarized.

Table 2. 8. The past studies conducted for building extraction to update maps and detect changes

Previous Research	Data Source	Used Methodology	
Murakami, Nakagawa, Hasegawa, Shibata & Iwanami (1999)	Laser DEMs	Change Detection	2D
Huertas & Nevatia (2000)	Aerial Images Site Models	Change Detection	3D Detection Delineation
Teng & Fairbairn (2002)	Aerial Images	Fuzzy Expert System Adaptive Neuro-Fuzzy System	2D Detection
Niederost (2002)	Aerial Images Digitized 1:25000 map	Classification	3D Detection Delineation
Knudsen & Olsen (2003)	Aerial Images National Topographic Map Database (TOP10DK)	Unsupervised Spectral Classification Mahalanobis Classification	2D Detection
Jung (2004)	Multitemporal Stereo Aerial Images	Classification	2D Detection Delineation
Holland, Boyd & Marshall (2006)	High Resolution Satellite Images		2D Detection Delineation

Murakami et al. (1999) presented a method to detect changes of the buildings and update the building database using the DSM data sets that were acquired at different times. They simply subtracted the DSM data sets from each other. In a study conducted by Huertas and Nevatia (2000), the aerial images and site models were used to detect the building changes. Their method basically contains four steps that are site model to image registration, site model validation, structural change detection, and site model updating. Teng and Fairbairn (2002) utilized a fuzzy expert system and an adaptive neuro-fuzzy system to train, adapt, and recognize objects in three complex aerial scenes. Niederost (2002) presented a methodology for map updating. This methodology consists of two steps which are vegetation separation from man-made objects using unsupervised isoclustering and blob detection from nDSM. In this study after detecting the building blobs, various approaches were developed for building reconstruction. Knudsen and Olsen (2003) proposed a method for building detection using vector and spectral data to update digital map databases. In their method, it was assumed that new buildings were spectrally similar to existing buildings in the same area. First, aerial photo and map data were fused. Then, building classes were divided into a number of spectrally more homogeneous clusters by using an unsupervised classification. The homogenous clusters were then used as training sets in the next step, Mahalanobis Classification. The results of the change detection tests showed that in most cases the changes were detected. Jung (2004) attempted to detect building changes from aerial stereopairs for geographic database updating. Initially, DEMs were generated from multitemporal stereo images, and region of interest areas were determined by comparing these DEMs. Then, the region of interest areas of four images (stereopairs images of two dates) was classified as building and non-building. Finally, the classification results of changes were compared and the building changes were determined.

Holland et al. (2006) examined the potential of high resolution satellite sensor imagery for topographic map updating. They concluded that, high resolution satellite images with meter or sub-meter resolution can be used to update 1:6000 - 1:10000 scaled maps and these images may have greater potential in change detection and existing map data examination.

In addition, building extraction for map updating is very important when extensive damage of buildings is the case after a disaster. There are studies conducted to resolve this problem. Turker and San (2004) and Turker and Sumer (2008) detected collapsed buildings utilizing the integrated processing and analysis of post-earthquake aerial imagery and existing vector building boundaries. Turker and Cetinkaya (2005) detected the collapsed buildings using DEMs created from pre- and post-earthquake stereo aerial photographs.

## **CHAPTER 3**

### **THE STUDY AREA AND DATA SETS**

In this chapter first, the study area is described. Then, detailed information about the raster and vector data sets used in the study is provided.

#### **3.1. The Study Area**

The selected study area is located in the Batikent district of Ankara, the capital city of Turkey (Figure 3.1). Batikent is situated in north-west of Ankara. The northern parts of the study area are rugged and steep, while the middle and the southern parts, where the residential areas exist, are relatively flat. In the area, the height range is between 710m and 1140m.

The Batikent Project, which was implemented in the area, is the biggest mass housing project through cooperatives in Turkey. The project covers 10 square kilometers and planned for 50000 housing units and 250000 people. The project was started in 1979 by Kent-Koop (Union of Batikent Housing Construction Cooperatives), which was constituted by associations and labor unions of artisans under the leadership of the Metropolitan Municipality of Ankara. This project was the first mass housing project that reveals the success of public and private partnerships in the housing field in Turkey (Batikent, Kent-Koop, 2007). Therefore, Batikent is a planned and regularly developed settlement, which includes buildings with different shapes and usage, such as the residential and industrial facilities. Thus, the area was suitable for implementing the developed building extraction and updating techniques from high resolution space imagery.



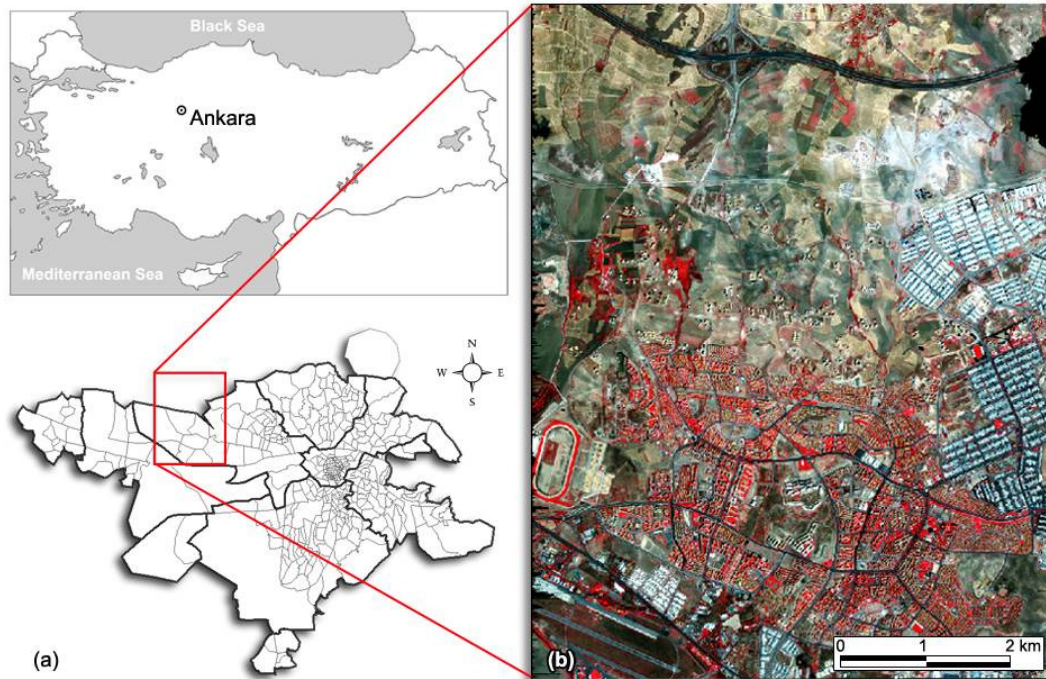


Figure 3. 1. The location of the study area: (a) The Batikent district of Ankara and (b) the false color composite of the IKONOS pan-sharpened image covering the study area.

In the selected area of study, different types of buildings exist according to their usage, dwelling type, and storey. The photographs taken from the study area are given in Appendix A. The residential buildings are usually rectangular/square and the mutual lines are usually parallel to each other, while the angles between the adjacent lines are perpendicular. In addition to rectangular and right angle shaped buildings, the area also contains buildings with different shapes, such as circular, ring, C and S shapes (Figure 3.2). The roofs of most of the buildings are in brick color however, several exist in gray and white colors. In the area, there are low-rise (one or two storeys), middle-rise (three-to-five storeys) and high-rise (more than five storeys) residential buildings. The area contains two industrial zones that are namely Ivedik and OSTIM. These industrial zones are specialized especially on machine and machine equipments, electric and electronics, metal and metal treatment, plastic rubber automotive, technical tools, benches and equipments. The industrial buildings are usually in rectangular shape and their roofs are in gray, white, and blue colors.

Almost all of the industrial buildings are two or three storeys buildings and compared with the residential buildings they have much larger sizes. In the present study, the buildings were classified as given in table 3.1.

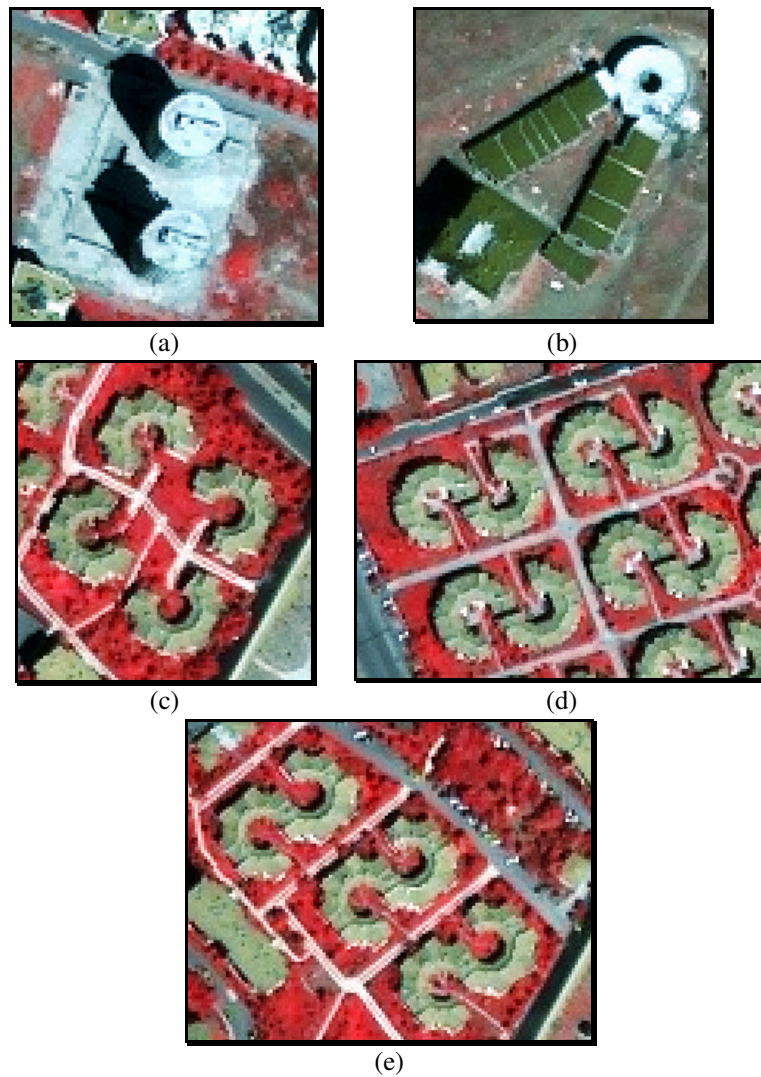


Figure 3. 2. The false color composite of IKONOS pan-sharpened image of the circular buildings (a) the “circle” shape buildings, (b) the “ring” shape building, (c), (d) the “C” shape buildings and (e) the “S” shape buildings

Table 3. 1. The classification of the buildings

I. Residential Buildings	
I.1. Rectangular	I.2. Circular
I.1.1. Detached	I.2.1. “Circle” Shape
I.1.1.1. Low-rise buildings	I.2.2. “Ring” Shape
I.1.1.2. Middle-rise buildings	I.2.3. “C” Shape
I.1.1.3. High-rise buildings	I.2.4. “S” Shape
I.1.2. Semi-Detached	
I.1.2.1. Low-rise buildings	
I.1.2.2. Middle-rise buildings	
I.1.2.3. High-rise buildings	
I.1.3. Terraced	
I.1.3.1. Low-rise buildings	
I.1.3.2. Middle-rise buildings	
I.1.3.3. High-rise buildings	
II. Industrial Buildings	
II.1. Rectangular	

### 3.2. Data

The data sets used include the IKONOS stereo panchromatic and pan-sharpened images, the existing digital vector database, and the development plans. In the building delineation part of the study, only the raster data sets were used. On the other hand, in the building database updating part of the study, both the raster and vector data sets were used.

#### 3.2.1. Raster Data

The raster data used include the IKONOS Panchromatic and Pan-Sharpended Stereo Images. The IKONOS images were acquired on August 4, 2002. They were along

track stereo images and in “Geo” data format, which is the most economical product within all IKONOS products. Accuracy of the Geo product, specified pre-launch at 250m CE90, turned out to be significantly better with an accuracy of 15m CE90 exclusive of terrain displacement (Dial et al., 2003). The collection parameters of the IKONOS image pairs are given in table 3.2.

Table 3. 2. The information about the IKONOS stereo image pairs used in the study.

	Left Stereo	Right Stereo
Date	2002-08-04	2002-08-04
Time (local)	08:54	08:55
Nominal Collection Azimuth (°)	3.8600	225.1120
Nominal Collection Elevation (°)	64.82024	81.16643
Sun Angle Azimuth (°)	145.1390	145.5635
Sun Angle Elevation (°)	63.98285	64.07870

At the time this study was started (2003), the high resolution space images had been collected using two satellites, which are IKONOS and QuickBird. Of these satellites, the IKONOS image was selected to be used in this study. There are two main reasons for selecting the IKONOS image. First, the studies have shown that the IKONOS Geo stereo imagery has higher geometric integrity and the potential to generate sub-metre positioning accuracies (Baltsavias et al., 2001b). Second, the IKONOS images provide better matching than the QuickBird images and therefore, they provide better DSMs. Toutin (2004) compared the DSMs generated from IKONOS and QuickBird images and found that the DSM generated from IKONOS images gave slightly better results.

### 3.2.2. Vector Data

The vector data sets used include:

- Existing Vector Database,

- Contour Lines and 3D Points,
- Existing Building Database,
- Reference Building Database, and
- Development Plan.

The Contour Lines and 3D points were used to generate the Digital Terrain Model (DTM). The Existing Building Database was used for the updating part of the study and the Development Plans were used to determine the boundaries for building extraction. To assess the accuracies of the results, the existing building database was updated and the reference building database was generated.

- **Existing Vector Database**

The 1:1000-scale existing digital vector data with approximately 20cm accuracy both in planimetry and height were available. The database includes Contour Lines, 3D points, and Existing Digital Building Database. The vector data was referenced to Datum ED 50 and Transverse Mercator (Gauss - Krueger) projection. The parameters of the Transverse Mercator projection system are given in table 3.3.

Table 3. 3. The parameters of the Transverse Mercator Projection System

True Origin		False		Scale
Longitude	Latitude	Easting	Northing	
33°00'00.0000"E	0°00'00.0000"N	500000.000	0.000	1.0000000000

- **Contour Lines and 3D Points**

The 1:1000-scale contour lines and 3D points were available and these data sets were used for DTM generation. In turn, this DTM will be used as the reference data for

assessing the accuracy of the generated DSM. The 1:1000-scale contour lines were drawn with 50cm interval.

- **Existing Building Database**

The existing building database, which was generated in 1999 from stereo aerial images, was available in digital form. There was a three-year time lapse between the date of image acquisition (2002) and the date of existing vector building database (1999). The existing building database was used for selecting the building models for the database updating part of the study (Chapter 6).

- **Reference Building Database**

To evaluate the results of the proposed building extraction, the existing building database was updated and the reference building database was generated. To do that the disappeared and the new buildings were visually detected from the screen. Then, the reference building database was generated by deleting the disappeared buildings and manually delineating the boundaries of the new buildings.

In the Existing Building Database, the building boundaries were delineated from the footprints of the buildings and not from the rooftops. However, in the present case, the buildings from high resolution satellite imagery will be delineated from their rooftops. Therefore, since the image used in this study is not a true orthoimage the delineated boundaries will not match with the footprints. Thus, the existing building boundaries were slightly shifted in order to precisely match them with the rooftops of the buildings.

The height difference between rooftops and footprints of the buildings causes relief displacement in aerial/satellite images. The amount of displacement changes according to the heights of the buildings as well as the viewing angle. As can be seen in figure 3.3, the building with white roof has one storey. Therefore, no shift is necessary for this building, while for other buildings, which are much higher, a shift is needed.



Figure 3. 3. The reference building database (a) before and (b) after shifting the existing building boundaries.

- **Development Plan**

An implementary development plan shows the base for urban blocks, their density and arrangement, roads and the implementation stages, which are necessary for the implementation on a 1:1000 scale map and that control the development and the construction details within an urban zone.

The existing development plans, obtained from the Metropolitan Municipality of Ankara, were in paper form. Therefore, these maps were first converted into raster form by scanning them and then, they were georeferenced. Next, the boundaries of the urban blocks were manually digitized from the georeferenced plans. The scanned paper maps and the digitized urban blocks are illustrated in figures 3.4 and 3.5, respectively. The boundaries of the digitized urban blocks were used to determine the boundaries for building extraction.



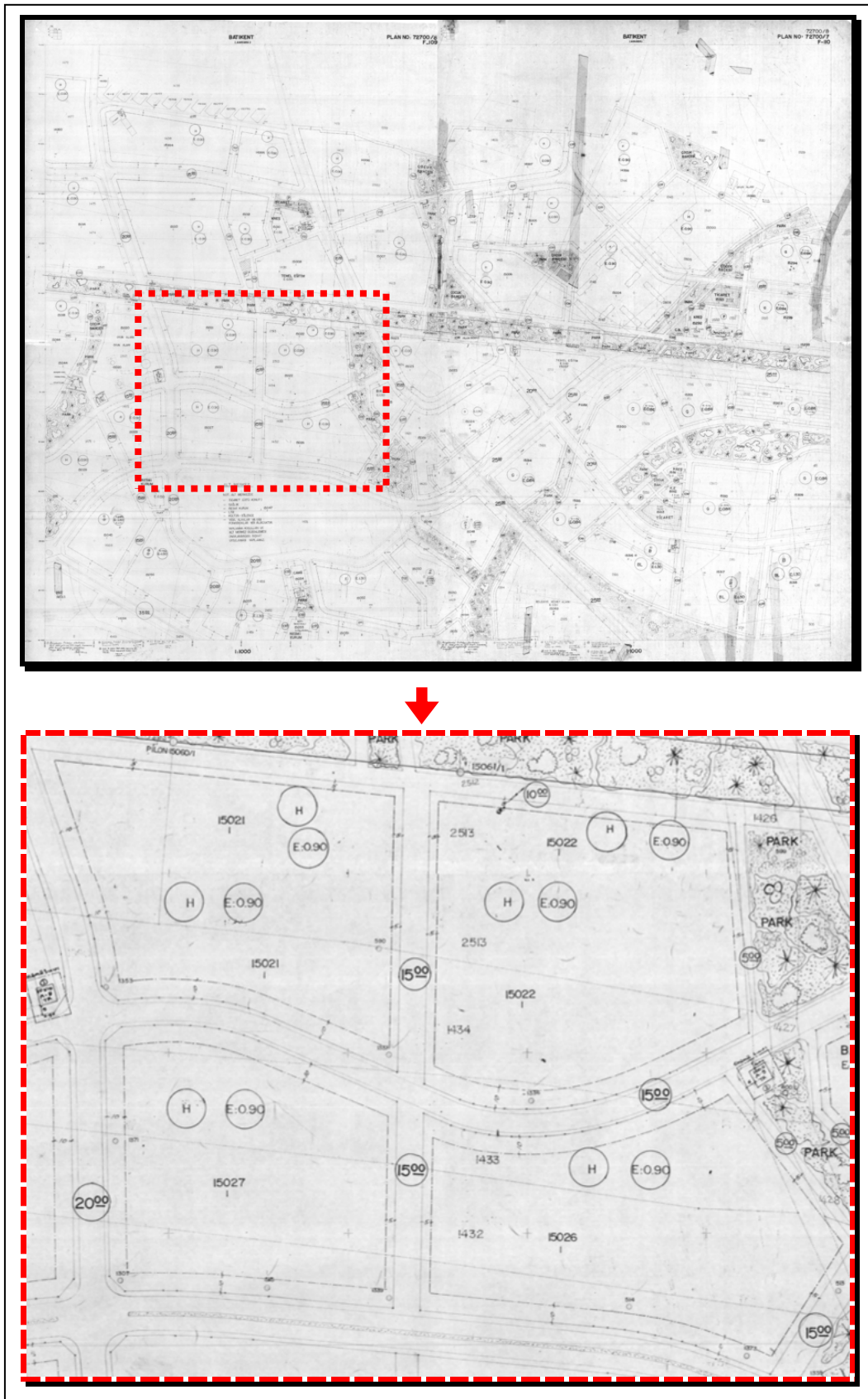


Figure 3. 4. The scanned development plans.



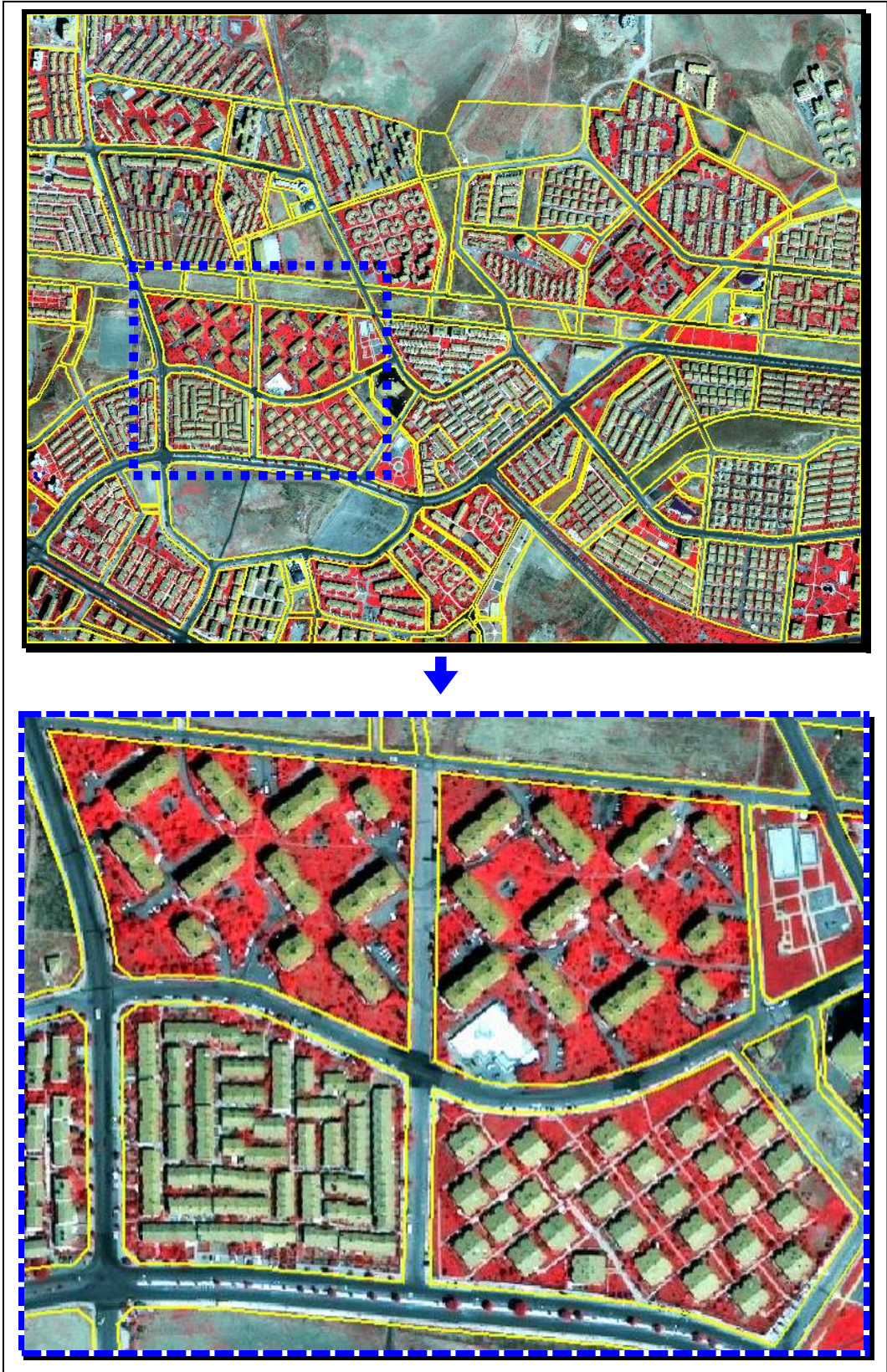


Figure 3. 5. The false color pan-sharpened IKONOS satellite image with the digitized urban block boundaries overlaid.

## **CHAPTER 4**

### **BUILDING DETECTION THROUGH SUPPORT VECTOR MACHINES CLASSIFICATION**

In this chapter, the building detection part of the study is described. For three study areas, the Support Vector Machines (SVM) classification conducted using three different sample sizes (500, 1000 and 2000) and different band combinations are given and the accuracy assessment results are discussed. First, the methodology of the developed building detection procedure is described. Then, the preparations of the additional bands, which are used in the classification process, are explained. After that, the steps of the SVM classification are provided. Finally, the experimental results of the SVM classification are given.

#### **4.1. The Methodology**

In this study, before delineating the building boundaries and updating the existing building database, the candidate building patches are detected first. The steps followed in detecting the building patches are as follows;

- Calculating the Normalized Digital Surface Model (nDSM),
- Orthoimage Generation,
- Calculating the Normalized Difference Vegetation Index (NDVI),
- Principal Component Analysis (PCA),
- Support Vector Machines (SVM) Classification, and
- Determination of the Candidate Building Patches.

The flowchart for detecting the candidate building patches is given in Figure 4.1. First, a Digital Terrain Model (DTM) is generated from existing vector data, which includes contour lines and 3D points. Then, a Digital Surface Model (DSM) is generated from high resolution stereo panchromatic image pairs. After generating the DTM and DSM, a normalized Digital Surface Model (nDSM) is calculated by subtracting DSM from DTM. This is followed by generating an orthoimage from the high resolution satellite images using the DSM. Next, a Normalized Difference Vegetation Index (NDVI) and the Principal Components (PC) (PC1, PC2, PC3 and PC4) are calculated. To detect the candidate building patches, the orthorectified pan-sharpened image along with additional bands (nDSM, NDVI, PC1, PC2, PC3, and PC4) is classified using the SVM classifier. Finally, the artefacts are removed using the morphological operations. Through image classification procedure, the building and non-building patches are detected and the non-building patches are excluded from the further building delineation procedure.

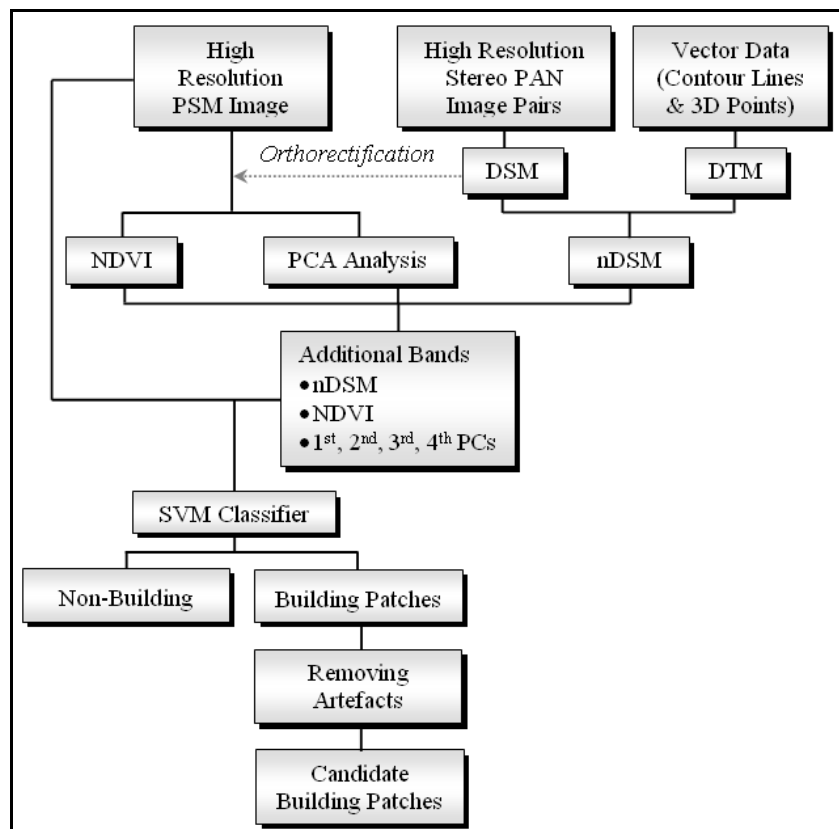


Figure 4. 1. The flowchart of the building detection procedure.



## 4.2. Test Areas

In order to perform the classification, three sub-areas that show different characteristics (residential, industrial) were selected from the study area (Figure 4.2). The Sub-Area I covers the residential part of Batikent and includes buildings with different shapes, sizes, and dwelling types. In this area, the buildings have different colored roofs. The Sub-Area II was also selected from the residential part of Batikent, and compared with Sub-Area I this area includes more regular buildings. Sub-Area II also contains buildings with different colored roofs, shapes, and sizes. The Sub-Area III covers an industrial part of Batikent, where the roofs are usually in gray tones. The sizes of the industrial buildings are larger than the residential buildings located in Sub-Area I and Sub-Area II.

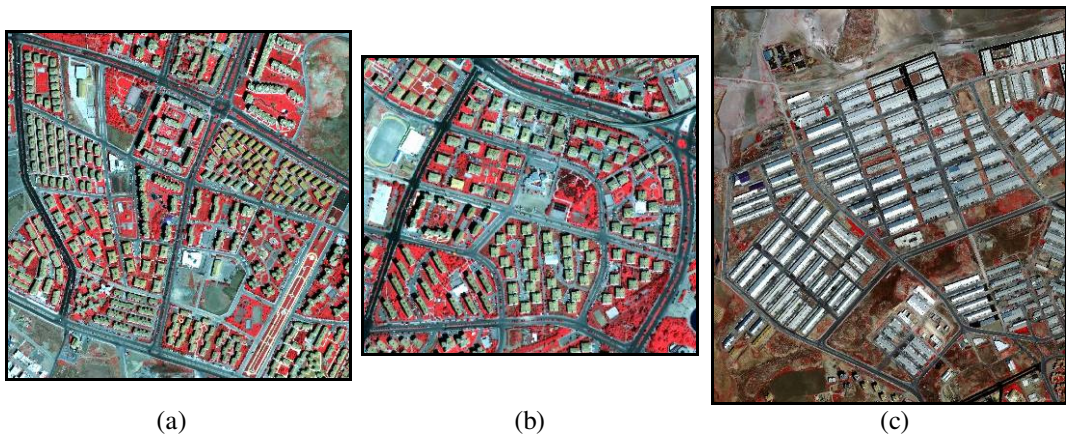


Figure 4. 2. The selected sub-areas: (a) Sub-Area I, (b) Sub-Area II, and (c) Sub-Area III.

## 4.3. Calculating the Normalized Digital Surface Model

In building extraction, the basic idea of using an nDSM is that the man-made objects with different heights above the terrain can be detected by applying a threshold to nDSM (Figure 4.3). To calculate nDSM, a DSM was generated from IKONOS stereo panchromatic images and a DTM was generated from contour lines. Then, an nDSM was calculated by subtracting DTM from DSM.

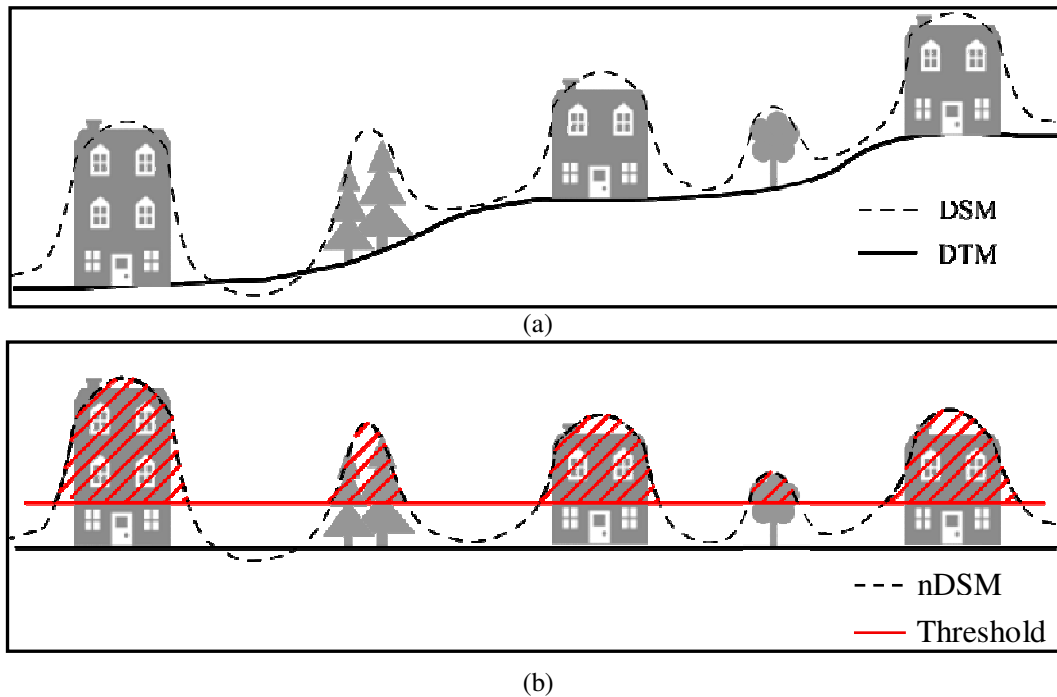


Figure 4. 3. The schematic representations of (a) the DTM and DSM, and (b) the nDSM and the applied threshold.

#### 4.3.1. Calculating the Digital Surface Model

A Digital Surface Model (DSM) includes objects with a height over ground as well as topography. Therefore, DSM is an important data source for the building extraction studies. A DSM can be derived by stereo matching from aerial/space images, measured directly by a laser/Lidar scanner system, or it can be generated from digitized topographic maps. In this study, the DSM was generated from high resolution panchromatic stereo satellite images. This is because it is cheaper and easier to access to stereo satellite images when compared with the aerial images and Lidar data. On the other hand, in Turkey, which is a developing country, it is rather difficult to get Lidar data because of the bureaucratic complexity and its relatively higher cost.

Therefore, in the present case, a DSM was generated from the stereo pairs of the IKONOS panchromatic images using the OrthoEngine module of the PCI Geomatica software. From the IKONOS stereo images, it is possible to generate a DEM with

1.5m to 3m accuracy. In preparation for the launch of high resolution civilian satellites, it was demonstrated that IKONOS stereo images can have a potential for generating DEMs with about 2m (Ridley et al., 1997).

The DSM generation using the OrthoEngine Module of the PCI Geomatica software contains the following four steps;

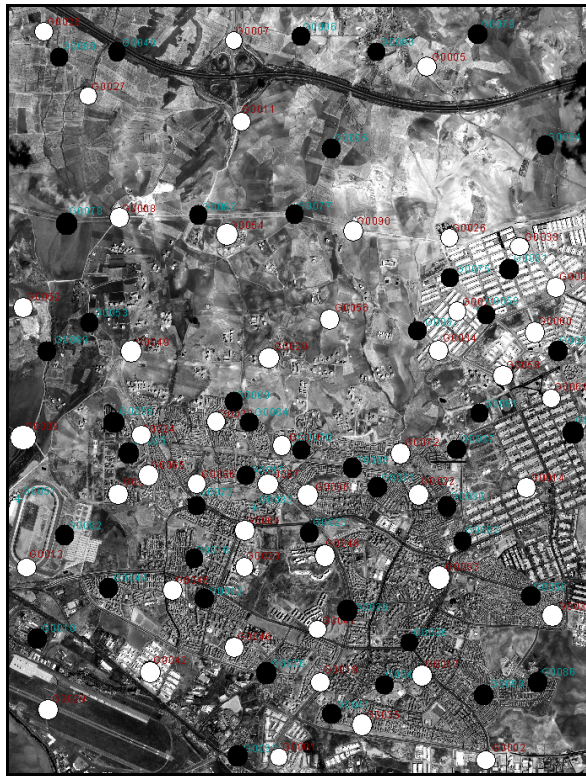
- (i) GCP Collection,
- (ii) DSM Generation,
- (iii) DSM Editing and Geocoding, and
- (iv) Accuracy Assessment.

#### (i) GCP Collection

The Ground Control Points (GCPs), which are necessary to calculate the stereo model, were collected using Differential Global Positioning System (DGPS) and from existing 1:1000-scale digital orthophotos and maps. For both GCP collection methods, the GCPs were homogeneously distributed within the study area (Figure 4.4).

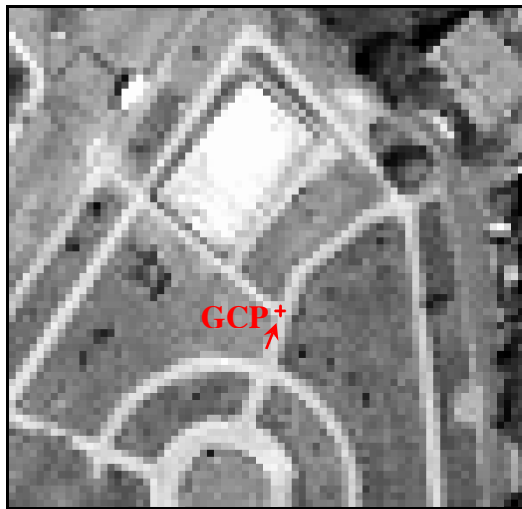
In the DGPS method, the double frequency sensor type Ashtech Z-Surveyor GPS receivers were used. A total of 48 GCPs were collected from open space that provide appropriate satellite viewing and usually from the corners of pavements and gardens and from road intersections (Figure 4.5). After the fieldwork, the raw DGPS data were evaluated using the Ashtech Office Suite V2.0 software. At the end of these processes, the GCPs were acquired with approximately 1cm accuracy in Transverse Mercator (TM) projection and European Datum 1950 (ED 50).

In addition, 48 points were also collected from existing digital orthophotos and digital maps. The GCPs were selected from those points that can be clearly seen in digital orthophotos and maps. The projection system and the datum of digital orthophotos and maps were also Transverse Mercator and European Datum 1950 (ED50), respectively.



- GCP (Ground Control Point)
- ICP (Independent Check Point)

Figure 4. 4. The locations of the collected GCPs (white points) and ICPs (black points) on the IKONOS panchromatic image.



(a)



(b)

Figure 4. 5. The location of a GCP (a) in the panchromatic satellite image (the red arrow indicates the direction of the photograph) and (b) in the field.

## (ii) DSM Generation

Three DSMs were generated from the IKONOS stereo panchromatic images. The first DSM was generated using the control points collected through DGPS. Of the 48 DGPS points, 24 were used as GCPs, and the remaining 24 points were used as Independent Check Points (ICPs). The second DSM was generated using the control points collected from digital orthophotos and maps. Similar to the first DSM, for the generation of the second DSM, 24 points were used as GCPs and the remaining 24 were used as ICPs. The third DSM was generated using the all collected points (96 points in total). Of these points, 48 were used as GCPs and the remaining 48 were used as ICPs.

The DSMs were generated using the OrthoEngine Module of the PCI Geomatica software, in which the Toutin's rigorous mathematical model is used. This model was developed at the Canada Centre for Remote Sensing (CCRS), Natural Resources Canada. The model can be used for high and low resolution satellite imagery. The model has been adapted to the IKONOS images by considering the image characteristics and metadata file (Toutin and Cheng, 2001). It reflects the physical reality of the complete viewing geometry and reflects all the distortions generated during the image acquisition as follows (Toutin and Cheng, 2002):

- (1) Distortions due to the platform,
- (2) Distortions due to the sensor,
- (3) Distortions due to the earth, and
- (4) Deformations due to the cartographic projection.

When generating the DSM using the OrthoEngine module of the PCI Geomatica software, the 3D stereo model computation is initialized with the approximate parameter values and then refined by an iterative least-squares bundle adjustment with the GCPs. After finding the optimum parameters, the next step is image matching. To increase the speed of the correlation process and reduce the possibility of incorrect matches during the image matching operation epipolar images are



generated from the stereo image pairs. Epipolar images are stereo pairs that are reprojected so that the left and right images have a common orientation (PCI Geomatics, 2006). The matching algorithm used generates correlation coefficient values between 0 and 1, where 0 represents a total mismatch and 1 represents a complete match. Then, a second-order surface is fitted around the maximum correlation coefficients to find the match position to sub-pixel accuracy. The difference in location between the images provides the disparity, or parallax, arising from the terrain relief. The parameters used in DSM generation are given in table 4.1. Pixel sampling interval controls the size of the pixel in the final DEM relative to input images. Erroneous pixel value is the value given to the failed pixels during DEM generation and the background pixel value is the value given to the background pixels.

Table 4. 1. The parameters used in DSM generation.

Pixel Sampling Interval	Erroneous Pixel Value	Background Pixel Value
2	- 100	- 150

### (iii) DSM Editing and Geocoding

The computed DSM is not georeferenced and it contains errors. Therefore, first the erroneous pixels must be removed and then, the DSM must be geocoded. Due to the problems in correlation, the matching of some of the pixels failed and therefore, this caused erroneous pixels in the DSM. In the present case, the errors were due to the bright roofs (Figure 4.6 (a)) and the cloud shadows in the image. To remove erroneous pixels (Figure 4.6 (b)), the DSM was edited using the masking, interpolation, and the filtering operations of the OrthoEngine module of PCI Geomatica. The edited and filtered DSMs are illustrated in figures 4.6 (c) and 4.6 (d), respectively. Finally, the resulting DSM was geocoded (Figure 4.7).

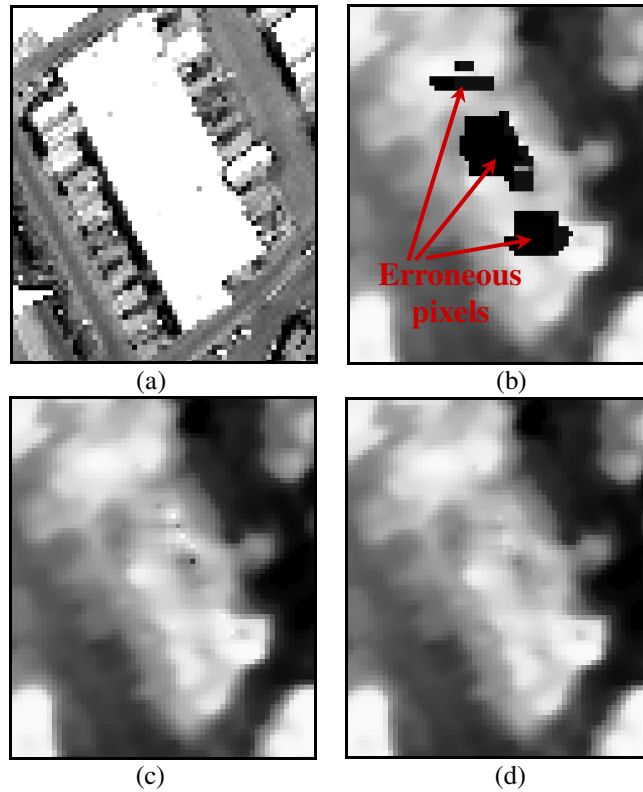


Figure 4. 6. (a) A building with a bright roof in the IKONOS panchromatic satellite image and (b) the erroneous pixels in the DSM corresponding to this building. The DSM (c) after applying an editing process to remove the erroneous pixels and (d) after filtering the edited DSM.

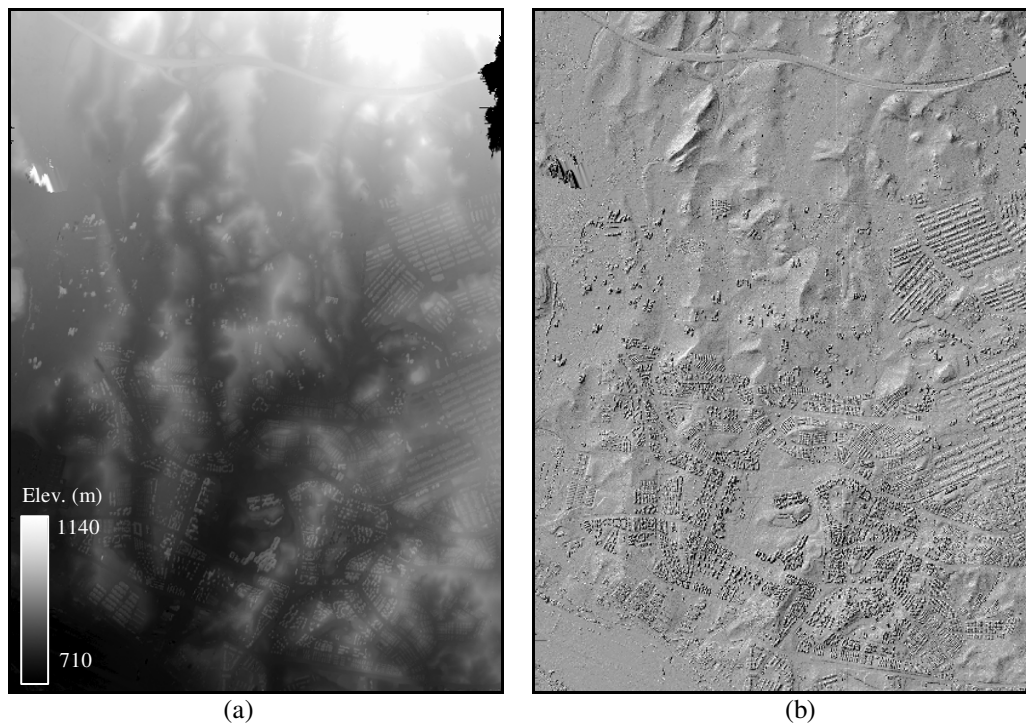


Figure 4. 7. (a) The DSM after the editing and geocoding operations and (b) a shaded relief of the surface.

(vi) Accuracy Assessment

The generated DSMs were assessed using two methods. In the first method, the accuracy assessment was performed using the ICPs. In the second method, the accuracy assessment was performed by comparing the profiles that were taken from the generated DSM and the reference DTM.

In the first evaluation method, the Root Mean Square Errors (RMSEs) were calculated for the generated three DSMs using both GCPs and ICPs (Table 4.2). In addition, for each DSM, the minimum, maximum, and mean Z errors were also calculated (Table 4.3).

Table 4. 2. The RMSEs of the DSMs, which were generated using the GCPs collected through DGPS, from orthophotos and maps, and using all GCPs.

GPS Source	Images	RMSE (m)									
		Ground Control Points (GCPs)					Independent Check Points (ICPs)				
		No of GCPs	XY	X	Y	Z	No of ICPs	XY	X	Y	Z
DGPS	Left	24	0,41	0,31	0,26	0,7	24	0,49	0,35	0,34	0,5
	Right		0,44	0,29	0,33			0,44	0,26	0,36	
Orthophoto and Maps	Left	24	0,47	0,28	0,38	0,6	24	0,65	0,44	0,48	0,7
	Right		0,47	0,31	0,35			0,58	0,38	0,44	
All points	Left	48	0,45	0,31	0,32	0,7	48	0,55	0,36	0,42	0,6
	Right		0,49	0,33	0,36			0,65	0,37	0,53	

Table 4. 3. The Z value errors of the DSMs, which were generated using the GCPs collected using DGPS, from orthophotos and maps, and all GCPs.

GPS Source	Z Value Errors	No of GCPs	GCP	No of ICPs	ICP
DGPS	Mean Error (m)	24	0,58	24	0,36
	Maximum Error (m)		1,80		1,00
	Minimum Error (m)		0		0
Orthophoto and Maps	Mean Error (m)	24	0,49	24	0,53
	Maximum Error (m)		1,50		1,20
	Minimum Error (m)		0		0
All points	Mean Error (m)	48	0,56	48	0,46
	Maximum Error (m)		1,50		1,70
	Minimum Error (m)		0		0

In the second evaluation method, the elevations from DSM and reference DTM were compared using the profiles taken in horizontal, vertical, and diagonal directions. For all profiles, the computed minimum, maximum, and the mean errors are illustrated in table 4.4. The reference DTM illustrates the topography and it does not include the heights of the objects, such as buildings and trees. Therefore, the 3D objects were masked out from the generated DSMs. An example profile and the comparison between DSM and DTM are given in figure 4.8. For the five transects, the elevation profiles of DSM, DTM and their locations are given in Appendix B.

Table 4. 4. The Z value errors of the transects of DSMs, which were generated using the GCPs collected using DGPS, from orthophotos and maps, and all GCPs.

GPS Source	Error	Profiles				
		Vertical	Horizontal1	Horizontal2	Diagonal1	Diagonal2
DGPS	Mean Error (m)	0,62	0,57	0,73	0,71	0,69
	Max. Error (m)	6,59	2,77	3,28	8,15	3,76
	Min. Error (m)	0	0	0	0	0
Orthophoto and Maps	Mean Error (m)	0,57	0,58	0,62	0,67	0,71
	Max. Error (m)	4,87	2,86	3,51	5,90	4,12
	Min. Error (m)	0	0	0	0	0
All points	Mean Error (m)	0,57	0,53	0,65	0,64	0,62
	Max. Error (m)	6,88	2,90	4,45	5,88	3,80
	Min. Error (m)	0	0	0	0	0

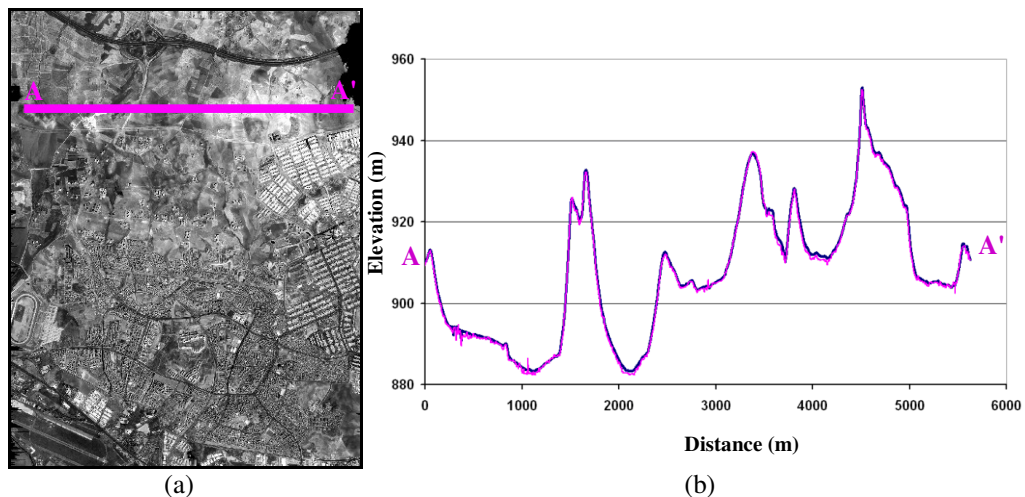


Figure 4. 8. (a) A horizontal profile in the panchromatic IKONOS image and (b) the comparison between the generated DSM and the reference DTM along this profile.

The assessment results indicate that no significant difference exist between the three DSMs that were generated using different GCP sources. The accuracy of each DSM generated using the automatic image matching technique was computed to be approximately 0.7m. On the other hand, a significant difference was not observed between the DSMs generated using 48 and 96 control points. Therefore, it was found that increasing the number of control points too much do not necessarily increase the accuracy considerably.

The results indicate that a RMSE between  $\pm 0.5\text{m}$  and  $\pm 0.7\text{m}$  can be achieved in DSMs generated from IKONOS panchromatic stereo images using the GCPs with high accuracy. It was found that the DSM generated using the DGPS points provided slightly better results. Therefore, in this study, the DSM generated using the DGPS points was used.

#### **4.3.2. Calculating the Digital Terrain Model**

A Digital Terrain Model (DTM) is the elevation model for landscape other than the altitude of the land surface and it does not include the above ground objects. A DTM can be generated from contour lines or from the ground points of Lidar/Laser data. In this study, DTM was calculated from existing digital vector database which includes contour lines and 3D points using the “Import and Build DEM” menu of the Orthoengine Module of PCI Geomatica (figure 4.9). For DTM generation, this module uses finite difference interpolation method and performs the interpolation in three steps. First, the vector elevation values are allocated into the corresponding pixels in the raster DEM. Then, the elevations of the remaining pixels are interpolated using the Distance Transform algorithm by estimating the values allocated in the first step. Finally, the raster DEM is smoothed iteratively using the Finite Difference algorithm. During the iterations, the pixels that are allocated in the first step are kept originally, while the interpolated pixel values are updated based on the neighborhood values (PCI Geomatics, 2006).

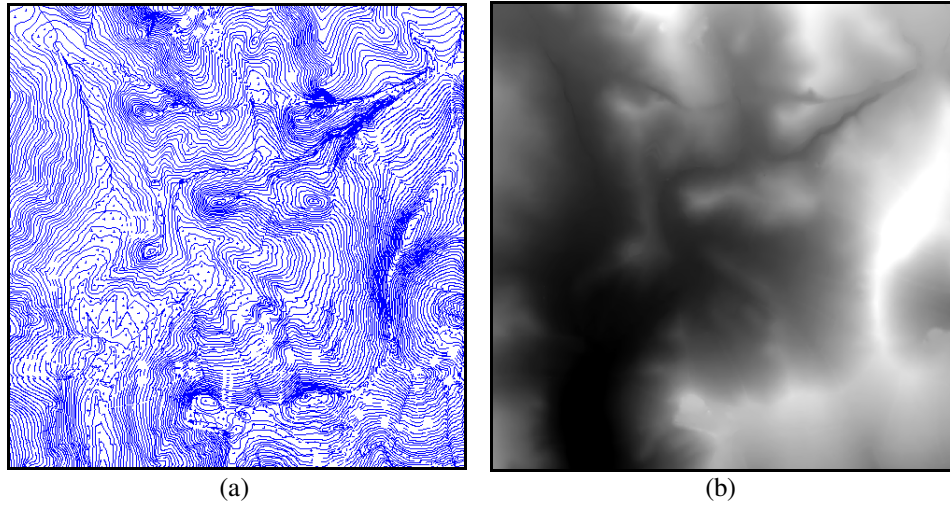


Figure 4. 9. (a) A subset from the contour lines and (b) the generated DTM.

In the present case, the resolution of the DTM generated was taken to be 1m and the DTM was referenced to Transverse Mercator (TM) projection and Datum 1950 (ED 50). The generated DTM and the shaded relief of the terrain are illustrated in figures 4.10 (a) and 4.10 (b), respectively.

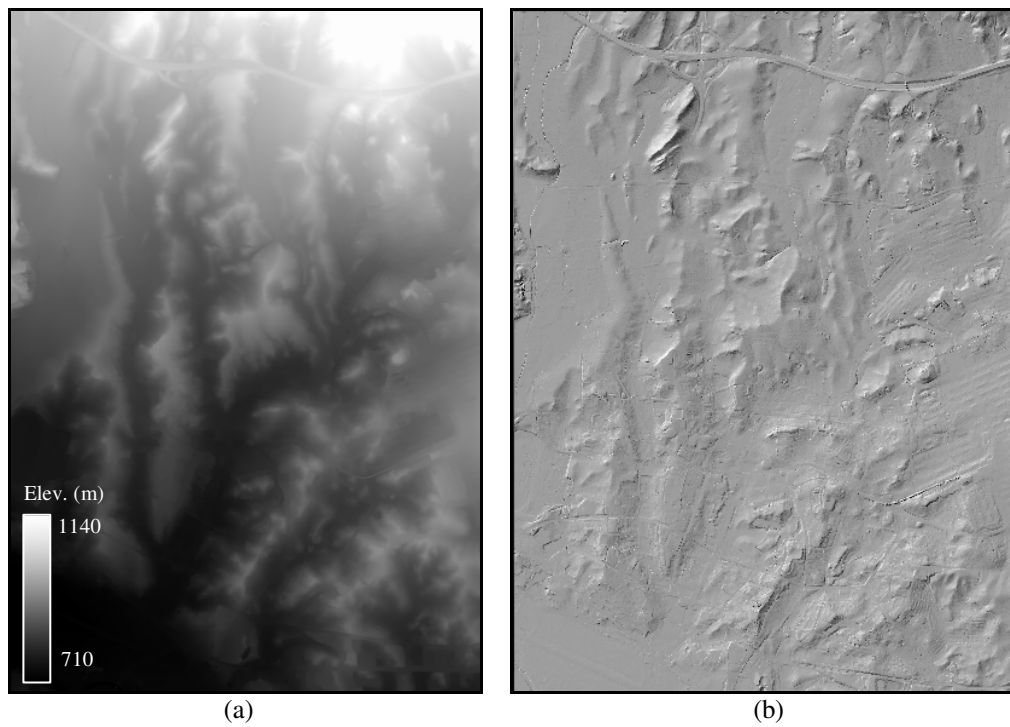


Figure 4. 10. (a) The DTM and (b) the shaded relief of the terrain.

### 4.3.3. nDSM Calculation

After computing the DTM and DSM, the nDSM was calculated by subtracting DTM from DSM (Equation 4.1).

$$DN_{(nDSM)} = DN_{(DSM)} - DN_{(DTM)} \quad (\text{Equation 4.1})$$

Next, a threshold was applied to nDSM for separating the above ground features from the terrain surface. In this study, the threshold value was determined to be 3m based on the assumption that the heights of the buildings cannot be below 3m. The calculated nDSM and the nDSM after applying the 3m threshold are illustrated in Figures 4.11 (a) and 4.11 (b), respectively. In figures 4.12, 4.13, and 4.14, the shaded relieves of DTM, DSM, and nDSM after thresholding are illustrated for the selected three sub-areas that have different characteristics.

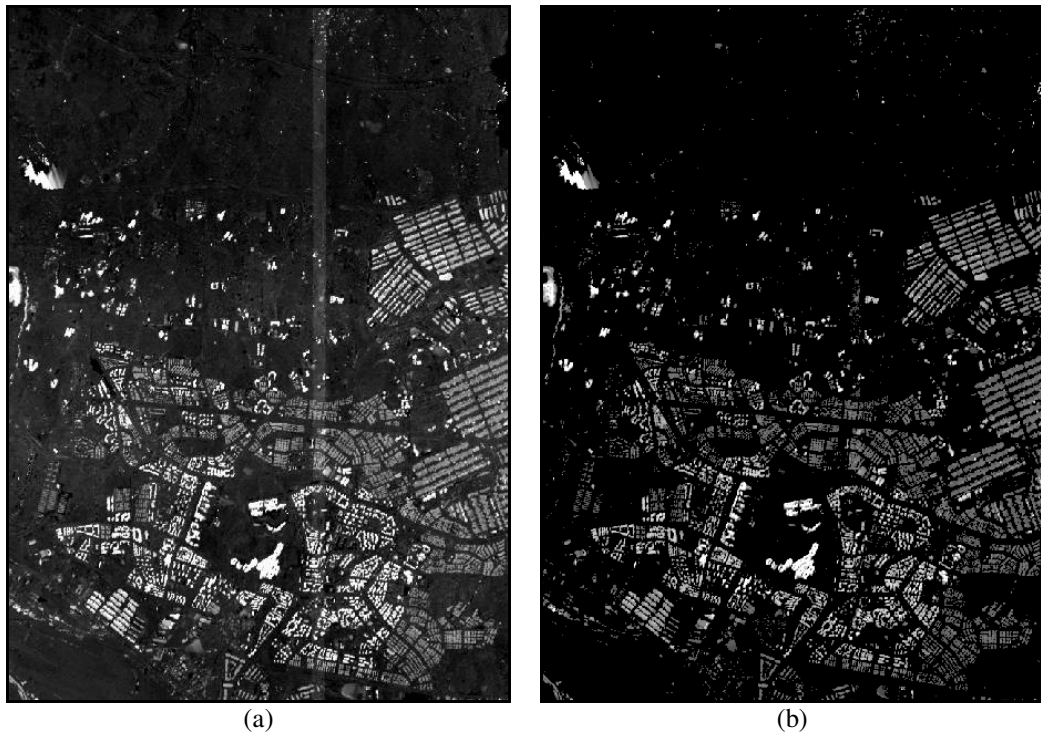


Figure 4. 11. (a) The calculated nDSM and (b) nDSM after applying a threshold.



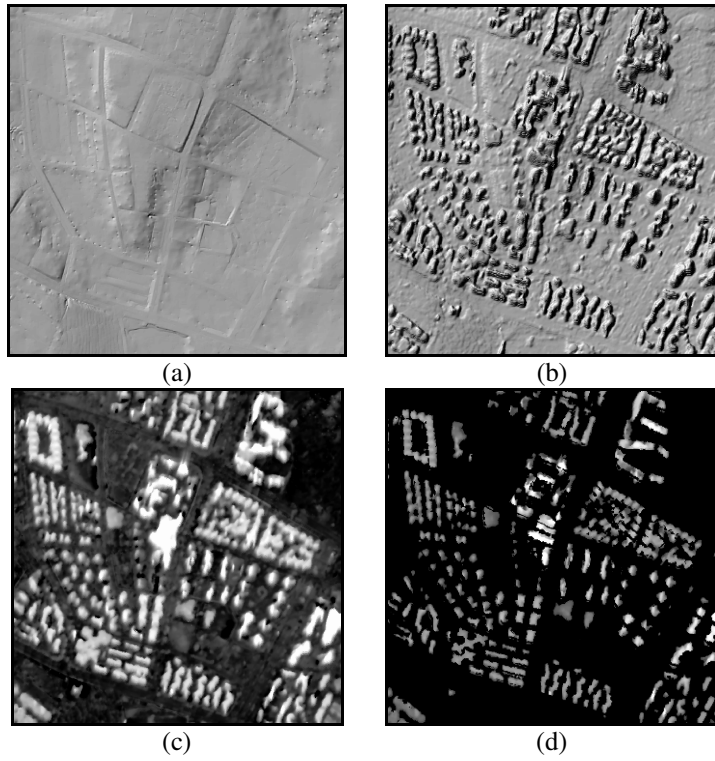


Figure 4. 12. For Sub-Area I, (a) the DTM, (b) the DSM, (c) the nDSM, and (d) the thresholded nDSM images.

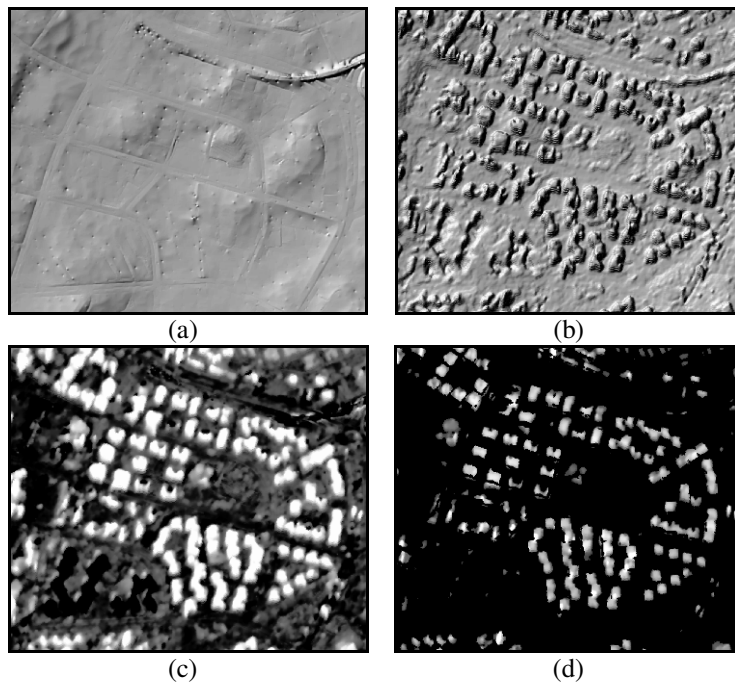


Figure 4. 13. For Sub-Area II, the (a) the DTM, (b) the DSM, (c) the nDSM, and (d) the thresholded nDSM images.



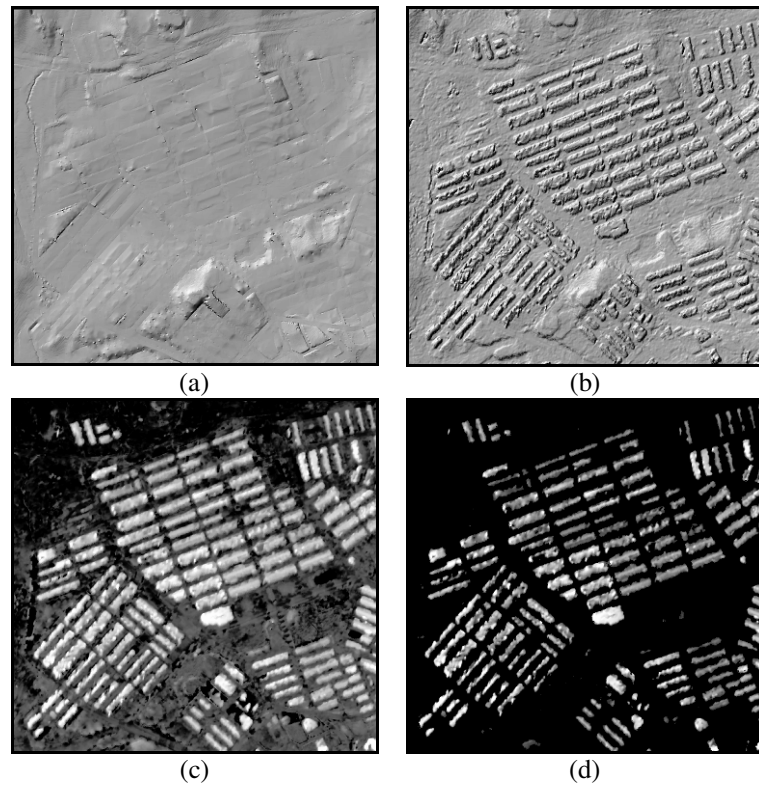


Figure 4. 14. For Sub-Area III, (a) the DTM, (b) the DSM, (c) the nDSM and (d) the thresholded nDSM images.

#### 4.4. Orthorectification

The topographic variations on earth surface and the tilt of the sensors affect the distance with which features on satellite or aerial images are displayed. Before rectification, the features in aerial or satellite images cannot be shown in their correct locations due to displacements caused by the terrain relief and the tilt of the sensor. The orthorectification process transforms the central projection of an image into an orthogonal view of the ground with uniform scale, thereby removing the distorting affects of terrain relief and tilt optical projection (Tao et al., 2004).

To correct relief displacements for images with medium or low resolutions, a DTM is required. However, aerial photos and high resolution satellite images can provide a great deal of ground information including man-made structures. Thus, the surface

discontinuity caused by buildings should be taken into account during the orthorectification procedure. Under such circumstances, a DSM delineating the canopy of the object surface is preferable (Rau et.al., 2002). Therefore, in this study, to orthorectify the high resolution stereo satellite images the DSM was used.

In this study, the IKONOS images used are Geo product with about 15m accuracy. Therefore, to remove geometric distortions including relief displacement, the orthoimages were generated. This was necessary to overlay the images with the existing GIS database accurately and use them as the base map for feature extraction. For orthorectifying the panchromatic and pan-sharpened IKONOS satellite images, the DSM generated from the IKONOS panchromatic stereo images was used. The IKONOS images before and after the orthorectification are illustrated in figures 4.15 (a) and 4.15 (b), respectively.



Figure 4. 15. The IKONOS pan sharpened image with the vector building boundaries overlaid (a) before orthorectification and (b) after orthorectification.

#### **4.5. Calculating the Normalized Difference Vegetation Index**

The Normalized NDVI is used to detect the vegetated areas in an image. The NDVI image was calculated using the red and near-infrared bands of the orthorectified IKONOS pan-sharpened images using the following equation (Equation 4.2);

$$NDVI = \frac{PSM 4 - PSM 3}{PSM 4 + PSM 3} \quad (\text{Equation 4.2})$$

where; PSM4 is the NIR band and PSM3 is the red band of the IKONOS pan-sharpened satellite image. The values of the NDVI image range from -1 to 1. Therefore, these values were rescaled from 0 to 255 using the following equation (Equation 4.3):

$$NDVI = \frac{PSM 4 - PSM 3}{PSM 4 + PSM 3} * 128 + 127.5 \quad (\text{Equation 4.3})$$

The vegetated areas were separated from non-vegetated areas using an empirically determined threshold value of 145. The NDVI image and the segmented vegetation areas after applying a threshold are given in figures 4.16 (a) and 4.16 (b), respectively. For the selected three sub-areas, the generated NDVI images are illustrated in figure 4.17.

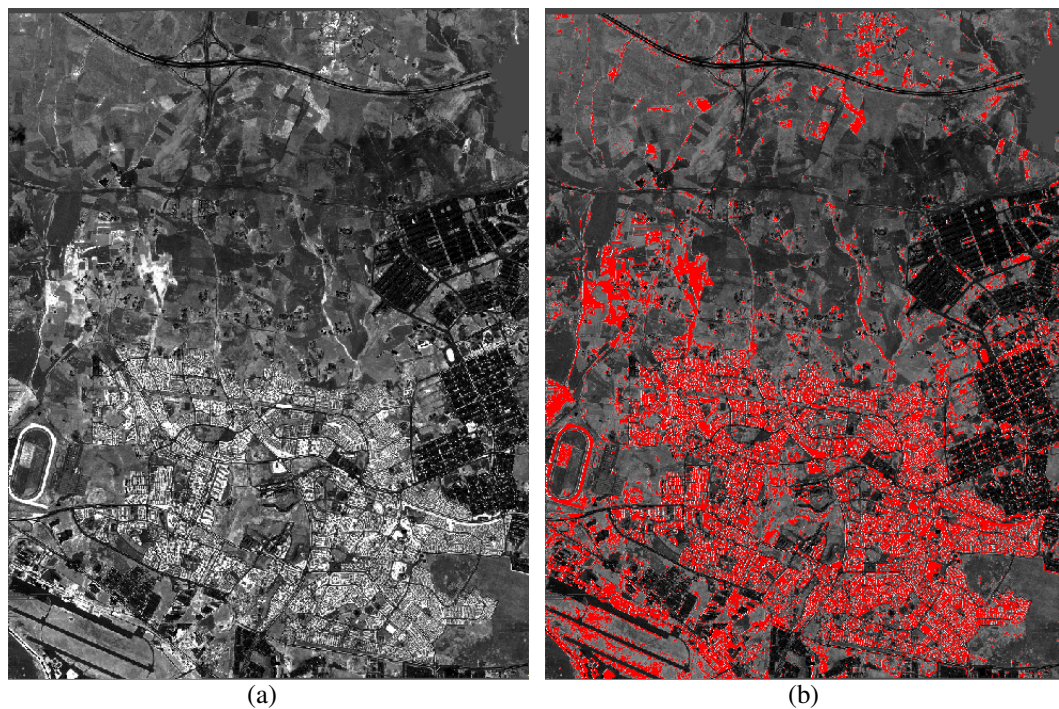


Figure 4. 16. (a) The NDVI image and (b) bitmap after applying a threshold to NDVI image.



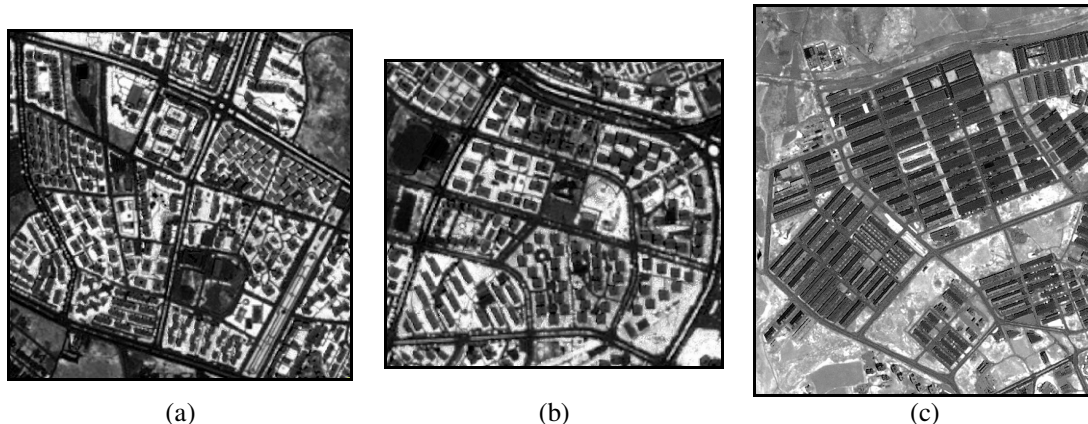


Figure 4. 17. The calculated NDVI images for (a) Sub-Area I, (b) Sub-Area II, and (c) Sub-Area III.

#### 4.6. Principal Component Analysis

Principal Component Analysis (PCA) is a technique designed to reduce redundancy in multispectral data (Lillesand and Kiefer, 1999). It is mainly used to reduce the number of bands. Singh and Harrison (1985) claim that the results of PCA may be more interpretable than the original data. In the present case the PCA was performed using the IKONOS pan-sharpened image bands (red, green, blue and NIR). The principal components generated (four components) are illustrated in figure 4.18. In figure 4.19, the principal components of three sub-areas are given. It is evident that when compared with the other components, the buildings can be differentiated more clearly in the 2<sup>nd</sup> and 3<sup>rd</sup> components. The spectral statistics of the original IKONOS pan-sharpened images and the principal components are provided in tables 4.5 and 4.6, respectively.

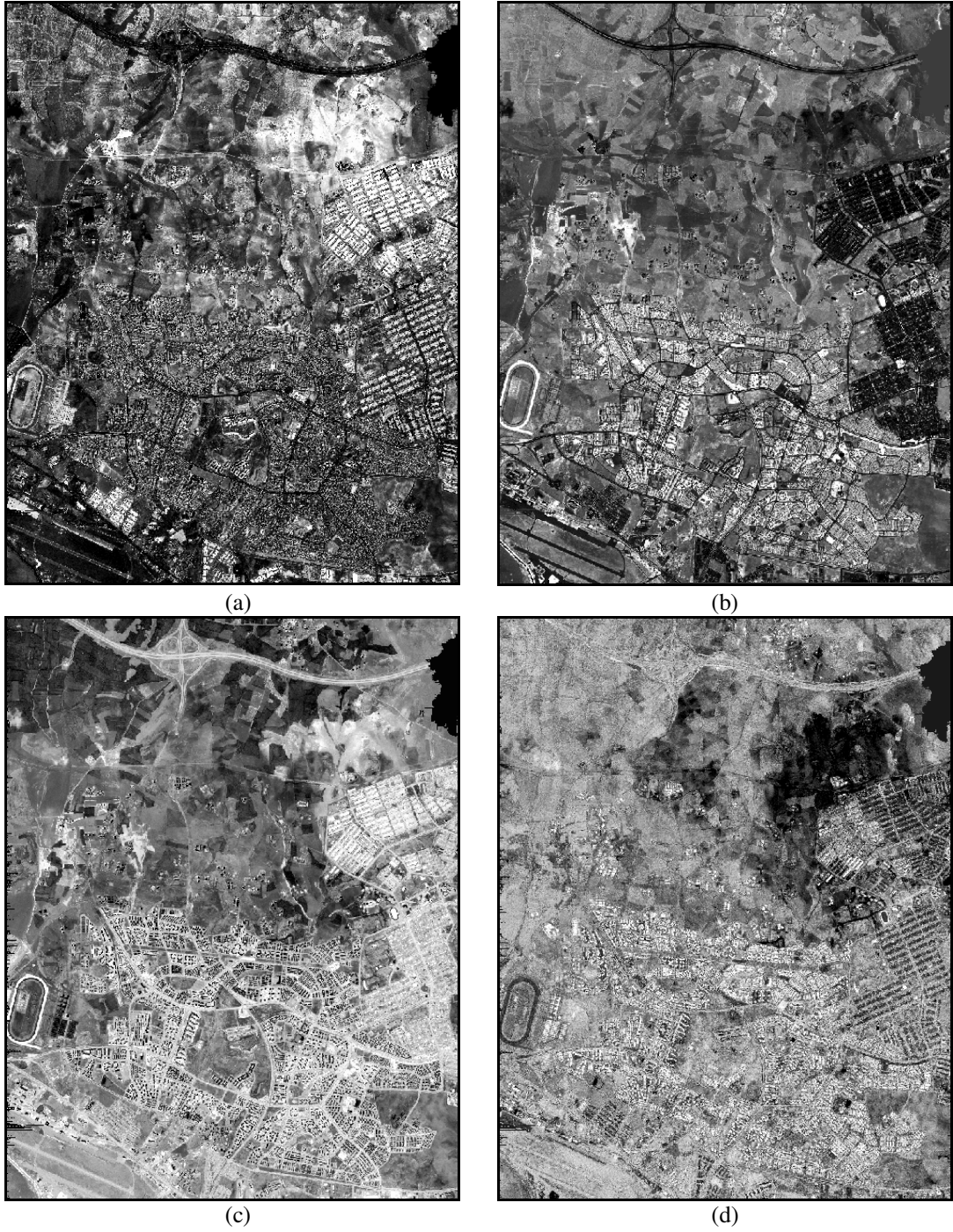


Figure 4. 18. The results of principal component analysis of the IKONOS Pan-Sharpener Image: (a) 1st PC, (b) 2nd PC, (c) 3rd PC and (d) 4th PC.



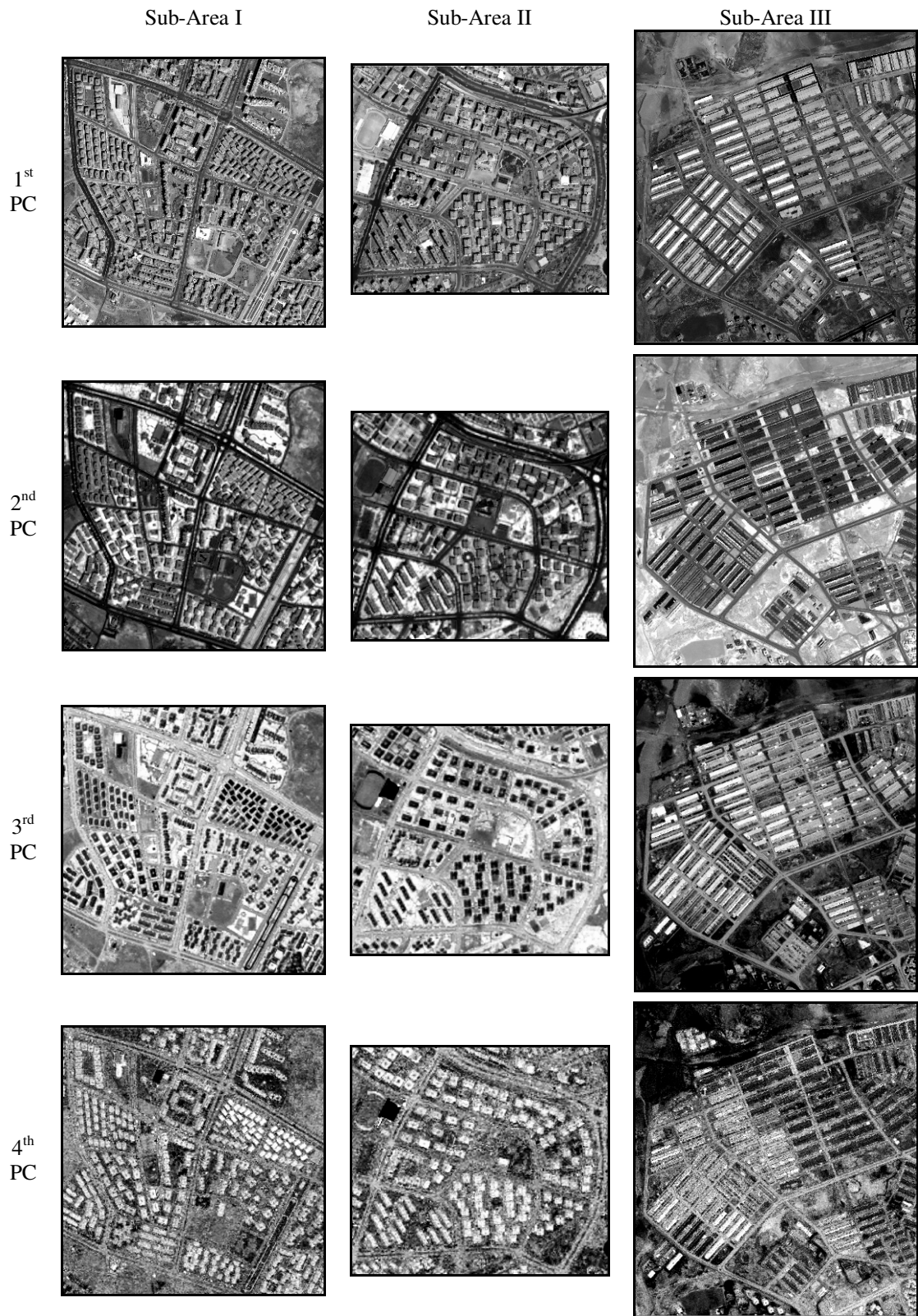


Figure 4. 19. For three sub-areas, the principal components of the IKONOS Pan-Sharpned Image.

Table 4. 5. The spectral statistics of the IKONOS Pan-sharpened image.

Bands	IKONOS PSM Bands		
	Mean	Median	Std. Dev.
1	520.988	510	141.07
2	660.998	650	200.671
3	624.191	622	211.368
4	666.643	670	199.85

Table 4. 6. The spectral statistics of the principal components.

Eigen Channels	Principal Components		
	Eigen Value	Std. Dev.	Variance (%)
1	132476.100	363.888	91.45%
2	10295.380	101.458	7.11%
3	1942.119	44.083	1.34%
4	151.115	12.283	0.10%

#### 4.7. The Support Vector Machines Classification

SVM is a supervised classification technique derived from statistical learning theory. The fundamentals of SVM were developed by Vapnik (1995). There are basically three steps in SVM classification. First, the trainings of the classes are represented as feature vectors. Next, to perform the separation, these feature vectors are mapped into a feature space by using the kernel function. Finally, an n-dimensional hyperplane that optimally separates the classes are created.

To classify the pixels accurately, SVM develops a model using the training data of two separable classes with  $i$  samples represented by  $(x_1, r_1), \dots, (x_i, r_i)$ , where  $x_i \in \mathbb{R}^n$  and  $r \in \{1, -1\}$  in the  $n$  dimensional space. Here,  $x_i$  is the spectral value of the training data while  $r_i$  is the class label for a training case.

During the learning process, SVM optimizes the hyperplane position to have a maximum margin between the classes that are on different sides of the hyperplane. There may be many hyperplanes that separate the classes; however the aim is to find the optimum one and to maximize the margin (Figure 4.20). A hyperplane that separates the classes can be defined by the following equation (Equation 4.4):

$$w \cdot x + b = 0 \quad (\text{Equation 4.4})$$

where,  $w$  is the normal to the hyperplane,  $x$  is a point lying on the hyperplane, and  $b$  is the bias.

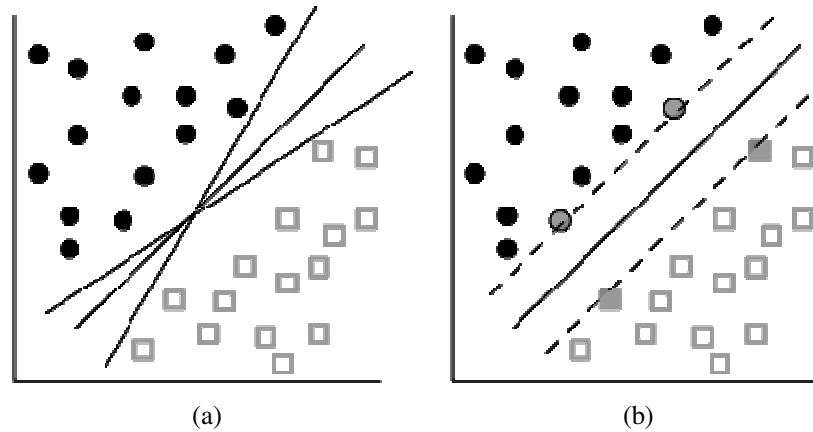


Figure 4. 20. In the linear separable case (a) the possible hyperplanes and (b) the optimum hyperplanes.

For the linearly separable two class case, a hyperplane can be defined as

$$w \cdot x_i + b \geq +1 \quad \text{for all } r_i = +1, \quad (\text{Equation 4.5})$$

$$w \cdot x_i + b \leq -1 \quad \text{for all } r_i = -1. \quad (\text{Equation 4.6})$$

The equations 4.5 and 4.6 can be combined into a single equation (Equation 4.7);

$$r_i (w \cdot x_i + b) - 1 \geq 0 \quad (\text{Equation 4.7})$$

The points on these hyperplanes are called the “support vectors”. These hyperplanes are used to define the optimal separating hyperplane. The optimal separating hyperplane is parallel to the hyperplanes and stays in the middle of them. The margin between these planes is  $2/\|w\|$  ( $\|w\|$  is the Euclidean norm of  $w$ ). The maximization



of this margin causes the optimization problem given below and equation 4.7 is the constraint:

$$\min \{1/2 \|w\|^2\} \quad (\text{Equation 4.8})$$

This problem can be defined by Lagrange multipliers:

$$\text{Maximize: } \sum_{i=1}^k \alpha_i - \frac{1}{2} \sum_{i=1}^k \sum_{j=1}^k \alpha_i \alpha_j r_i r_j (x_i \cdot x_j), \quad (\text{Equation 4.9})$$

$$\text{Subject to: } \sum_{i=1}^k \alpha_i r_i = 0 \quad \text{and} \quad \alpha_i \geq 0, \quad i = 1, 2, \dots, k \quad (\text{Equation 4.10})$$

The decision rule is then applied for classifying the data into two classes; +1 indicating one class and -1 the other class.

$$f(x) = \text{sign} \left( \sum_{sv} r_i \alpha_i^o (x_i \cdot x) + b^o \right) \quad (\text{Equation 4.11})$$

If the classes in the dataset are mixed, the data may not be separated linearly. In the non-linear separable case, equation 4.9 cannot be fulfilled as constraint and therefore slack variable ( $\xi$ ) and penalty parameter (C) are defined. With the addition of these parameters the optimization problem and the constraints becomes:

$$\min = \left[ \frac{\|w\|^2}{2} + C \sum_{i=1}^r \xi_i \right] \quad (\text{Equation 4.12})$$

$$r_i (w \cdot x_i + b) \geq 1 - \xi_i \quad (\text{Equation 4.13})$$

The penalty parameter (C) value is a form of regularization parameter and defines the trade off between the number of noisy training samples and classifier complexity. The approach can be adapted to allow for non-linear surfaces by transferring the training data into a high dimensional (feature) space (Figure 4.21).

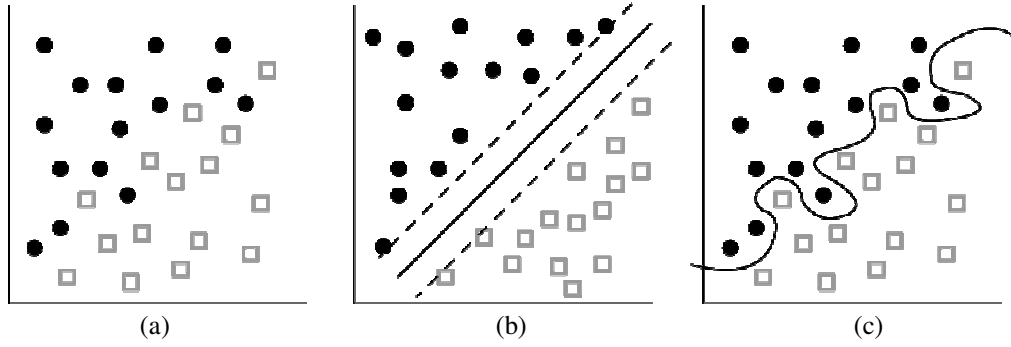


Figure 4. 21. The processes of SVM classification (a) The feature vectors of two classes in input space (b) The feature vectors of two classes separated by a hyperplane in feature space (c) The separated two classes in input space.

This time the problem can be defined by Lagrange multipliers using kernel function (K):

$$\text{Maximize: } \sum_{i=1}^k \alpha_i - \frac{1}{2} \sum_{i=1}^k \sum_{i=1}^k \alpha_i \alpha_i r_i r_i K(x_i, x_j), \quad (\text{Equation 4.14})$$

$$\text{Subject to: } \sum_{i=1}^k \alpha_i r_i = 0 \text{ and } 0 \leq \alpha_i \leq C, \quad i = 1, 2, \dots, k \quad (\text{Equation 4.15})$$

Using kernel function leads to change in decision rule as given below:

$$f(x) = \text{sign} \left( \sum_{sv} r_i \alpha_i^o K(x_i, x) + b^o \right) \quad (\text{Equation 4.16})$$

There are different types of kernel types for different applications. The most common kernel types are:

$$\text{Linear: } K(x_i, x_j) = x_i^T x_j$$

$$\text{Polynomial: } K(x_i, x_j) = (\gamma x_i^T x_j + r)^d, \quad \gamma > 0$$

$$\text{RBF: } K(x_i, x_j) = \exp(-\gamma \|x_i - x_j\|^2), \quad \gamma > 0$$

$$\text{Sigmoid: } K(x_i, x_j) = \tanh(\gamma x_i^T x_j + r)$$

where:

$\gamma$  is the gamma term in the kernel function for all kernel types except linear.

$d$  is the polynomial degree term in the kernel function for the polynomial kernel.

$r$  is the bias term in the kernel function for the polynomial and sigmoid kernels.

Originally the SVMs were designed for binary classification and then extended for multi-class classification. In this study, to detect the building patches binary SVM classification was used because the interest was on a single class. Foody et al. (2006) claimed that one class SVM classification has a great potential in remote sensing. Boyd et al. (2006) used this classification technique for mapping a specific class for the priority habitats monitoring. Sanchez et al. (2007) used it for mapping a specific class from Landsat 7 ETM+ image. As is well known, in conventional supervised classification all classes must be defined and trained in detail. But if the interest is to a single class, the use of a conventional supervised image classification technique may be inappropriate (Foody et al., 2006).

The past studies have shown that the SVM concept has much promise in the classification of remote sensing images providing more accuracy than the standard parametric and popular alternatives (Huang et al, 2002; Zhu and Blumberg, 2002; Pal and Mather, 2005; Foody and Mathur, 2004). Watanachaturaporn et al. (2008) compared SVM classifier with Maximum Likelihood Classifier (MLC), Backpropagation Neural Network Classifier (BPNN), Radial Basis Function Neural Network Classifier (RBFNET) and Decision Tree Classifier (DTC) and found that SVM classifier produced significantly higher accuracy than the others.

Thus, in the present case, the SVM classification was used for detecting the buildings and the above selected sub-areas were separated into building and non-building classes. As is well known, the incorporation of ancillary data in the classification process improves the results. Therefore, in addition to original four spectral bands ( $B_1$ ,  $B_2$ ,  $B_3$ , and  $B_4$ ) of the IKONOS pan-sharpened image, the nDSM ( $B_{nDSM}$ ), NDVI ( $B_{NDVI}$ ), First Principal Component ( $B_{PC1}$ ), Second Principal Component ( $B_{PC2}$ ), Third Principal Component ( $B_{PC3}$ ) and Fourth Principal Component ( $B_{PC4}$ ) images were also used in the classification process. The inclusion of the nDSM band would be beneficial for the building extraction process because the buildings are clearly

separated from the terrain. Similarly, the use of NDVI image is expected to be beneficial to separate those buildings that are surrounded by the trees and green vegetated areas. In addition, the Principal Components were also used as additional bands as they may be more interpretable than the original data. It appears that industrial buildings with white or blue concrete roofs can be more clearly differentiated from the surrounding land/objects using the 2<sup>nd</sup> Principal Component, while the residential buildings with tile-roofs can be more clearly differentiated using the 3<sup>rd</sup> Principal Component. Therefore, the Principal Components may increase the classification accuracy. The bands used in the classification process were labeled as follows:

- $B_1$  ⇒ Blue band of the IKONOS pan-sharpened image
- $B_2$  ⇒ Green band of the IKONOS pan-sharpened image
- $B_3$  ⇒ Red band of the IKONOS pan-sharpened image
- $B_4$  ⇒ Near-infrared band of the IKONOS pan-sharpened image
- $B_{nDSM}$  ⇒ nDSM (after applying the threshold value of 3m) band
- $B_{NDVI}$  ⇒ The NDVI band
- $B_{PC1}$  ⇒ 1<sup>st</sup> Principal Component of the IKONOS pan-sharpened image
- $B_{PC2}$  ⇒ 2<sup>nd</sup> Principal Component of the IKONOS pan-sharpened image
- $B_{PC3}$  ⇒ 3<sup>rd</sup> Principal Component of the IKONOS pan-sharpened image
- $B_{PC4}$  ⇒ 4<sup>th</sup> Principal Component of the IKONOS pan-sharpened image

By using the above given bands, fourteen image data sets were generated to perform the SVM classification (Table 4.7). Of these data sets, Data-Set 1 contains the original bands ( $B_1$ ,  $B_2$ ,  $B_3$  and  $B_4$ ) only. In addition to original bands, Data-Sets 2, 3, 4, 5, 6, and 7 contain, respectively the bands  $B_{nDSM}$ ,  $B_{NDVI}$ ,  $B_{PC1}$ ,  $B_{PC2}$ ,  $B_{PC3}$ , and  $B_{PC4}$ . Each of the Data-Sets 8, 9, and 10 contains additional two bands as well as the original bands, which are  $B_{nDSM}$ ,  $B_{NDVI}$ ;  $B_{nDSM}$ ,  $B_{PC2}$ ;  $B_{nDSM}$ ,  $B_{PC3}$ , respectively. Data-Sets 11 and 12 contain additional three bands in addition to the original bands. While the additional bands of Data-Set 11 are  $B_{nDSM}$ ,  $B_{NDVI}$  and  $B_{PC2}$ , Data-Set 12 includes the additional bands of  $B_{nDSM}$ ,  $B_{NDVI}$  and  $B_{PC3}$ . Data-Set 13 contains all PCs

as additional bands. The final data set, Data-Set 14, includes all of the original and the derived bands.

Table 4. 7. The data sets and their band combinations used in the SVM classification.

Data-Sets	Band Combinations
Data-Set 1	B <sub>1</sub> , B <sub>2</sub> , B <sub>3</sub> , B <sub>4</sub>
Data-Set 2	B <sub>1</sub> , B <sub>2</sub> , B <sub>3</sub> , B <sub>4</sub> , B <sub>nDSM</sub>
Data-Set 3	B <sub>1</sub> , B <sub>2</sub> , B <sub>3</sub> , B <sub>4</sub> , B <sub>NNDVI</sub>
Data-Set 4	B <sub>1</sub> , B <sub>2</sub> , B <sub>3</sub> , B <sub>4</sub> , B <sub>PC1</sub>
Data-Set 5	B <sub>1</sub> , B <sub>2</sub> , B <sub>3</sub> , B <sub>4</sub> , B <sub>PC2</sub>
Data-Set 6	B <sub>1</sub> , B <sub>2</sub> , B <sub>3</sub> , B <sub>4</sub> , B <sub>PC3</sub>
Data-Set 7	B <sub>1</sub> , B <sub>2</sub> , B <sub>3</sub> , B <sub>4</sub> , B <sub>PC4</sub>
Data-Set 8	B <sub>1</sub> , B <sub>2</sub> , B <sub>3</sub> , B <sub>4</sub> , B <sub>nDSM</sub> , B <sub>NNDVI</sub>
Data-Set 9	B <sub>1</sub> , B <sub>2</sub> , B <sub>3</sub> , B <sub>4</sub> , B <sub>nDSM</sub> , B <sub>PC2</sub>
Data-Set 10	B <sub>1</sub> , B <sub>2</sub> , B <sub>3</sub> , B <sub>4</sub> , B <sub>nDSM</sub> , B <sub>PC3</sub>
Data-Set 11	B <sub>1</sub> , B <sub>2</sub> , B <sub>3</sub> , B <sub>4</sub> , B <sub>nDSM</sub> , B <sub>NNDVI</sub> , B <sub>PC2</sub>
Data-Set 12	B <sub>1</sub> , B <sub>2</sub> , B <sub>3</sub> , B <sub>4</sub> , B <sub>nDSM</sub> , B <sub>NNDVI</sub> , B <sub>PC3</sub>
Data-Set 13	B <sub>1</sub> , B <sub>2</sub> , B <sub>3</sub> , B <sub>4</sub> , B <sub>PC1</sub> , B <sub>PC2</sub> , B <sub>PC3</sub> , B <sub>PC4</sub>
Data-Set 14	B <sub>1</sub> , B <sub>2</sub> , B <sub>3</sub> , B <sub>4</sub> , B <sub>nDSM</sub> , B <sub>NNDVI</sub> , B <sub>PC1</sub> , B <sub>PC2</sub> , B <sub>PC3</sub> , B <sub>PC4</sub>

In this study, the building class was the class of interest, while the other classes including vegetation, road, bareland, shadow, pavement, etc. composed the non-building class. For both the building and the non-building classes, equal numbers of training pixels were collected. For non-building classes, the percentages of the training pixels were determined according to the distribution of these classes. Initially, the training areas were collected roughly. Then, from these areas, the determined numbers of pixels were selected randomly. While collecting the training samples, the focus was on the class of interest. For each class and sub-classes, the numbers of training pixels collected are illustrated in tables 4.8, 4.9, and 4.10.

Table 4. 8. The number of training pixels collected for Sub-Area I.

Classes	Sub-Classes	Training Pixel Size	Training Pixel Size	Training Pixel Size
Building (50%)	Building (50%)	250	500	1000
	Vegetation (20%)	100	200	400
	Road (14%)	70	140	280
Non-Building (50%)	Bareland (12%)	60	120	240
	Shadow (2%)	10	20	40
	Pavement (2%)	10	20	40
Total (100%)	Total (100%)	500	1000	2000

Table 4. 9. The number of training pixels collected for Sub-Area II.

Classes	Sub-Classes	Training Pixel Size	Training Pixel Size	Training Pixel Size
Building (50%)	Building (50%)	250	500	1000
	Vegetation (20%)	100	200	400
Non-Building (50%)	Road (20%)	100	200	400
	Bareland (5%)	25	50	100
	Shadow (3%)	15	30	60
	Pavement (2%)	10	20	40
Total (100%)	Total (100%)	500	1000	2000

Table 4. 10. The number of training pixels collected for Sub-Area III.

Classes	Sub-Classes	Training Pixel Size	Training Pixel Size	Training Pixel Size
Building (50%)	Building (50%)	250	500	1000
	Bareland (26%)	130	260	520
Non-Building (50%)	Road (16%)	80	160	320
	Vegetation (4%)	20	40	80
	Pavement (2%)	10	20	40
	Shadow (2%)	10	20	40
Total (100%)	Total (100%)	500	1000	2000

After collecting the training pixels, the test pixels were collected from different locations than the training pixels. To test the results of the classifications, which were performed using three different training sizes of 500, 1000, and 2000, the test pixels of three different sizes (2000, 4000 and 8000) were collected roughly. Then, from the roughly selected test areas, the determined numbers of pixels were selected randomly. These pixels were different from the training pixels because they must represent the unbiased reference information. For each class and sub-classes, the numbers of test pixels collected are illustrated in tables 4.11, 4.12, and 4.13.

Table 4. 11. The number of test pixels collected for Sub-Area I.

Classes	Sub-Classes	Test Pixel Size	Test Pixel Size	Test Pixel Size
Building (50%)	Building (50%)	1000	2000	4000
	Vegetation (20%)	400	800	1600
Non-Building (50%)	Road (14%)	280	560	1120
	Bareland (12%)	240	480	960
	Pavement (2%)	40	80	160
	Shadow (2%)	40	80	160
Total (100%)	Total (100%)	2000	4000	8000

Table 4. 12. The number of test pixels collected for Sub-Area II.

Classes	Sub-Classes	Test Pixel Size	Test Pixel Size	Test Pixel Size
Building (50%)	Building (50%)	1000	2000	4000
	Vegetation (20%)	400	800	1600
Non-Building (50%)	Road (20%)	400	800	1600
	Bareland (5%)	100	200	400
	Shadow (3%)	60	120	240
	Pavement (2%)	40	80	160
Total (100%)	Total (100%)	2000	4000	8000

Table 4. 13. The number of test pixels collected for Sub-Area III.

Classes	Sub-Classes	Test Pixel Size	Test Pixel Size	Test Pixel Size
Building (50%)	Building (50%)	1000	2000	4000
	Bareland (24%)	520	1040	2080
Non-Building (50%)	Road (12%)	320	640	1280
	Vegetation (10%)	80	160	320
	Pavement (2%)	40	80	160
	Shadow (2%)	40	80	160
Total (100%)	Total (100%)	2000	4000	8000

Next, for the above defined band combinations, the spectral separabilities were computed from the training areas using a statistical method based on Jeffries-Matusita (Richards, 1999) to know the amount of class separability between the building and non-building classes. In the present case, the spectral separabilities were performed to evaluate the effect of the additional bands to the spectral separability.

The Jeffries-Matusita distance is computed as follows:

$$J_{ij} = \sqrt{2(1 - e^{-B})} \quad (\text{Equation 4.17})$$

where; B is the Bhattacharyya distance, given by

$$B = \frac{1}{8} (\mu_i - \mu_j)^T \left( \frac{\Sigma_i + \Sigma_j}{2} \right)^{-1} (\mu_i - \mu_j) + \frac{1}{2} \ln \left( \frac{\left| \frac{\Sigma_i + \Sigma_j}{2} \right|}{|\Sigma_i|^{1/2} |\Sigma_j|^{1/2}} \right) \quad (\text{Equation 4.18})$$

$i$  and  $j$  are the two signature (classes) being compared,

$\mu$  is the mean vector of signature  $i$ .

The separability values range from 0 to 2 and specify how well the selected training areas are statistically separable. The higher values indicate that the training areas are spectrally well separable. On the other hand, the lower values indicate that the classes spectrally overlap. For the selected three sub-areas and three different training sizes, the spectral separability values are given in tables 4.14, 4.15, and 4.16.

Table 4. 14. For Sub-Area I, the spectral separability values of the data sets.

Sub-Area I	Band Combinations	Spectral Separability		
		500 Train	1000 Train	2000 Train
Data-Set 1	B <sub>1</sub> , B <sub>2</sub> , B <sub>3</sub> , B <sub>4</sub>	1.78	1.76	1.75
Data-Set 2	B <sub>1</sub> , B <sub>2</sub> , B <sub>3</sub> , B <sub>4</sub> , B <sub>nDSM</sub>	1.96	1.94	1.93
Data-Set 3	B <sub>1</sub> , B <sub>2</sub> , B <sub>3</sub> , B <sub>4</sub> , B <sub>NNDVI</sub>	1.88	1.86	1.86
Data-Set 4	B <sub>1</sub> , B <sub>2</sub> , B <sub>3</sub> , B <sub>4</sub> , B <sub>PC1</sub>	1.78	1.76	1.75
Data-Set 5	B <sub>1</sub> , B <sub>2</sub> , B <sub>3</sub> , B <sub>4</sub> , B <sub>PC2</sub>	1.79	1.76	1.75
Data-Set 6	B <sub>1</sub> , B <sub>2</sub> , B <sub>3</sub> , B <sub>4</sub> , B <sub>PC3</sub>	1.79	1.76	1.75
Data-Set 7	B <sub>1</sub> , B <sub>2</sub> , B <sub>3</sub> , B <sub>4</sub> , B <sub>PC4</sub>	1.79	1.76	1.75
Data-Set 8	B <sub>1</sub> , B <sub>2</sub> , B <sub>3</sub> , B <sub>4</sub> , B <sub>nDSM</sub> , B <sub>NNDVI</sub>	1.98	1.97	1.96
Data-Set 9	B <sub>1</sub> , B <sub>2</sub> , B <sub>3</sub> , B <sub>4</sub> , B <sub>nDSM</sub> , B <sub>PC2</sub>	1.96	1.94	1.93
Data-Set 10	B <sub>1</sub> , B <sub>2</sub> , B <sub>3</sub> , B <sub>4</sub> , B <sub>nDSM</sub> , B <sub>PC3</sub>	1.96	1.94	1.93
Data-Set 11	B <sub>1</sub> , B <sub>2</sub> , B <sub>3</sub> , B <sub>4</sub> , B <sub>nDSM</sub> , B <sub>NNDVI</sub> , B <sub>PC2</sub>	1.98	1.97	1.96
Data-Set 12	B <sub>1</sub> , B <sub>2</sub> , B <sub>3</sub> , B <sub>4</sub> , B <sub>nDSM</sub> , B <sub>NNDVI</sub> , B <sub>PC3</sub>	1.98	1.97	1.96
Data-Set 13	B <sub>1</sub> , B <sub>2</sub> , B <sub>3</sub> , B <sub>4</sub> , B <sub>PC1</sub> , B <sub>PC2</sub> , B <sub>PC3</sub> , B <sub>PC4</sub>	1.79	1.76	1.75
Data-Set 14	B <sub>1</sub> , B <sub>2</sub> , B <sub>3</sub> , B <sub>4</sub> , B <sub>nDSM</sub> , B <sub>NNDVI</sub> , B <sub>PC1</sub> , B <sub>PC2</sub> , B <sub>PC3</sub> , B <sub>PC4</sub>	1.98	1.97	1.96



Table 4. 15. For Sub-Area II, the spectral separability values of the data sets.

Sub-Area II	Band Combinations	Spectral Separability		
		500 Train	1000 Train	2000 Train
Data-Set 1	B <sub>1</sub> , B <sub>2</sub> , B <sub>3</sub> , B <sub>4</sub>	1.80	1.79	1.78
Data-Set 2	B <sub>1</sub> , B <sub>2</sub> , B <sub>3</sub> , B <sub>4</sub> , B <sub>nDSM</sub>	1.91	1.88	1.88
Data-Set 3	B <sub>1</sub> , B <sub>2</sub> , B <sub>3</sub> , B <sub>4</sub> , B <sub>NNDVI</sub>	1.90	1.90	1.89
Data-Set 4	B <sub>1</sub> , B <sub>2</sub> , B <sub>3</sub> , B <sub>4</sub> , B <sub>PC1</sub>	1.80	1.79	1.78
Data-Set 5	B <sub>1</sub> , B <sub>2</sub> , B <sub>3</sub> , B <sub>4</sub> , B <sub>PC2</sub>	1.80	1.79	1.78
Data-Set 6	B <sub>1</sub> , B <sub>2</sub> , B <sub>3</sub> , B <sub>4</sub> , B <sub>PC3</sub>	1.80	1.79	1.78
Data-Set 7	B <sub>1</sub> , B <sub>2</sub> , B <sub>3</sub> , B <sub>4</sub> , B <sub>PC4</sub>	1.80	1.79	1.78
Data-Set 8	B <sub>1</sub> , B <sub>2</sub> , B <sub>3</sub> , B <sub>4</sub> , B <sub>nDSM</sub> , B <sub>NNDVI</sub>	1.96	1.94	1.94
Data-Set 9	B <sub>1</sub> , B <sub>2</sub> , B <sub>3</sub> , B <sub>4</sub> , B <sub>nDSM</sub> , B <sub>PC2</sub>	1.91	1.88	1.88
Data-Set 10	B <sub>1</sub> , B <sub>2</sub> , B <sub>3</sub> , B <sub>4</sub> , B <sub>nDSM</sub> , B <sub>PC3</sub>	1.91	1.88	1.88
Data-Set 11	B <sub>1</sub> , B <sub>2</sub> , B <sub>3</sub> , B <sub>4</sub> , B <sub>nDSM</sub> , B <sub>NNDVI</sub> , B <sub>PC2</sub>	1.96	1.94	1.94
Data-Set 12	B <sub>1</sub> , B <sub>2</sub> , B <sub>3</sub> , B <sub>4</sub> , B <sub>nDSM</sub> , B <sub>NNDVI</sub> , B <sub>PC3</sub>	1.96	1.94	1.94
Data-Set 13	B <sub>1</sub> , B <sub>2</sub> , B <sub>3</sub> , B <sub>4</sub> , B <sub>PC1</sub> , B <sub>PC2</sub> , B <sub>PC3</sub> , B <sub>PC4</sub>	1.81	1.79	1.78
Data-Set 14	B <sub>1</sub> , B <sub>2</sub> , B <sub>3</sub> , B <sub>4</sub> , B <sub>nDSM</sub> , B <sub>NNDVI</sub> , B <sub>PC1</sub> , B <sub>PC2</sub> , B <sub>PC3</sub> , B <sub>PC4</sub>	1.96	1.94	1.94

Table 4. 16. For Sub-Area III, the spectral separability values of the data sets.

Sub-Area III	Band Combinations	Spectral Separability		
		500 Train	1000 Train	2000 Train
Data-Set 1	B <sub>1</sub> , B <sub>2</sub> , B <sub>3</sub> , B <sub>4</sub>	1.40	1.45	1.46
Data-Set 2	B <sub>1</sub> , B <sub>2</sub> , B <sub>3</sub> , B <sub>4</sub> , B <sub>nDSM</sub>	1.85	1.89	1.89
Data-Set 3	B <sub>1</sub> , B <sub>2</sub> , B <sub>3</sub> , B <sub>4</sub> , B <sub>NNDVI</sub>	1.47	1.53	1.53
Data-Set 4	B <sub>1</sub> , B <sub>2</sub> , B <sub>3</sub> , B <sub>4</sub> , B <sub>PC1</sub>	1.41	1.45	1.46
Data-Set 5	B <sub>1</sub> , B <sub>2</sub> , B <sub>3</sub> , B <sub>4</sub> , B <sub>PC2</sub>	1.41	1.45	1.46
Data-Set 6	B <sub>1</sub> , B <sub>2</sub> , B <sub>3</sub> , B <sub>4</sub> , B <sub>PC3</sub>	1.41	1.45	1.46
Data-Set 7	B <sub>1</sub> , B <sub>2</sub> , B <sub>3</sub> , B <sub>4</sub> , B <sub>PC4</sub>	1.41	1.45	1.46
Data-Set 8	B <sub>1</sub> , B <sub>2</sub> , B <sub>3</sub> , B <sub>4</sub> , B <sub>nDSM</sub> , B <sub>NNDVI</sub>	1.88	1.91	1.91
Data-Set 9	B <sub>1</sub> , B <sub>2</sub> , B <sub>3</sub> , B <sub>4</sub> , B <sub>nDSM</sub> , B <sub>PC2</sub>	1.85	1.89	1.89
Data-Set 10	B <sub>1</sub> , B <sub>2</sub> , B <sub>3</sub> , B <sub>4</sub> , B <sub>nDSM</sub> , B <sub>PC3</sub>	1.85	1.89	1.89
Data-Set 11	B <sub>1</sub> , B <sub>2</sub> , B <sub>3</sub> , B <sub>4</sub> , B <sub>nDSM</sub> , B <sub>NNDVI</sub> , B <sub>PC2</sub>	1.88	1.91	1.91
Data-Set 12	B <sub>1</sub> , B <sub>2</sub> , B <sub>3</sub> , B <sub>4</sub> , B <sub>nDSM</sub> , B <sub>NNDVI</sub> , B <sub>PC3</sub>	1.88	1.91	1.91
Data-Set 13	B <sub>1</sub> , B <sub>2</sub> , B <sub>3</sub> , B <sub>4</sub> , B <sub>PC1</sub> , B <sub>PC2</sub> , B <sub>PC3</sub> , B <sub>PC4</sub>	1.42	1.46	1.46
Data-Set 14	B <sub>1</sub> , B <sub>2</sub> , B <sub>3</sub> , B <sub>4</sub> , B <sub>nDSM</sub> , B <sub>NNDVI</sub> , B <sub>PC1</sub> , B <sub>PC2</sub> , B <sub>PC3</sub> , B <sub>PC4</sub>	1.88	1.92	1.91

The computed spectral separability values indicate that using the first, second, third or fourth principal components as additional bands (Data-Set 4, Data-Set 5, Data-Set 6 and Data-Set 7) do not increase the separabilities when compared with four original bands. On the other hand, using nDSM as an additional band appears to remarkably increase the class separability for all sub-areas. This was an expected result because

nDSM is directly related with the building heights. The use of NDVI image as an additional band increased the class separability for Sub-Area I and Sub-Area II. However, for Sub-Area III, the increase is rather low. This is due to the fact that in Sub-Area I and Sub-Area II the buildings are mostly surrounded by the green vegetated areas. But, when compared to Sub-Area I and Sub-Area II, Sub-Area III contains less vegetation. Therefore, the effect of NDVI image into the spectral separability of Sub-Area III becomes less than expected. On the other hand, the use of PC images as additional bands do not increase the separability values remarkably.

After evaluating the spectral separabilities of the data sets, it was observed that Data-Set 8, Data-Set 11, Data-Set 12, and Data-Set 14 provide better separabilities than the other data sets. Data-Set 2, Data-Set 9, and Data-Set 10 also provide good separability but their separability values stayed lower than Data-Sets 8, 11, 12, and 14. The data sets with the lowest separabilities are Data-Set 1, Data-Set 4, Data-Set 5, Data-Set 6, Data-Set 7, and Data-Set 13. The results indicate that increasing the training size do not considerably affect the class separabilities.

When performing the SVM classification, the selection of the kernel method, determination of the ‘C’ parameter, and the parameters related to the kernel are also important. In this study, the Radial Basis Function was selected as the kernel method. The Radial Basis Function (RBF), which can handle linearly non-separable problems, works well in most cases (ENVI Manual, 2006). The mathematical representation of RBF kernel is as follows:

$$K(x_i, x_j) = \exp(-\gamma \|x_i - x_j\|^2), \gamma > 0 \quad (\text{Equation 4.19})$$

where:

$\gamma$  is the gamma term in the RBF kernel function.

In this study,  $\gamma$  was determined as the inverse of the number of bands in the input image and “C” was taken to be “1000”.

#### 4.8. Determining the Candidate Building Patches

After performing the one-class SVM classification, those areas classified as building represent the candidate building patches. However, due to the misclassification, the candidate building patches may contain artefacts. Therefore, these artefacts were removed using the morphological operations. The morphological operations are image processing operations which process images based on the shapes. In the present case, to eliminate specific image details smaller than the structuring element, the “opening” and “closing” operations, which are based on erosion and dilation operations, with an isotropic structuring element was used. Therefore, the global shape of the objects was not distorted (Sonka et al, 1998).

The erosion and dilation operations are fundamental to morphological image processing (Gonzales et al, 2004). The erosion creates an image that has thinner objects than the input image. The erosion of an image  $f$  by a structuring element  $k$  is symbolized as  $f \ominus k$ . To calculate the erosion, the structuring element  $k$  is located as its origin on image pixel coordinates  $(x, y)$  and the following rule is applied to each pixel;

$$\begin{aligned} & \text{if } k \text{ fits } f \\ & \quad g(x, y) = 1 \\ & \text{Else} \\ & \quad g(x, y) = 0 \end{aligned}$$

On the other hand, the dilation creates an image that has thicker objects than the input image. The dilation of an image  $f$  by a structuring element  $k$  is indicated as  $f \oplus k$ . To calculate the dilation, the structuring element  $k$  is located as its origin on image pixel coordinates  $(x, y)$  and the following rule is applied to each pixel;

$$\begin{aligned} & \text{If } k \text{ hits } f \\ & \quad g(x, y) = 1 \\ & \text{Else} \\ & \quad g(x, y) = 0 \end{aligned}$$

Erosion followed by dilation creates opening. The opening of image  $f$  by the structuring element  $k$  is denoted by “ $f \circ k$ ” and is defined as in equation 4.20. The dilation followed by erosion is called closing. The closing of image  $f$  by the structuring element  $k$  is denoted by “ $f \bullet k$ ” and is defined as in equation 4.21.

$$f \circ k = (f \ominus k) \oplus k \quad (\text{Equation 4.20})$$

$$f \bullet k = (f \oplus k) \ominus k \quad (\text{Equation 4.21})$$

An opening filter removes thin protrusions, outward pointing boundary irregularities, thin joins, and small isolated objects. On the other hand, a closing filter removes the thin gulf, the inward-pointing boundary irregularities and small holes (Gonzales et al, 2004). Therefore, combining a closing and an opening can be quite effective for removing the artefacts or noise. In the present case, those candidate building patches smaller than a threshold value were considered to be artefacts and therefore eliminated from further processes. The threshold value was determined to be 50 pixels for the IKONOS panchromatic image ( $50\text{m}^2$ ) because it is assumed that objects smaller than  $50\text{m}^2$  cannot be a building. For an urban block, the candidate building patches before and after removing the artefacts are illustrated in figure 4.22.

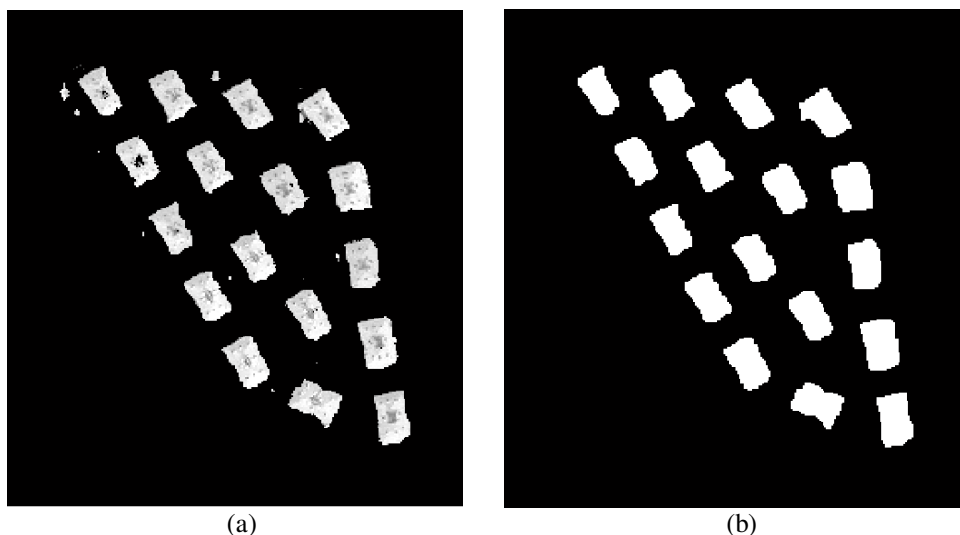


Figure 4. 22. For an urban block, the candidate building patches (a) before and (b) after removing the artefacts.

After removing the artefacts, a binary building patch image was obtained. To get the panchromatic building patch image, the building patches were masked in the panchromatic image, the zero values were assigned to non-building areas, and further building extraction operations were carried out using these candidate building patches only.

#### **4.9. The Accuracy Assessment**

To compute the classification accuracies and to discover the best data set and best training sample size, initially a confusion matrix was generated using the previously collected test data. The classification results provide the locations of the candidate building patches. Therefore, in addition to the classification accuracy, the accuracies of the building patches were also calculated using the reference building boundaries. Then, these vector boundaries were rasterized to compare the results.

##### **4.9.1. Accuracy Assessment of the SVM Classification**

To assess the accuracy of the SVM classification for each data set, a confusion matrix, which shows the comparison of the classes with test data, was generated and the accuracy measures of *Error of Omission*, *Error of Commission*, *Producer's Accuracy*, *User's Accuracy*, *Overall Accuracy*, and *Kappa Coefficient* were calculated. The obtained confusion matrices are given in Appendix C.

##### **4.9.2. Accuracy Assessment of Building Detection**

In order to assess the accuracy of building detection, the pixels were classified into one of the below given four categories by comparing the detected building patches with the rasterized reference buildings (Figure 4.23).

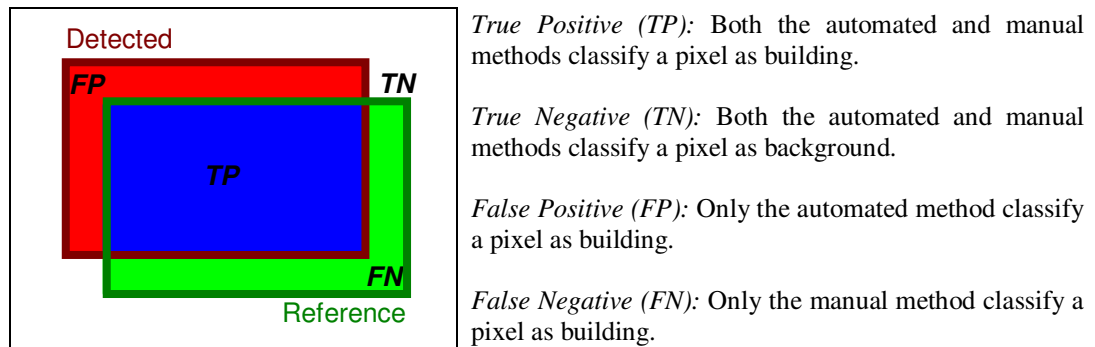


Figure 4. 23. Schematic representation of True Positive (TP), True Negative (TN), False Positive (FP) and False Negative (FN) areas.

After counting the pixels that fall into above categories, the following summary statistics were computed (Shufelt and McKeown, 1993):

$$\text{Branching Factor (BF): } FP / TP \quad (\text{Equation 4.22})$$

$$\text{Miss Factor (MF): } FN / TP \quad (\text{Equation 4.23})$$

$$\text{Building Detection Percentage (BDP): } 100 \times TP / (TP + FN) \quad (\text{Equation 4.24})$$

$$\text{Quality Percentage (QP): } 100 \times TP / (TP + FP + FN) \quad (\text{Equation 4.25})$$

These measurements give us an idea about the accuracy of the detected building patches. The ‘Branching Factor’ indicates the rate of incorrectly labeled building pixels. The ‘Miss Factor’ describes the rate of building pixels missed. The ‘Building Detection Percentage’ gives the percentage of building pixels correctly detected by the automatic process and the ‘Quality Percentage’ is the overall measure of performance, which accounts for all misclassifications and describes how likely a building pixel produced by the automatic detection is true.

#### 4.10. The Experimental Results

In general, the SVM classifier gave quite accurate results for the proposed building detection. The use of ancillary data increased the accuracy of building detection considerably. The use of nDSM as an additional band in the classification process increased the accuracy significantly, while using the NDVI image increased the

accuracy slightly. On the other hand, using the Principal Component images did not have a remarkable effect in the accuracy. When the effect of the size of training samples on classification accuracy is evaluated it can be stated that, in general, increasing the training size did not affect the accuracy significantly. Therefore, it can be concluded that a small training size (i.e. 500 pixels) would be enough for performing the SVM classification.

#### 4.10.1. The Results of SVM

##### 4.10.1.1. Sub-Area I

The accuracy assessment results of the SVM classification using 500, 1000 and 2000 training samples are given in table 4.17. The graphical representation of overall accuracy and Kappa Coefficient values are provided in figures 4.24 and 4.25. For all data sets (14 in total) used, the outputs of the SVM classification using 500 training pixels are illustrated in figure 4.26 and using 1000 and 2000 training samples are given in Appendix D.

Table 4. 17. For Sub-Area I, the Overall Accuracies and Kappa Coefficients.

Sub-Area I	Overall Accuracy (%)			Kappa Coefficient		
	Train 500/ Test 2000	Train 1000/ Test 4000	Train 2000/ Test 8000	Train 500/ Test 2000	Train 1000/ Test 4000	Train 2000/ Test 8000
Data-Set 1	95.55	96.03	95.35	0.9110	0.9205	0.9070
Data-Set 2	98.70	98.48	98.65	0.9740	0.9695	0.9730
Data-Set 3	95.45	95.78	95.69	0.9090	0.9155	0.9137
Data-Set 4	95.25	95.75	95.31	0.9050	0.9150	0.9063
Data-Set 5	95.50	96.13	95.63	0.9100	0.9225	0.9125
Data-Set 6	95.80	96.05	95.60	0.9160	0.9210	0.9120
Data-Set 7	95.75	95.83	95.54	0.9150	0.9165	0.9107
Data-Set 8	98.60	98.43	98.60	0.9720	0.9685	0.9720
Data-Set 9	98.65	98.40	98.66	0.9730	0.9680	0.9732
Data-Set 10	98.85	98.73	98.64	0.9770	0.9745	0.9728
Data-Set 11	98.65	98.43	98.59	0.9730	0.9685	0.9718
Data-Set 12	98.70	98.73	98.68	0.9740	0.9745	0.9735
Data-Set 13	96.50	96.03	95.94	0.9300	0.9205	0.9187
Data-Set 14	98.65	98.35	98.71	0.9730	0.9670	0.9742

For Sub-Area I, the results of SVM classification using 500 training samples appear to be quite satisfactory with the overall accuracy and Kappa Coefficient values computed in the range of 95.25% – 98.85% and 0.9050 – 0.9770, respectively. For Data-Sets 2, 8, 9, 10, 11, 12, and 14, the overall accuracies were computed on the order of 98%, while the Kappa Coefficients were found to be on the order of 0.97. The other data-sets provided comparatively lower values with respect to these two measurements.

The classification using 1000 training samples provided overall accuracies that range from 95.75% to 98.73% and Kappa Coefficients that range from 0.9150 to 0.9745. Similar to 500 training samples, Data-Sets 2, 8, 9, 10, 11, 12, and 14 provided the best results with the overall accuracies higher than 98% and Kappa Coefficients higher than 0.9670. However, for the other data-sets, these accuracy measurements provided relatively lower values.

The SVM classification using 2000 training samples provided overall accuracies between 95.31% and 98.71%, while the Kappa Coefficients were computed between 0.9063 and 0.9742. Similar to 500 and 1000 training samples, Data-Sets 2, 8, 9, 10, 11, 12, and 14 provided the best results with the overall accuracies higher than 98% and the Kappa Coefficients higher than 0.97. Conversely, for the other data-sets, these measurements provided relatively lower values.

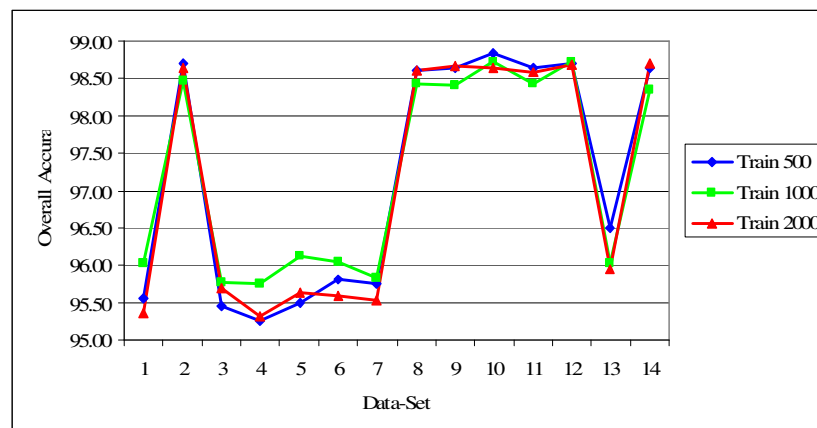


Figure 4. 24. For each data set, the overall accuracies computed using 500, 1000 and 2000 training samples in Sub-Area I.



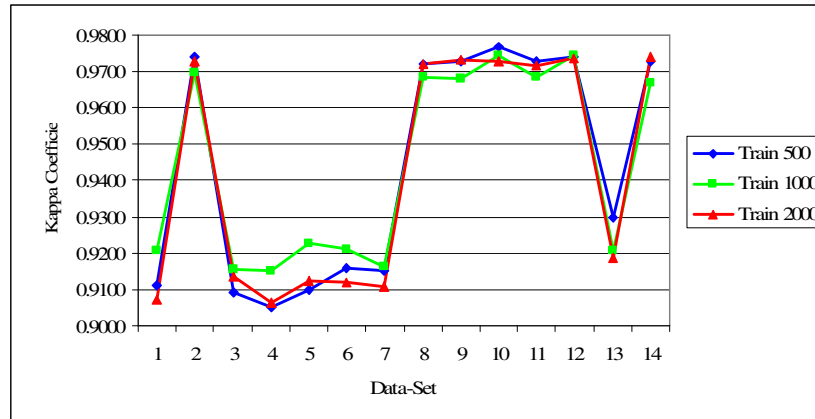


Figure 4. 25. For each data set, the kappa coefficients computed using 500, 1000 and 2000 training samples in Sub-Area I.

When the effect of training sample size on the classification accuracy is evaluated it was observed that, increasing the sample size did not significantly affect the results (Figures 4.24 and 4.25). In SVM classification, the training samples near to the hyperplanes are most informative (Foody and Mathur, 2004). Therefore, the accuracy of SVM classification is affected by the location of the training samples in the feature space rather than the size of the input training samples (Mathur and Foody, 2008). In addition, it can be seen in the spectral separabilities that, for this area, the separability values were the highest for 500 training samples, while they were computed to be the lowest for 2000 training samples.

The results of SVM classification, which was conducted using different data sets, are illustrated in Figure 4.26. When these results are assessed visually it can be stated that, those data-sets that include nDSM as an additional band provided better results. This is because those buildings having similar reflectance values with the other classes can be detected successfully with the help of the height information.

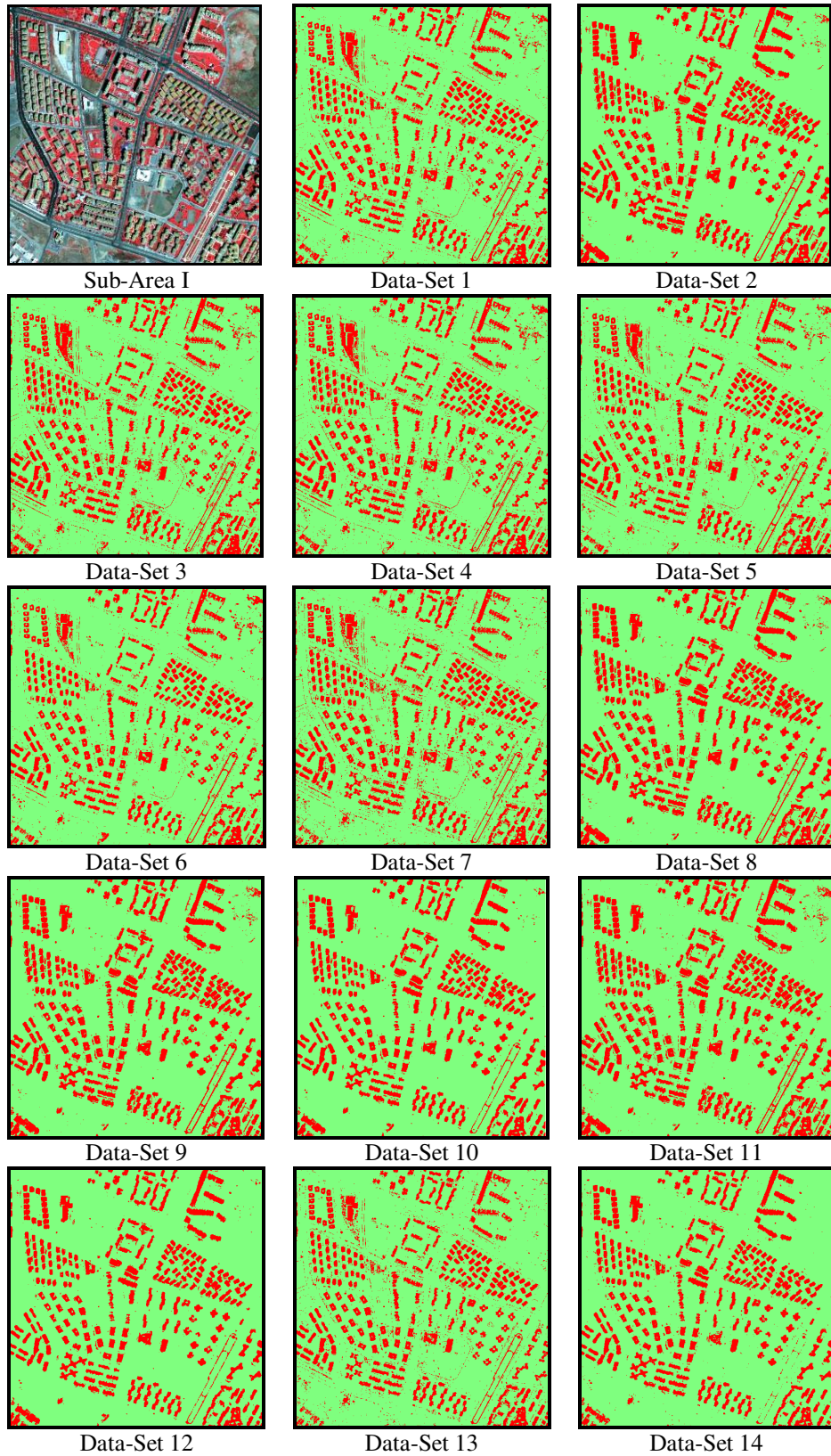


Figure 4. 26. For Sub-Area I, the results of SVM classification using 14 Data-Sets and 500 training samples.

#### 4.10.1.2. Sub-Area II

For Sub-Area II, the accuracy assessment results of the SVM classification using 500, 1000 and 2000 training samples are given in table 4.18. The graphical representations of the overall accuracies and Kappa Coefficients are provided in figures 4.27 and 4.28. For all data sets (14 in total) used, the outputs of the SVM classification using 500 training pixels are illustrated in figure 4.29 and using 1000 and 2000 training samples are given in Appendix D.

Table 4. 18. For Sub-Area II, the Overall Accuracies and Kappa Coefficients.

Sub-Area II	Overall Accuracy (%)			Kappa Coefficient		
	Train 500/ Test 2000	Train 1000/ Test 4000	Train 2000/ Test 8000	Train 500/ Test 2000	Train 1000/ Test 4000	Train 2000/ Test 8000
Data-Set 1	93.65	93.35	92.15	0.8730	0.8670	0.8430
Data-Set 2	96.50	97.15	97.16	0.9300	0.9430	0.9433
Data-Set 3	93.65	93.85	92.16	0.8730	0.8770	0.8433
Data-Set 4	93.65	94.10	91.84	0.8730	0.8820	0.8367
Data-Set 5	93.65	94.78	95.14	0.8730	0.8955	0.9028
Data-Set 6	93.80	94.83	95.50	0.8760	0.8965	0.9100
Data-Set 7	93.85	91.60	92.31	0.8770	0.8320	0.8462
Data-Set 8	96.05	96.88	96.98	0.9210	0.9375	0.9395
Data-Set 9	96.20	97.15	97.05	0.9240	0.9430	0.9410
Data-Set 10	96.30	96.70	97.15	0.9260	0.9340	0.9430
Data-Set 11	96.20	96.83	96.93	0.9240	0.9365	0.9385
Data-Set 12	96.20	96.68	96.59	0.9240	0.9335	0.9317
Data-Set 13	94.85	94.18	96.01	0.8970	0.8835	0.9203
Data-Set 14	94.50	94.90	94.88	0.8900	0.8980	0.8975

The results of SVM classification using 500 training samples appear to be quite satisfactory with the overall accuracies and Kappa Coefficients in the range of 93.65% – 96.50% and 0.8730 – 0.9300, respectively. For Data-Sets 2, 8, 9, 10, 11, and 12, the overall accuracies were computed to be on the order of 96% and Kappa Coefficients were found to be on the order of 0.92. The other data-sets provided slightly lower values with respect to these two measurements.

The SVM classification using 1000 training samples provided overall accuracies ranging from 91.60% to 97.15% and Kappa Coefficients ranging from 0.8320 to 0.9430. Same as above, Data-Sets 2, 8, 9, 10, 11, and 12 provided the highest accuracies with the overall accuracies higher than 96% and Kappa Coefficients

higher than 0.9335. For the other data sets, these measurements gave relatively lower values.

The SVM classification using 2000 training samples provided overall accuracies between 92.15% and 97.16%, while the Kappa Coefficients were computed to be between 0.8367 and 0.9433. In this case, Data-Sets 2, 8, 9, 10, 11, 12, and 13 provided the best results with the overall accuracies higher than 96% and Kappa Coefficients higher than 0.92. Conversely, for the other data-sets, these measurements gave relatively lower values.

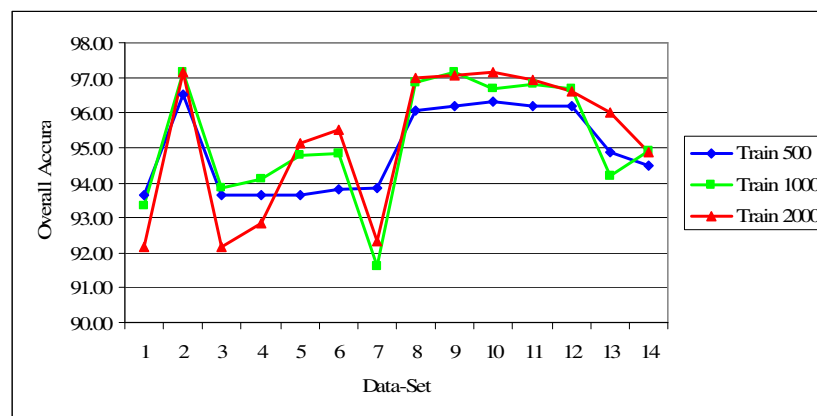


Figure 4. 27. For each data set, the overall accuracies computed using 500, 1000, and 2000 training samples in Sub-Area II.

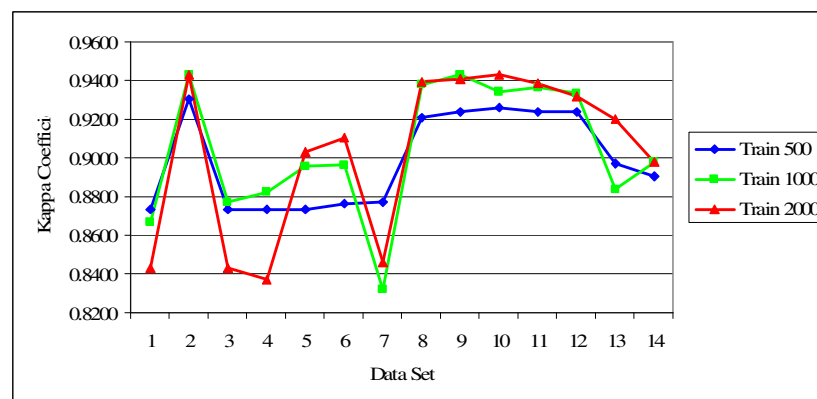


Figure 4. 28. For each data set, the kappa coefficients computed using 500, 1000, and 2000 training samples in Sub-Area II.

For this sub-area, increasing the sample size did not affect the accuracy significantly (Figure 4.27 and 4.28). The results of SVM classification conducted using different data sets are illustrated in Figure 4.29. When the results are compared visually it can be stated that the data-sets that include nDSM as an additional band provides better results.

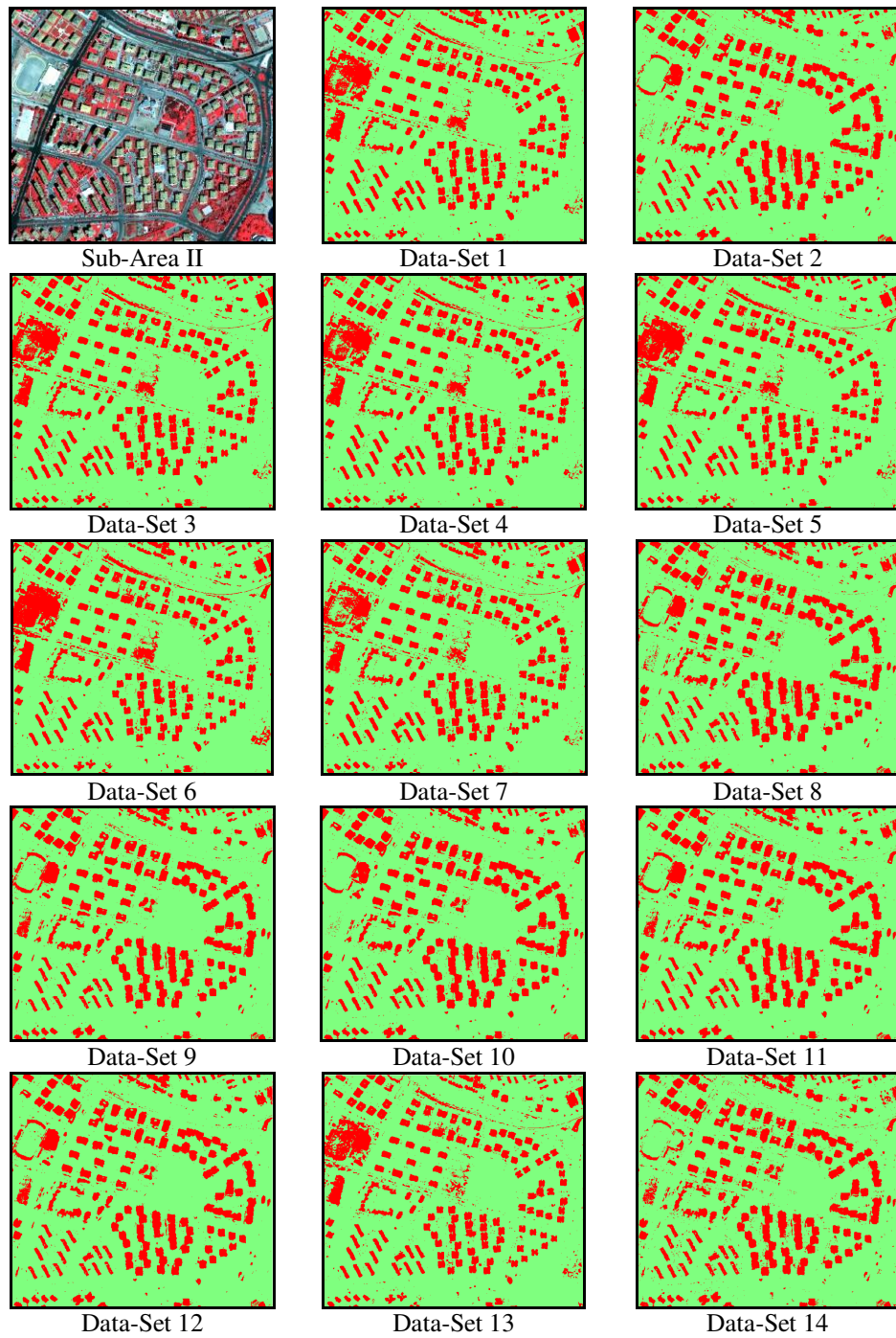


Figure 4. 29. For Sub-Area II, the results of SVM classification using 14 Data-Sets and 500 samples.

### 4.10.1.3. Sub-Area III

For Sub-Area III, the results of accuracy assessment of the SVM classification using 500, 1000, and 2000 training samples are given in table 4.19. The graphical representation of overall accuracies and Kappa Coefficients are provided in figures 4.30 and 4.31. For the 14 data sets, the outputs of the SVM classification conducted using 500 training pixels are illustrated in figure 4.32, and using 1000 and 2000 training samples are given in Appendix D.

Table 4. 19. For Sub-Area III, the Overall Accuracies and Kappa Coefficients.

Sub-area III	Overall Accuracy (%)			Kappa Coefficient		
	Train 500/ Test 2000	Train 1000/ Test 4000	Train 2000/ Test 8000	Train 500/ Test 2000	Train 1000/ Test 4000	Train 2000/ Test 8000
Data-Set 1	90.05	91.95	92.64	0.8010	0.8390	0.8528
Data-Set 2	96.55	97.30	97.40	0.9310	0.9460	0.9480
Data-Set 3	90.10	91.63	92.04	0.8020	0.8325	0.8408
Data-Set 4	89.70	91.65	92.01	0.7940	0.8330	0.8403
Data-Set 5	92.90	93.28	93.46	0.8580	0.8655	0.8692
Data-Set 6	93.40	94.23	94.06	0.8680	0.8845	0.8812
Data-Set 7	90.70	91.98	92.83	0.8140	0.8395	0.8565
Data-Set 8	96.85	97.40	97.48	0.9370	0.9480	0.9495
Data-Set 9	95.20	97.28	97.31	0.9040	0.9455	0.9463
Data-Set 10	95.85	96.20	96.64	0.9170	0.9240	0.9327
Data-Set 11	96.65	97.88	97.85	0.9130	0.9575	0.9570
Data-Set 12	96.05	96.45	97.53	0.9210	0.9290	0.9505
Data-Set 13	94.70	95.10	95.15	0.8940	0.9020	0.9030
Data-Set 14	96.30	96.95	97.70	0.9260	0.9390	0.9540

In this sub-area, the results of SVM classification, which was conducted using 500 training samples, were found to be quite satisfactory with the overall accuracies and Kappa Coefficients in the range of 89.70% – 96.85% and 0.7940 – 0.9370, respectively. For Data-Sets 2, 8, 11, 12, and 14, the overall accuracies were computed on the order of 96% while Kappa Coefficients were computed on the order of 0.92. The other data-sets provided slightly lower values with respect to these two measurements.

With the use of 1000 training samples, the overall classification accuracies were computed in the range from 91.63% to 97.88% and Kappa Coefficients were computed in the range from 0.8325 to 0.9475. In this case, Data-Sets 2, 8, 9, 11, and 14 provided the highest overall accuracy of 97% and the highest Kappa Coefficient of higher than 0.9390. On the other hand, for the other data-sets, these measurements gave relatively lower values.

With the use of 2000 training samples, the SVM classification provided overall accuracies between 92.01% and 97.85%, while the Kappa Coefficients were computed between 0.8403 and 0.9570. In this case, Data-Sets 2, 8, 9, 11, 12, and 14 provided the highest overall accuracy of higher than 97% and the highest Kappa Coefficient of higher than 0.94. Conversely, for the other data-sets, these measurements provided relatively lower values.

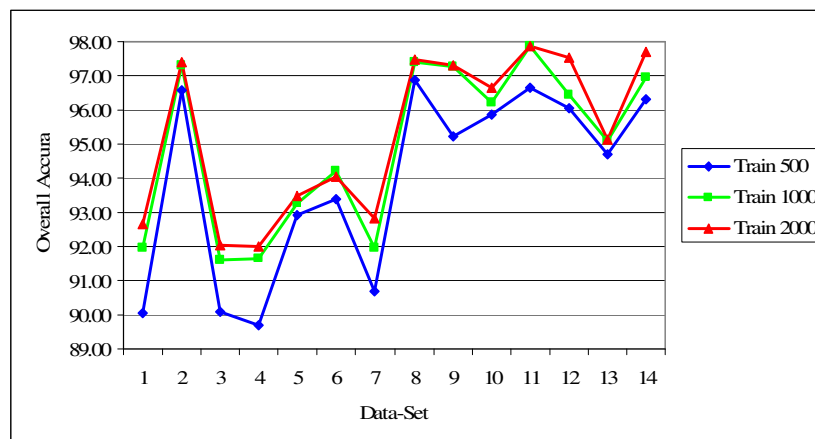


Figure 4. 30. For each data set, the overall accuracies computed using 500, 1000, and 2000 training samples in Sub-Area III.

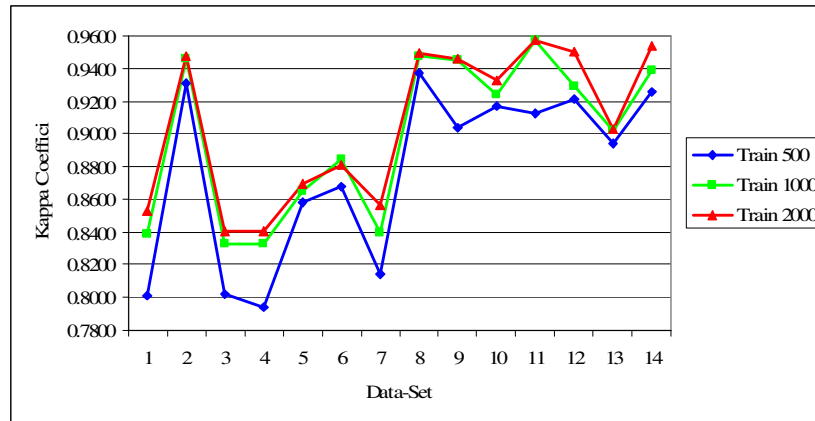


Figure 4. 31. For each data set, the kappa coefficients computed using 500, 1000, and 2000 training samples in Sub-Area III.

For this sub-area, if the effect of the size of training samples on classification accuracy is evaluated it can be stated that, in general, increasing the training size increased the accuracy. However, the increase was not observed to be more than 3% (Figure 4.30 and 4.31).



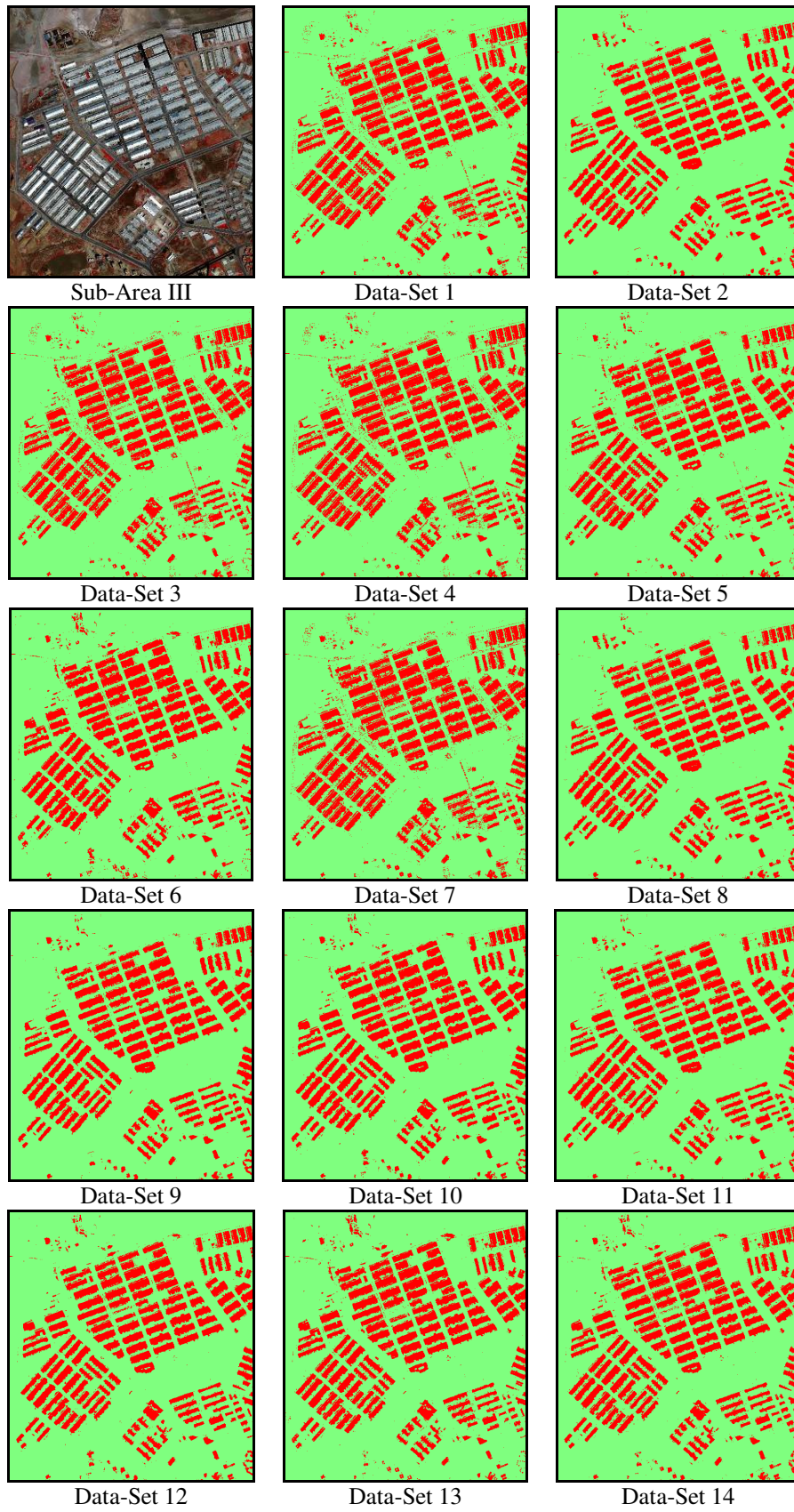


Figure 4. 32. For Sub-Area III, the results of SVM classification using 14 Data-Sets and 500 samples.

## 4.10.2. The Results of Building Detection

### 4.10.2.1. Sub-Area I

The accuracy assessment results of the detected building patches using the SVM classification with 500, 1000, and 2000 training samples are given in table 4.20. The graphical representation of the BDP and QP measurements are provided in figure 4.33.

Table 4. 20. For Sub-Area I, the quantitative evaluation of SVM classification using 500, 1000, and 2000 training samples.

Data-Set	Train 500				Train 1000				Train 2000			
	BF	MF	BDP	QP	BF	MF	BDP	QP	BF	MF	BDP	QP
1	0.44	0.20	83.02	60.93	0.35	0.24	80.73	63.01	0.38	0.23	81.39	62.02
2	0.43	0.11	90.10	65.11	0.35	0.13	88.75	67.88	0.36	0.12	89.55	67.89
3	0.50	0.19	83.82	59.03	0.39	0.23	81.24	61.74	0.39	0.22	81.96	62.14
4	0.50	0.19	83.88	59.14	0.37	0.24	80.96	62.40	0.39	0.23	81.62	61.77
5	0.40	0.21	82.53	61.91	0.35	0.23	81.39	63.52	0.35	0.23	81.57	63.43
6	0.36	0.24	80.61	62.51	0.34	0.25	80.28	63.23	0.35	0.24	80.91	63.02
7	0.48	0.20	83.40	59.68	0.42	0.22	81.66	60.62	0.40	0.23	81.21	61.45
8	0.43	0.11	90.28	65.06	0.32	0.13	88.29	68.71	0.34	0.12	89.32	68.29
9	0.45	0.10	90.60	64.48	0.35	0.13	88.79	67.96	0.36	0.12	89.65	67.73
10	0.32	0.14	87.58	68.62	0.28	0.14	87.57	70.21	0.32	0.13	88.79	69.11
11	0.47	0.10	91.18	63.85	0.33	0.13	88.63	68.57	0.34	0.12	89.34	68.70
12	0.30	0.15	86.95	68.79	0.28	0.14	87.46	70.28	0.32	0.12	89.02	69.23
13	0.37	0.22	81.73	62.56	0.36	0.24	80.70	62.54	0.37	0.23	81.52	62.70
14	0.27	0.15	86.78	70.16	0.28	0.15	86.80	69.96	0.30	0.13	88.15	69.51

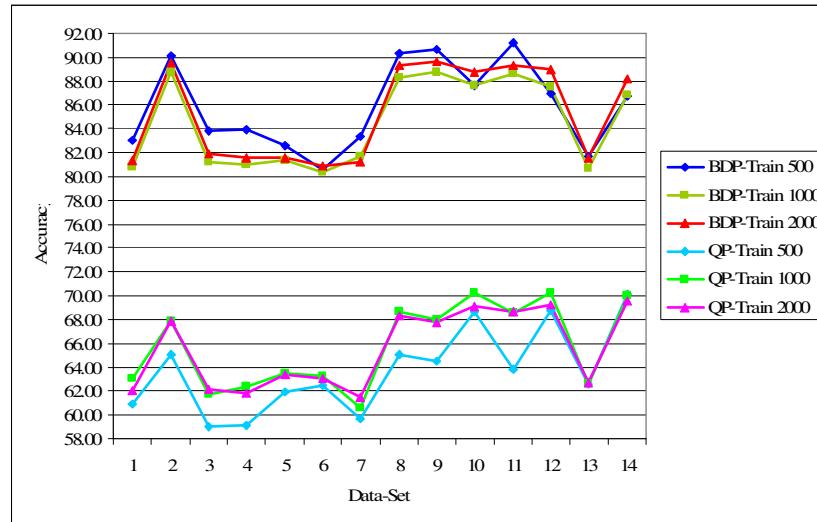


Figure 4. 33. For each data set, the BDP and QP measurements computed for the classifications conducted using 500, 1000, and 2000 training samples in Sub-Area I.

For Data-Sets 2, 8, 9, 11, and 14, with the use of 500 training samples, the BDP values were computed to be higher than 90% providing the best building detection results. For Data-Sets 10 and 12, the BDP was computed to be approximately 87%. However, for Data-Sets 1, 3, 4, 5, 6, 7, and 13, the same evaluation factor resulted in relatively lower values on the order of about 83%. The SVM classification using Data-Sets 2, 8, 10, 12, and 14 provided the best QP values (higher than 67%), while for Data-Sets 9 and 11, the QP values were computed to be about 63%. On the other hand, for Data-Sets 1, 3, 4, 5, 6, 7, and 13, the QP values were relatively low.

For the same sub-area, the results of building detection conducted using 1000 training samples were found to be quite similar to the results of 500 training samples. For Data-Sets 2, 8, 9, and 11, the BDB values were computed to be higher than 88% and, for this case, these are the best results obtained for the building detection procedure. For Data-Sets 10, 12, and 14, the BDP was computed approximately as 87%. However, for Data-Sets 1, 3, 4, 5, 6, 7, and 13, the same evaluation factor resulted in relatively lower values of about 80%. When the results are assessed using the accuracy measure of QP it can be said that Data-Sets 2, 8, 9, 10, 11, and 12 provided the best results (higher than 67%), while Data-Sets 5 and 6 resulted in

lower values of about 63%. On the other hand, Data-Sets 1, 3, 4, 7, and 13 provided the lowest QP values.

For the classification using 2000 training samples, the BDB values were computed to be quite high (higher than 89%) for Data-Sets 2, 8, 9, 11, and 12, which provided the best results. For Data-Sets 10 and 14, the BDP was computed approximately as 88%. However, for Data-Sets 1, 3, 4, 5, 6, 7, and 13, the same evaluation factor resulted in rather lower values of about 81%. When the results are assessed using the accuracy measure of QP it can be said that Data-Sets 8, 10, 11, 12, and 14 provided the best results with the accuracy measure of higher than 67%. While Data-Sets 2 and 9 resulted in moderate QP values of about 63%, Data-Sets 1, 3, 4, 5, 6, 7, and 13 provided the lowest QP accuracies.

The effect of the training sample sizes on the classification accuracy is represented graphically in figures 4.34 and 4.35. As can be seen in these figures, based on the results obtained from this sub-area, increasing the sample size does not necessarily increase the BDP and QP values.

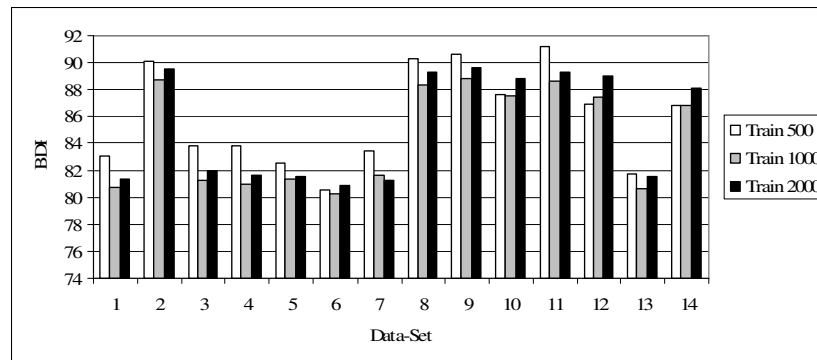


Figure 4. 34. The comparison of BDP values using 500, 1000, and 2000 training samples for Sub-Area I.

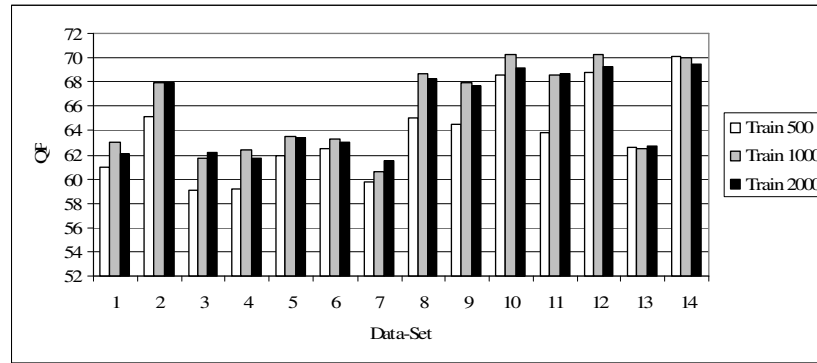


Figure 4. 35. The comparison of QP values using 500, 1000, and 2000 training samples for Sub-Area I.

#### 4.10.2.2. Sub-Area II

The accuracy assessment results of the detected building patches using the SVM classification with 500, 1000, and 2000 training samples are given in table 4.21. The graphical representation of BDP and QP measurements is provided in figure 4.36.

Table 4. 21. For Sub-Area II, the quantitative evaluation of the SVM classification using 500, 1000, and 2000 training samples.

Data-Set	Train 500				Train 1000				Train 2000			
	BF	MF	BDP	QP	BF	MF	BDP	QP	BF	MF	BDP	QP
1	0.58	0.14	87.34	58.06	0.54	0.15	86.84	59.01	0.68	0.19	84.26	53.44
2	0.47	0.11	90.44	63.40	0.39	0.11	90.49	66.83	0.41	0.10	90.71	66.28
3	0.58	0.15	87.19	57.82	0.56	0.16	86.13	58.08	0.66	0.18	84.66	54.25
4	0.58	0.15	87.16	58.04	0.53	0.15	86.99	59.43	0.68	0.18	84.40	53.62
5	0.57	0.17	85.13	57.18	0.60	0.18	84.94	56.41	0.63	0.21	82.73	54.35
6	0.67	0.17	85.40	54.41	0.60	0.18	85.04	56.20	0.64	0.19	83.75	54.42
7	0.55	0.13	88.42	59.51	0.50	0.19	84.07	59.05	0.60	0.19	84.11	55.96
8	0.50	0.10	90.70	62.28	0.42	0.10	90.77	65.62	0.40	0.10	90.63	66.43
9	0.51	0.11	90.17	61.74	0.41	0.11	90.31	65.71	0.43	0.11	90.31	65.19
10	0.49	0.10	91.31	63.26	0.42	0.10	90.78	65.68	0.42	0.10	91.11	65.74
11	0.52	0.11	90.43	61.61	0.47	0.10	90.79	63.78	0.43	0.11	90.47	65.02
12	0.50	0.10	91.21	62.68	0.47	0.10	90.65	63.61	0.43	0.10	90.70	65.21
13	0.54	0.17	85.18	58.49	0.56	0.18	84.54	57.26	0.58	0.19	84.05	56.46
14	0.55	0.12	89.22	59.70	0.50	0.11	89.72	61.95	0.46	0.11	89.74	63.54

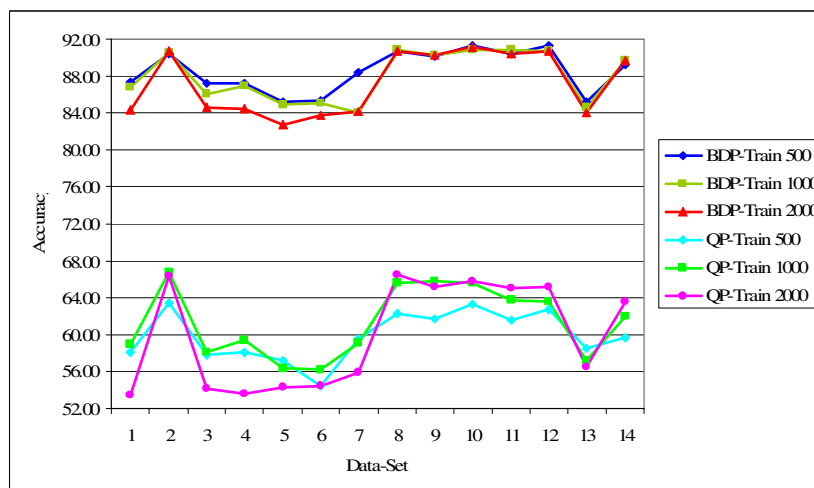


Figure 4. 36. For each data set, the BDP and QP measurements computed for the classifications conducted using 500, 1000, and 2000 training samples in Sub-Area II.

For Data-Sets 2, 8, 9, 10, 11, and 12, with the use of 500 training samples, the BDP values were computed to be higher than %90 providing the best building detection results. For Data-Sets 7 and 14, the BDP was computed to be approximately 89%. However, for Data-Sets 1, 3, 4, 5, 6, and 13, the same evaluation factor resulted in slightly lower values of about 87%. For Data-Sets 2, 8, 10, and 12, the SVM classification provided the highest QP values (higher than 63%), while for Data-Sets 7, 11, and 14, the QP values were computed to be about 59%. On the other hand, for Data-Sets 1, 3, 4, 5, 6, and 13, the QP values computed were relatively low.

The results obtained using 1000 training samples were found to be quite similar to the results of 500 training samples. For Data-Sets 2, 8, 9, 10, 11, and 12, the BDP values were quite similar to the results of 500 training samples. For these data sets, the BDB values were computed to be higher than 90% and, for this case, these are the best building detection results. For Data-Set 14, the BDP was computed to be 89.72%. However, for Data-Sets 1, 3, 4, 5, 7, and 13, the same evaluation factor resulted in relatively lower values. When the results are assessed using the accuracy measure of QP it can be said that Data-Sets 2, 8, 9, and 10 provided the best results

(higher than 65%), while Data-Sets 11, 12, and 14 resulted in moderate (about 63%) values. Conversely, Data-Sets 1, 3, 4, 5, 6, 7, and 13 provided the lowest QP values.

For the classification using 2000 training samples, the BDP values were computed to be quite high (higher than 89%) for Data-Sets 2, 8, 9, 10, 11, and 12, which provided the best building detection results. For Data-Set 14, the BDP was computed to be 89.74%. However, for Data-Sets 1, 3, 4, 5, 6, 7, and 13, the same evaluation factor resulted in lower values. When the results are assessed using the accuracy measure of QP it can be said that Data-Sets 2, 8, 9, 10, 11, and 12 provided the best results with the accuracy measure of higher than 65%. While Data-Set 14 resulted in moderate QP values (63.54%), Data-Sets 1, 3, 4, 5, 6, 7, and 13 provided the lowest QP accuracies.

In figures 4.37 and 4.38, the effect of the training sample sizes on the classification accuracy is represented. As can be seen in these figures, based on the results obtained from this sub-area, increasing the sample size does not increase the BDP and QP values.

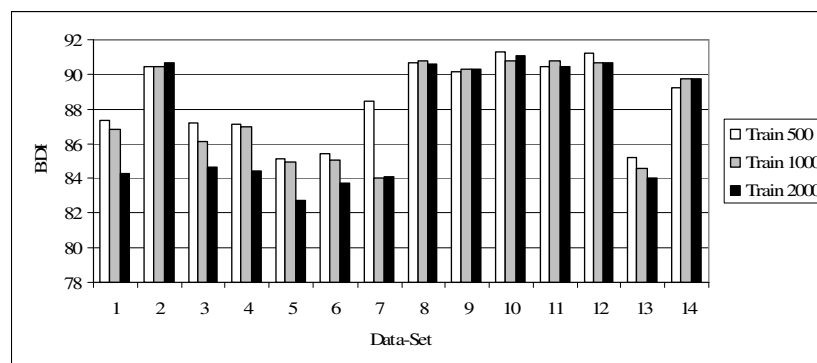


Figure 4. 37. The comparison of BDP values using 500, 1000, and 2000 training samples for Sub-Area II.

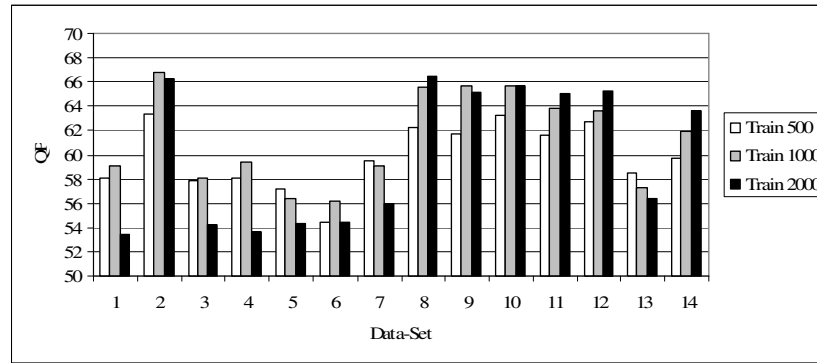


Figure 4. 38. The comparison of QP values using 500, 1000, and 2000 training samples for Sub-Area II.

#### 4.10.2.3. Sub-Area III

For sub-area III, the accuracy assessment results of the detected building patches using the SVM classification with 500, 1000 and 2000 training samples are given in table 4.22. The graphical representation of BDP and QP measurements using 14 data sets is provided in figure 4.39.

Table 4. 22. For Sub-Area III, the quantitative evaluation of the SVM classification using 500, 1000, and 2000 training samples.

Data-Set	Train 500				Train 1000				Train 2000			
	BF	MF	BDP	QP	BF	MF	BDP	QP	BF	MF	BDP	QP
1	0.46	0.10	91.07	64.09	0.42	0.09	91.39	65.84	0.41	0.08	92.29	67.14
2	0.34	0.04	95.79	72.20	0.31	0.04	96.12	73.86	0.29	0.04	95.77	74.94
3	0.48	0.09	91.54	63.42	0.44	0.09	91.55	65.16	0.41	0.09	91.80	66.66
4	0.50	0.10	91.22	62.53	0.45	0.10	91.29	64.83	0.41	0.09	91.79	66.61
5	0.39	0.09	92.11	67.88	0.39	0.08	92.32	67.70	0.39	0.08	92.69	68.03
6	0.45	0.07	93.88	65.96	0.45	0.06	93.94	65.99	0.43	0.07	93.81	66.68
7	0.52	0.09	92.15	62.32	0.44	0.09	91.58	65.12	0.41	0.08	92.64	67.26
8	0.34	0.05	95.65	72.26	0.32	0.04	96.07	73.34	0.29	0.04	95.79	75.14
9	0.33	0.05	95.50	72.39	0.34	0.03	96.81	73.08	0.29	0.04	96.14	75.25
10	0.37	0.04	95.95	71.01	0.34	0.04	96.26	72.36	0.33	0.04	96.61	73.14
11	0.32	0.05	95.27	72.82	0.31	0.04	96.61	74.10	0.28	0.04	96.20	75.89
12	0.35	0.04	95.71	71.70	0.33	0.04	96.10	72.83	0.32	0.03	96.65	73.73
13	0.40	0.07	93.72	68.21	0.43	0.06	94.22	66.93	0.42	0.06	94.38	67.68
14	0.36	0.05	95.50	71.22	0.34	0.04	95.89	72.20	0.34	0.03	96.81	72.93



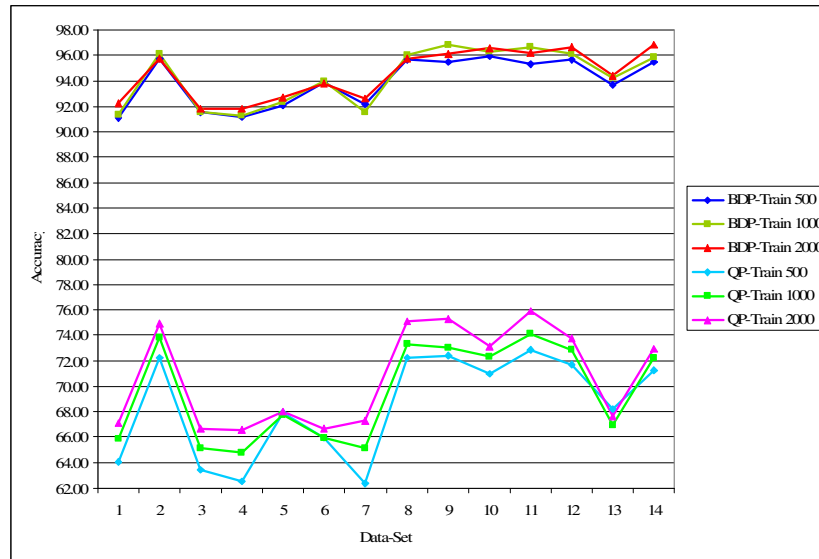


Figure 4. 39. For each data set, the BDP and QP measurements computed for the classifications conducted using 500, 1000, and 2000 training samples in Sub-Area III.

For Data-Sets 2, 8, 9, 10, 11, 12, and 14, with the use of 500 training samples, the BDP values were computed to be higher than 95% providing the best results. For Data-Sets 6 and 13, the BDP values were computed to be approximately 94%. However, for Data-Sets 1, 3, 4, 5, and 7, the same evaluation factor resulted in relatively lower values of about 91%. The SVM classification conducted using Data-Sets 2, 8, 9, and 11 provided the best QP values (higher than 72%), while for Data-Sets 10, 12, and 14, the QP values were computed to be about 71%. On the other hand, for Data-Sets 1, 3, 4, 5, 6, 7, and 13, the QP values computed were relatively low.

The results of the building detection procedure performed through SVM classification using 1000 training samples were found to be quite similar to the results of using 500 training samples. For Data-Sets 2, 8, 9, 10, 11, and 12, the BDP values were computed to be higher than 96% providing, for this case, the best results. For Data-Sets 6, 13, and 14, the BDP values were computed to be about 94%. However, for Data-Sets 1, 3, 4, 5, and 7, the same evaluation factor resulted in relatively lower values. When the results are assessed using the accuracy measure of

QP it can be said that Data-Sets 2, 8, 9, and 11 provided the best results (higher than 73%), while Data-Sets 10, 12, and 14 resulted in moderate QP values (about 72%). On the other hand, Data-Sets 1, 3, 4, 5, 6, and 7, provided the lowest (lower than 68%) QP values.

For the classification using 2000 training samples, the BDP values were computed to be remarkably high (higher than 95%) for Data-Sets 2, 8, 9, 10, 11, 12, and 14 providing the best results for this case. For Data-Sets 6 and 13, the BDP values were computed to be about 94%. However, for Data-Sets 1, 3, 4, 5, and 7, the same evaluation factor resulted in slightly lower values of about 92%. When the results are assessed using the accuracy measure of QP it can be said that Data-Sets 2, 8, 9, and 11 provided the best results with the accuracy measure of about 75%. While Data-Sets 10, 12, and 14 resulted in moderate QP values of about 73%, Data-Sets 1, 3, 4, 5, 6, 7, and 13 provided the lowest accuracies.

The effect of the training sample sizes on classification accuracy is represented in figures 4.40 and 4.41. As can be seen in these figures, for most of the data-sets used, increasing the sample size increases the BDP and QP accuracies slightly.

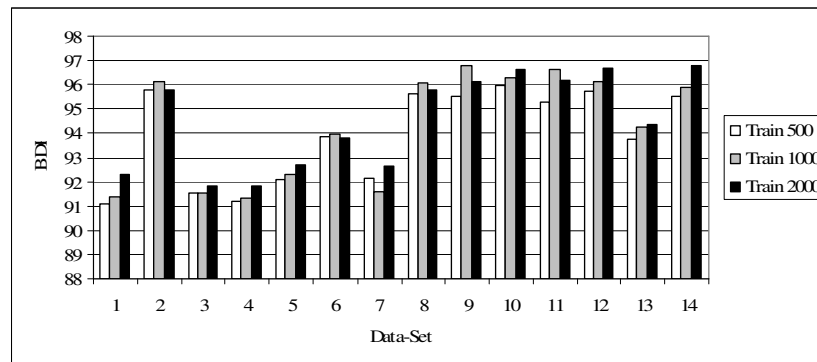


Figure 4. 40. The comparison of BDP values using 500, 1000, and 2000 training samples for Sub-Area III.

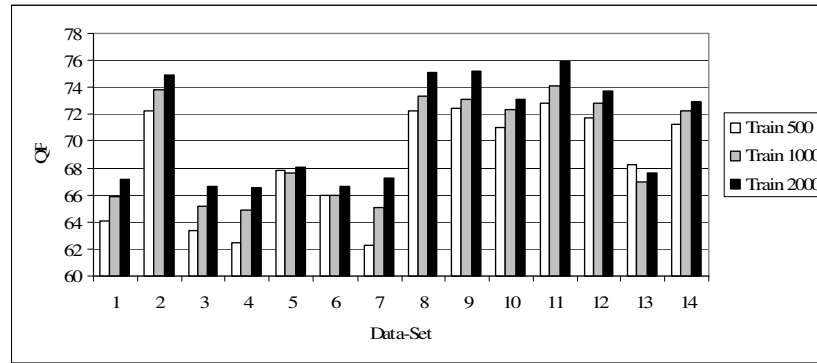


Figure 4. 41. The comparison of QP values using 500, 1000, and 2000 training samples for Sub-Area III.

When the SVM classification accuracies computed for three sub-areas are evaluated it can be stated that, the BDP values were found to be considerably high staying between 80% and 97%. In SVM classification, the use of additional bands improves the results significantly. In this study, it was proven that the inclusion of an nDSM as ancillary data is very important. It was also found that in most cases, using an NDVI image as an additional band also increases the accuracy but not as high as nDSM. Using both the nDSM and NDVI images as additional bands in the classification process together with the original bands ( $B_1$ ,  $B_2$ ,  $B_3$  and  $B_4$ ) increases the BDP and QP values considerably. But, unexpectedly the inclusion of the 1<sup>st</sup>, 2<sup>nd</sup>, 3<sup>rd</sup>, and 4<sup>th</sup> Principal Components ( $B_{PC1}$ ,  $B_{PC2}$ ,  $B_{PC3}$ , and  $B_{PC4}$ ) into the classification process did not lead to prominent difference in the accuracy level.

Concerning the effect of training sample size on classification accuracy, it can be stated that generally increasing the training size increases the accuracy. However, in the present case the increase was not observed to be more than 3%. The results obtained in this study indicate that, for a high resolution image measuring about 2000 pixels x 2000 lines, smaller training size (i.e. 500 pixels) appear to be enough to perform SVM classification. The SVM classification uses the training samples that lie at the edge of the class distributions in feature space. Therefore, when using SVM Classifier, providing complete description of the classes is not necessary and a small set of training samples would be enough. The accuracy of a SVM classification

depends not so much on the size of input training data but more on the location of training data in the feature space.

## **CHAPTER 5**

### **BUILDING DELINEATION BASED ON HOUGH TRANSFORM AND BOUNDARY TRACING TECHNIQUES**

In this chapter, the building boundary delineation from the building patches is described. Two approaches were developed for delineating the building boundaries, which are based on (i) Hough transform and (ii) Boundary tracing. First, the methodology of the Hough transform based approach is given, the processing steps are described and the results of the delineation process are provided. Then, the methodology of the Boundary tracing based approach is given, the processes are explained and the results are presented. Finally, the results obtained from two approaches are compared and discussed in detail.

After detecting the building patches (Chapter 4), the next step is the delineation of these patches to obtain the building boundaries. The building detection process described in the previous chapter provides the area of interest for delineating the buildings. Once the areas of interests are known the unnecessary edges that belong to objects other than buildings are excluded. The previously detected building patches are in raster form. To obtain the building boundaries, the detected building patches must be converted into vector form.

The first approach starts with an edge detection which is followed by Hough transform and perceptual grouping. In the second approach, the previously detected edges are vectorized using the Boundary tracing algorithm and the results are refined using a line simplification algorithm and vector filters. The general flowchart that

shows the basic steps of the proposed building delineation from the high resolution satellite images is given in figure 5.1.

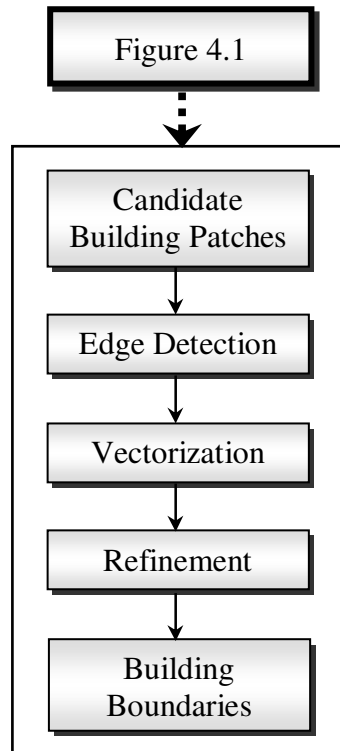


Figure 5. 1. The delineation of building boundaries.

### **5.1. Building Delineation Based on Hough Transform**

The man-made objects usually have shapes with straight and circular edges that project to straight and elliptical boundaries in an image and therefore, using Hough transform may be effective to delineate the building boundaries. Thus, in this study, the previously detected building patches were applied a Hough transform for delineating the building boundaries.

Although the predominant building shape is rectangular in the study area, there are also buildings with different shapes. Therefore, in the present study, the delineation process was carried out for the rectangular and circular shaped buildings.

### 5.1.1. The Methodology

The flowchart of the developed approach is given in figure 5.2. Initially the edges are detected using an edge detection algorithm. The resulting image is a binary image that shows the edges of the building patches. These edges that are in raster form are converted into vector form using a Hough transform, which is a widely used method to extract lines or curves that form the objects. After detecting the lines or curves in vector form, the next step is grouping them perceptually to obtain the building boundaries.

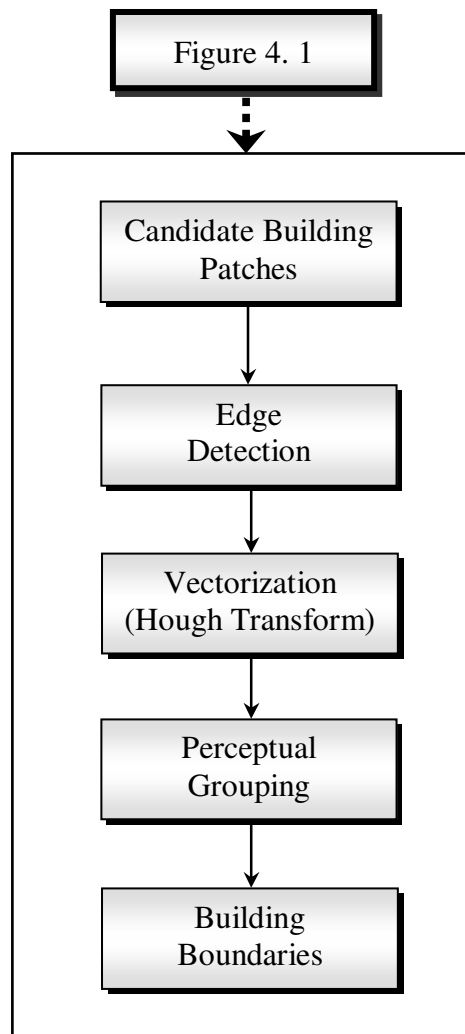


Figure 5. 2. The flowchart of Hough transform based approach.

If the orientations of the objects are different, then the Hough transform may not provide good results. In addition, in the building delineation stage, especially for the complex buildings (such as “C” shape and “S” shape buildings), it becomes important to deal with each patch individually. Otherwise, the patches close to each other may not be delineated successfully. Therefore, to handle these problems, the patches were delineated sequentially one after the other. To do that each candidate building patch was labeled using the label matrix operation. The pixels that belong to separate building patches were assigned unique integers starting from 1 to the number of candidate building patches, and the background pixels were assigned the value of 0. This is a very useful tool because it allows objects to be separated and analysed individually. Then, each patch was delineated independently using a label matrix. The schematic representation of a label matrix generation is given in figure 5.3. Next, the corresponding original values of the building patches are sequentially generated. After that, the developed Hough transform and Boundary tracing based approaches are applied to these candidate building patches for delineating the boundaries.

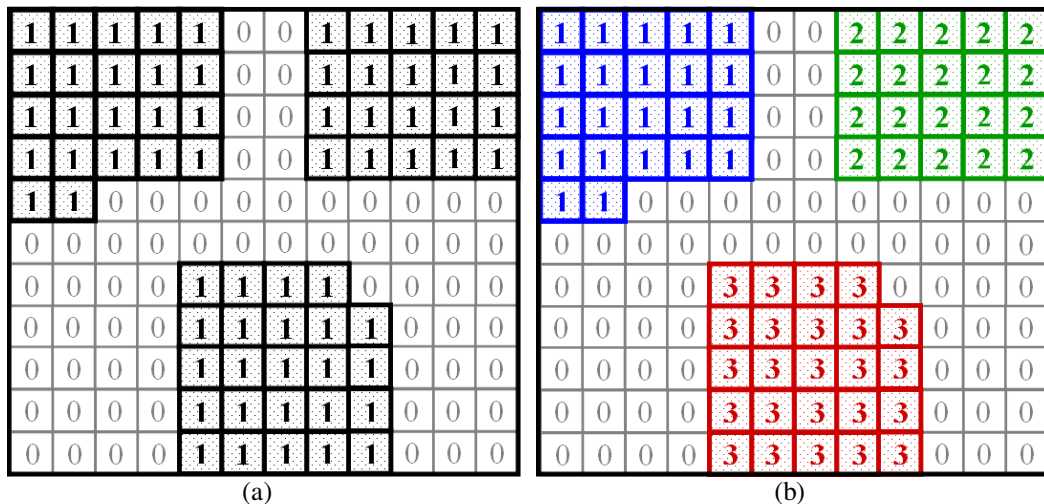


Figure 5. 3. The schematic representation of (a) a binary image that includes separated components and (b) generated label matrix.



### **5.1.2. Delineation of the Rectangular Shape Buildings**

The shapes of the buildings are usually rectangle, the mutual lines are usually parallel to each other, and the adjacent lines intersect at right angles. To delineate the boundaries of the rectangular buildings, the edges were detected first using the Canny Edge Detection algorithm. Then, the Hough transform was used to vectorize the detected edges. Finally, the vector lines were grouped to generate the building boundaries.

#### **5.1.2.1. Edge Detection**

To extract the edges from the previously detected building patches, the Canny Edge Detection algorithm was used. The Canny Edge Detector produces one pixel wide edges and connects the broken lines that are important for further processing. The edges are the pixels, where there is an abrupt change in the intensity level of pixels and they are important sources for finding the object boundaries. In the proposed approach, the patches are processed one at a time. Therefore, processing the candidate building patches only decreases the number of unnecessary edges. The edge detection operation results in a binary image that contains the edge segments of the buildings.

The Canny Edge Detector (Canny, 1983 and Canny, 1986) is a complicated approach for generating an edge map from an image. The steps followed for the Canny Edge Detection are as follows (Sonka et al., 1998):

- Smoothing the image with a Gaussian filter,
- Computing the gradient magnitude and orientation using finite-difference approximations for the partial derivatives,
- Applying non-maxima suppression to the gradient magnitude, and
- Using a hysteresis thresholding algorithm to detect and link edges.

Initially a Gaussian Filter (Equation 5.1) is applied to remove the noise and details in the image and also to smooth the image. The standard deviation ( $\sigma$ ) determines the width of the filter. The larger  $\sigma$  removes the noise, while smoothes away the weak edges. Then, to find the edge strength the gradient magnitude is computed (Equation 5.2).

$$G(x, y) = \frac{1}{2\pi\sigma^2} e^{-\frac{x^2 + y^2}{2\sigma^2}} \quad (\text{Equation 5. 1})$$

$$|G_n * g| = |\nabla(G * g)| \quad (\text{Equation 5. 2})$$

After computing the gradient, the locations of the edges are found by using non-maximal suppression, which thins the wide edges in gradient magnitude to the one pixel wide edges.

The algorithm for the Non-Maximal Suppression is as follows (Sonka et al., 1998):

- Quantize edge directions eight ways according to the 8-connectivity,
- For each pixel that is non-zero edge magnitude, inspect the two adjacent pixels indicated by the direction of its edge,
- If the edge magnitude of either of these two exceeds that of the pixel under inspection, mark it for deletion, and
- After inspecting all pixels, re-scan the image and delete the marked edges.

Although the image is smoothed initially, the non-maxima suppressed magnitude image may include many false edges caused by noise and fine texture. To handle this problem, a threshold is applied to the image. In Canny Edge Detection, a more useful thresholding “hysteresis thresholding”, which uses two thresholds  $T_{\text{low}}$  and  $T_{\text{high}}$ , is used. Of these thresholds,  $T_{\text{high}}$  is used to determine the definite edges. Then, these pixels are tried to grow by searching the surrounding pixels with gradient magnitudes higher than  $T_{\text{low}}$  because if the weak pixels are connected to these edges, they are more likely to be true edges in the image.

### 5.1.2.2. Hough Transform

The vectorization of the edge image was carried out using the Hough transform, through which the analytically defined shapes, such as lines, circles or ellipses in images can be detected. This is a strong method and can even be used successfully for the extraction of overlapping or semi-occluded objects in noisy images (Ecabert and Thiran, 2004).

In Hough transform, a point  $(x_i, y_i)$  and all the lines that pass from it are considered. Infinitely many lines pass through  $(x_i, y_i)$ , all of which satisfy the slope-intercept equation:

$$y_i = ax_i + b \quad (\text{Equation 5. 3})$$

where  $a$  is the slope of the line and  $b$  is the  $y$  intercept. For all lines that pass through a point  $(x_i, y_i)$ , there is a unique value of  $b$  for  $a$ :

$$b = -x_i a + y_i \quad (\text{Equation 5. 4})$$

A point in the  $xy$ -plane corresponds to a line in the  $ab$ -plane (Duda and Hart, 1972). Figure 5.4 provides these concepts.

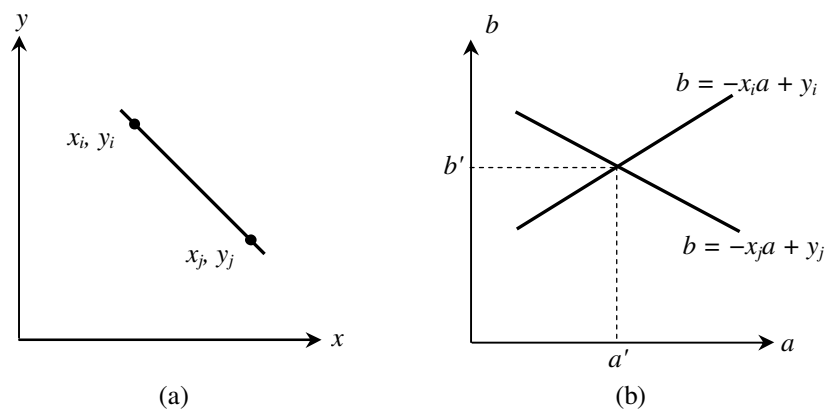


Figure 5. 4. (a) A line in the  $xy$ -plane and (b) the corresponding lines to the points in the normal plane.

The difficulty in slope-intercept approach is that the slope of the line move towards to infinity when the line is about vertical and the slope is 0 when the line is horizontal. To handle this problem, in the Hough transform normal representation of a line can be used (Equation 5.5).

$$r = x \cos \theta + y \sin \theta \quad (\text{Equation 5. 5})$$

where,  $r$  represent the length and  $\theta$  is an angle from the origin of a normal to the line.

In other words, a line is described as being at an angle  $90^\circ$  from  $\theta$ , and being  $r$  units away from the origin at its closest point. In figure 5.5 the line in  $xy$ -plane and its transformation to the  $r\theta$ -plane is illustrated. By transforming all the possible lines through a point into the  $r\theta$ -plane a sinusoidal curve is created which is unique to that point. A point in the  $xy$ -plane corresponds to a sinusoidal curve in the  $r\theta$ -plane (Duda and Hart, 1972).

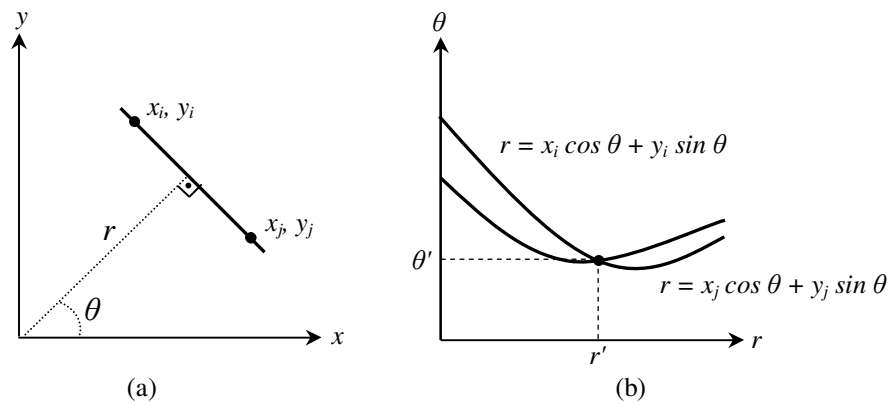


Figure 5. 5. (a)  $r, \theta$  parameterization of lines in the  $xy$ -plane and (b) the sinusoidal curves in the  $r\theta$  plane.

The computational attractiveness of the Hough transform arises from sub-dividing the  $r\theta$  parameter space into so-called accumulator cells (Gonzales et al., 2004). The

transform is implemented by quantizing the Hough parameter space into accumulator cells. In the beginning, the accumulator cells are set to zero. As the algorithm runs, each  $(x_i, y_i)$  is transformed into a discretized  $(r, \theta)$  curve and the accumulator cells that lie along this curve are incremented. Resulting peaks in the accumulator array represent strong evidence that a corresponding straight line exists in the image.

The algorithm for the Hough transform is as follows (Morse, 2000);

- Find edges on the candidate building patch image

- For each feature point

- For each possibility  $i$  in the accumulator that passes through the feature point

- Increment that position in the accumulator

- Find local maxima in the accumulator

- If desired, map each maximum in the accumulator

- Back to the image space

### **5.1.2.3. Perceptual Grouping**

After vectorizing the edges, the next step is to group the lines using perceptual grouping and to delineate building boundaries. The algorithm to delineate the building boundaries using the perceptual grouping procedure is as follows;

- For each candidate building patch

- Find the centroid point of the candidate building patch

- Merge the collinear lines, unless the distances between them is smaller than the determined threshold

- Select the longest Hough line segment

- Select the longest Hough line segment that is perpendicular to the longest Hough line segment

- Find the intersection point between these two line segments

Compute the distance between the intersection point and the centroid of the building patch

Calculate the coordinates of a new point, which has equal distance from the centroid of the building patch and in the opposite direction.

Draw lines that are parallel to the above two longest Hough lines and cross over the new point

Delineate the building boundary

End for

As explained in the above algorithm, for each building patch, the first step is finding the centroid of the patch. Next, the collinear Hough lines are merged together, unless the distance between the line segments are smaller than the minimum distance between the buildings (Figure 5.6 (a)). Then, the dominant line is found (Figure 5.6 (c)). In this study, the longest Hough line is accepted to be the dominant line because it is most likely that the dominant line represents the true edge of the building. After detecting the longest line, the second longest line perpendicular ( $90^\circ \pm 10^\circ$ ) to the dominant line is selected from the remaining Hough line segments (Figure 5.6 (d)). The boundaries of the building are delineated based on these two lines. Next, the intersection point of these two lines is calculated and these lines are extended or shortened to end with this point (Figure 5.6 (e)). After that, the distance between the intersection point and the centroid of the building patch is calculated and a new point, which has an equal distance from the centroid of the building patch in the opposite direction, is generated (Figure 5.6 (f)). Next, two new lines are drawn passing through the new point and one parallel to the longest line and the other parallel to the longest perpendicular line (Figure 5.6 (g)). As a final step, these four lines are combined to generate the building boundary (Figure 5.6 (h)). In figure 5.7, the schematic representation of a building delineation is shown.

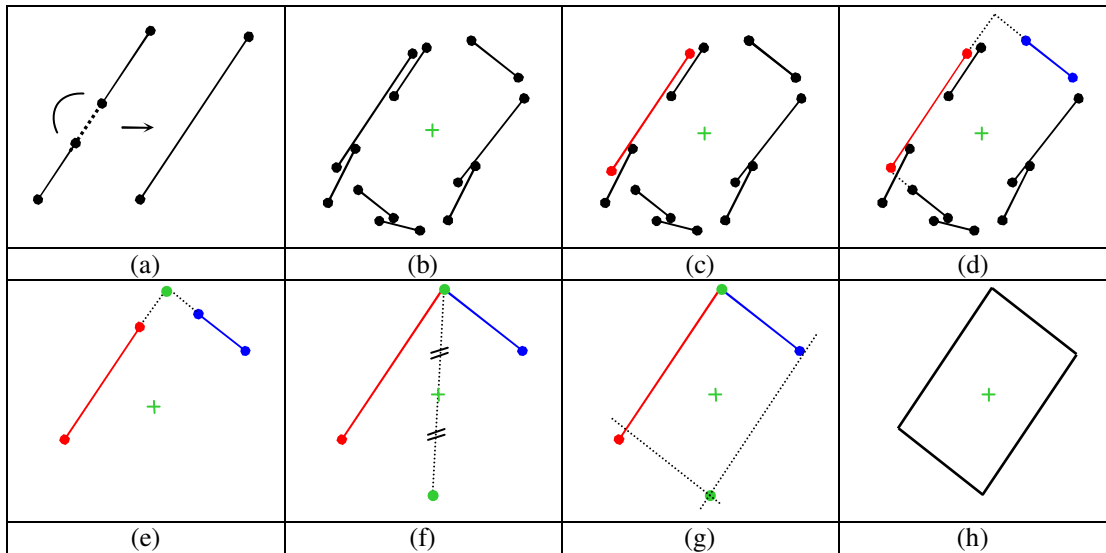


Figure 5. 6. The stages of perceptual grouping.

The developed algorithm for delineating the boundaries of the rectangular buildings was implemented in the residential and industrial areas. The residential areas were grouped according to dwelling types as explained in chapter 3.

In this study, the parameters used to delineate the rectangular buildings were divided into three groups that are related to (i) canny edge detection (*high threshold*, *low threshold* and *sigma*), (ii) Hough transform (*theta resolution*, *r resolution* and *minimum line*), and (iii) perceptual grouping (*gap range* and *theta range*).

*High Threshold ( $T_{high}$ ):* The higher threshold of the hysteresis thresholding. In this study, it was taken as 0.4.

*Low Threshold ( $T_{low}$ ):* The lower threshold of the hysteresis thresholding. In this study, it was taken as 0.3.

*Sigma ( $\sigma$ ):* It is the standard deviation of the Gaussian filter. In this study, the sigma value was used to be “1”.

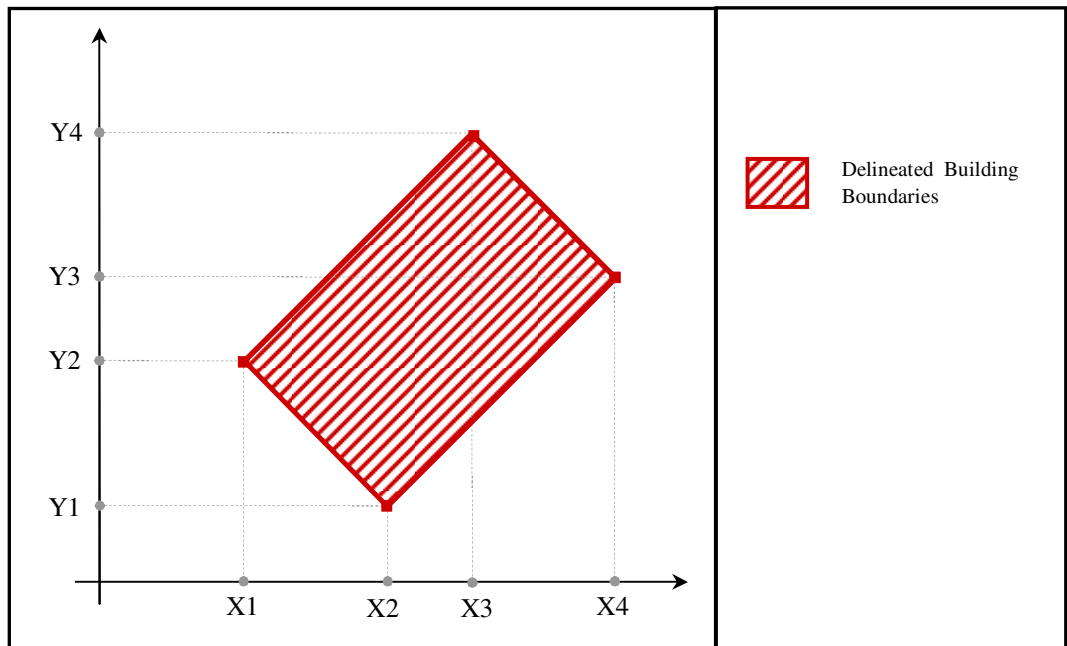
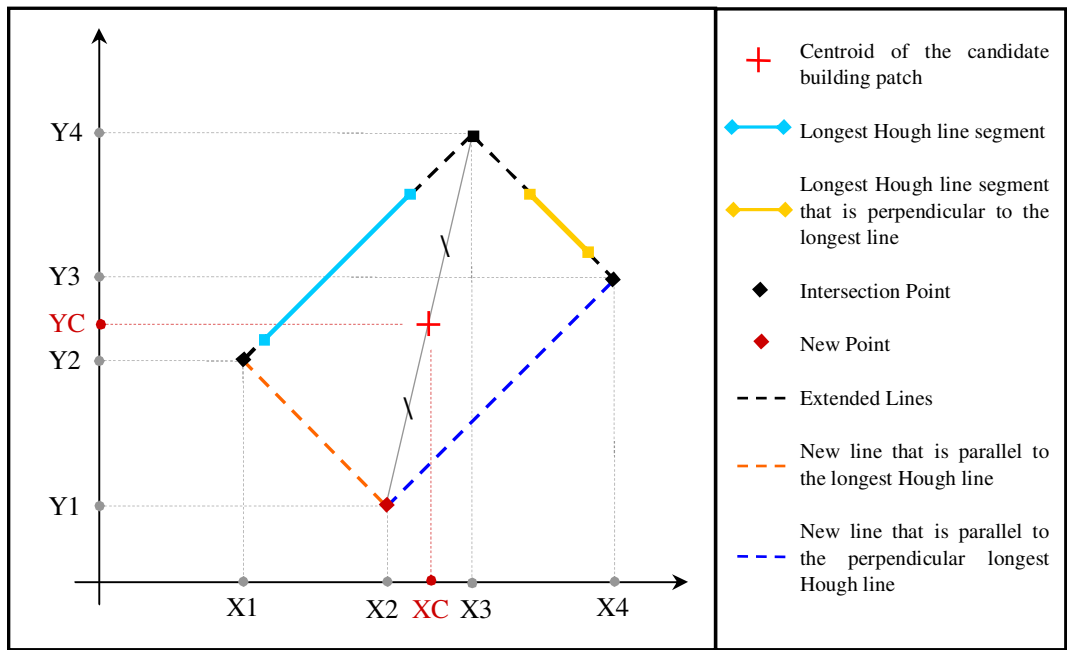


Figure 5. 7. The schematic representation of the algorithm.



*Theta Resolution ( $\theta_{resolution}$ ):* It denotes the spacing of the Hough transform bins along the theta axis in degrees and this value was taken to be “1” in this study.

*r Resolution ( $r_{resolution}$ ):* It states the spacing of the Hough transform bins along the intervals in the r axis and this value was taken to be “1” in this study.

*Minimum Line ( $L_{min}$ ):* This parameter is used to decide which Hough lines are discarded. The lines that are shorter than this value are deleted. In this study, it was determined to be “1”.

*Gap range ( $L_{gap}$ ):* It is used to merge the collinear Hough line segments, when the distance between them is less than the specified proximity value. This value is determined regarding to the minimum distances between the buildings. If the gap between the lines is smaller than this value, these lines are grouped.

*Theta range ( $\theta_{range}$ ):* It is the flexibility range for the perpendicularity between the Hough line segments. In this study, the lines that have  $90^\circ \pm 10^\circ$  angles were grouped together.

### **5.1.3. Delineation of the Circular Buildings**

Before delineating the circular buildings, the buildings that have circular shapes are grouped as follows:

- “Circle” Shape Buildings,
- “Ring” Shape Buildings,
- “C” Shape Buildings, and
- “S” Shape Buildings.

To delineate the “circle” and the “ring” shape buildings, applying the edge detection and Circular Hough transform algorithms sequentially to the building patches is enough. However, to delineate the “C” and “S” shape buildings, the results of Circular Hough transform should be refined, due to the complexity of these shapes.

### 5.1.3.1. Delineating the “Circle” and “Ring” Shape Buildings

The delineation of the “circle” and “ring” shape buildings consists of the following steps:

- Smoothing the building patch images,
  - Edge Detection, and
  - Circular Hough Transform.
- 
- **Smoothing the building patch images**

The aim of the smoothing process is to suppress noise or other small variations in the image. Blurring can be done with a uniform or non-uniform kernel. The most common example of the latter is Gaussian filter, in which the coefficients are samples from a two dimensional Gaussian function (Efford, 2000).

$$h(x, y) = \exp\left[\frac{-(x^2 + y^2)}{2\sigma^2}\right] \quad (\text{Equation 5. 6})$$

The filter coefficients decrease in size with the increasing distance from the filter’s centre. Hence, more weight is given to the central pixels than the edge pixels. Larger values of  $\sigma$  produce more blurred images. The Gaussian smoothing has several advantages (Efford, 2000). First, the filter is rotationally symmetric. Therefore, there will be no directional bias in the amount of smoothing. Second, the Gaussian filter is separable that allows for fast computation. Third, more weight is given to the central pixels than the edge pixels.

- **Edge Detection**

A variety of methods using gradient information have been developed to relax the workload as well as the storage requirements for the classical Circular Hough transform (Davies, 1987). In this study, gradient based edge detection was used to detect the edge pixels. Gradient operators are based on local derivatives of the image

function. The derivatives are bigger where there are sudden variations in the image and smaller where there is no variation in the image. The gradient vector of  $g$  at  $(x_0, y_0)$  is as follows;

$$\vec{\nabla}g(x_0, y_0) = \left( \frac{\partial g}{\partial x}(x_0, y_0), \frac{\partial g}{\partial y}(x_0, y_0) \right) \quad (\text{Equation 5. 7})$$

In the present case, a Circular Hough transform was applied on the gradient field of the image of the building patches.

- **The Circular Hough Transform**

The original Hough transform was designed to detect lines and curves (Hough, 1962). However, it can be extended to detect analytic shapes. The Circular Hough transform is a modified version of curve detection. The aim of Circular Hough transform is to extract circular objects from digital images. It is similar to the Hough transform for lines, but uses the parametric form for a circle. Each edge point  $(x_i, y_i)$  generates a circle in a 3D parameter space with radius  $r$  and the circle can be expressed with equation 5.8.

$$(x - a)^2 + (y - b)^2 = r^2 \quad (\text{Equations 5. 8})$$

The parametric representation of the circle is as given in equations 5.9 and 5.10.

$$x = a + r \cos(\theta) \quad (\text{Equations 5. 9})$$

$$y = b + r \sin(\theta) \quad (\text{Equations 5. 10})$$

Therefore, the accumulator space for Circular Hough transform must be three dimensional (Figure 5.8)

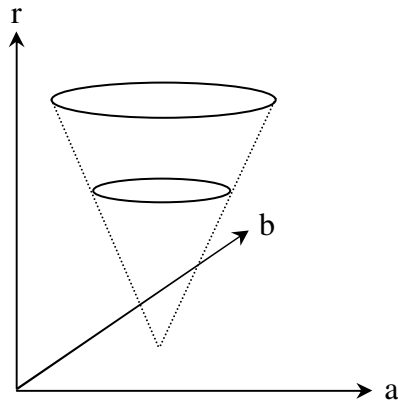


Figure 5. 8. The Circular Hough transform parameter space.

To find the circles using Circular Hough transform, for each edge point, a circle is drawn in the parameter space with the desired radius. The accumulator array is incremented for the coordinates that belong to the perimeter of the drawn circle. This process is performed for all edges. At the end of this process the highest numbers in the accumulator space corresponds to the centers of the circles in the image space (Figure 5.9).

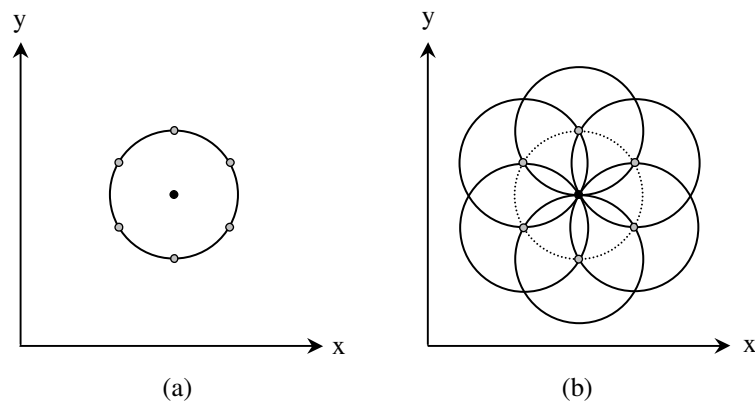


Figure 5. 9. A Circular Hough transform (a) in x-y space and (b) in parameter space.

The algorithm for the Circular Hough transform is as follows (Pedersen, 2007; Morse, 2000):

Find edges on the candidate building patch image

For each edge point

Draw a circle with center in the edge point with radius  $r$

Increment all coordinates that the perimeter of the circle passes through in the accumulator

Find local maxima in the accumulator

Map the found parameters ( $r$ ,  $a$ ,  $b$ ) corresponding to the maxima back to the original image

The parameters used in the Circular Hough transform include *Segment\_no*, *Radius range*, and *Tolerance value for concentric circles*.

*Segment\_no*: The number of segments (points on the detected circle) determines the number of sides the "polygon" will have. The more the number of segments the smoother the circle (Figure 5.10). Therefore, in this study the segment number was used as 32.

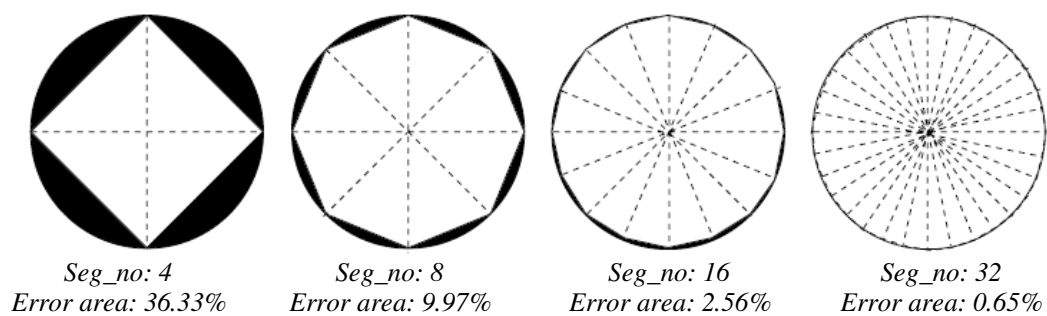


Figure 5. 10. Reduction in the error area as “Seg\_no” increases from an initial value of 4 up to a final value of 32. The error area is calculated dividing the circular area,  $\pi*r^2$ , by the inscribed polygon area,  $seg\_no*r^2.\sin * (\pi/seg\_no) * \cos(\pi/seg\_no)$ . The error (black area) is getting smaller while the seg\_no increases and is almost negligible for seg\_no = 32 (Ujaldon et al., 2008).

*Radius range:* In the developed algorithm, the possible radius ranges (minimum and maximum values) of the circular buildings are determined by the user.

*Tolerance value for concentric circles:* For “ring”, “C” and “S” shape buildings; it is the case that there is concentric circles/semi-circles. For these cases a tolerance value is determined to detect the multiple circles that have same center point.

### **5.1.3.2. Delineating the “C” Shape Buildings**

The steps followed to delineate the “C” Shape Buildings are as follows:

- Smoothing the building patch images,
- Edge Detection,
- Circular Hough transform,
- Semi-circle generation by evaluating the pixels under the circle points,
- Finding the start/end points of concentric semi circles, and
- Grouping the points and delineating the building boundaries.

The first three steps are same as the steps followed for the delineation of the “circle” and “ring” shaped buildings. To delineate the “C” shape buildings, the circles are converted to semi-circles. Next, the start and end points of the semi-circles are determined. Then, the points are grouped to delineate the buildings. The schematic representation of delineating a “C” Shape building is given in figure 5.11. The algorithm is as follows:

```
For each candidate building patches
    Apply Circular Hough transform
    If the pixel value under the circle points is not zero
        Keep the point
    Else
        Delete the point
    End if
```

Compute the distances between the sequential circle points  
    Determine the start and end points of semi-circles  
    Group the semi-circle points and delineate the building boundary  
End for

After applying the Circular Hough transform, the semi-circles are generated by evaluating the building patch pixels that correspond to the circle points (Figure 5.11 (a)). If the pixel under the circle point is not a building pixel then, the point is deleted. Otherwise, the point is preserved (Figure 5.11 (b)). Using this process therefore, the semi-circles are detected. Next, to find the start and end points of the semi-circles, the distances between the sequential points are calculated (Figure 5.11 (c)). Those points, between which the distance is the maximum, are determined to be the start and end points of the semi-circles (Figure 5.11 (d)). The points corresponding to semi circles are grouped sequentially starting from the start point and finishing at the end point of the outside circle. Then, the similar grouping process is also carried out from the end point to starting point of the inside circle to form the “C” shape building (Figure 5.11 (e) and (f)).

### **5.1.3.3. Delineating the “S” Shape Buildings**

The steps to delineate the “S” Shape Buildings are as follows:

- Smoothing the building patch image,
- Edge Detection,
- Circular Hough transform,
- Semi-circle generation by evaluating the pixels under the circle points,
- Finding the start and end points of the semi-concentric circles,
- Finding the nearest points of the outside and inside semi-circles that have different centroids, and
- Grouping the points and delineating building boundaries.

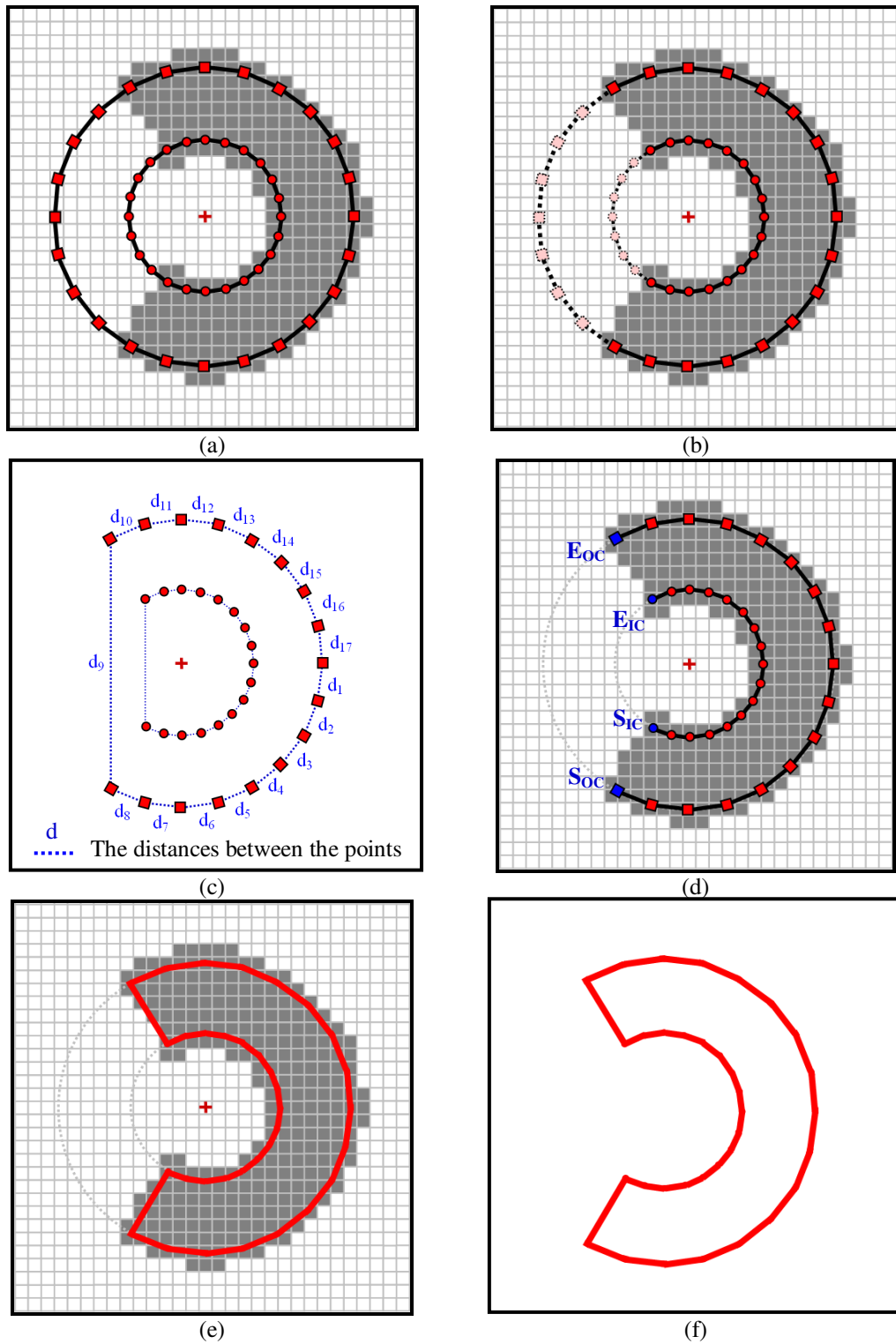


Figure 5. 11. The steps of the algorithm to delineate the “C” shape buildings. (a) The detected circles with segment number of 24 (b) Semi-circle generation by deleting the circle points that have non-building pixels under them (c) Calculating the distances between sequential semi-circle points to determine the start and end points of the semi-circles (d) Detecting the determined start and end points of the outside and inside circles:  $S_{oc} - E_{oc}$  &  $S_{ic} - E_{ic}$  (e) Overlaying the delineated “C” shape building boundary with the building patch and (f) the final delineated boundary of the “C” shape building.



The first five steps of delineating the “S” shape buildings are same as for the “C” shape buildings. Therefore, after the first five steps, the nearest points of the outside and inside semi-circles, which have different centroids, are found. Then, these points are grouped to delineate the buildings. The schematic representation of delineating an “S” shape building is given in figure 5.12. The algorithm for delineating the “S” shape buildings is as follows:

```
For each candidate building patches
    Apply Circular Hough transform
    If the pixel value under the circle points is not equal to the zero
        Keep the point
    Else
        Delete the point
    End if
    Compute the distances between the sequential circle points
    Determine the start and end points of semi-circles
    Find the nearest points of the outside and inside semi-circles that have
    different centroids.
    Group the semi-circle points and delineate the building boundary
End for
```

After applying the Circular Hough transform, the semi-circles are generated and the start and end points (S1, S2, E1, E2) of the semi-circles are found as explained for the “C” shape building delineation process (Figure 5.12 (a)-(c)). Then, the points of the inside semi-circle 1 and outside semi-circle 2, which are closest to each other, are detected. Similarly, the points of the inside semi-circle 2 and outside semi-circle 1, which are closest to each other, are also detected (Figure 5.12 (d)). Next, for each semi-circle, starting from the above detected closest points, those points falling inside the building patch (shown in pink color in figure 5.12 (d)) are deleted in clockwise direction. Finally, the semi-circle points are grouped sequentially to form the “S” shape building (Figure 5.12 (e)).

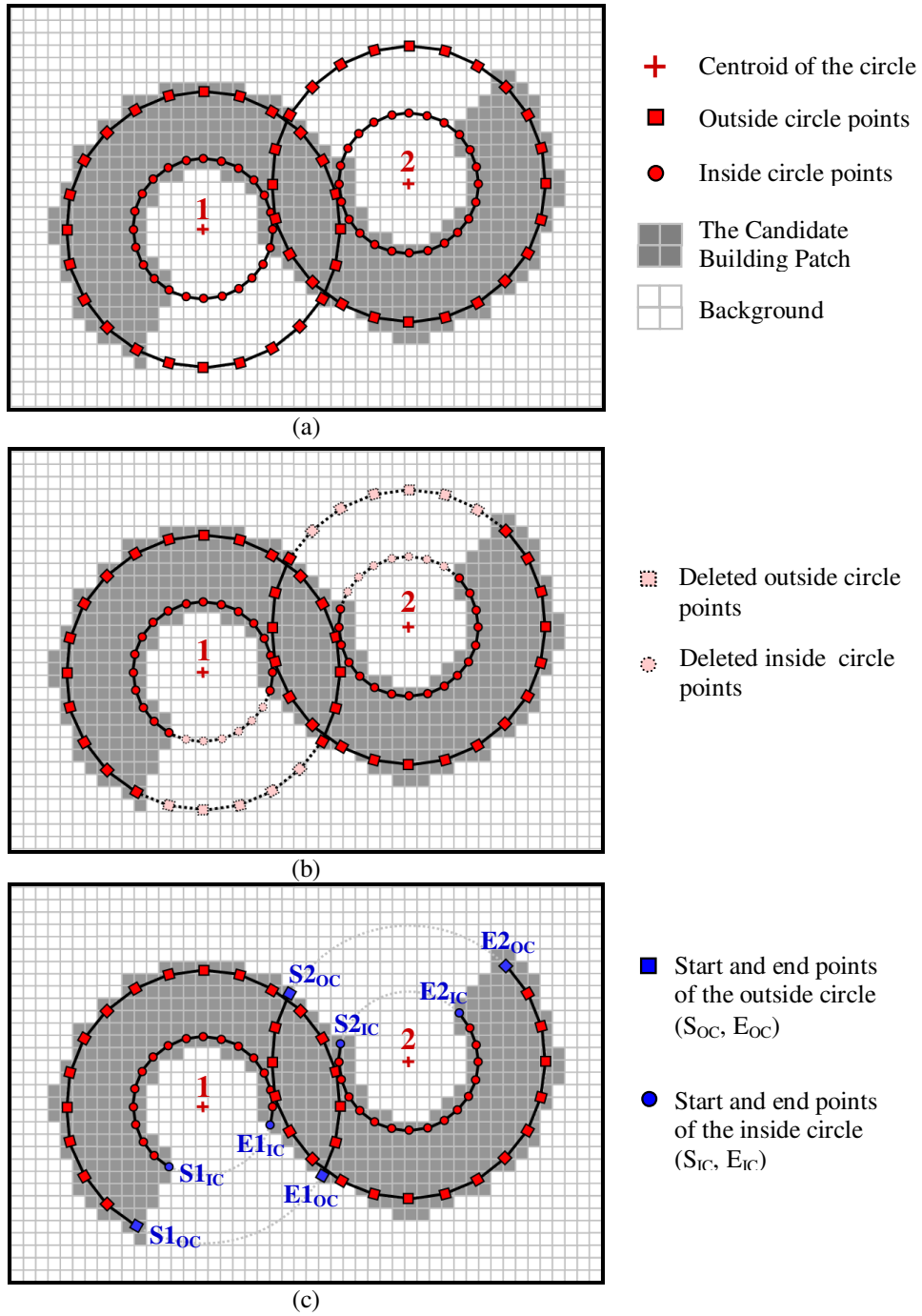


Figure 5. 12. The steps of the developed algorithm to delineate “S” shape buildings. (a) The detected circles with segment number of 24. (b) Semi-circle generation by deleting the circle points that have non-building pixels under them. (c) The determined start and end points of the outside and inside circles:  $S1_{OC} - E1_{OC}$  &  $S1_{IC} - E1_{IC}$  and  $S2_{OC} - E2_{OC}$  &  $S2_{IC} - E2_{IC}$ . (d) Finding the nearest points of the inside and outside semi-circles (e) The delineated “S” shape building boundary overlaid with building patch.

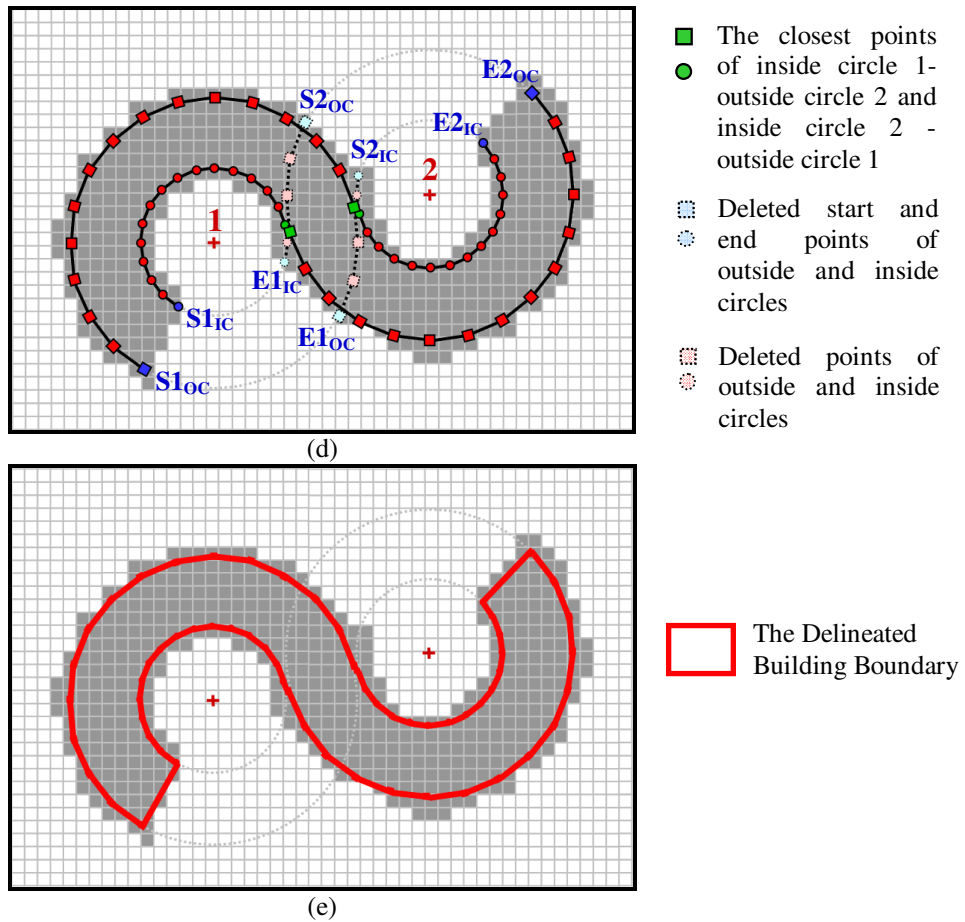


Figure 5.12. Continued

#### 5.1.4. The Experimental Results

To assess the results of building delineation, the areas were classified into the categories TP, TN, FP, and FN, which were described in Chapter 4.9.2. Then, for each urban block, the overall quality measures of BF, MF, BDP, and QP were calculated (Chapter 4.9.2).

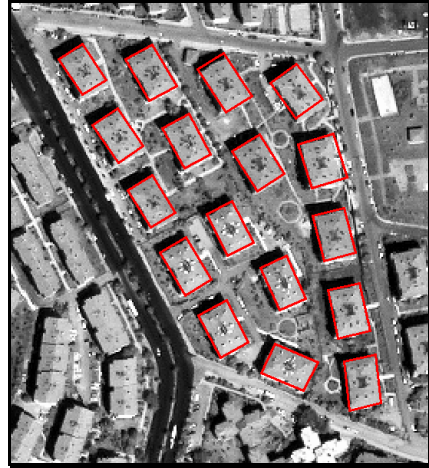
The developed algorithm was tested in the residential and industrial urban areas that contain different shapes and dwelling types. In figure 5.13, the delineated building boundaries are illustrated for six urban blocks that contain the detached rectangular buildings. Of these urban blocks, Urban Block 1 includes the low-rise buildings (two storeys), Urban Block 6 contains high-rise buildings (eight storeys) and the remaining urban blocks (Urban Blocks 2, 3, 4, and 5) contain middle-rise buildings (about four or five storeys).



(a) Urban Block 1



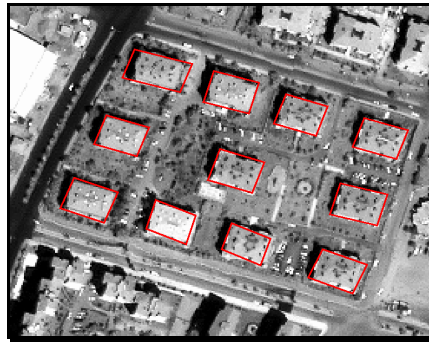
(b) Urban Block 2



(c) Urban Block 3



(d) Urban Block 4



(e) Urban Block 5



(f) Urban Block 6

Figure 5. 13. The delineated detached building boundaries using Hough transform based approach for urban blocks that contain (a) low-rise, (b - e) middle-rise, and (f) high-rise buildings.

By evaluating the results visually it can be stated that almost all buildings were delineated successfully. In the area there were a total of 107 detached buildings. Of these buildings, 105 were delineated successfully with the accuracy rate of 98.13% (Table 5.1). In Urban Block 3 and Urban Block 6, two buildings were not able to be delineated because these buildings were quite small and low.

Table 5. 1. Error matrix of the delineated building boundaries using Hough transform based approach for the detached dwelling types.

	Count	%
Delineated Buildings / Reference Buildings	105 / 107	98,13 / 100

The quality assessments for the selected six urban blocks are given in table 5.2. For all urban blocks, the delineation was observed to be quite accurate with the BDPs higher than 92.44% and QPs higher than 69.70%. The average BDP and QP values were computed to be 95.04% and 77.95%, respectively. On the other hand, the average BF, which gives the rate of false positive areas, and the average MF, which gives the rate of false negative areas, were computed to be 0.23 and 0.05, respectively.

Table 5. 2. The quality assessment results of the urban blocks that contain detached buildings using Hough transform based approach.

	TP	FP	FN	BF	MF	BDP	QP
Urban Block 1	7700	1545	630	0.20	0.08	92.44	77.97
Urban Block 2	6976	1655	262	0.24	0.04	96.38	78.44
Urban Block 3	8704	1099	644	0.13	0.07	93.11	83.32
Urban Block 4	7112	2080	203	0.29	0.03	97.22	75.70
Urban Block 5	5800	1043	259	0.18	0.04	95.73	81.67
Urban Block 6	5550	2229	184	0.40	0.03	96.79	69.70
Average	41842	9651	2182	0.23	0.05	95.04	77.95

The results of building delineation obtained for the semi-detached buildings are illustrated in figure 5.14. The Urban Blocks 1, 2, 3, and 4 contain middle-rise buildings and Urban Block 6 contains high-rise buildings.





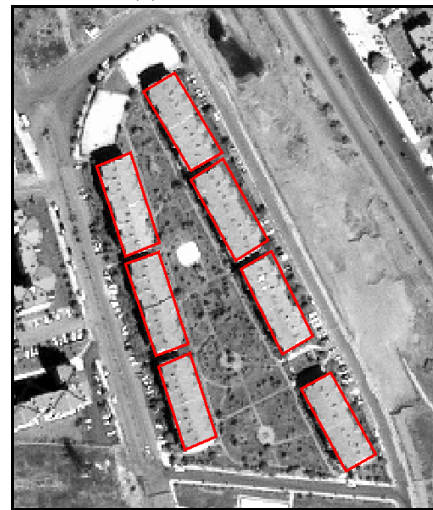
(a) Urban Block 1



(b) Urban Block 2



(c) Urban Block 3



(d) Urban Block 4



(e) Urban Block 5

Figure 5. 14. The delineated semi-detached building boundaries using Hough transform based approach for urban blocks that contain (a - d) middle-rise and (e) high-rise buildings.

The visual assessment of the results indicate that, almost all buildings were delineated successfully (figure 5.14). Of the total 77 semi-detached buildings

contained in these urban blocks, 74 were delineated successfully providing an accuracy of 96.10% (table 5.3). As expected, the small buildings in Urban Blocks 2 and 3 were not able to be delineated. In Urban Blocks 1, 2, and 5, several buildings have similar reflectance values with the other objects, such as pavements and roads. However, the developed algorithm was able to delineate these buildings.

Table 5. 3. Error matrix of the delineated building boundaries using Hough transform based approach for the semi-detached dwelling types.

	Count	%
Delineated Buildings / Reference Buildings	74 / 77	96,10 / 100

The results of the quality assessment for five urban blocks are given in table 5.4. The results indicate that the delineation process is quite satisfactory with the BDP values higher than 94.57% and the QP values higher than 74.57%. In addition, the BFs, which represent the rate of incorrectly labeled buildings, were measured lower than 0.29; while the MFs, which represent the rate of missed buildings, were computed to be lower than 0.06. The average BDP and QP values were computed to be 95.86% and 81.63%, respectively. In addition, the average BF and MF values were found to be 0.18 and 0.04, respectively.

Table 5. 4. The quality assessment results for urban blocks that contain semi-detached buildings using Hough transform based approach.

	TP	FP	FN	BF	MF	BDP	QP
Urban Block 1	10572	1466	607	0.14	0.06	94.57	83.61
Urban Block 2	9066	1477	449	0.16	0.05	95.28	82.48
Urban Block 3	5469	1607	258	0.29	0.05	95.50	74.57
Urban Block 4	4936	1168	106	0.24	0.02	97.90	79.48
Urban Block 5	7521	1112	204	0.15	0.03	97.36	85.11
Average	37564	6830	1624	0.18	0.04	95.86	81.63

For five urban blocks, the delineated building boundaries are illustrated in figure 5.15.



(a) Urban Block 1



(b) Urban Block 2



(c) Urban Block 3



(d) Urban Block 4



(e) Urban Block 5



(f) Urban Block 6



(g) Urban Block 7

Figure 5. 15. The delineated terraced building boundaries using Hough transform based approach for urban blocks that contain (a - d) low-rise and (e - g) middle-rise buildings.



The visual assessment of the results indicate that the building boundaries were delineated successfully (figure 5.15). Of the total 123 buildings, 122 were delineated successfully (table 5.5). In Urban Block 7 the small, semi-occluded building was not able to be delineated. It was observed that buildings smaller than 50m<sup>2</sup> were not able to be detected because when removing the artefacts in the building detection part of this study (Chapter 4), the patches smaller than a 50m<sup>2</sup> were considered to be artefacts and therefore, they were eliminated from the building patch image. In addition, in Urban Block 1, two buildings, which are close to each other but not adjoined, were delineated erroneously as a joint one building.

Table 5. 5. Error matrix of the delineated building boundaries using Hough transform based approach for terraced dwelling type.

	Count	%
Delineated Buildings / Reference Buildings	122 / 123	99,19 / 100

The results of the quality assessment for the selected seven urban blocks are given in table 5.6. The average BDP and QP values were computed to be 95.21% and 78.14%, respectively. In addition, the average BF and MF values were found to be 0.23 and 0.05, respectively.

Table 5. 6. The results of quality assessment for urban blocks that include the terraced buildings using Hough transform based approach.

	TP	FP	FN	BF	MF	BDP	QP
Urban Block 1	7402	2152	131	0.29	0.02	98.26	76.43
Urban Block 2	6537	1920	240	0.29	0.04	96.46	75.16
Urban Block 3	8795	1362	1155	0.15	0.13	88.39	77.75
Urban Block 4	8909	1876	344	0.21	0.04	96.28	80.05
Urban Block 5	8777	2455	318	0.28	0.04	96.50	75.99
Urban Block 6	5866	1006	176	0.17	0.03	97.09	83.23
Urban Block 7	5813	1180	259	0.20	0.04	95.73	80.16
Average	52099	11951	2623	0.23	0.05	95.21	78.14

For rectangular buildings, the average quality assessment results are given in table 5.7. The results indicate that using the developed approach the building boundaries can be delineated quite successfully with the BDP and QP accuracies of 93.54% and

79.05%, respectively (Table 5.7). Of the total 307 buildings, 301 were delineated successfully providing the accuracy of 98.05%.

Table 5. 7. The average quality assessment results for the rectangular residential buildings using Hough transform based approach.

	TP	FP	FN	BF	MF	BDP	QP
Residential Rectangular Buildings	131505	28432	6429	0.22	0.05	95.34	79.05

The results of the delineated circular buildings are shown in figure 5.16. The quality assessment results are provided in table 5.8. The visual assessments of the results indicate that the circular buildings, even the complex ones, can be delineated successfully with the developed approach. The results also indicate that the accuracy of delineation is quite high, 78.74% for BDP and 66.81% for QP.

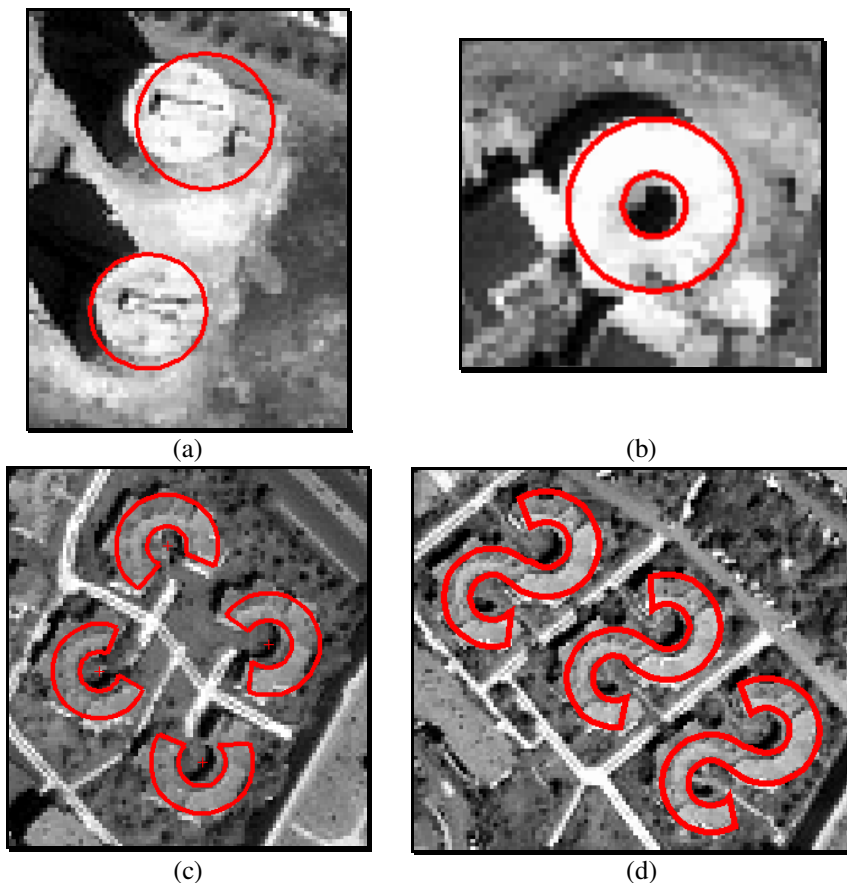


Figure 5. 16. The delineated circular building boundaries using Hough transform approach: (a) the circle shape buildings, (b) the ring shape buildings, (c) the C shape buildings, and (d) the S shape buildings.

Table 5. 8. The quality assessment results for the circular buildings using Hough transform based approach.

	TP	FP	FN	BF	MF	BDP	QP
Circle Shape	582	318	62	0.55	0.11	90.37	60.50
Ring Shape	312	15	38	0.05	0.12	89.14	85.48
C Shape	1051	190	480	0.19	1.47	68.50	61.00
S Shape	1691	253	598	0.15	0.35	73.88	66.52
Average	2585	586	698	0.23	0.27	78.74	66.81

The developed algorithm was also tested in industrial areas, where the delineated boundaries are illustrated in figure 5.17. The visual assessments of the results indicate that the delineation process was quite satisfactory.



Figure 5. 17. The delineated rectangular building boundaries using Hough transform based approach for industrial areas; (a) industrial area 1 and (b) industrial area 2.

For the industrial areas, the quality assessment results are given in table 5.9. The average BDP and QP values were computed to be 93.45% and 79.51%, respectively. On the other hand, the average BF and MF values were found to be 0.19 and 0.07, respectively.

Table 5. 9. The quality assessment results for industrial buildings using Hough transform based approach.

	TP	FP	FN	BF	MF	BDP	QP
Industrial Area 1	217364	31439	13458	0.14	0.06	94.17	82.88
Industrial Area 2	93955	26981	8354	0.29	0.09	91.83	72.67
Average	311319	58420	21812	0.19	0.07	93.45	79.51

## 5.2. Building Delineation Based on Boundary Tracing

In this part of the study, a method is presented for automatic building delineation from the previously detected building patches using the Boundary tracing algorithm. The boundary delineation process includes, Canny edge detection, Boundary tracing, Douglas Peucker line simplification, and vector filters.

### 5.2.1. The Methodology

The developed approach consists of four steps (Figure 5.18), which are (i) edge detection, (ii) Boundary tracing, (iii) line simplification and (iv) filtering the vector line segments. First, the edges of the previously detected building patches are detected using the Canny edge detection algorithm. Then, these edges are vectorized using the Boundary tracing algorithm and they are simplified to remove the undulations. Finally, the topological errors are removed using the vector filters to obtain the regularized boundaries.

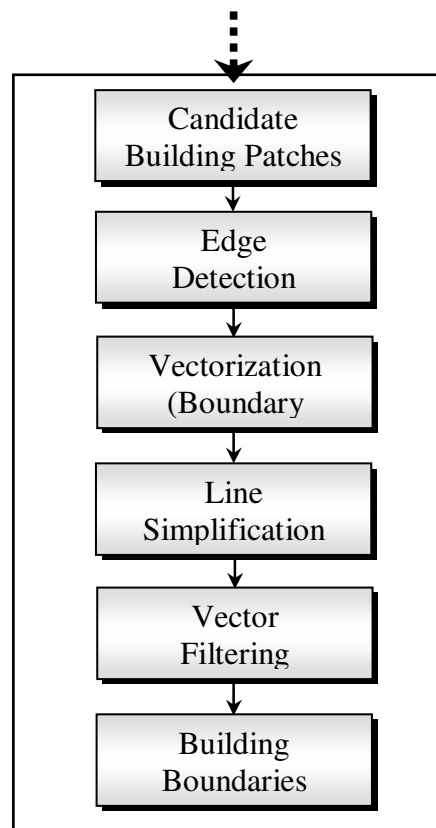


Figure 5. 18. The flowchart of the Boundary tracing based approach.

### 5.2.2. Edge Detection:

To extract the edges, the “Canny Edge Detection” algorithm was used. The description of the Canny Edge Detection algorithm is provided in Chapter 5.1.2.1.

### 5.2.3. Boundary Tracing

After performing the edge detection operation, the edge segments were vectorized using the Boundary tracing algorithm, which detects the boundaries of the objects in the binary image. Therefore, the input data should be a binary image, in which nonzero pixels represent an object while the pixels with zero values correspond to the background. In the vectorization algorithm used, initially the starting point and the direction are determined and the row and column coordinates of the starting point are recorded (figure 5.19). Then, the coordinates of the next object pixel connecting to the starting point are detected in the search direction. For each pixel belonging to the object considered, the row and column coordinates are determined in the binary image by following the specified direction. During the Boundary tracing process, the boundary pixels of the buildings are analysed and the vector line segments are generated from the input binary image. The vector lines are then generated by connecting the coordinates of the detected object pixels. To trace the boundaries accurately, the method analyzes the shape, width, and the intersections of the boundaries.

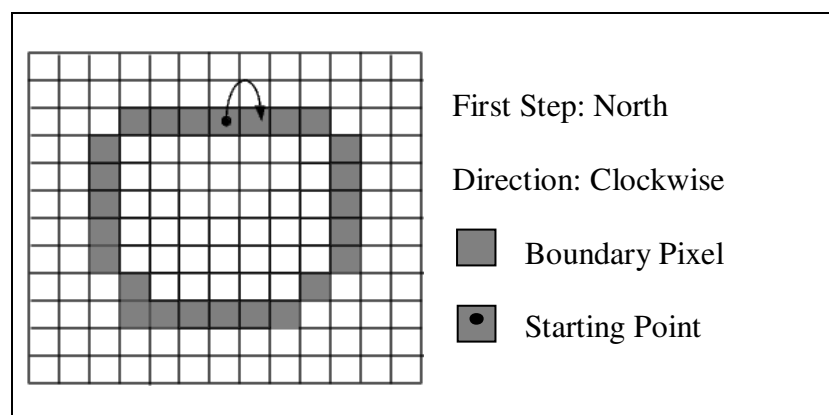


Figure 5. 19. The first step and the direction parameters used for the Boundary tracing algorithm

#### **5.2.4. Line Simplification**

There will be undulations on the generated vector boundaries and therefore, they should be removed using a line simplification algorithm. In the present case, the simplifications of the lines were carried out using the well known Douglas-Peucker algorithm, which is one of the most widely used line simplification algorithms. This algorithm uses the closeness of a vertex to an edge segment to simplify the lines (Sunday, 2007). This method recursively subdivides a polygon until the vertices can be replaced by a straight line segment, within the tolerance. The algorithm starts with a coarse initial estimation, which is an edge. Then, the distance between this edge and vertices are calculated. If there are vertices that have distance more than a specified tolerance,  $\epsilon > 0$ , then the vertex that is farthest from the edge is added to the simplification. In this way, a new estimation for the simplified polygon is created. This process continues recursively for each edge of the building boundaries until all vertices of the original polygon are within the tolerance of the simplification.

In the present case, the unimportant geometric details in the polygonal objects were eliminated using the “reducem” function of the Mapping Toolbox of Matlab. This function utilizes the Douglas-Peucker algorithm (Matlab 7 Manual, 2005).

#### **5.2.5. Vector Filtering**

After simplifying the line segments using the “Douglas Peucker” algorithm, the topological errors were removed using the vector filters of the TNT image processing/analysis software. The vector filters used in this study include Sliver Polygons, Dangling Lines, Remove Bubbles, Undershoots, Remove Islands, and Dissolve Polygons (TNTmips Manual, 2002). The ‘Sliver Polygons’ function removes thin or small areal polygons that commonly occur along the borders of the polygons. The “Dangling Lines” filter removes the small lines that are not attached to other elements or only one end attached to another element. The small polygons that are usually artefacts were removed using the “Remove Bubles” function. The “Undershoots” filter closes gaps by extending the line within the specified snap distance. The “Remove Islands” filter removes the island polygons (polygon lie

entirely within other polygon) and the “Dissolve Polygons” filter generates a new vector object removing lines between adjacent polygons that share the specified attribute. The building boundaries obtained after the vector filtering operation became the final building boundaries of the Boundary tracing based approach.

### 5.2.6. The Experimental Results

The developed algorithm was tested using the residential and industrial urban areas that contain different shapes and dwelling types. In figure 5.20, the delineated building boundaries for detached rectangular buildings are given. The results indicate that almost all buildings were delineated successfully. Of the total 107 detached buildings located in these blocks, 105 were successfully delineated providing an accuracy of 98.13% (table 5.10). Unfortunately, the approach was not successful for delineating the small buildings.

Table 5. 10. Error matrix of the delineated building boundaries using Boundary tracing based approach for detached dwelling type.

	Count	%
Delineated Buildings / Reference Buildings	105 / 107	98,13 / 100

For the six urban blocks tested, the quality assessment results are provided in table 5.11. The average building detection (BDP) and quality (QP) percentages were computed to be 86.97% and 78.86%, respectively. On the other hand, the average branching factor (BF) and the miss factor (MF) values were found to be 0.12 and 0.15, respectively.





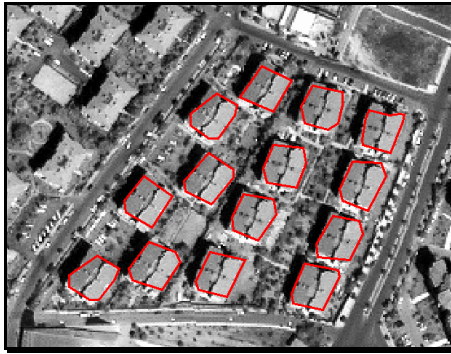
(a) Urban Block 1



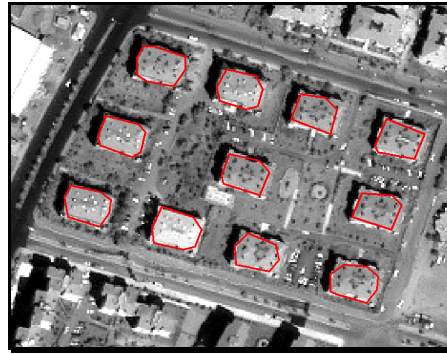
(b) Urban Block 2



(c) Urban Block 3



(d) Urban Block 4



(e) Urban Block 5



(f) Urban Block 6

Figure 5. 20. The delineated detached building boundaries using Boundary tracing approach for urban blocks that contain (a) low-rise, (b - e) middle-rise, and (f) high-rise buildings.



Table 5. 11. The quality assessment results for six urban blocks that contain detached buildings using Boundary tracing based approach.

	TP	FP	FN	BF	MF	BDP	QP
Urban Block 1	6766	397	1564	0.06	0.23	81.22	77.53
Urban Block 2	6872	1113	366	0.16	0.05	94.94	82.29
Urban Block 3	7839	557	1509	0.07	0.19	83.86	79.14
Urban Block 4	6451	812	864	0.13	0.13	88.19	79.38
Urban Block 5	5019	305	1040	0.06	0.21	82.84	78.87
Urban Block 6	5342	1343	392	0.25	0.07	93.16	75.48
Average	38289	4527	5735	0.12	0.15	86.97	78.86

The results of building delineation obtained for the semi-detached buildings are illustrated in figure 5.21. Of the total 77 semi-detached buildings contained within these urban blocks, 74 were delineated successfully providing an accuracy of 96.10% (Table 5.12). In Urban Blocks 2 and 3, the small buildings were not able to be delineated. However, the buildings that have similar reflectance values with other classes were able to be delineated in building blocks 1, 2, and 5.

Table 5. 12. Error matrix of the delineated building boundaries using Boundary tracing based approach for the semi-detached dwelling type

	Count	%
Delineated Buildings / Reference Buildings	74 / 77	96,10 / 100

The results of the quality assessment for the selected five urban blocks are given in table 5.13. The average building detection percentage (BDP) and the average quality percentages (QP) were computed as 91.10% and 82.10%, respectively. On the other hand, the average branching factor (BF) and the average miss factor (MF) values were found to be 0.12 and 0.10, respectively.



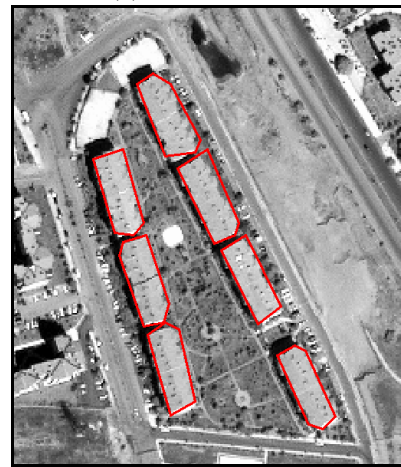
(a) Urban Block 1



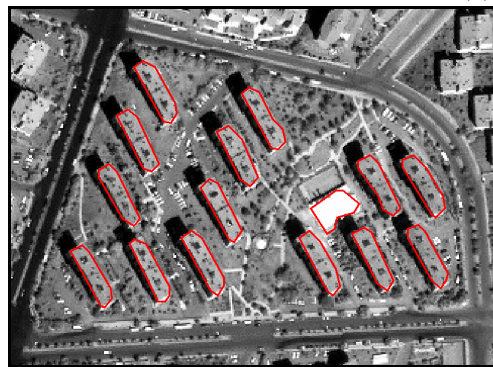
(b) Urban Block 2



(c) Urban Block 3



(d) Urban Block 4



(e) Urban Block 5

Figure 5. 21. The delineated semi-detached building boundaries using Boundary tracing approach for urban blocks that contain (a - d) middle-rise and (e) high-rise buildings.

Table 5. 13. The quality assessment results for urban blocks that contain semi-detached buildings using Boundary tracing based approach.

	TP	FP	FN	BF	MF	BDP	QP
Urban Block 1	9818	751	1361	0.08	0.14	87.83	82.30
Urban Block 2	8981	1350	534	0.15	0.06	94.39	82.66
Urban Block 3	5104	784	623	0.15	0.12	89.12	78.39
Urban Block 4	4808	986	234	0.21	0.05	95.36	79.76
Urban Block 5	6988	421	737	0.06	0.11	90.46	85.78
Average	35699	4292	3489	0.12	0.10	91.10	82.10

The building delineation results of the terraced buildings are illustrated in figure 5.22. The results indicate that the building boundaries were delineated successfully. Of the total 123 buildings, 122 were delineated correctly representing a high percentage of accuracy (table 5.14). However, in Urban Block 7, one of the buildings was not able to be delineated because it is small and its roof is occluded by the trees. In addition, the buildings that are very close to each other but not adjoined were delineated erroneously as a joined building.

Table 5. 14. Error matrix of the delineated building boundaries using Boundary tracing based approach for the terraced dwelling type.

	Count	%
Delineated Buildings / Reference Buildings	122 / 123	99,19 / 100

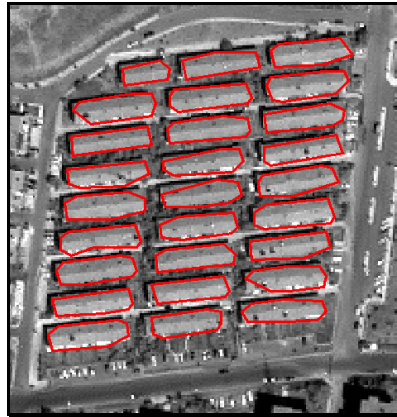
For these seven blocks, the results of the quality assessment are given in table 5.15. The average building detection percentage (BDP) and the average quality percentage (QP) values were computed as 92.81% and 76.42%, respectively. In addition, the average branching factor (BF) and the average miss factor (MF) values were found to be 0.23 and 0.08, respectively.



(a) Urban Block 1



(b) Urban Block 2



(c) Urban Block 3



(d) Urban Block 4



(e) Urban Block 5



(f) Urban Block 6



(g) Urban Block 7

Figure 5. 22. The delineated terraced building boundaries using Boundary tracing approach for urban blocks that contain (a - d) low-rise and (e - g) middle-rise buildings.

Table 5. 15. The quality assessment results for the urban blocks that contain terraced buildings using Boundary tracing based approach.

	TP	FP	FN	BF	MF	BDP	QP
Urban Block 1	7283	2372	250	0.33	0.03	96.68	73.53
Urban Block 2	6353	1742	424	0.27	0.07	93.74	74.57
Urban Block 3	8706	1383	1244	0.16	0.14	87.50	76.82
Urban Block 4	8732	2176	521	0.25	0.06	94.37	76.40
Urban Block 5	8707	2200	388	0.25	0.04	95.73	77.09
Urban Block 6	5781	1377	261	0.24	0.05	95.68	77.92
Urban Block 7	5224	487	848	0.09	0.16	86.03	79.65
Average	50786	11737	3936	0.23	0.08	92.81	76.42

The average quality assessment results for the rectangular buildings are given in table 5.16. The results indicate that the developed approach was quite successful for delineating the boundaries of rectangular buildings. Of the total 307 buildings, 301 were delineated correctly providing 98.05% accuracy.

Table 5. 16. The average quality assessment results for the rectangular residential buildings using Boundary tracing based approach.

	TP	FP	FN	BF	MF	BDP	QP
Residential Rectangular Buildings	124774	20556	13160	0.16	0.11	90.46	78.73

The delineated circular buildings using the developed approach are given in figure 5.23. Although all the buildings were delineated, a large amount of undulations are evident in the boundaries of several buildings. The quality assessment results for circular buildings are given in table 5.17.



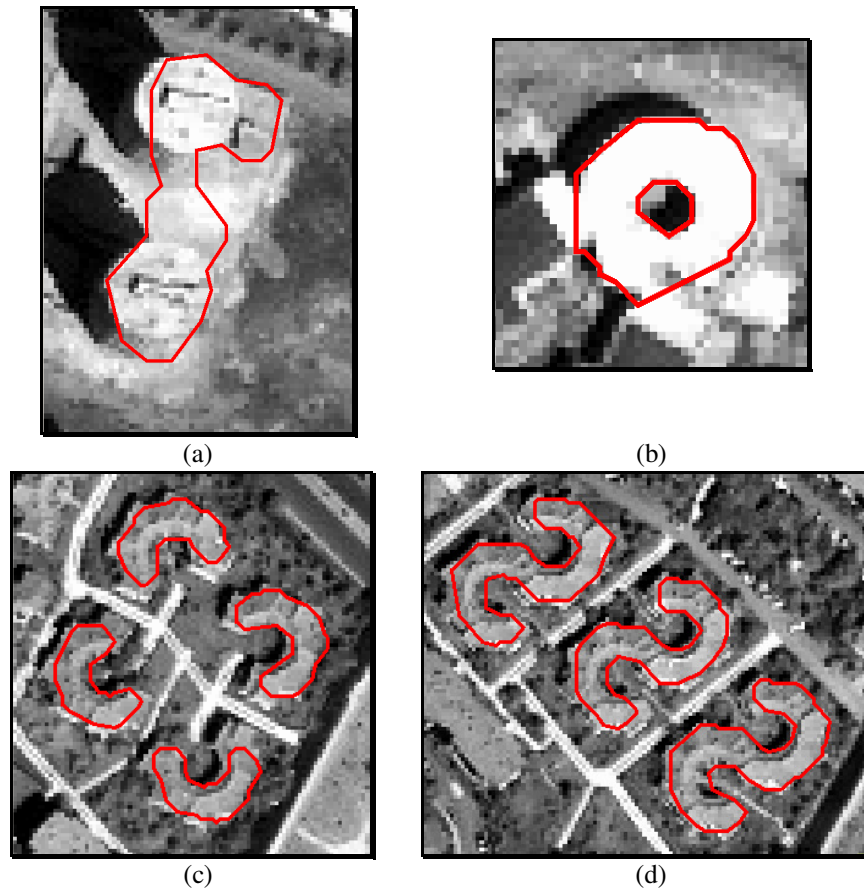


Figure 5. 23. The delineated circular building boundaries using Boundary tracing approach: (a) the circle shape buildings, (b) the ring shape buildings, (c) the C shape buildings, and (d) the S shape buildings.

Table 5. 17. The quality assessment results for circular buildings using Boundary tracing based approach.

	TP	FP	FN	BF	MF	BDP	QP
Circle Shape	576	430	68	0.75	0.12	89.44	53.63
Ring Shape	335	47	15	0.14	0.04	95.71	84.38
C Shape	1051	188	481	0.18	0.46	68.60	61.10
S Shape	1784	352	505	0.20	0.28	77.94	67.55
Average	3746	1017	1069	0.27	0.29	77.80	64.23

As can be seen from the results, for all types of circular buildings, the BDPs stayed higher than 68%, while the QPs were computed to be above 53%. On the other hand, the average BF, MF, BDP, and QP values were computed to be 0.27, 0.29, 77.80, and 64.23, respectively.

The delineated industrial buildings using the developed approach are illustrated in figure 5.24. For the industrial buildings, the results of the quality assessment are given in table 5.18. For Industrial Area 1 and Industrial Area 2, the delineation results were quite successful with the BDP value on the order of 93% and the QP values above 75%. The average BDPs and the average QPs were computed as 93.59% and 80.39%, respectively. On the other hand, the average branching and miss factor values were found to be 0.18 and 0.07, respectively.

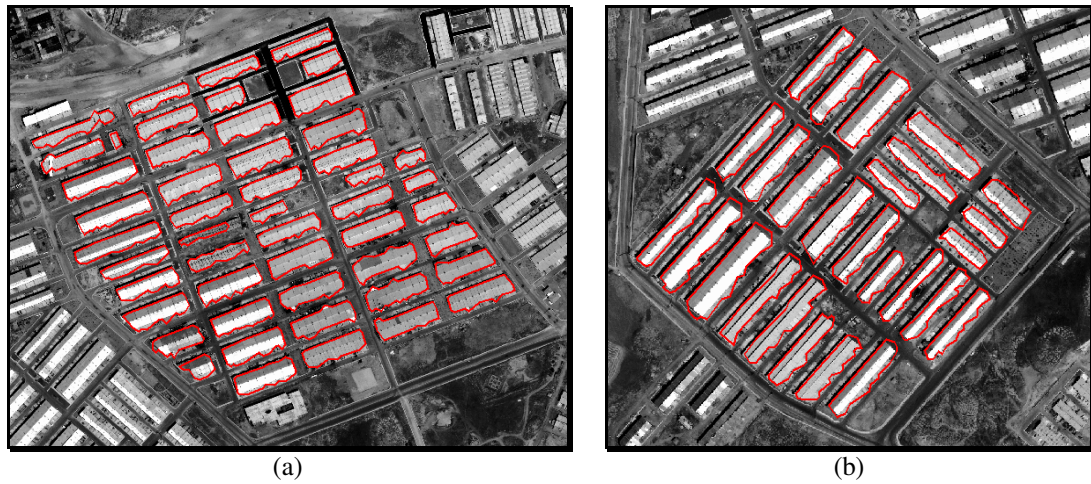


Figure 5. 24. The delineated rectangular building boundaries using Boundary tracing based approach for industrial areas; (a) industrial area 1 and (b) industrial area 2.

Table 5. 18. The quality assessment results for the industrial buildings using Boundary tracing based approach.

	TP	FP	FN	BF	MF	BDP	QP
Industrial Area 1	216719	30559	14103	0.14	0.07	93.89	82.91
Industrial Area 2	95056	24135	7253	0.25	0.08	92.91	75.18
Average	311775	54694	21356	0.18	0.07	93.59	80.39

### 5.3. Discussions of the Results

The delineation results of the residential areas, which contain different dwelling types, indicate that for almost all cases the BDP and QP values were computed to be higher for the Hough transform approach than the Boundary tracing approach.

For detached dwelling types, the average BDP values were computed as 95.04% and 86.07%, respectively for the Hough transform and Boundary tracing approaches, while the QP values were found to be 77.95% and 78.86%, respectively. As can be seen, the Hough transform approach provided about 9% higher BDP value than the Boundary tracing approach. On the other hand, no difference was observed in the accuracy measure of QP between two approaches.

For semi-detached dwelling types, the average BDP were computed to be 95.86% and 91.10%, respectively for the Hough transform and Boundary tracing approaches, while the QP values were found to be 81.63% and 82.10%, respectively. Similar to detached dwelling types, the BDP value for the Hough transform approach was about 5% higher than the Boundary tracing approach while no difference was observed in the QP values between two approaches.

For the terraced dwelling types, the average BDP values were computed to be 95.21% and 92.81%, respectively for the Hough transform and Boundary tracing approaches, while the average QP values were 78.14% and 76.42%, respectively. In this case, both the BDP and QP accuracy measures stayed slightly higher for the Hough transform approach than the Boundary tracing approach.

For residential (rectangular and circular) and industrial areas, the average accuracies computed for both the Hough transform and Boundary tracing approaches are given in table 5.19.

Table 5. 19. The comparison of the results of the Hough transform and Boundary tracing approaches.

Approach	Usage / Shape	BF	MF	BDP	QP
Hough Transform	Residential /Rectangular	0.22	0.05	95.34	79.05
	Residential/ Circular	0.23	0.27	78.74	66.81
	Industrial	0.19	0.07	93.45	79.51
Boundary Tracing	Residential /Rectangular	0.16	0.11	90.46	78.73
	Residential /Circular	0.27	0.29	77.80	64.23
	Industrial	0.18	0.07	93.59	80.39



As can be seen in table 5.19, the BDP and the QP values were computed to be quite high using both approaches. However, in general, the Hough transform approach appears to have provided better results for building delineation. For rectangular buildings, the BDP values were computed to be about 5% higher for the Hough transform approach than the Boundary tracing approach, while the QP values showed no significant difference. For the delineation of the circular buildings, the results obtained for both approaches were quite similar. While the BDP and QP values were computed to be 78.74% and 66.81%, respectively for the Hough transform approach, the same accuracy measures were found to be 77.80% and 64.23% for the Boundary tracing approach.

For industrial buildings, the delineation accuracies were found to be quite similar for both approaches. While the BDP and QP accuracy measures were computed to be 93.45% and 79.51% for the Hough transform approach, the same accuracy measures were found to be 93.59% and 80.39% for the Boundary tracing approach.

When the results are compared visually it can be stated that the Hough transform can be said to perform better if the mutual lines of the buildings are parallel and the angles between the adjacent lines are perpendicular. However, in the reverse case, the Boundary tracing algorithm appears to provide better results (Figure 5.25).



Figure 5. 25. The results of delineating a building using (a) the Hough transform based approach and (b) the Boundary tracing based approach.

It was observed that the Boundary tracing based approach is more dependent on the detected building patches than the Hough transform approach. This is because in the Boundary tracing based approach the edges of the building patches are directly converted into vector form whereas, in the Hough transform approach, the transformation is applied to detected edges. On the other hand, the Hough transform based approach is also successful for delineating the semi-occluded and the overlaid objects (Figure 5.26).

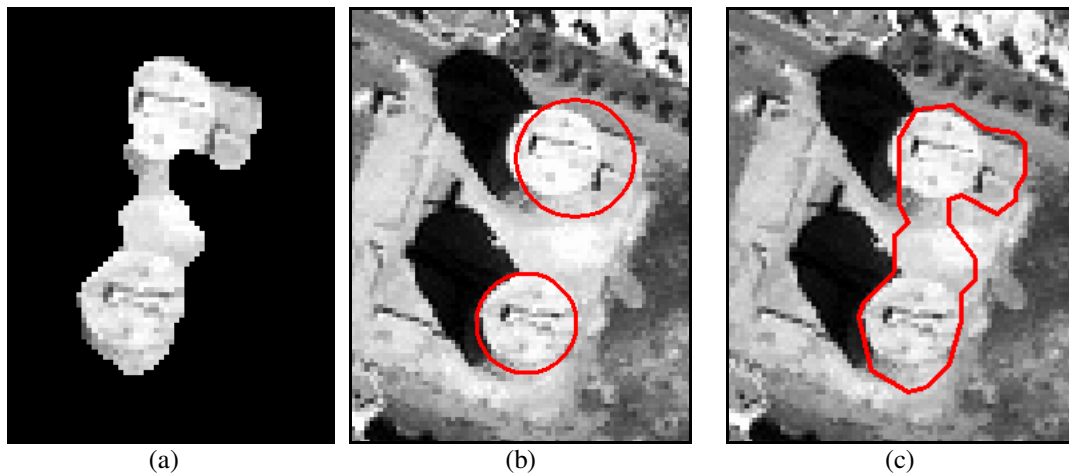


Figure 5. 26. (a) A detected building patch and the results of delineating the circular buildings using (b) the Hough transform approach and (c) the Boundary tracing approach.

The developed approaches are quite successful to delineate the rectangular and circular buildings. However, in several cases the proposed approaches may fail in delineating the boundaries of the buildings:

- **Small Buildings:** In the developed approach the building delineation is performed to the detected building patches. The buildings that are small in size may not be detected as building patches, because after detecting the patches through SVM classification, to remove the artefacts morphological operations (opening, closing) were performed and the patches that are smaller than  $50\text{m}^2$  were removed as explained in Chapter 4.8. Therefore, the small size building patches were eliminated from the building patch image while removing the artefacts and could not be delineated. The small sized two buildings from the study area are illustrated in Figure 5.27 (a)

and the detected building patches before and after removing the artefacts are given in figures 5.27 (b) and (c), respectively.

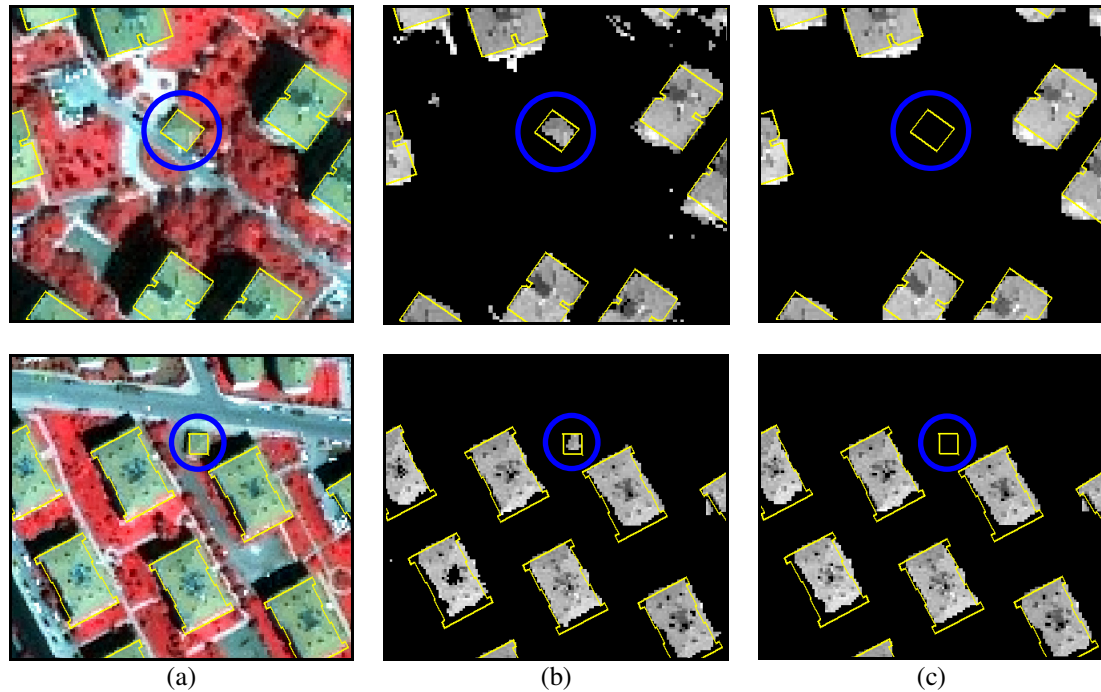


Figure 5. 27. (a) The small buildings overlaid with the reference building boundaries, (b) the detected building patches, (c) the detected building patches after removing the artefacts.

- **Semi-Occluded Buildings:** The Hough transform approach appears to be successful for delineating the occluded objects. However, if the object is quite small and the occlusion is high as shown in figure 5.28, the delineation process may very well fail.

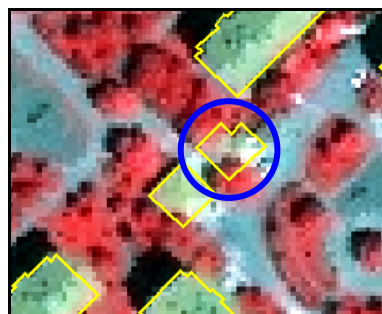


Figure 5. 28. An occluded small building overlaid with the reference building boundary.

- **Buildings that are close to each other:** If the buildings are located close to each other as in figure 5.29 then, these buildings may not be delineated separately. This is of course directly related with the spatial resolution of the image used, which imposes restrictions on the separability of the closely located buildings.

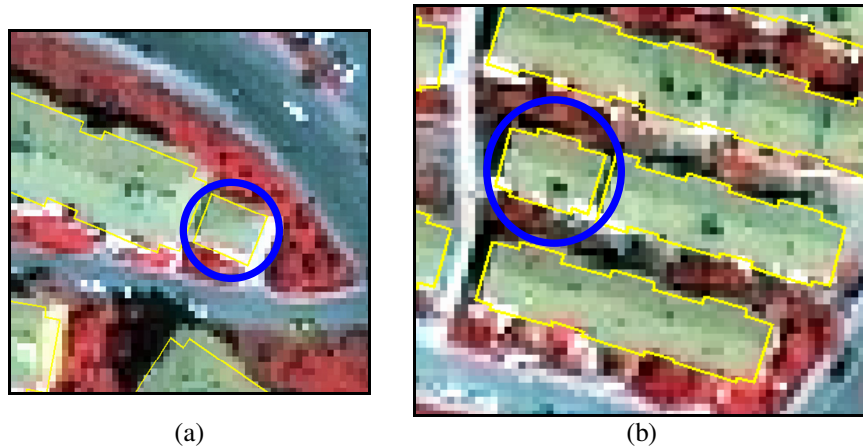


Figure 5. 29. The closely located buildings overlaid with the reference building boundaries.

- **Buildings that have roofs with different reflectance values:** In the present case, most of the buildings, which have different reflectance values, were successfully extracted using both approaches. For example, the buildings shown in figure 5.30 were delineated successfully despite having different spectral reflectances. However in some cases, the extraction of the buildings was not possible due to the spectral reflectances of the roofs. For example, in figure 5.31 (a) the building was not able to be delineated due to its different reflectance values as well as its height which is quite low. Similarly, the terraced buildings shown in figure 5.31 (b) were delineated as two separate buildings due to the variation of the spectral reflectance on the roof of the building.



Figure 5. 30. Buildings with different roof materials illustrating different reflectance values

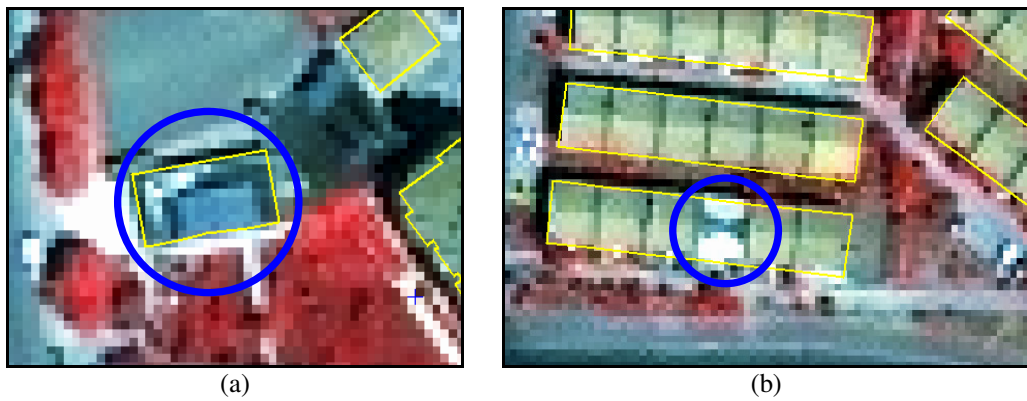


Figure 5. 31. Buildings showing different spectral reflectance values and spectral heterogeneity.

- **Adjoining Buildings:** Due to the limitation of the developed approaches, the adjoining buildings cannot be delineated separately. The semi-detached and terraced buildings that are shown in figures 5.32 (a) and (b), respectively can be given as the examples for this case.



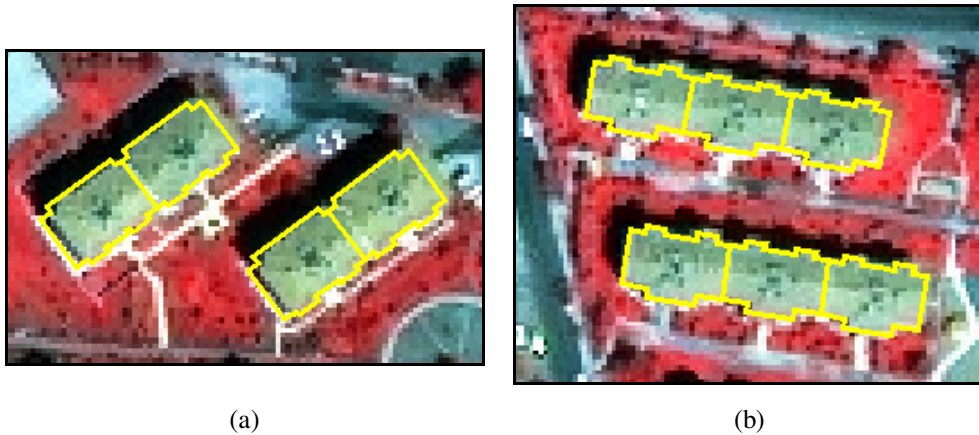


Figure 5. 32. The adjoining buildings that cannot be delineated separately using the developed approaches.

- **Buildings having similar reflectance values with the surrounding areas:** If the pixels outside and inside a building have similar reflectance values then, it becomes quite difficult to detect and delineate this building. In figure 5.33, an example is shown for this case.

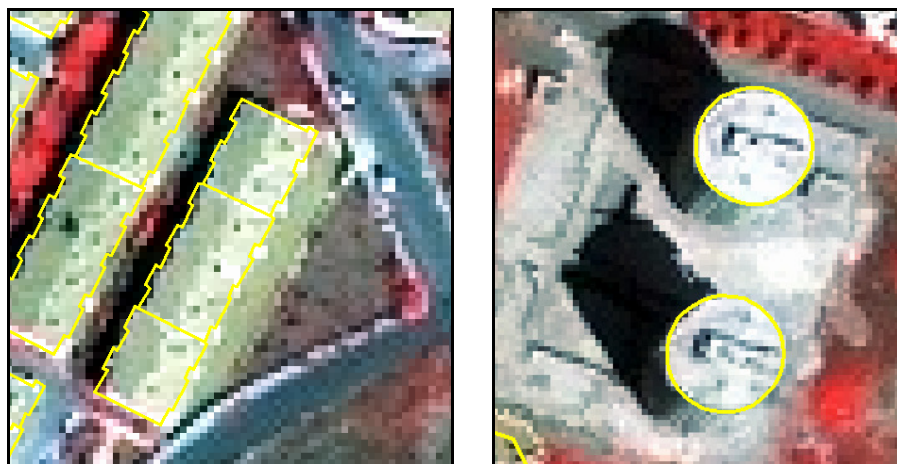


Figure 5. 33. Buildings having similar reflectance values with the surrounding areas.

## **CHAPTER 6**

### **UPDATING AN EXISTING BUILDING DATABASE USING A MODEL BASED APPROACH**

Nowadays, almost all cities have 2D GIS databases or maps. Although these databases are usually not up to date, due to rapid urban growth particularly in developing countries, they are still important data sources for urban object extraction. The difficulties in building delineation from remote sensing imagery may be reduced using existing building boundaries as a priori information stored in a GIS. Thus, updating building databases from remote sensing images is a challenging and an important task. In building extraction studies, ignoring the evidence of existing building boundaries may lead to repetition of the same processes and redundancy.

Therefore, in this part of the study, an approach is presented for updating an existing building database from high resolution satellite images. First, the developed methodology is explained. In the second and third sections, respectively the preparation of a building database and the building patches are described. In section 6.4 the shape characterization parameters are explained. In section 6.5, the selection process of the building models is described. The procedures to assign building models to building patches are given in section 6.6. In section 6.7 the results are presented and finally in section 6.8, the discussions are given.

#### **6.1. The Methodology**

Updating existing GIS databases with continuous changes is an important task. An approach was developed to update existing building boundary database. In the

approach, the building models are determined from the existing building database. As is well known, within mass housing areas monotone ordering is predominant with respect to floor, location, orientation and relation with each other (Keles, 1967). Therefore, within an urban block of a mass housing area the types and the shapes of the buildings are usually similar. This is due to the fact that, within an urban block, the structuring criteria, such as dwelling types and the number of floors determined in the development plans are usually similar. In addition, the buildings falling within an urban block are usually constructed by a housing cooperative and therefore, the settlements developed by the cooperatives become regular settlements. This regularization is because of the acceleration and simplification of the construction and planning (Croitoru and Doytsher, 2003). Thus, it becomes possible to detect new buildings by first determining the building models from an existing building database and then matching them to previously detected building patches.

The main steps followed in the developed approach to update an existing building database are given in figure 6.1. These steps can be summarized as follows:

- Preparing the Existing Building Database,
- Preparing the Candidate Building Patches,
- Shape Characterization
- Selecting the Building Models, and
- Testing the Building Models against the Candidate Building Patches.

To test and demonstrate the developed concept, the building patches previously detected using the SVM classifier and an existing building database are used. Initially, the database is analyzed using the previously classified image in order to detect the destroyed buildings. If the percentages of the pixels classified as building stay higher than the preset threshold, the building is considered to exist. Otherwise, the building is accepted to be destroyed and therefore, the building polygon is removed from the database.



To delineate those buildings constructed after the compilation of the vector database, a model-based approach, which utilizes the existing building database, was developed. Building patches that correspond to existing building polygons are masked out from the building patch image and therefore, an image that includes only the new building patches are generated. Then, for each building patch, to select the most proper building model the shape parameters were calculated for both building patch and existing building polygons. The building polygon which most closely resembles to the building patch based on the size and shape parameters is selected as building model from existing building database. After that, the selected building model is rotated with specified angle intervals and assigned to the building patch to obtain optimum rotation of the building by calculating the matching areas. These processing steps are repeated for all building patches. The algorithm was developed for updating an existing building database. Therefore, the procedure is valid for the structured residential areas only.

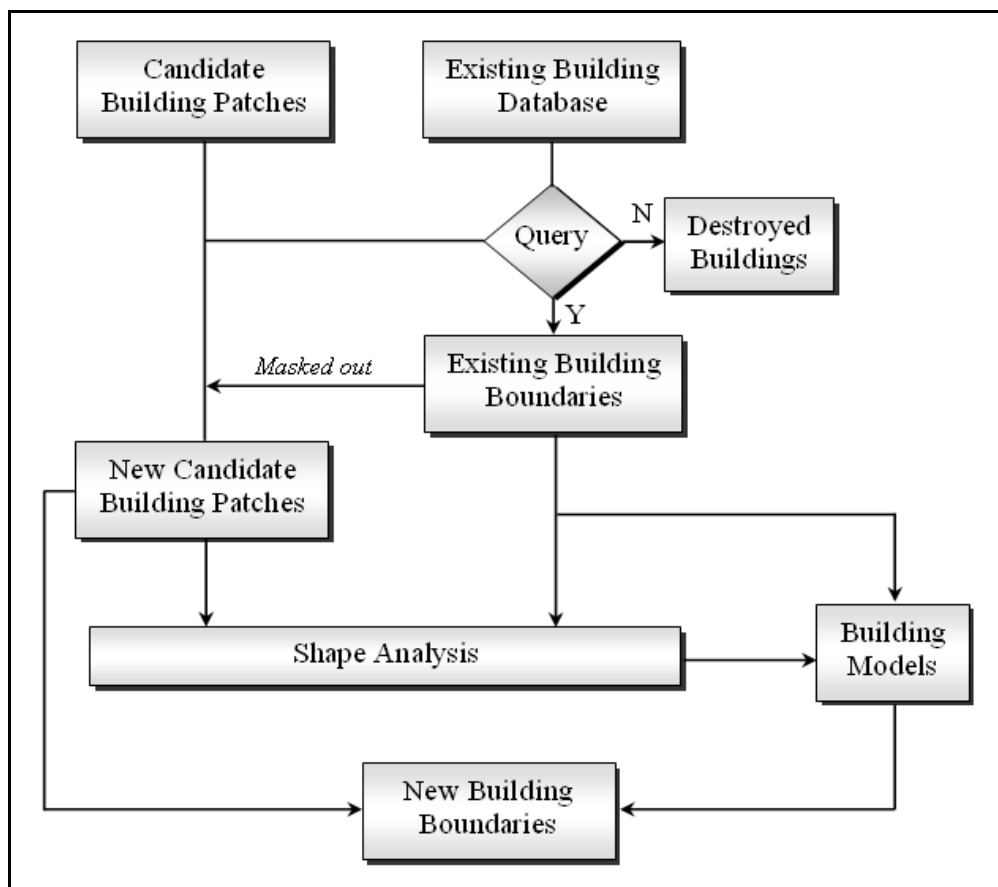


Figure 6. 1. The flowchart of the existing building database update method.

## 6.2. Preparing the Existing Building Database

As mentioned earlier, the available existing vector building database used in this study was compiled in 1999. On the other hand, the images covering the study area were acquired in 2002. Therefore, there is a three-year time lapse between the date of image acquisition and the date of existing vector building database. Thus, for updating a building database, the following three conditions were considered:

- The building exists both in vector database and in the image,
- The building exists in vector database but it disappears in the image, and
- The building exists in the image but disappears in the vector database.

In the first condition, the building exists both in vector building database and in the image. In this case, the existing building must be preserved in the vector database and no update is necessary. In the second condition, the building is not seen in the image. In this case, the building must be removed from the existing building database since the building must have been destroyed between the time of vector data compilation and the time of image acquisition. The third condition corresponds to new buildings constructed after the compilation of the existing building database. Therefore, the boundaries of the new buildings must be extracted and the existing database must be updated with the detected new buildings.

In the proposed approach, an existing building database was utilized for detecting the buildings by means of analyzing the above given three cases. In the first and second cases, the attribute tables of the vector database were updated by analyzing the classified image within the boundaries of each building. The pixels that fall within each building boundary were counted and they were inserted into the attribute database as new data values. Then, those pixels labeled as building in the classified image were counted and their percentage was computed. After updating the attribute table of the vector data, the buildings that still exist and the once destroyed were detected by invoking the following query.

*If %building\_class > 70*  
*Vector = “building”*  
*Else Vector <> “building”*

where; *%building\_class* represents the building class percentage within the building boundary.

For a building polygon analyzed, if the ratio between the pixels classified as building and the total number of pixels is higher than 70%, this building was preserved. Otherwise, the vector polygon was removed. In figure 6.2, the red and blue colored polygons indicate the destroyed and the standing buildings, respectively.



Figure 6. 2. The boundaries of destroyed and existing buildings are represented in red and blue colors, respectively.

### **6.3. Preparing the Building Patches**

The building patches detected previously using the SVM classification include both the existing and new buildings. To update the existing building database with the new building boundaries, the building patch image, which include solely the new buildings, should be generated by removing the patches corresponding to existing

buildings. To do that, the existing buildings were rasterized and masked out from the building patch image. After this processing, a new building patch image that includes the new buildings only was generated. However, because of the differences between the detected building patches that belong to existing buildings and the rasterized existing building polygons, the image may include artefacts. Therefore, these artefacts were removed using morphological operations that were explained in Chapter 4.8. For a selected test area, the steps used for detecting new candidate building patches are illustrated in figure 6.3.

#### **6.4. Shape Characterization**

Shape is an important object property and the shape parameters are crucial resources for comparing and classifying the objects. In the present case, in order to select the most proper building models from existing building boundaries, the shape descriptor parameters were used. For each building patch, a building model was selected from the existing building database by analyzing and comparing the shape parameters of the building patches and existing buildings. Therefore, all existing buildings that fall within the test area were evaluated as the building models. The parameters used to describe the shape of building polygons and each of the building patch include area, perimeter, major axes length, minor axes length, elongation, compactness, and solidity.

The *area* of an object measures the size of a region enclosed by a polygon or the actual number of pixels in the region. Area is an important parameter to define the shapes.

The *perimeter* of a polygon is the sum of the lengths of all its sides, or the perimeter of a patch is the number of pixels around the boundary. Perimeter is another important parameter to define the shapes of objects.

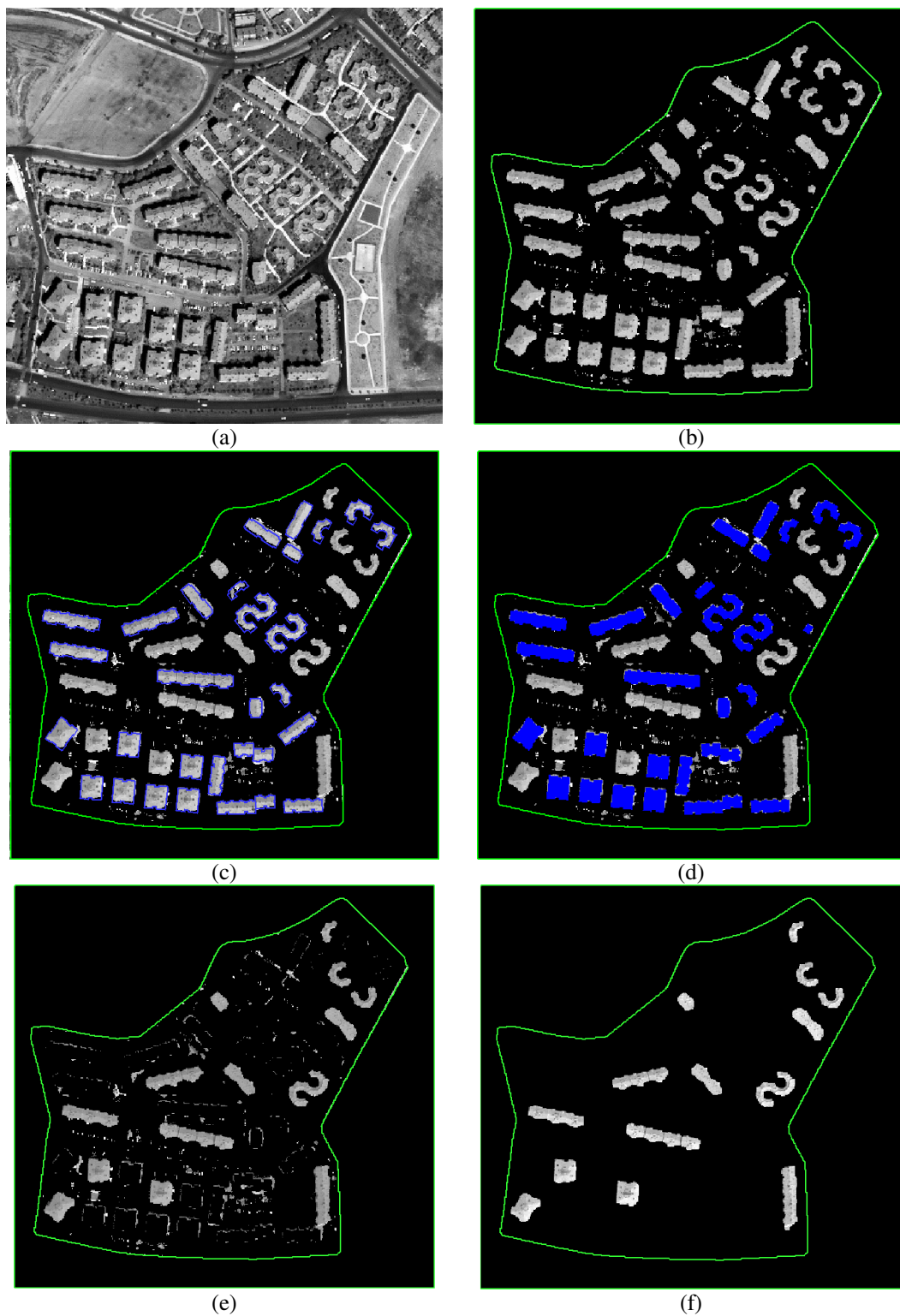


Figure 6. 3. For a test area, the preparation of new candidate building patches. (a) Panchromatic image, (b) detected building patches, (c) existing building boundaries overlaid with the building patches, (d) the rasterized existing building boundaries overlaid with the candidate building patches, (e) candidate building patches after masking the existing building boundaries, and (f) the candidate building patches after removing the artefacts.

The *major and minor axes* are important parameters to extract shape properties. The longest axis within a shape is known as major axis and the minor axis is perpendicular to the major axis. Assuming each shape (S) is represented by a set of points  $(S = (x_1, y_1), (x_2, y_2), \dots, (x_n, y_n))$  and C is the covariance matrix. The eigenaxes of S are defined as the eigenvectors of C. The large and small eigenvalues of C are associated with major and minor axes lengths respectively. The algorithm that calculates the major and minor axes of the shape represented in  $g(p, q)$  is as follows (Costa and Cesar, 2000)

1. Calculate the edges of g;
2. Store the coordinates of the edge points into the vectors b and c;

$n = \text{length}(b);$

*For*  $i = 1$  *to*  $n$  *do*

$X(i, 1) = b(i);$

$X(i, 2) = c(i);$

*End*

3. Calculate the covariance matrix C of X;
4. Calculate the eigenvectors and the eigenvalues of C and store them into array e vectors and into the vector e values

The *elongation* (aspect ratio) is the ratio between the major and minor axes' lengths. This parameter is calculated using equation 6.1.

$$\text{Elongation} = \frac{\text{Major Axis Length}}{\text{Minor Axis Length}} \quad (\text{Equation 6.1})$$

The shapes that have higher elongation value indicate more elongated objects.

The *compactness* parameter describes the surface irregularities and this parameter is calculated as follows:

$$Compactness = \frac{4\pi \times Area}{Perimeter^2} \quad (\text{Equation 6.2})$$

The compactness parameter takes a value between 0 and 1. While the higher values indicate more compact shaped objects, the lower values indicate incompact shaped objects.

The *solidity* is defined as the proportion of the area of a region to the area in the convex hull. It can be computed using the following equation (Equation 6.3):

$$Solidity = \frac{Area}{ConvexArea} \quad (\text{Equation 6.3})$$

where; Convex Area is the area of convex hull, which is the smallest convex polygon that can contain the area.

For the selected test area, the building patches and their Building IDs are illustrated in figure 6.4, while the existing building boundaries and their Building IDs are shown in figure 6.5. For each of the candidate building patches, the above mentioned shape parameters were computed (table 6.1). Similarly, the shape parameters were computed for the existing buildings and these values are provided in table 6.2.

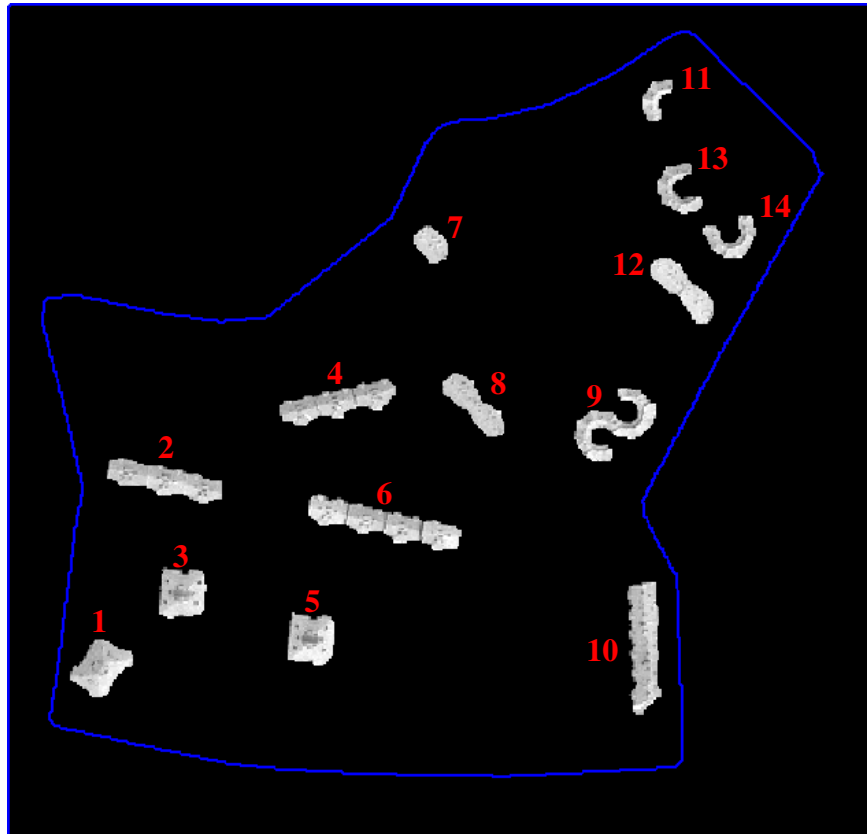


Figure 6. 4. The candidate building patches.

Table 6. 1. The shape parameters computed for the building patches.

ID	Area	Perimeter	MajorA	MinorA	Elongation	Compactness	Solidity
1	636.00	101.74	124.01	78.64	1.58	0.77	0.92
2	791.00	149.84	396.09	32.33	12.25	0.44	0.86
3	603.00	93.80	96.52	87.04	1.11	0.86	0.96
4	782.00	152.33	377.23	33.30	11.33	0.42	0.84
5	611.00	96.87	97.23	88.17	1.10	0.82	0.94
6	1090.00	197.64	655.93	36.11	18.17	0.35	0.83
7	250.00	59.11	51.21	26.77	1.91	0.90	0.95
8	500.00	106.57	184.16	29.22	6.30	0.55	0.84
9	722.00	195.54	204.24	65.58	3.11	0.24	0.64
10	1002.00	169.60	482.14	44.41	10.86	0.44	0.85
11	212.00	65.21	57.33	17.64	3.25	0.63	0.82
12	538.00	109.40	205.91	31.06	6.63	0.56	0.87
13	339.00	101.60	75.95	41.87	0.81	0.41	0.69
14	325.00	99.60	78.44	40.58	1.93	0.41	0.69



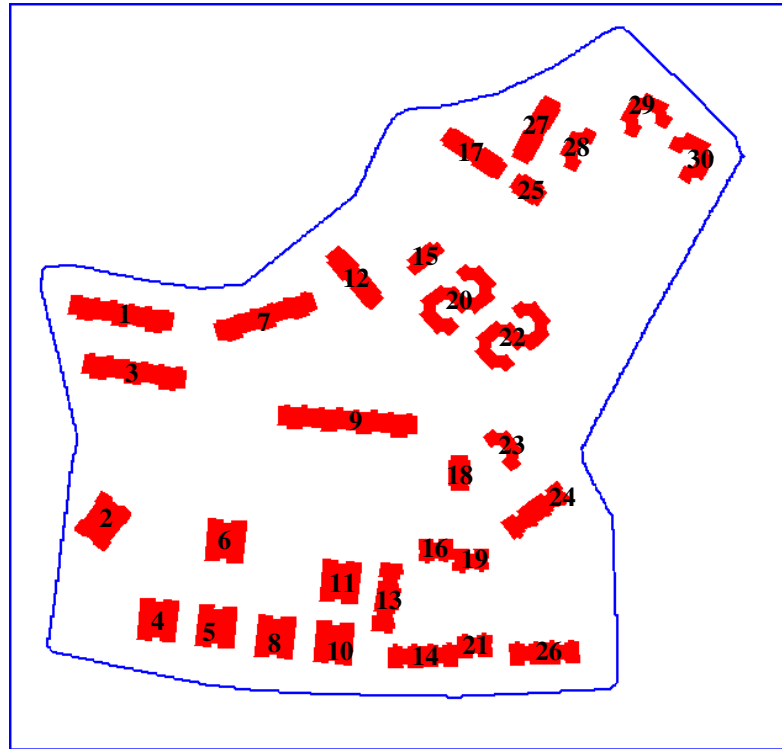


Figure 6. 5. The existing buildings

Table 6. 2. The shape parameters computed for the existing building boundaries.

ID	Area	Perimeter	MajorA	MinorA	Elongation	Compactness	Solidity
1	787.83	172.58	385.99	37.25	10.36	0.33	0.89
2	607.78	109.40	153.25	71.96	2.13	0.64	0.92
3	790.98	171.93	368.95	38.75	9.52	0.34	0.88
4	567.22	104.21	157.71	42.11	3.75	0.66	0.97
5	560.93	104.06	154.55	47.28	3.27	0.65	0.97
6	560.99	103.61	155.01	47.15	3.29	0.66	0.97
7	777.78	168.97	352.50	37.28	9.46	0.34	0.88
8	560.10	103.35	154.53	47.07	3.28	0.66	0.97
9	1053.25	221.38	625.22	38.39	16.29	0.27	0.87
10	555.27	103.47	153.35	46.54	3.29	0.65	0.97
11	563.05	104.22	154.98	47.23	3.28	0.65	0.97
12	503.84	112.73	205.11	33.80	6.07	0.50	0.95
13	533.19	135.77	195.96	29.57	6.63	0.36	0.90
14	532.79	135.12	178.65	29.89	5.98	0.37	0.90
15	79.64	39.00	51.87	15.55	3.34	0.66	0.35
16	263.56	80.11	52.05	27.66	1.88	0.52	0.91
17	498.83	112.97	204.08	33.25	6.14	0.49	0.95
18	255.84	67.28	75.12	34.70	2.17	0.71	0.97
19	265.16	82.61	59.89	24.27	2.47	0.49	0.89
20	771.47	222.88	207.49	73.05	2.84	0.20	0.66
21	269.14	80.94	49.58	28.20	1.76	0.52	0.91
22	766.19	221.80	201.39	74.18	2.71	0.20	0.66
23	258.84	84.69	89.08	24.51	3.64	0.45	0.78
24	534.58	136.35	196.70	29.43	6.68	0.36	0.90
25	249.45	66.99	74.05	33.27	2.23	0.70	0.97
26	528.07	134.23	196.06	27.78	7.06	0.37	0.90
27	512.77	113.25	192.78	35.27	5.47	0.50	0.95
28	255.37	84.65	88.87	24.88	3.57	0.45	0.78
29	383.08	118.95	89.65	54.28	1.65	0.34	0.66
30	386.34	119.34	92.18	54.00	1.71	0.34	0.66

## 6.5. Selecting the Building Models

In order to define the most suitable building model, each of the building polygons in the database was tested against each building patch. To do that an automatic selection procedure was developed. The algorithm for the developed procedure is as follows:

1. For each building patch, calculating the difference of the shape parameter between the building patch and all of the existing building polygons,
2. Determining the minimum and maximum values of these differences,
3. Rescaling these differences between 0 and 1,
4. Calculating the total difference values by adding all rescaled shape parameter differences,
5. For each candidate building patch, determining the minimum difference value in order to select the optimum building model,
6. From the existing building database, selecting the building model based on the minimum difference value between the existing building polygon and the building patch.

The source code of this algorithm is given in Appendix E. The attributes of the existing building database are illustrated in table 6.3. For each building patch, the selected building model was saved as a new shape file to be used as a building model for further processing.

Table 6. 3. The fields of the existing building database

FIELD
BuildID
IGDS_Color
IGDS_Graph
IGDS_Level
Address_No
Build_No
Name
Z
Area
Perimeter

In the selected test area, the existing buildings and a building selected as a model are illustrated in figures 6.6 (a) and 6.6 (b), respectively.

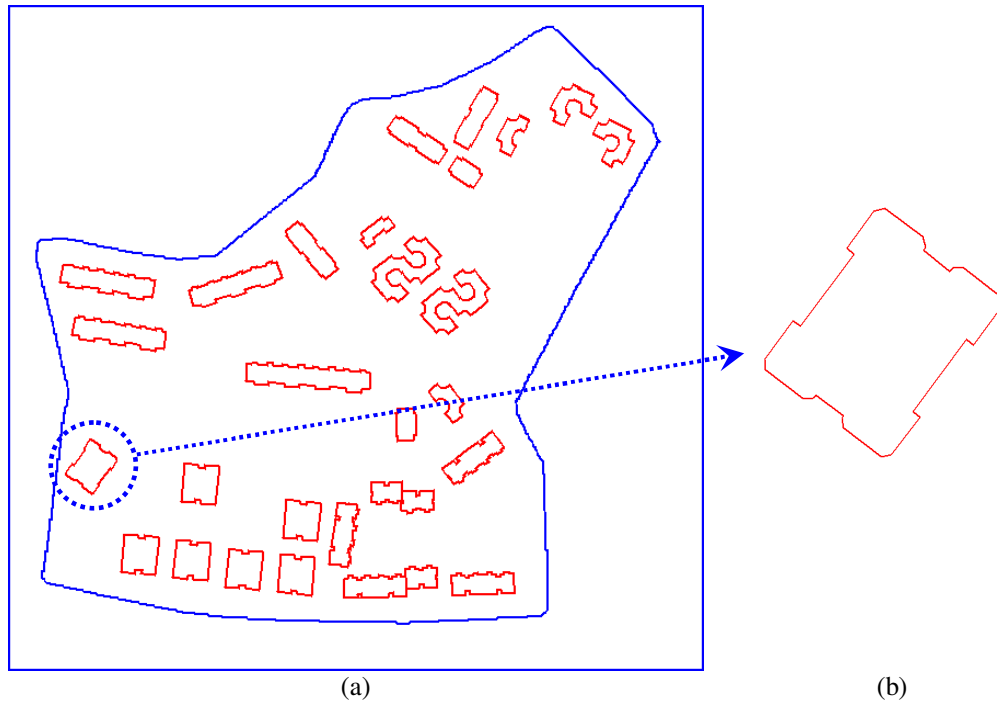


Figure 6. 6. (a) An existing building database and (b) a building selected as a model for the first candidate building patch.

## 6.6. Testing the Building Models against the Candidate Building Patches

After selecting the building model for each building patch, the model was analyzed against the patch. This procedure consists of five main steps: (i) finding the centroid of the building patch being processed, (ii) finding the centroid of the building model, (iii) rotating the building model with a specified angle, and (iv) testing the rotated building models against the candidate building patch by computing the overlapping area between the building model and the building patch for each rotation.

### (i) Finding the centroid of the candidate building patch

The centroid of the building patch being processed was computed using the “centroid” property of “regionprops” function of Matlab. “Regionprops” is a tool to measure the properties of image regions and the “centroid” is 1\*2 vector; the center of mass of the region (Matlab 7 Manual, 2007). The first and second elements of the “centroid” are the x and y coordinates of the centroid of the mass, respectively. Therefore, using this property, for each candidate building patch, the x and y coordinates of the centroid were determined. The centroids of building patches of an urban block are illustrated in figure 6.7.

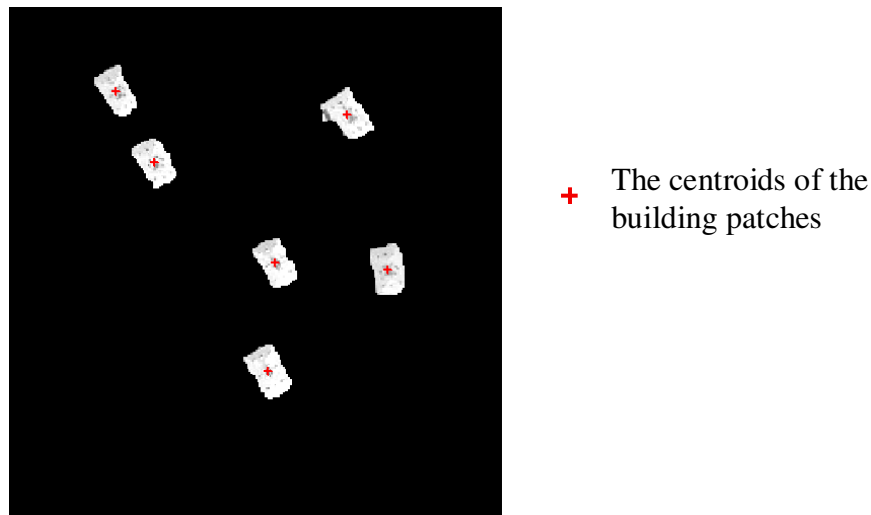


Figure 6. 7. The centroids of building patches of an urban block.

### (ii) Finding the centroid of the Building Model

The centroid of a building model was computed by using its corner coordinates. To find the centroid of a building model, the average value of the X and Y coordinates were calculated (Equations 6.4, 6.5, and 6.6). The centroid of a selected building model is illustrated in figure 6.8.

$$\text{Centroid} = \text{Average\_X}, \text{Average\_Y} \quad (\text{Equation 6.4})$$

$$\text{Average\_X} = \frac{X_1 + X_2 + \dots + X_n}{n} \quad (\text{Equation 6.5})$$

$$\text{Average\_Y} = \frac{Y_1 + Y_2 + \dots + Y_n}{n} \quad (\text{Equation 6.6})$$

where ;  $n$  is the number of the corner points of the selected building model.

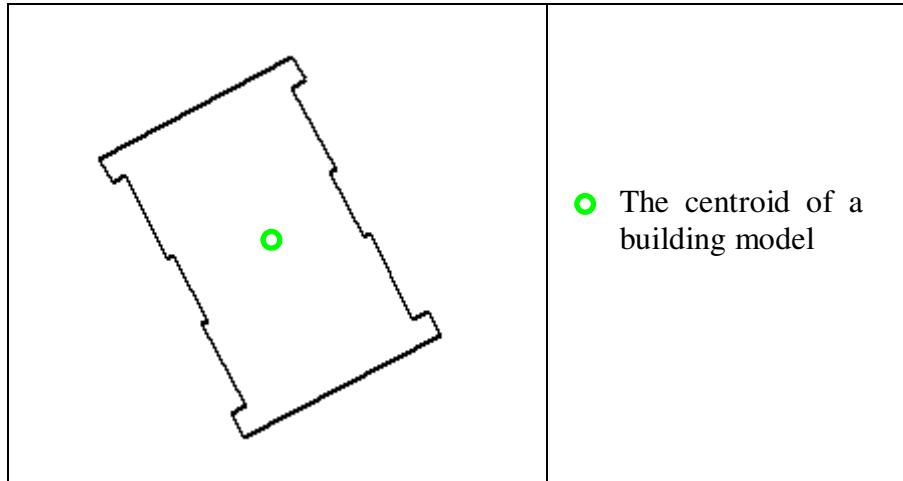


Figure 6. 8. The centroid of a selected building model.

### (iii) Rotating the Building Model

To find the largest overlap between the building model selected and the building patches analyzed, the building model was rotated with the specified angle intervals. The rotations of a building model per 60°, 45°, 30°, 15°, 10°, and 5° from 0° to 360° are shown in figure 6.9. Rotating the building model with smaller angles may provide better results. This is because rotation with smaller angles generates more cases for defining the building orientation providing a higher accuracy to measure the overlapping area between the model and the patch. On the other hand, in the case of very coarse orientation, the overlapping area will be computed for less number of cases. Thus in this study, the rotation angle of the building model was selected as 1°.

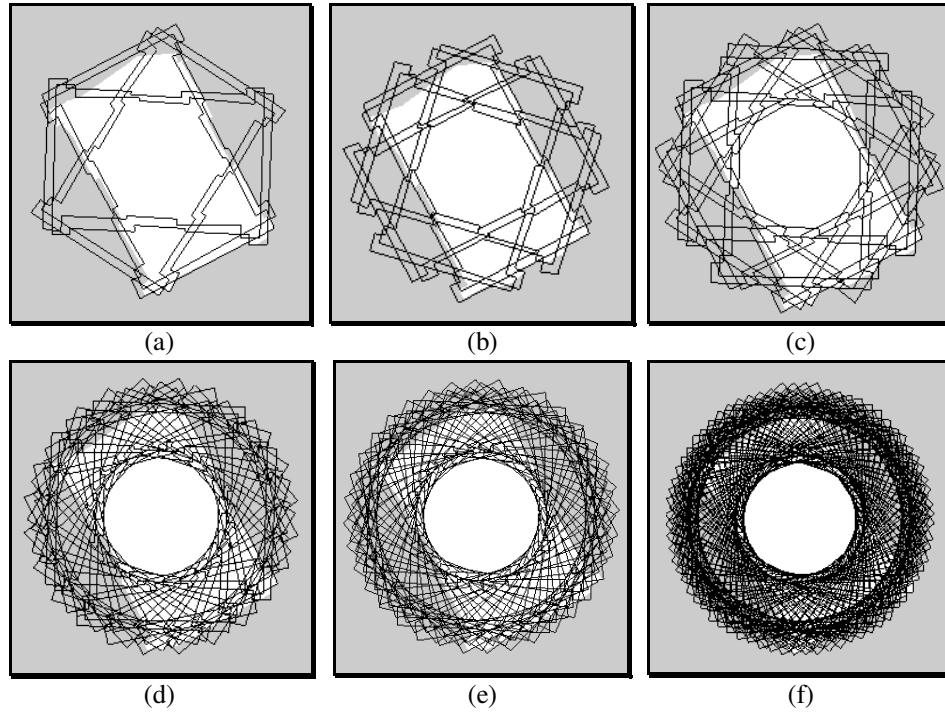


Figure 6. 9. The rotation of a building model over a building patch (white area) per (a) 60°, (b) 45°, (c) 30°, (d) 15°, (e) 10° and (f) 5° from 0° to 360°.

To rotate the building model selected with a specified angle, a “rotation matrix” was calculated (Equation 6.7) and the coordinates of the building model was multiplied with the rotation matrix (Equation 6.8). The rotation of a building model with a specified angle is illustrated in figure 6.10.

$$RM = [\cos(\theta) \ -\sin(\theta); \ \sin(\theta) \ \cos(\theta)]; \quad \text{(Equation 6.7)}$$

$$RBM = RM * BM2; \quad \text{(Equation 6.8)}$$

where;  $RM$  = Rotation Matrix

$RBM$  = Rotated Building Model

$BM2$  = [BM.X; BM.Y] (X and Y values of the Building Model)

$\theta$  = Angle

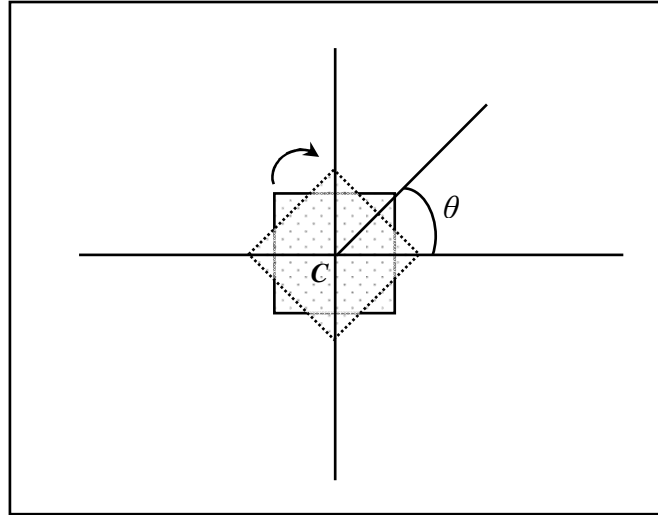


Figure 6. 10. The rotation of a polygon with a specified angle.

**(iv) Testing the rotated building models against the building patches**

Before starting to rotate the building model, the centroids of the building model and the patch being analyzed must coincide. To do that it is necessary to know the amount of shift between their centroids. Therefore, the differences in X and Y between the centroids of the building model and the building patch were computed using the equations 6.9 and 6.10.

$$\Delta X(i) = ( C ( i, 1 ) - Average\_X ); \quad \text{(Equation 6.9)}$$

$$\Delta Y(i) = ( C ( i, 2 ) - Average\_Y ); \quad \text{(Equation 6.10)}$$

where;  $i$  is the number of the centroids of the building areas.

Then, the computed differences were added to the corner coordinates of the building model. The next step was to determine the true orientation of the building model. To do this, for each rotation, the overlapping area between the building model and the vectorized building patch being analyzed was calculated and the rotation angle that provides the largest overlap was selected to be the true orientation of the building model (figure 6.11).

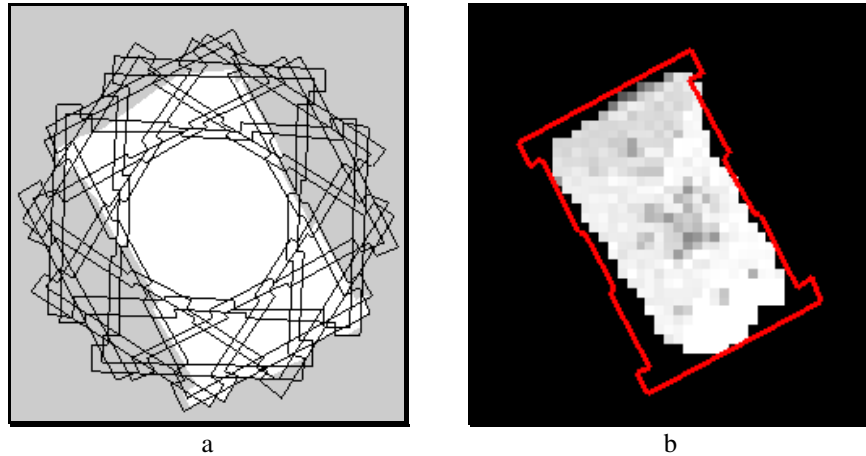


Figure 6. 11. (a) The rotation of a building model over a candidate building patch (white area) and (b) the true orientation of the building model found based on the intersection between the building model and the building patch.

### 6.7. The Experimental Results

The proposed algorithm was tested in the selected two test areas that contain buildings of different shapes. For these test areas, the updated building boundaries are given in figure 6.12. In figure 6.13, the overlay of the delineated building boundaries and the reference building boundaries are illustrated.





Figure 6. 12. The updated building boundaries. The blue polygons represent the existing building boundaries, while the red polygons illustrate the updated building boundaries.

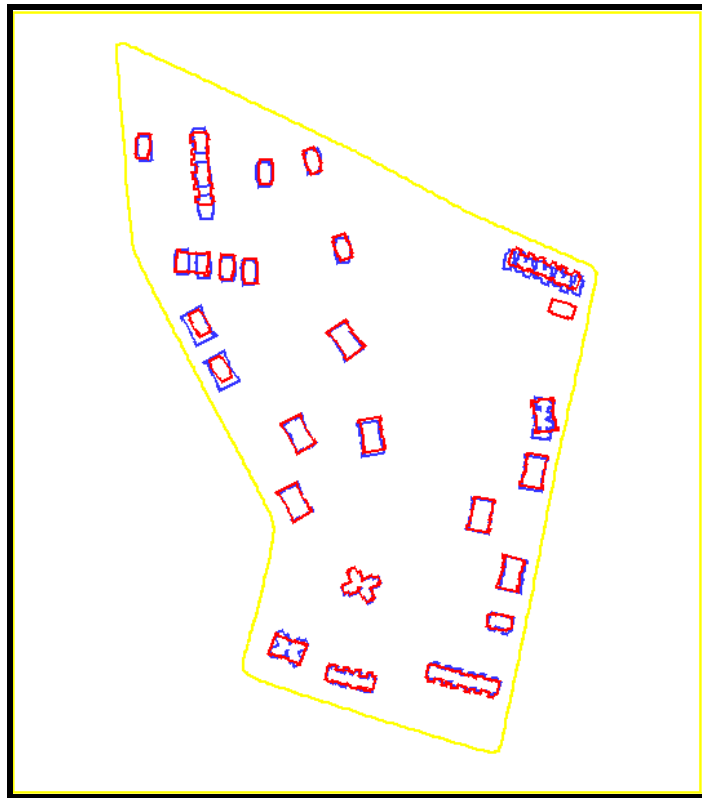
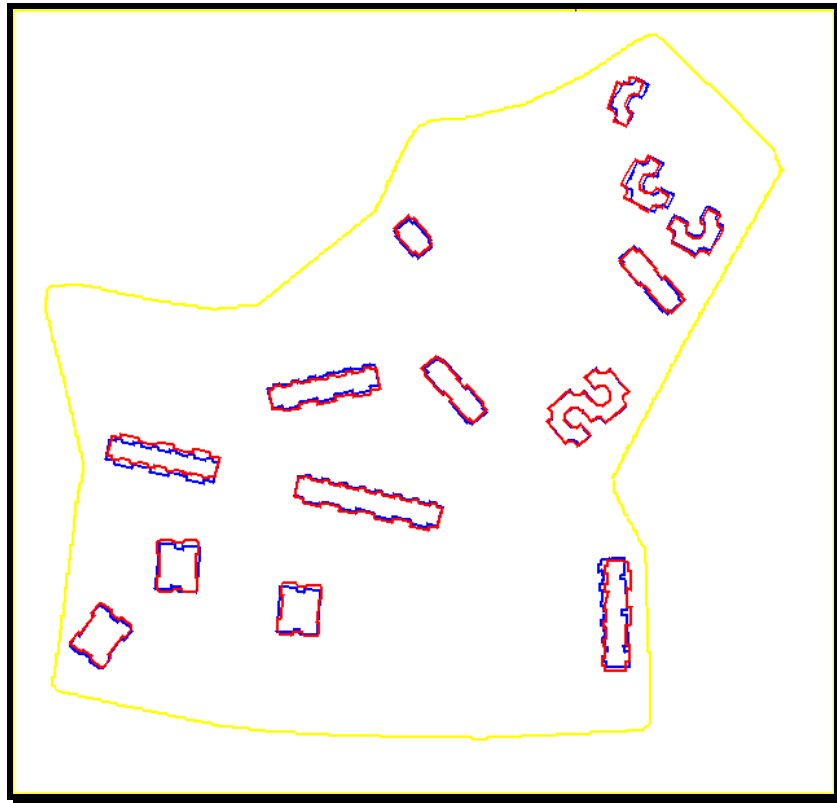


Figure 6. 13. The delineated new buildings and the reference buildings. The blue polygons represent the reference buildings, while the red polygons illustrate the delineated new buildings.

To assess the results of building delineation, the areas were classified into True Positive, False Positive, True Negative and False Negative categories by comparing the delineated building boundaries with the reference building boundaries (Shufelt and McKeown, 1993). Then, for each urban block, the Branching Factor (BF), Miss Factor (MF), Building Detection Percentage (BDP), and the Quality Percentage (QP) values were calculated. The descriptions of these accuracy measures are given in Chapter 4.9.2. For two test areas, the obtained quality assessment results are given in table 6.4.

Table 6. 4. The quality assessment results for two urban blocks.

<b>Test Area</b>	<b>BF</b>	<b>MF</b>	<b>BDP</b>	<b>QP</b>
1	0.14	0.12	88.95	79.04
2	0.24	0.21	82.44	68.53

For the first area, the BF, MF, BDP, and QP values were found to be 0.14, 0.12, 88.95 and 79.04, respectively. For the second urban block, these values were computed to be 0.24, 0.21, 82.44, and 68.53, respectively. The difference in the computed accuracies is believed to be due to the previously detected building patches. In addition, due to the resolution restriction of the satellite image, the detected building patch may not provide small protrusions and details. Therefore, if the shape of a building model is rather complex and has thin protrusions, there may be shifts in the matching process

## **6.8. Discussion of the Results**

Both the visual and quantitative analyses of the results obtained indicate that the proposed approach is quite promising for delineating building boundaries from high resolution satellite images by utilizing the existing building boundaries that are stored in a GIS as a priori information. In conventional building model-based approaches, all the possible building shapes must be determined and pre-defined as

building models. Therefore, the conventional approaches have a disadvantage that the shapes and the types of the buildings can be numerous. In addition, the compilation of a building-model library may become rather a difficult and formidable task (Shufelt, 1999). On the other hand, in conventional model-based approaches, the building models are usually defined as primitive shapes, such as square, rectangle, etc. or the combination of these shapes, such as “L” shape and “H” shape.

In the proposed approach, the building model is selected from an existing GIS database that includes building boundaries. Therefore, using the developed approach the buildings having very different and/or complicated shapes such as, “S” shape, “C” shape, etc. can be successfully delineated. It was observed that by utilizing an existing building boundary database as a model library appears to be quite effective for map updating with respect to buildings.

In several cases, the proposed approach may fail, however. These limitations and special cases can be summarized as follows:

1. If the area contains no buildings, it may be problematic to apply the proposed approach. This case may be faced at urban fringes. In order to delineate building patches that are located at an urban fringe (figure 6.14), the building models may be selected from the existing buildings located in the neighboring urban areas. But, the shapes of the new buildings to be extracted may become completely different from the existing buildings and therefore, no match can be found between the building patches and the model selected.

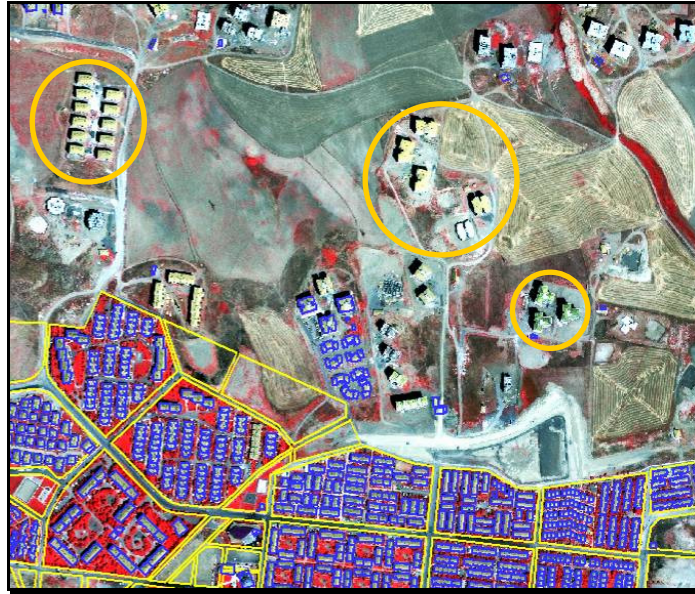


Figure 6. 14. The buildings in an urban fringe. Existing buildings and the development plan overlaid with the IKONOS false color image.

2. If the patches of new buildings are not similar to buildings in the existing building database, the existing buildings that have the most similar shape parameters to these building patches are selected as the building models from the existing building database. This case may result in erroneously delineated building boundaries.
3. The accuracy of delineation is directly affected by the detected building patches in such there may not be similarity between the building patch being analyzed and the reference buildings. For example, because of the resolution restriction of the satellite image the detected candidate building patches may not contain small protrusions of the buildings. On the other hand, those buildings that are quite close to each other may be detected as a joined one building. In addition, due to the surrounding objects of the buildings the building patch being analyzed may include artefacts. Due to these problems therefore, the delineated boundaries may not correctly represent the building boundaries (Figure 6.15).



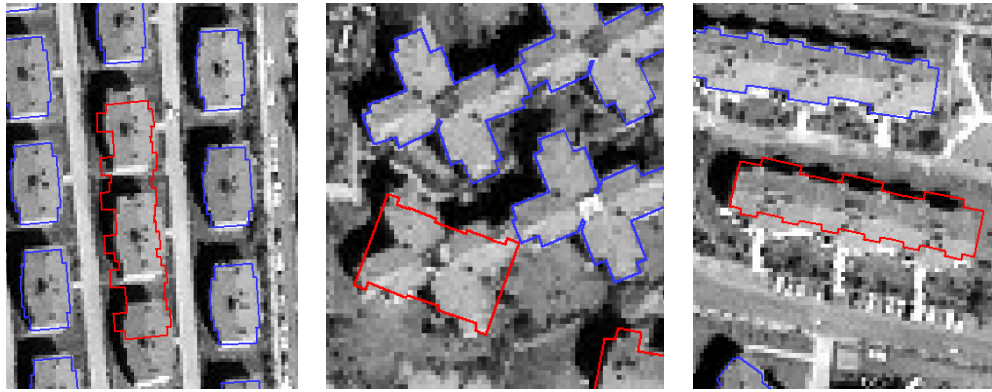


Figure 6. 15. The delineated building boundaries. Because of the artefacts on the building patches the delineated building boundaries do not correctly represent the boundaries of the buildings. The blue polygons represent the existing building boundaries, while the red polygons represent the delineated building boundaries.

4. If the buildings with different shapes that are contained within an existing database have similar shape parameters then, the building models can be selected erroneously (Figure 6.16).



Figure 6. 16. The delineated building boundaries. Because of the similar shape parameters the building models can be selected erroneously.

## CHAPTER 7

### CONCLUSIONS AND RECOMMENDATIONS

In this chapter, the conclusions reached for the developed approaches are described and the recommendations regarding to further studies are made. This chapter contains four sections. In the first section, the conclusions of the building detection procedure are provided. In the second section, the conclusions reached for the building delineation part of the study are given. In the third section, the conclusions of the existing building database updating procedure are presented. Finally, in section four, the recommendations are expressed.

#### 7.1. Building Detection

The following conclusions were reached for the SVM classification and building detection:

##### 7.1.1. SVM Classification

- The classification accuracies obtained indicate that, for building detection, the binary SVM classification provides quite accurate results. For all test areas, the overall accuracy and kappa coefficient values were computed to be noticeably high staying between 90% – 99% and 0.80 – 0.98, respectively.
  - For “Sub-area I”, the results of SVM classification appear to be quite satisfactory with the overall accuracies and Kappa Coefficients in the range of 95% – 99% and 0.90 – 0.98, respectively.

- For “Sub-area II”, the overall accuracies of the SVM classification were computed to be in the range of 92% - 97%, while the Kappa Coefficients were found to be in the range of 0.86 - 0.94.
  - For “Sub-area III”, the results of SVM classification appear to be quite satisfactory with the overall accuracies and Kappa Coefficients in the range of 90% - 97% and 0.80 - 0.96, respectively.
- If there are spectral overlaps between the classes, using the spectral bands only may result in lower classification accuracy. However, in the proposed building detection procedure, additional data sources were used as ancillary data during the classification procedure. Thus, with the use of ancillary data it was possible to detect the buildings even though they have similar reflectance values with the other classes, such as the pavements, roads, and bare lands.
  - The inclusion of ancillary data in the classification process has a significant effect in the accuracy of the SVM classifier. After using additional bands, the overall classification accuracy increased about 7%, while the Kappa Coefficient values increased about 0.13.
  - Including the individual Principal Component (PC) images as additional bands in the classification process do not lead to significant difference. However, it was found that using the 2<sup>nd</sup> or 3<sup>rd</sup> Principal Component images relatively increases the classification accuracy. On the other hand, including all PC images in the classification process as additional bands improves the overall accuracies up to 4%.
  - Using nDSM as an additional band increases the classification accuracy from 2.5% to 6.5%. On the other hand, using the NDVI image as an additional band do not increase the classification accuracy significantly.



- In general, increasing the number of training samples increases the accuracy of SVM classification. However, the increase was not observed to be more than 2%. Therefore, the results obtained in this study indicate that small training size (i.e. 500 pixels for a high resolution image measuring about 2000 pixels x 2000 lines) appears to be enough.

### 7.1.2. Building Detection

- The building detection process provides the approximate locations of the buildings and therefore, this processing step significantly reduces the search area, within which the building delineation process to be carried out.
- When the accuracies of the detected building patches are evaluated it can be stated that the BDP and QP values were computed to be considerably high staying in the range of 80% - 97% and 53% - 76%, respectively.
  - For sub-area I, the BDP values were computed to be in the range of 80% - 91%, while the QP values were found to be in the range of 59% - 70%.
  - For sub-area II, the BDP values stayed between 83% and 91%, while the QP values were in the range of 53% - 66%.
  - For sub-area III, the BDP values were quite high staying between 91% and 97%, while the QP values were computed in the range of 62% - 76%.
- The results obtained in this study have proven that, for building detection from high resolution space images, the inclusion of an nDSM as ancillary data is very important. It was also found that in most cases, using an NDVI image as an additional band also increases the accuracy but not as effective as nDSM. After including the nDSM and NDVI images as additional bands in

the classification process, the BDP values increased about 7%, while the increase in the QP values were in the range of 4% - 8%.

- The accuracy of the DSM generated from IKONOS panchromatic stereo images was computed to be  $\pm 0.7\text{m}$ , which is accurate enough to be used in the building detection procedure.
- After using nDSM as an additional band in the classification process, the building detection errors due to the spectral similarities between the classes were compensated. However, the nDSM inaccuracies, which are due to the errors in the matching process and the interpolation during the DSM generation, may lead to errors in the detection of the building patches.
- Buildings that are closer than 3m to each other may be detected as a joined building. This is basically because of the resolution restriction of the image, the spectral similarities between building roofs and the surrounding objects, and the inaccuracies of nDSM. If the contrast between closely located buildings is high due to land cover types, such as the cast shadows or green vegetation, these buildings can be detected separately from each other.

## **7.2. Building Delineation**

The following conclusions were made for the building delineation part of the study:

- In the proposed approach, to delineate the building boundaries, a panchromatic building patch image, which is generated by masking the classified building areas, is used. Therefore, by confining the search area over the candidate building patches, the building delineation process becomes easier because the unnecessary edges are not included in the process and therefore, the processing operations are carried out over the building areas only.

- The results obtained using the developed Hough transform and the Boundary tracing based approaches indicate that high resolution satellite imagery has a great potential in building delineation.
- The results show that the proposed approaches are quite successful for delineating buildings from high resolution satellite images with the average BDP values higher than 90% and the QP values higher than 78%.
  - For the residential rectangular buildings, the Hough transform based approach provided quite satisfactory results with the average BDP and QP values of 95.34% and 79.05%, respectively. On the other hand, the Boundary tracing based approach was slightly less successful than the Hough transform based approach providing the average BDP and QP values of 90.46% and 78.73%, respectively.
  - For the residential circular buildings, the Hough transform based approach provided the average BDP and QP values of 78.74% and 66.81%, respectively. On the other hand, for the Boundary tracing based approach, the average BDP and QP values were computed to be 77.80% and 64.23%, respectively.
  - For the industrial buildings, both approaches provided similar results. While the Hough transform based approach provided the average BDP and QP values of 93.45% and 79.51%, respectively, the Boundary tracing based approach provided the average BDP and QP values of 93.59 and 80.39, respectively.
- The results obtained in this study indicate that the Hough transform based building delineation procedure can be effectively used to delineate the rectangular shaped buildings.

- The results prove that the Circular Hough transform is a useful tool for the extraction of circular buildings.
- The developed algorithm to delineate the “C” and “S” shape buildings is quite successful and efficient.
- The building boundaries, delineated using the Boundary tracing based approach, are patch dependent. The building patch image may contain artefacts or the building details may be missing. Since the detected building patches are in raster form, the delineated building boundaries may have irregular shapes. Therefore, the delineated building boundaries using the boundary tracing based approach may need refinement process. For this purpose, line simplification and the consequent topological filters were used. However, further refinement may still be needed to shape the final building boundary. This is not the case in the Hough transform based approach because in this approach the edges are forced to generate regular shaped buildings based on the assumptions made for the perceptual organization.
- When the two approaches are compared, in general, the Hough transform based approach provides slightly better results than the Boundary tracing based approach. If the mutual lines of the buildings are parallel and the angles between the adjacent lines are perpendicular, and if the buildings are circular or curved shape, such as the “circle”, “ring”, “C”, and “S” shape, the Hough transform based approach provides better results both visually and quantitatively.
- The success of the developed building delineation approaches is dependent on the success of the detected building patches:
  - The adjoining buildings (semi-detached and terraced) were detected as one building. As well, the detection of the boundaries between the adjoining buildings was not possible from high resolution satellite

images. Therefore, the adjoining buildings were not able to be delineated separately.

- If the building patches are not detected accurately due to the surrounding land use classes that have similar reflectance values, the buildings cannot be delineated correctly.
- The buildings that are closer than 3m to each other were detected as a single joined building.
- On maps, the boundaries of the buildings represent the footprints rather than the rooftops. However, from space imagery, the buildings can be delineated from their rooftops. If the image is not a true orthoimage and the hangovers are not removed, the delineated boundaries do not represent the footprints, therefore.

### **7.3. Updating an Existing Building Database**

The following conclusions were reached from the existing database update part of the study:

- It was found that the high resolution satellite images have a great potential for updating the buildings in existing building databases.
- Using the proposed model-based approach, the boundaries of new buildings were delineated quite successfully with the BDP values ranging from 82.44% to 88.95% and the QP values ranging from 68.53% to 79.04%.
- For updating an existing building database, the integration of remote sensing imagery and GIS data is quite functional and efficient. Ignoring the evidence of existing building boundaries lead to repetition and redundancy. In addition,

using the existing building boundaries as a priori information will reduce the difficulties in building extraction procedure.

- The major advantage of the developed model-based approach is that there is no need to create a building model library.
- As is well known, in conventional building-model based approaches, all the possible building shapes must be pre-defined as the building models. The disadvantage of these approaches is that there may be a significant number of different shapes and types of buildings, which leads to difficulties in the creation of a building model library. However, in the developed approach it is assumed that the shapes of new buildings are similar to existing buildings located in the area. Therefore, with the proposed technique, the difficulties of the conventional approaches are handled by means of utilizing the existing buildings stored in a GIS.
- In conventional model-based approaches, the shapes of the building models in a building model library are usually limited to primitive shapes, such as square, rectangle, etc. or the combination of these shapes, such as 'L' shape, 'H' shape, etc. However, in the proposed approach, the number of building-models to be selected can be as many as the number of building shapes stored in a GIS database. Therefore, with the developed approach, the buildings having very different and/or complicated shapes, such as 'S' shape, 'C' shape, etc. can also be successfully delineated.
- For each building patch, the most proper building model is selected by computing and comparing the shape parameters of the building patch (in raster form) and the existing buildings (in vector form). It was found that using the shape parameters to define the optimum building model is quite helpful and efficient.

- If the buildings constructed after the compilation of the existing building database have different shapes from the buildings in the existing building database, the proposed approach may fail for detecting these buildings. This is because in this study an assumption was made that the shapes of new buildings are similar to the shapes of existing buildings in the same area. In this case, the building boundary with the most similar shape is selected as the building model from the existing building database.
- In the existing database, there may be more than one building with the similar shape parameters to the building patch being analyzed. In this case, the selection of the building model can be made wrongly.
- The success of the developed approach depends on the accuracy of the previously detected building patches.

#### **7.4. The Recommendations**

- The proposed approach can be applied using higher resolution satellite images such as Quickbird, GeoEye1, or high resolution digital aerial images.
- The DSM, which was generated in this study from high resolution satellite images, can be generated from Laser/Lidar or from aerial images.
- Textural bands can be used as additional bands in the classification for building detection and the resultant classified image may increase the building detection accuracy.
- The building delineation using Hough transform algorithm can be extended for delineating different shapes of buildings such as “L” shape, “H” shape, etc.

## REFERENCES

- Avrahami, Y., Raizman, Y., and Doytsher, Y., (2007), Semi-Automatic Approach Toward Mapping of Flat-Roofed Buildings within a Non-Stereoscopic Environment, *The Photogrammetric Record*, 22(117), pp.53-74.
- Baltsavias, B. P., (2004), Object Extraction and Revision by Image Analysis Using Existing Geodata and Knowledge: Current Status and Steps towards Operational Systems, *ISPRS Journal of Photogrammetry and Remote Sensing*, 58, pp.129-151.
- Baltsavias, E., Gruen, A., and Van Gool, L. (editors), (2001a) Automated Extraction of Man-Made Objects from Aerial and Space Images (III), A.A. Balkema Publishers, Lisse, The Netherlands, 415 p.
- Baltsavias, E., Pateraki, M., and Zhang, L., (2001b), Radiometric and Geometric Evaluation of IKONOS Geo Images and Their Use for 3D Building Modelling, Joint ISPRS Workshop, High Resolution Mapping from Space, Hannover, Germany, 19-21 September.
- Batikent, Kent-Koop, Turkey, <http://www.iisd.org/50comm/commdb/desc/d22.htm>, Last Accessed Date: 10<sup>th</sup> March 2007.
- Bellman, C. and Shortis, M, (2000), Early Stage Object Recognition Using Neural Networks, *International Archives of Photogrammetry and Remote Sensing*. Vol. XXXIII, Supplement B3. Amsterdam 2000.
- Benediktsson, J. A., Pesaresi, M., and Arnason, K., (2003), Classification and Feature Extraction for Remote Sensing Images from Urban Areas Based on Morphological Transformations, *IEEE Transactions on Geoscience and Remote Sensing*, Vol.41, No.9, pp. 1940-1949.



Boyd, D. S., Sanchez-Hernandez, C. and Foody, G. M., (2006), Mapping a Specific Class for Priority Habitats Monitoring from Satellite Sensor Data, *International Journal of Remote Sensing*, Vol.27, No. 13, 2631-2644.

Brenner, C., (2005), Building Reconstruction from Images and Laser Scanning, *International Journal of Applied Earth Observation and Geoinformation*, No.6, pp. 187-198.

Canny, J. F., (1983), Finding edges and lines in images. Technical Report AI-TR-720, MIT, Artificial Intelligence Laboratory, Cambridge, MA, 1983.

Canny, J. F., (1986), A Computational Approach to Edge Detection, *IEEE Transactions on Pattern Analysis and Machine Intelligence*, 8(6), 679-698.

Cha, J., Cofer, R. H., and Kozaitis, S.P., (2006), Extended Hough Transform for Linear Feature Detection, *Pattern Recognition*, 39, pp.1034-1043.

Costa, L.F., Cesar, R. M., (2000), *Shape Analysis and Classification: Theory and Practice*, CRC Press LLC.

Croitoru, A. and Doytsher, Y., (2003), Monocular Right-Angle Building Hypothesis Generation in Regularized Urban Areas by Pose Clustering, *Photogrammetric Engineering and Remote Sensing*, Vol.69, No.2, pp.151-169.

Croitoru, A. and Doytsher, Y., (2004), Right-Angle Rooftop Polygon Extraction in Regularised Urban Areas: Cutting the Corners, *The Photogrammetric Record*, 19(108), pp.311-341.

Dash, J., Steinle, E., Singh, R. P., and Baehr, H. P., (2004), Automatic Building Extraction from Laser Scanning Data: An Input Tool for Disaster Management, *Advances in Space Research*, No.33, pp.317-322.

Davies, E.R., (1987), The effect of noise on edge orientation computations. *Pattern Recognition Letters*, 6, pp.315-322.

Dial, G., Bowen H., Gerlach, F., Geodecki, J. and Oleszczuk, R., (2003), IKONOS satellite, imagery, and products, *Remote Sensing of Environment*, Vol. 88, pp.23-36.

Duda, R.O. and Hart P.E., (1972), Use of the Hough Transform to detect curves and lines in pictures, *Communications of the Association for Computing Machinery*, 15(1), pp.11-15.

Ecabert, O. and Thiran, J.P., (2004), Adaptive Hough Transform for the Detection of Natural Shapes Under Weak Affine Transformations, *Pattern Recognition Letters*, 25, pp.1411-1419.

Efford, N., (2000), *Digital Image Processing: A Practical Introduction Using Java*, Addison-Wesley, Pearson Education, ISBN 0-201-59623-7.

ENVI Manual, (2006), Version 4.3.

Foody, G. M. and Mathur, A., (2004), A relative Evaluation of Multiclass Image Classification by Support Vector Machines, *IEEE Transactions on Geoscience and Remote Sensing*, Vol.42, No. 6, pp. 1335-1343.

Foody, G. M., Mathur, A., Sanchez-Hernandez, C. and Boyd, D. S., (2006), Training Set Size Requirements for the Classification of a Specific Class, *Remote Sensing of Environment*, 104, pp.1-14.

Forlani, G., Nardinocchi, C., Scaioni, M., and Zingaretti, P., (2006), Complete Classification of Raw LIDAR data and 3D Reconstruction of Buildings, *Pattern Anal. Applic*, No.8, pp.357-374.

Fradkin, M., Maitre, H., and Roux, M., (2001), Building Detection from Multiple Aerial Images in Dense Urban Areas, *Computer Vision and Image Understanding*, 82, pp.181-207.

Fraser, C. S., Baltsavias, E., and Gruen, A., (2002), Processing of Ikonos Imagery for Submetre 3D Positioning and Building Extraction, *ISPRS Journal of Photogrammetry and Remote Sensing*, No.56, pp.177-194.

Fujii, K. and Arikawa, T., (2002), Urban Object Reconstruction Using Airborne Laser Elevation Image and Aerial Image, IEEE Transactions on Geoscience and Remote Sensing, Vol.40, No.10, pp.2234-2240.

Gamba, P. and Houshmand, B., (2002), Joint Analysis of SAR, LIDAR and Aerial Imagery for Simultaneous Extraction of Land Cover, DTM and 3D Shape of Buildings, International Journal of Remote Sensing, Vol.23, No.20, pp.4439-4450.

Gonzalez, R. C., Woods, R. E. and Eddins, S. L., (2004), Digital Image Processing Using Matlab, Pearson Education, Inc. Upper Saddle River, New Jersey.

Gruen, A., (2000), Semi-automated Approaches to Site Recording and Modeling, IAPRS, Vol.XXXIII, Amsterdam 2000.

Gruen, A., Baltsavias, E. and Henricsson, O. (editors), (1997), Automatic Extraction of Man-Made Objects from Aerial and Space Images (II), Birkhaeuser Verlag, Berlin, Germany, 393 p.

Gruen, A., Kuebler, O. and Agouris, P. (editors), (1995), Automatic Extraction of Man-Made Objects from Aerial and Space Images, Birkhaeuser Verlag, Berlin, Germany, 321 p.

Haala, N. and Brenner, C. (1998), Interpretation of Surface Models Using 2D Building Information, Computer Vision and Image Understanding, Vol.72, No.2, pp. 204-214.

Haala, N., and Brenner, C., (1999), Extraction of Buildings and Trees in Urban Environments, ISPRS Journal of Photogrammetry & Remote Sensing, Vol.54, pp.130-137.

Henricsson, O., (1998), The Role of Color Attributes and Similarity Grouping in 3D Building Reconstruction, Computer Vision and Image Understanding, Vol.72, No.2, pp. 163-184.

Holland, D. A., Boyd, D. S., Marshall, P., (2006), Updating Topographic Mapping in Great Britain Using Imagery from High Resolution Satellite Sensors, *ISPRS Journal of Photogrammetry and Remote Sensing*, No. 60, pp. 212-223.

Hongjian, Y. and Shiqiang, Z., (2006), 3D Building Reconstruction from Aerial CCD Image and Sparse Laser Sample Data, *Optics and Lasers in Engineering*, 44, pp.555-566.

Hough, P.V.C., (1962), *Methods and Means for Recognizing Complex Patterns*, U.S. Patent 3,069,654.

Huang, C., L. S. Davis, and J. R. G. Townshend, (2002), An Assessment of Support Vector Machines for Land Cover Classification, *International Journal of Remote Sensing*, vol. 23, no. 4, pp. 725–749.

Huertas, A. and Nevatia, R., (1988), Detecting Buildings in Aerial Images, *Computer Vision, Graphics, and Image Processing* 41, pp. 131-152.

Huertas, A. and Nevatia, R., (2000), Detecting Changes in Aerial Views of Man-Made Structures, *Image and Vision Computing*, No.18, pp. 583-596.

Irving, R. and McKeown, D. M., (1989), Methods for Exploiting the Relationship between Buildings and Their Shadows in Aerial Imagery; *IEEE Transactions on Systems, Man, and Cybernetics*, Vol.19, No.6, pp.1564-1575.

Jin, X. and Davis, C. H., (2005), Automated Building Extraction from High Resolution Satellite Imagery in Urban Areas Using Structural, Contextual, and Spectral Information, *EURASIP Journal on Applied Signal Processing*, 2005:14, pp. 2196-2206.

Jung, F., (2004), Detecting Building Changes from Multitemporal Aerial Stereopairs, *ISPRS Journal of Photogrammetry and Remote Sensing*, 58, 187-201.

Katartzis, A. and Sahli, H., (2008), A Stochastic Framework for the Identification of Building Rooftops Using a Single Remote Sensing Image, *IEEE Transactions on Geoscience and Remote Sensing*, Vol.46, No.1, pp.259-271.

Keles, R., (1967), Kooperatifçilik İlkeleri ve Sosyal Konut Politikası Açısından Türkiye’de Konut Kooperatifleri, Ankara, Gürsoy Basımevi.

Khoshelham, K. and Li, Z., (2004), A Model-Based Approach to Semi-Automated Reconstruction of Buildings from Aerial Images, *The Photogrammetric Record*, 19(108), pp.342-359.

Khoshelham, K., Li, Z., and King, B., (2005), A Split and Merge Technique for Automated Reconstruction of Roof Planes, *Photogrammetric Engineering and Remote Sensing*, Vol.71, No.7, pp.855-862.

Kim, Z and Nevatia, R., (2004), Automatic Description of Complex Buildings from Multiple Images; *Computer Vision and Image Understanding*, 96, pp.60-95.

Kim, Z., W., and Nevatia, R. (1999), Uncertain Reasoning and Learning for Feature Grouping, *Computer Vision and Image Understanding*, Vol.76, No3, pp.278-288.

Knudsen, T. and Olsen, B. P., (2003), Automated Change Detection for Updates of Digital Map Databases, *Photogrammetric Engineering and Remote Sensing*, Vol.69, No.11, pp.1289-1296.

Lee, D. H., Lee, K. M. and Lee, S. U., (2008), Fusion of Lidar and Imagery for Reliable Building Extraction, *Photogrammetric Engineering and Remote Sensing*, Vol.74, No.2, pp.215-225.

Lee, D. S., Shan, J. and Bethel, J. S., (2003), Class-Guided Building Extraction from IKONOS imagery, *Photogrammetric Engineering and Remote Sensing*, Vol.69, No.2, pp.143-150.

Lillesand, T.M. and Kiefer, R.W., (1999), *Remote Sensing and Image Interpretation*, 4<sup>th</sup> edition, John Wiley & Sons, Inc.

Lin, C. and Nevatia, R., (1998), Building Detection and Description from a Single Intensity Image, *Computer Vision and Image Understanding*, Vol.72, No.2, pp.101-121.

Liow, Y.-T. and Pavlidis, T., (1990), Use of Shadows for Extracting Buildings in Aerial Images; *Computer Vision, Graphics, and Image Processing*, 49, pp.242-277.

Ma, R. (2005), DEM Generation and Building Detection from Lidar Data, *Photogrammetric Engineering and Remote Sensing*, Vol.71, No.7, pp.847-854.

Madhavan, B. B., Wang, C., Tanahashi, H., Hirayu, H., Niwa, Y., Yamamoto, K., Tachibana, K., and Sasagawa, T., (2006), A Computer Vision Based Approach for 3D Building Modelling of Airborne Laser Scanner DSM Data, *Computers, Environment and Urban Systems*, No.30, pp. 54-77.

Mathur, A. and Foody, G. M., (2008), Crop Classification by Support Vector Machine with Intelligently Selected Training Data for an Operational Application, *International Journal of Remote Sensing*, Vol. 29 , No. 8, pp. 2227-2240.

MATLAB 7 Manual, (2005), Learning Matlab, Getting Started - Introduction to Matlab.

Mayer, H., (1999), Automatic Object Extraction from Aerial Imagery – A Survey Focusing on Buildings, *Computer Vision and Image Understanding*, Vol.74, No.2, pp.138-149.

Mayunga, S. D., Coleman, D. J., and Zhang, Y., (2007), A Semi-Automated Approach for Extracting Buildings from QuickBird Imagery Applied to Informal Settlement Mapping, *International Journal of Remote Sensing*, Vol.28, No.10, pp. 2343-2357.

Miliaresis, G. and Kokkas, N., (2007), Segmentation and Object-Based Classification for the Extraction of the Building Class from LIDAR DEMs, *Computers and Geosciences*, Vol.33, pp.1076-1087.

Morse, B. S., (2000), Lecture 15: Segmentation (Edge Based, Hough transform), Brigham Young University: Lecture Notes, [http://homepages.inf.ed.ac.uk/rbf/CVonline/LOCAL\\_COPIES/MORSE/hough.pdf](http://homepages.inf.ed.ac.uk/rbf/CVonline/LOCAL_COPIES/MORSE/hough.pdf), Last Accessed Date: 12<sup>th</sup> February 2009.

Murakami, H., Nakagawa, K., Hasegawa, H., Shibata, T., and Iwanami, E., (1999), Change Detection of Buildings Using an Airborne Laser Scanner, *ISPRS Journal of Photogrammetry and Remote Sensing*, 54, pp. 148-152.

Niederost, M., (2002), Detection and Reconstruction of Buildings for Automated Map Updating, PhD Thesis, Institute of Geodesy and Photogrammetry, ETH Zurich.

Noronha, S. and Nevatia, R. (2001), Detection and Modeling of Buildings from Multiple Aerial Images, *IEEE Transactions on Pattern Analysis and Machine Intelligence*, Vol.23, No.5, pp.501-518.

Pal, C., Swayne, D., and Frey, B., (2001), The Automated Extraction of Environmentally Relevant Features from Digital Imagery Using Bayesian Multi-Resolution Analysis, *Advances in Environmental Research*, 5, pp.435-444.

Pal, M. and Mather, P. M., (2005), Support Vector Machines for Classification in Remote Sensing, *International Journal of Remote Sensing*, vol.26, no.5, pp.1007–1011.

PCI Geomatics, (2006), OrthoEngine User Guide, Version 10.0.

Pedersen, S.J.K., (2007), Circular Hough Transform, [http://www.cvmt.dk/education/teaching/e07/MED3/IP/Simon\\_Pedersen\\_CircularHoughTransform.pdf](http://www.cvmt.dk/education/teaching/e07/MED3/IP/Simon_Pedersen_CircularHoughTransform.pdf), Last Accessed Date: 16<sup>th</sup> March 2009.

Peng, J. and Liu, Y.C., (2005), Model and Context-Driven Building Extraction in Dense Urban Aerial Images, *International Journal of Remote Sensing*, 26(7), pp.1289-1307.

Peng, J., Zhang D., and Liu, Y., (2005), An Improved Snake Model for Building Detection from urban Aerial Images, *Pattern Recognition Letters*, 26, pp.587-595.

Priestnall, G., Jafaar, J. and Duncan, A., (2000), Extracting Urban Features from LIDAR Digital Surface Models, *Computers, Environment and Urban Systems*, No.24, pp.65-78.

Rau, J.Y. and Chen, L.C., (2003), Robust Reconstruction of Building Models from Three-Dimensional Line Segments, *Photogrammetric Engineering and Remote Sensing*, Vol.69, No.2, pp.181-188.

Rau, J.Y., Chen, N.Y., and Chen, L.C. (2002), True Orthophoto Generation of Built-Up Areas Using Multi-View Images, *Photogrammetric engineering and Remote Sensing*, vol. 68, no. 6, pp. 581-588.

Richards, J.A., (1999), *Remote Sensing Digital Image Analysis*, Springer-Verlag, Berlin, p. 240.

Ridley, H.M., Atkinson, P.M., Aplin, P., Muller, J.P. and Dowman, I., (1997), Evaluating the Potential of the Forthcoming Commercial U.S. High Resolution Satellite Sensor Imagery at the Ordnance Survey, *Photogrammetric Engineering & Remote Sensing*, 68(7), pp. 997-1005.

Rottensteiner, F., Trinder, J. Clode, S. and Kubik, K., (2005), Using the Dempster-Schaffer Method for the Fusion of LIDAR Data and Multi-Spectral Images for Building Detection, *Information Fusion*, 6, pp. 283-300.

Rottensteiner, F., Trinder, J. Clode, S. and Kubik, K., (2007), Building Detection by Fusion of Airborne Laser Scanner Data and Multi-Spectral Images: Performance Evaluation and Sensitivity Analysis, *ISPRS Journal of Photogrammetry and Remote Sensing*, vol. 62, pp.135-149.

Ruether, H., Martine, H. M., and Mtaló, E.G., (2002), Application of Snakes and Dynamic Programming Optimization Technique in Modeling of Buildings in Informal Settlement Areas, *ISPRS Journal of Photogrammetry and Remote Sensing*, 56, pp.269-282.

Sahar, L. and Krupnik, A., (1999), Semiautomatic Extraction of Building Outlines from Large-Scale Aerial Images, *Photogrammetric Engineering and Remote Sensing*, Vol.65, No.4, pp.459-465.



Sampath, A. and Shan, J., (2007), Building Boundary Tracing and Regularization from Airborne Lidar Point Clouds, *Photogrammetric Engineering and Remote Sensing*, Vol.73, No.7, pp.805-812.

Sanchez-Hernandez, C., Boyd, D. S. and Foody G., M., (2007), One-Class Classification for a Specific Land-Cover Class: SVDD Classification of Fenland, *IEEE Transactions on Geoscience and Remote Sensing*, Vol.45, No. 4, pp.1061-1073.

Shackelford, A. K. and Davis, C. H., (2003), A Combined Fuzzy Pixel-Based and Object-Based Approach for Classification of High Resolution Multispectral Data Over Urban Areas, *IEEE Transactions on Geoscience and Remote Sensing*, Vol.41, No.10, pp. 2354-2363.

Shufelt, J., (1999), *Geometric Constraints for Object Detection and Delineation*, Kluwer Academic Publishers, Massachusetts, USA, 265 p.

Shufelt, J.A. and McKeown, D.M., (1993), Fusion of Molecular Cues to Detect Man-Made Structures in Aerial Imagery, *CVGIP: Image Understanding*, 57 (3), 307-330.

Singh, A., and Harrison, A., (1985), Standardized Principal Components, *International Journal of Remote Sensing*, 6, pp. 883-896.

Sohn, G. and Dowman, I., (2007), Data Fusion of High-Resolution Satellite Imagery and LIDAR Data for Automatic Building Extraction, *ISPRS Journal of Photogrammetry and Remote Sensing*, 62, pp. 43-63.

Sohn, G., Dowman, I.J., (2001), Extraction of buildings from high resolution satellite data. In: Grün, A., Baltsavias, E.P., Henricsson, O. (Eds.), *Automatic Extraction of Man-made Objects from Aerial and Space Images*, vol. III. Balkema Publishers, Lisse, pp.345–356.

Sonka, M., Hlavac, V. and Boyle, R., (1998), *Image Processing, Analysis, and Machine Vision*, PWS Publishing

Sowmya, A. and Trinder, J., (2000), Modelling and Representation Issues in Automated Feature Extraction from Aerial and Satellite Images, ISPRS Journal of Photogrammetry and Remote Sensing, No. 55, pp.34-47.

Sunar Erbek, F. Ulubay, A., Maktav, D. and Yagiz, E., (2005), The Use of Satellite Image Maps for Urban Planning in Turkey, International Journal of Remote Sensing, Vol.26, No.4, pp.775-784.

Sunday D., Geometric algorithms, <http://geometryalgorithms.com/Archive/algorithm\ 0205/algorithm\ 0205.htm>, Last Accessed Date:10<sup>th</sup> March 2007.

Suveg, I. and Vosselman, G., (2004), Reconstruction of 3D building Models from Aerial Images and Maps, ISPRS Journal of Photogrammetry and Remote Sensing, 58, pp. 202-224.

Tao, C. V., Hu, Y. and Jiang, W., (2004), Photogrammetric Exploitation of IKONOS imagery for mapping applications, International Journal of Remote Sensing, Vol.25, No.14, pp. 2833-2853.

Teng, C. H. and Fairbairn, D., (2002), Comparing Expert Systems and Neural Fuzzy Systems for Object Recognition in Map Dataset Revision, International Journal of Remote Sensing, 2002, Vol.23, No.3, pp.555-567.

TNTmips Manual, (2002), Version 6.9.

Toutin, Th. and Cheng, P. (2001), DEM with stereo IKONOS: A reality if ..., Earth Observation Magazine, 10(7):13-17. URL: [http://www.ccrs.nrcan.gc.ca/ccrs/rd/sci\\_pub/bibpdf/13113.pdf](http://www.ccrs.nrcan.gc.ca/ccrs/rd/sci_pub/bibpdf/13113.pdf), Last Accessed Date: 05<sup>th</sup> March 2004.

Toutin, Th. and Cheng, P. (2002), Comparison of Automated Digital Elevation Model Extraction Results Using Along-Track ASTER and Across-Track SPOT Stereo Images, SPIE Journal, Optical Engineering, (41)9, pp2102-2106.

Toutin, Th., (2004), Comparison of Stereo-Extracted DTM from Different High-Resolution Sensors: SPOT-5 EROS-A IKONOS-II and QuickBird, IEEE Transactions on Geoscience and Remote Sensing, Vol.42, No.10, pp.2121-2129.

Tseng, Y. H. and Wang, S. (2003), Semiautomated Building Extraction Based on CSG Model-Image Fitting, *Photogrammetric Engineering and Remote Sensing*, Vol.69, No.2, pp.171-180.

Tupin, F. and Roux, M., (2003), Detection of Building Outlines Based on the Fusion of SAR and Optical Features, *ISPRS Journal of Photogrammetry and Remote Sensing*, 58, pp. 71-82.

Turker, M. and Cetinkaya, B., (2005), Automatic Detection of Earthquake-Damaged Buildings Using DEMs Created from Pre- and Post-Earthquake Stereo Aerial Photographs, *International Journal of Remote Sensing*, Vol.26, No.4, pp.823–832.

Turker, M. and San, B.T., (2004), Detection of Collapsed Buildings Caused by the 1999 Izmit, Turkey Earthquake Through Digital Analysis of Post-Event Aerial Photographs, *International Journal of Remote Sensing*, Vol.25, No.21, pp.4701–4714.

Turker, M. and Sumer, E., (2008), Building-Based Damage Detection Due to Earthquake Using Watershed Segmentation of the Post-Event Aerial Images, *International Journal of Remote Sensing*, Vol.29, No.11, pp.3073–3089.

Ujaldon, M., Ruiz, A. and Guil, N., (2008), On the Computation of the Circle Hough Transform by a GPU Rasterizer, *Pattern Recognition Letters* 29, pp. 309-318.

Ünsalan, C. and Boyer, K. L., (2005), A System to Detect Houses and Residential Street Networks in Multispectral Satellite Images, *Computer Vision and Image Understanding*, 98, pp. 423-461.

Vapnik, V. N., (1995), *The Nature of Statistical Learning Theory*, New York: Springer-Verlag, ISBN 0-387-94559-8.

Watanachaturaporn, P., Arora M. K., Varshney P. K. (2008), Multisource Classification Using Support Vector Machines: An Empirical Comparison with Decision Tree and Neural Network Classifiers, *Photogrammetric Engineering and Remote Sensing*, Vol. 74, No. 2, pp. 239 – 246.

Weidner, U., and Förstner, W., (1995), Towards Automatic Building Extraction from High-Resolution Digital Elevation Models, *ISPRS Journal of Photogrammetry and Remote Sensing*, Vol.50, No.4, pp.38-49.

Zhou, G., Song, C., Simmers, J. and Cheng, P., (2004), Urban 3D GIS from LIDAR and Digital Aerial Images, *Computers and Geosciences*, 30, pp.345-353.

Zhu, G. and D. G. Blumberg, (2002), Classification Using ASTER Data and SVM Algorithms: The case study of Beer Sheva, Israel, *Remote Sens. Environ.*, vol. 80, no. 2, pp. 233–240.

## APPENDIX A

### PHOTOGRAPHS FROM THE STUDY AREA

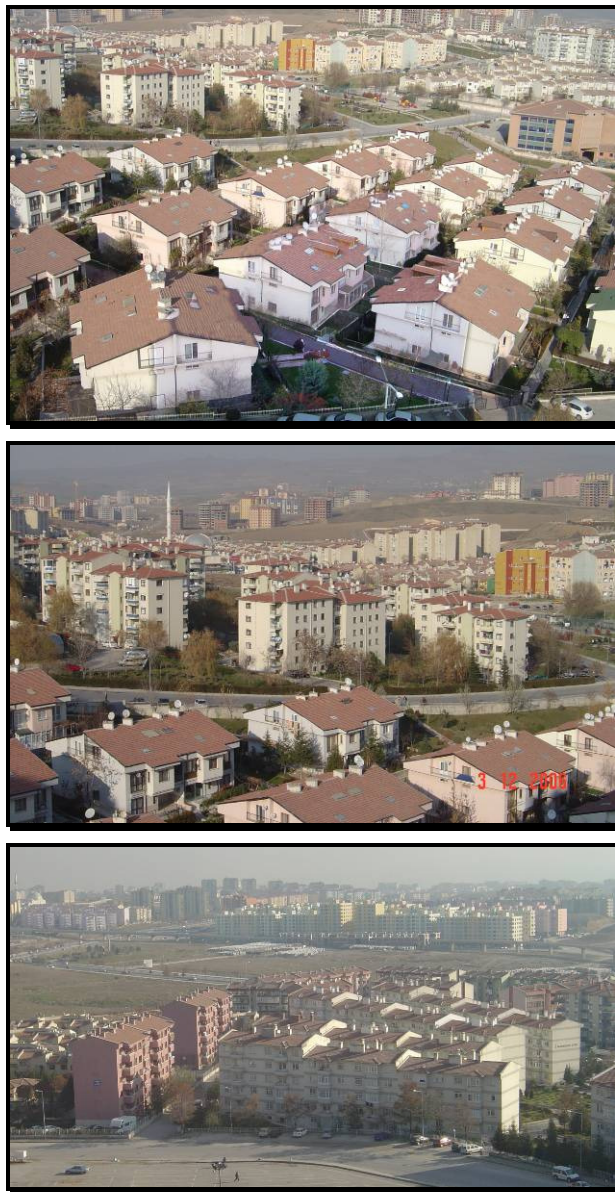


Figure A. 1. Photographs taken from the study area



Figure A. 1. Continued



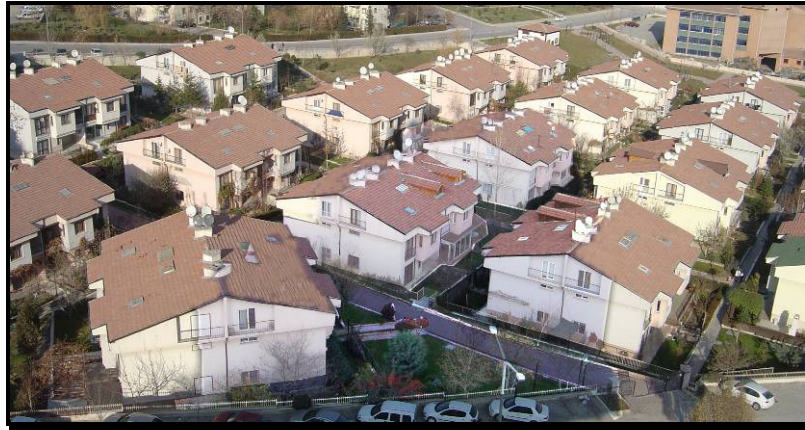


Figure A. 2. Photographs of detached rectangular shaped residential buildings from the study area



Figure A. 3. Photographs of semi-detached rectangular shaped residential buildings from the study area





Figure A. 4. Photographs of terraced rectangular shaped residential buildings from the study area



Figure A. 5. Photographs of “circle”, “C” and “S” shaped residential buildings from the study area





Figure A. 6. Photographs of rectangular shaped industrial buildings from the study area

## APPENDIX B

### EVALUATION OF THE DIGITAL SURFACE MODEL

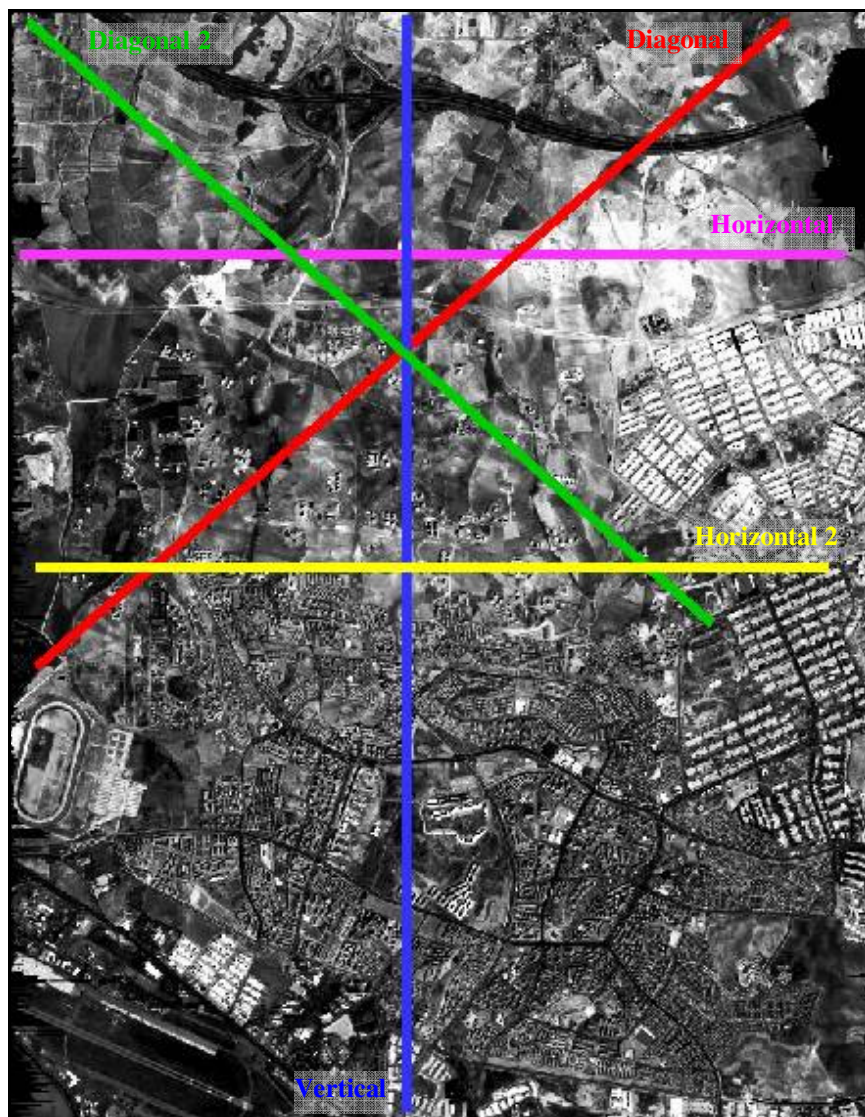


Figure B. 1. The panchromatic IKONOS image and five profiles

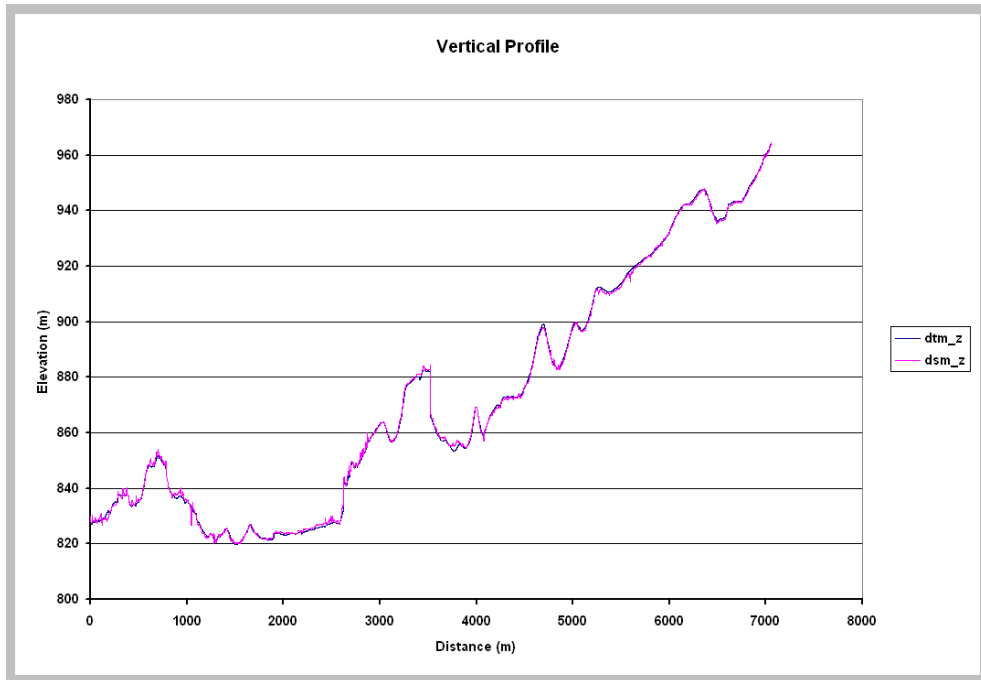


Figure B. 2. The graphic of the vertical profile.

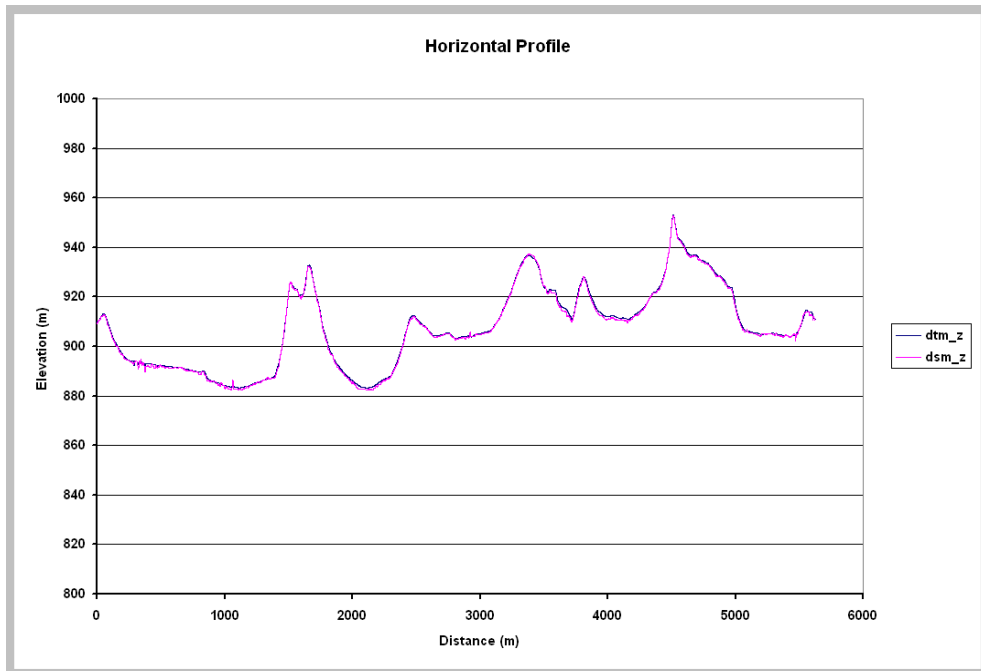


Figure B. 3. The graphic of the horizontal profile.

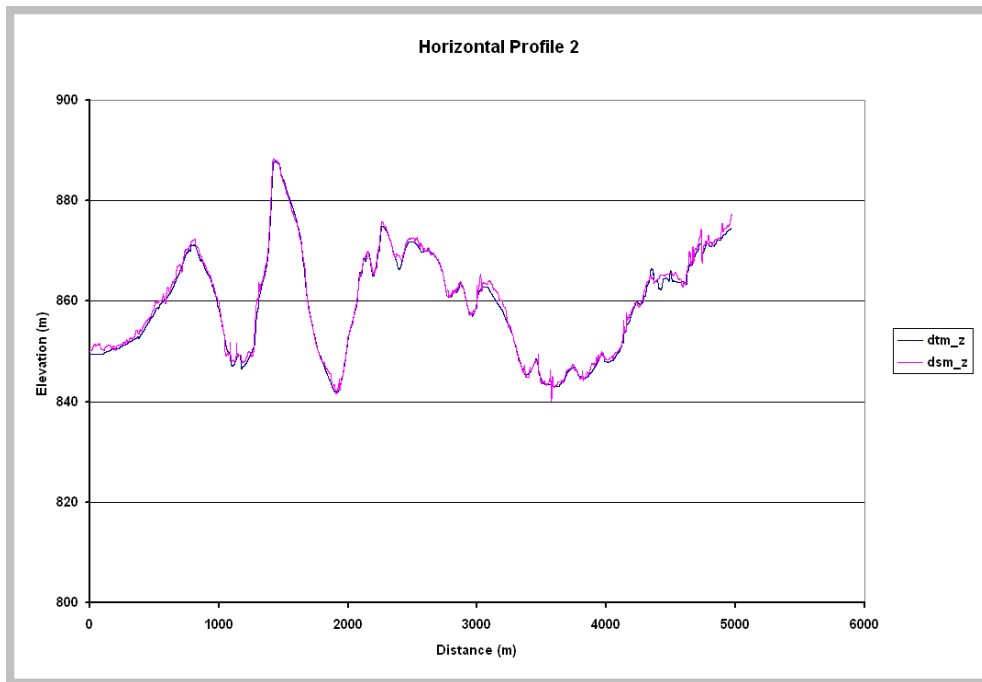


Figure B. 4. The graphic of the horizontal profile 2.

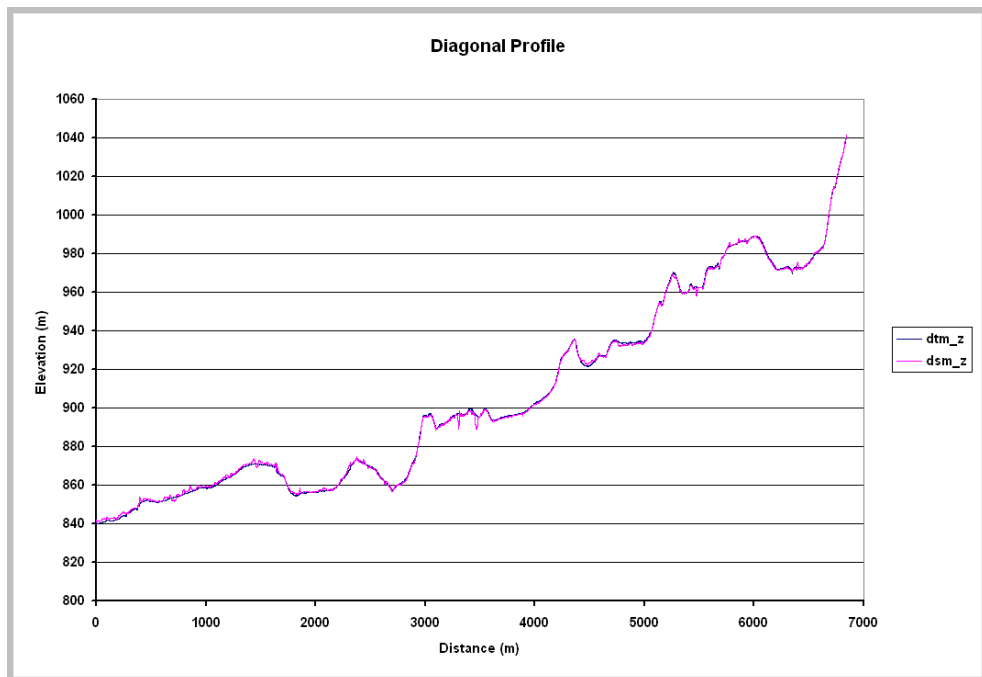


Figure B. 5. The graphic of the diagonal profile.

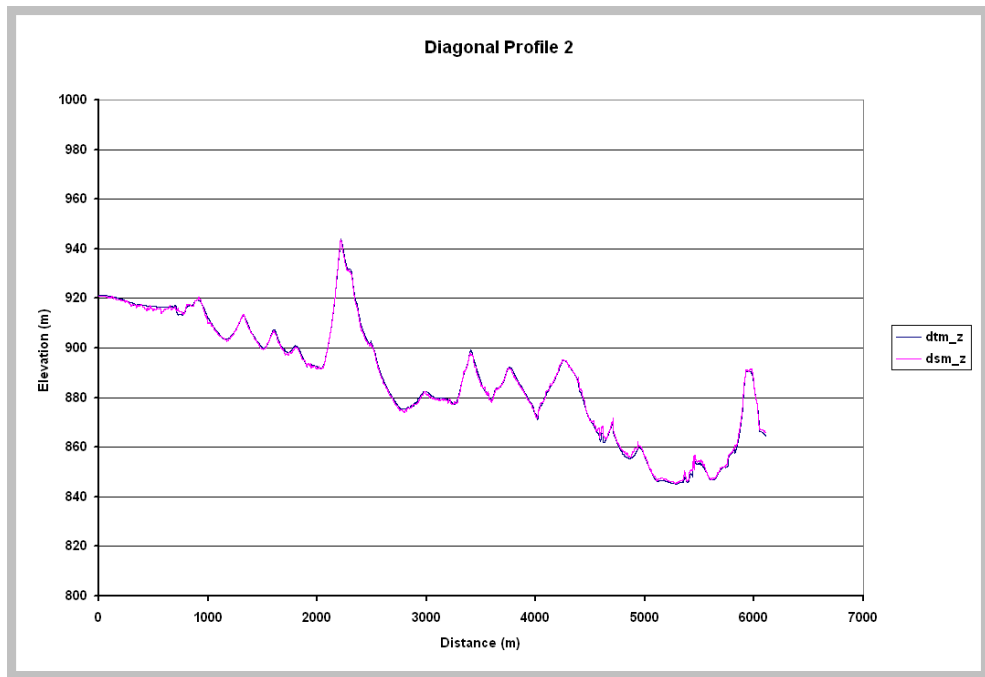


Figure B. 6. The graphic of the diagonal profile 2.

## APPENDIX C

### ACCURACY ASSESSMENT RESULTS OF THE SVM CLASSIFICATION

Table C. 1. For the data-sets (14 in total) of Sub-Area I, the SVM classification accuracies computed using 2000 test pixels.

Data-Set 1	Ground Truth		Total	Data-Set 2	Ground Truth		Total
	B	NB			B	NB	
B	952	41	993	B	981	7	988
NB	48	959	1007	NB	19	933	1012
Total	1000	1000	2000	Total	1000	1000	2000
PA	95.20	95.87		PA	98.10	99.30	
UA	95.90	95.23		UA	99.29	98.12	
OA	95.55			OA	98.70		
KC	0.9110			KC	0.9740		

B: Building  
 NB: Non-Building  
 PA: Producer's Accuracy  
 UA: User's Accuracy  
 OA: Overall Accuracy  
 KC: Kappa Coefficient

Data-Set 3	Ground Truth		Total	Data-Set 4	Ground Truth		Total
	B	NB			B	NB	
B	957	48	1005	B	953	48	1001
NB	43	952	995	NB	47	952	999
Total	1000	1000	2000	Total	1000	1000	2000
PA	95.70	95.20		PA	95.30	95.20	
UA	95.22	95.68		UA	95.20	95.30	
OA	95.45			OA	95.25		
KC	0.9090			KC	0.9050		

Data-Set 5	Ground Truth		Total	Data-Set 6	Ground Truth		Total
	B	NB			B	NB	
B	947	37	984	B	944	28	972
NB	53	963	1016	NB	56	972	1028
Total	1000	1000	2000	Total	1000	1000	2000
PA	94.70	96.30		PA	94.40	97.20	
UA	96.24	94.78		UA	97.12	94.55	
OA	95.50			OA	95.80		
KC	0.9100			KC	0.9160		



Table C. 1. Continued

Data-Set 7	Ground Truth		Total
	B	NB	
B	952	37	989
NB	48	963	1011
Total	1000	1000	2000
PA	95.20	96.30	
UA	96.26	95.25	
OA	95.75		
KC	0.9150		

Data-Set 8	Ground Truth		Total
	B	NB	
B	981	9	990
NB	19	991	1010
Total	1000	1000	2000
PA	98.10	99.10	
UA	99.09	98.12	
OA	98.60		
KC	0.9720		

Data-Set 9	Ground Truth		Total
	B	NB	
B	982	9	991
NB	18	991	1009
Total	1000	1000	2000
PA	98.20	99.10	
UA	99.09	98.22	
OA	98.65		
KC	0.9730		

Data-Set 10	Ground Truth		Total
	B	NB	
B	983	6	989
NB	17	994	1011
Total	1000	1000	2000
PA	98.30	99.40	
UA	99.39	98.32	
OA	98.85		
KC	0.9770		

Data-Set 11	Ground Truth		Total
	B	NB	
B	982	9	991
NB	18	991	1009
Total	1000	1000	2000
PA	98.20	99.10	
UA	99.09	98.22	
OA	98.65		
KC	0.9730		

Data-Set 12	Ground Truth		Total
	B	NB	
B	979	5	984
NB	21	995	1016
Total	1000	1000	2000
PA	97.90	99.50	
UA	99.49	97.93	
OA	98.70		
KC	0.9740		

Data-Set 13	Ground Truth		Total
	B	NB	
B	956	26	982
NB	44	974	1018
Total	1000	1000	2000
PA	95.60	97.40	
UA	97.35	95.68	
OA	96.50		
KC	0.9300		

Data-Set 14	Ground Truth		Total
	B	NB	
B	974	1	975
NB	26	999	1025
Total	1000	1000	2000
PA	97.40	99.70	
UA	99.90	97.46	
OA	98.65		
KC	0.9730		

Table C. 2. For the data-sets (14 in total) of Sub-Area I, the SVM classification accuracies computed using 4000 test pixels.

Data-Set 1	Ground Truth		Total	Data-Set 2	Ground Truth		Total
	B	NB			B	NB	
B	1904	41	1993	B	1944	5	1949
NB	96	959	1007	NB	56	1995	2051
Total	2000	2000	4000	Total	2000	2000	4000
PA	95.20	96.85		PA	97.20	99.75	
UA	96.80	95.28		UA	99.74	97.27	
OA	96.03			OA	98.48		
KC	0.9205			KC	0.9695		

Data-Set 3	Ground Truth		Total	Data-Set 4	Ground Truth		Total
	B	NB			B	NB	
B	1902	71	1973	B	1908	78	1986
NB	98	1929	2027	NB	92	1922	2014
Total	2000	2000	4000	Total	2000	2000	4000
PA	95.10	96.45		PA	95.40	96.10	
UA	96.40	95.17		UA	96.07	95.43	
OA	95.78			OA	95.75		
KC	0.9155			KC	0.9150		

Data-Set 5	Ground Truth		Total	Data-Set 6	Ground Truth		Total
	B	NB			B	NB	
B	1903	58	1961	B	1898	56	1954
NB	97	1942	2039	NB	102	1944	2046
Total	2000	2000	4000	Total	2000	2000	4000
PA	95.15	97.10		PA	94.90	97.20	
UA	97.04	95.24		UA	97.13	95.01	
OA	96.13			OA	96.05		
KC	0.9225			KC	0.9210		

Data-Set 7	Ground Truth		Total	Data-Set 8	Ground Truth		Total
	B	NB			B	NB	
B	1901	68	1969	B	1950	13	1963
NB	99	1932	2031	NB	50	1987	2037
Total	2000	2000	4000	Total	2000	2000	4000
PA	95.05	96.60		PA	97.50	99.35	
UA	96.55	95.13		UA	99.34	97.55	
OA	95.83			OA	98.43		
KC	0.9165			KC	0.9685		

Table C. 2. Continued

Data-Set 9	Ground Truth		Total
	B	NB	
B	1943	7	1950
NB	57	1993	2050
Total	2000	2000	4000
PA	97.15	99.65	
UA	99.64	97.22	
OA	98.40		
KC	0.9680		

Data-Set 10	Ground Truth		Total
	B	NB	
B	1949	0	1949
NB	51	2000	2051
Total	2000	2000	4000
PA	97.45	100.0	
UA	100.0	97.51	
OA	98.73		
KC	0.9745		

Data-Set 11	Ground Truth		Total
	B	NB	
B	1950	13	1963
NB	50	1987	2037
Total	2000	2000	4000
PA	97.50	99.35	
UA	99.34	97.55	
OA	98.43		
KC	0.9685		

Data-Set 12	Ground Truth		Total
	B	NB	
B	1953	4	1957
NB	47	1996	2043
Total	2000	2000	4000
PA	97.65	99.80	
UA	99.80	97.70	
OA	98.73		
KC	0.9745		

Data-Set 13	Ground Truth		Total
	B	NB	
B	1899	58	1957
NB	101	1942	2043
Total	2000	2000	4000
PA	94.95	97.10	
UA	97.04	95.06	
OA	96.03		
KC	0.9205		

Data-Set 14	Ground Truth		Total
	B	NB	
B	1936	2	1938
NB	64	1998	2062
Total	2000	2000	4000
PA	96.80	99.90	
UA	99.90	96.90	
OA	98.35		
KC	0.9670		

Table C. 3. For the data-sets (14 in total) of Sub-Area I, the SVM classification accuracies computed using 8000 test pixels.

Data-Set 1	Ground Truth		Total	Data-Set 2	Ground Truth		Total
	B	NB			B	NB	
B	3776	148	3924	B	3894	2	3896
NB	224	3852	4076	NB	106	3998	4104
Total	4000	4000	8000	Total	4000	4000	8000
PA	94.40	96.30		PA	97.35	99.95	
UA	96.23	94.50		UA	99.95	97.42	
OA	95.35			OA	98.65		
KC	0.9070			KC	0.9730		

Data-Set 3	Ground Truth		Total	Data-Set 4	Ground Truth		Total
	B	NB			B	NB	
B	3789	134	3923	B	3777	152	3929
NB	211	3866	4077	NB	223	3848	4071
Total	4000	4000	8000	Total	4000	4000	8000
PA	94.72	96.65		PA	94.42	96.20	
UA	96.58	94.82		UA	96.13	94.52	
OA	95.69			OA	95.31		
KC	0.9137			KC	0.9063		

Data-Set 5	Ground Truth		Total	Data-Set 6	Ground Truth		Total
	B	NB			B	NB	
B	3769	119	3888	B	3770	122	3892
NB	231	3881	4112	NB	230	3878	4108
Total	4000	4000	8000	Total	4000	4000	8000
PA	94.22	97.03		PA	94.25	96.95	
UA	96.94	94.38		UA	96.87	94.40	
OA	95.63			OA	95.60		
KC	0.9125			KC	0.9120		

Data-Set 7	Ground Truth		Total	Data-Set 8	Ground Truth		Total
	B	NB			B	NB	
B	3757	114	3871	B	3894	6	3900
NB	243	3886	4129	NB	106	3994	4100
Total	4000	4000	8000	Total	4000	4000	8000
PA	93.92	97.15		PA	97.35	99.85	
UA	97.06	94.11		UA	99.85	97.41	
OA	95.54			OA	98.60		
KC	0.9107			KC	0.9720		

Table C. 3. Continued

Data-Set 9	Ground Truth		Total
	B	NB	
B	3895	2	3897
NB	105	3998	4103
Total	4000	4000	8000
PA	97.38	99.95	
UA	99.95	97.44	
OA	98.66		
KC	0.9732		

Data-Set 10	Ground Truth		Total
	B	NB	
B	3893	2	3895
NB	107	3998	4105
Total	4000	4000	8000
PA	97.33	99.95	
UA	99.95	97.39	
OA	98.64		
KC	0.9728		

Data-Set 11	Ground Truth		Total
	B	NB	
B	3892	5	3897
NB	108	3995	4103
Total	4000	4000	8000
PA	97.30	99.88	
UA	99.87	97.37	
OA	98.59		
KC	0.9718		

Data-Set 12	Ground Truth		Total
	B	NB	
B	3897	3	3900
NB	103	3997	4100
Total	4000	4000	8000
PA	97.42	99.92	
UA	99.92	97.49	
OA	98.68		
KC	0.9735		

Data-Set 13	Ground Truth		Total
	B	NB	
B	3780	105	3885
NB	220	3895	4115
Total	4000	4000	8000
PA	94.50	97.38	
UA	97.30	94.65	
OA	95.94		
KC	0.9187		

Data-Set 14	Ground Truth		Total
	B	NB	
B	3900	3	3903
NB	100	3997	4097
Total	4000	4000	8000
PA	97.50	99.92	
UA	99.92	97.56	
OA	98.71		
KC	0.9742		

Table C. 4. For the data-sets (14 in total) of Sub-Area II, the SVM classification accuracies computed using 2000 test pixels.

Data-Set 1	Ground Truth		Total	Data-Set 2	Ground Truth		Total
	B	NB			B	NB	
B	966	93	1059	B	976	46	1022
NB	34	907	941	NB	24	954	978
Total	1000	1000	2000	Total	1000	1000	2000
PA	96.60	90.70		PA	97.60	95.40	
UA	91.22	96.39		UA	95.50	97.55	
OA	93.65			OA	96.50		
KC	0.8730			KC	0.9300		

Data-Set 3	Ground Truth		Total	Data-Set 4	Ground Truth		Total
	B	NB			B	NB	
B	967	94	1061	B	967	94	1061
NB	33	906	939	NB	33	906	939
Total	1000	1000	2000	Total	1000	1000	2000
PA	96.70	90.60		PA	96.70	90.60	
UA	91.14	96.49		UA	91.14	96.49	
OA	93.65			OA	93.65		
KC	0.8730			KC	0.8730		

Data-Set 5	Ground Truth		Total	Data-Set 6	Ground Truth		Total
	B	NB			B	NB	
B	965	92	1057	B	970	94	1064
NB	35	908	943	NB	30	906	936
Total	1000	1000	2000	Total	1000	1000	2000
PA	96.50	90.80		PA	97.00	90.60	
UA	91.30	96.29		UA	91.17	96.79	
OA	93.65			OA	93.80		
KC	0.8730			KC	0.8760		

Data-Set 7	Ground Truth		Total	Data-Set 8	Ground Truth		Total
	B	NB			B	NB	
B	969	92	1061	B	972	51	1023
NB	31	908	939	NB	28	949	977
Total	1000	1000	2000	Total	1000	1000	2000
PA	96.90	90.80		PA	97.20	94.90	
UA	91.33	96.70		UA	95.01	97.13	
OA	93.85			OA	96.05		
KC	0.8770			KC	0.9210		

Table C. 4. Continued

Data-Set 9	Ground Truth		Total
	B	NB	
B	976	52	1028
NB	24	948	972
Total	1000	1000	2000
PA	97.60	94.80	
UA	94.94	97.53	
OA	96.20		
KC	0.9240		

Data-Set 10	Ground Truth		Total
	B	NB	
B	974	48	1022
NB	26	952	978
Total	1000	1000	2000
PA	97.40	95.20	
UA	95.30	97.34	
OA	96.30		
KC	0.9260		

Data-Set 11	Ground Truth		Total
	B	NB	
B	977	53	1030
NB	23	947	970
Total	1000	1000	2000
PA	97.70	94.70	
UA	94.85	97.63	
OA	96.20		
KC	0.9240		

Data-Set 12	Ground Truth		Total
	B	NB	
B	978	54	1032
NB	22	946	968
Total	1000	1000	2000
PA	97.80	94.60	
UA	94.77	97.73	
OA	96.20		
KC	0.9240		

Data-Set 13	Ground Truth		Total
	B	NB	
B	969	72	1041
NB	31	928	959
Total	1000	1000	2000
PA	96.90	92.80	
UA	93.08	96.77	
OA	94.85		
KC	0.8970		

Data-Set 14	Ground Truth		Total
	B	NB	
B	922	32	954
NB	78	968	1046
Total	1000	1000	2000
PA	92.20	96.80	
UA	96.65	92.54	
OA	94.50		
KC	0.8900		

Table C. 5. For the data-sets (14 in total) of Sub-Area II, the SVM classification accuracies computed using 4000 test pixels.

Data-Set 1	Ground Truth		Total	Data-Set 2	Ground Truth		Total
	B	NB			B	NB	
B	1893	159	2052	B	1956	70	2026
NB	107	1841	1948	NB	44	1930	1974
Total	2000	2000	4000	Total	2000	2000	4000
PA	94.65	92.05		PA	97.80	96.50	
UA	92.25	94.51		UA	96.54	97.77	
OA	93.35			OA	97.15		
KC	0.8670			KC	0.9430		

Data-Set 3	Ground Truth		Total	Data-Set 4	Ground Truth		Total
	B	NB			B	NB	
B	1932	178	2110	B	1931	167	2098
NB	68	1822	1890	NB	69	1833	1902
Total	2000	2000	4000	Total	2000	2000	4000
PA	96.60	91.10		PA	96.55	91.65	
UA	91.56	96.40		UA	92.04	96.37	
OA	93.85			OA	94.10		
KC	0.8770			KC	0.8820		

Data-Set 5	Ground Truth		Total	Data-Set 6	Ground Truth		Total
	B	NB			B	NB	
B	1953	162	2115	B	1952	159	2111
NB	47	1838	1885	NB	48	1841	1889
Total	2000	2000	4000	Total	2000	2000	4000
PA	97.65	91.90		PA	97.60	92.05	
UA	92.34	97.51		UA	92.47	97.46	
OA	94.78			OA	94.83		
KC	0.8955			KC	0.8965		

Data-Set 7	Ground Truth		Total	Data-Set 8	Ground Truth		Total
	B	NB			B	NB	
B	1788	124	1912	B	1960	85	2045
NB	212	1876	2088	NB	40	1915	1955
Total	2000	2000	4000	Total	2000	2000	4000
PA	89.40	93.80		PA	98.00	95.75	
UA	93.51	89.85		UA	95.84	97.95	
OA	91.60			OA	96.88		
KC	0.8320			KC	0.9375		



Table C. 5. Continued

Data-Set 9	Ground Truth		Total
	B	NB	
B	1968	82	2050
NB	32	1918	1950
Total	2000	2000	4000
PA	98.40	95.90	
UA	96.00	98.36	
OA	97.15		
KC	0.9430		

Data-Set 10	Ground Truth		Total
	B	NB	
B	1923	55	1978
NB	77	1945	2022
Total	2000	2000	4000
PA	96.15	97.25	
UA	97.22	96.19	
OA	96.70		
KC	0.9340		

Data-Set 11	Ground Truth		Total
	B	NB	
B	1965	92	2057
NB	35	1908	1943
Total	2000	2000	4000
PA	98.25	95.40	
UA	95.53	98.20	
OA	96.83		
KC	0.9365		

Data-Set 12	Ground Truth		Total
	B	NB	
B	1952	85	2037
NB	48	1915	1963
Total	2000	2000	4000
PA	97.60	95.75	
UA	95.83	97.55	
OA	96.68		
KC	0.9335		

Data-Set 13	Ground Truth		Total
	B	NB	
B	1892	125	2017
NB	108	1875	1983
Total	2000	2000	4000
PA	94.60	93.75	
UA	93.80	94.55	
OA	94.18		
KC	0.8835		

Data-Set 14	Ground Truth		Total
	B	NB	
B	1847	51	1898
NB	153	1949	2102
Total	2000	2000	4000
PA	92.35	97.45	
UA	97.31	97.72	
OA	94.90		
KC	0.8980		

Table C. 6. For the data-sets (14 in total) of Sub-Area II, the SVM classification accuracies computed using 8000 test pixels.

Data-Set 1	Ground Truth		Total	Data-Set 2	Ground Truth		Total
	B	NB			B	NB	
B	3679	307	3986	B	3909	136	4045
NB	321	3693	4014	NB	91	3864	3955
Total	4000	4000	8000	Total	4000	4000	8000
PA	91.97	92.33		PA	97.72	96.60	
UA	92.30	92.00		UA	96.64	97.70	
OA	92.15			OA	97.16		
KC	0.8430			KC	0.9433		

Data-Set 3	Ground Truth		Total	Data-Set 4	Ground Truth		Total
	B	NB			B	NB	
B	3718	345	4063	B	3667	320	3987
NB	282	3655	3937	NB	333	3680	4013
Total	4000	4000	8000	Total	4000	4000	8000
PA	92.95	91.38		PA	91.67	92.00	
UA	91.51	92.84		UA	91.97	91.70	
OA	92.16			OA	91.84		
KC	0.8433			KC	0.8367		

Data-Set 5	Ground Truth		Total	Data-Set 6	Ground Truth		Total
	B	NB			B	NB	
B	3907	296	4203	B	3904	264	4168
NB	93	3704	3797	NB	96	3736	3832
Total	4000	4000	8000	Total	4000	4000	8000
PA	97.67	92.60		PA	97.60	93.40	
UA	92.96	97.55		UA	93.67	97.49	
OA	95.14			OA	95.50		
KC	0.9028			KC	0.9100		

Data-Set 7	Ground Truth		Total	Data-Set 8	Ground Truth		Total
	B	NB			B	NB	
B	3656	271	3927	B	3908	150	4058
NB	344	3729	4073	NB	92	3850	3942
Total	4000	4000	8000	Total	4000	4000	8000
PA	91.40	93.22		PA	97.70	96.25	
UA	93.10	91.55		UA	96.30	97.67	
OA	92.31			OA	96.98		
KC	0.8462			KC	0.9395		

Table C. 6. Continued

Data-Set 9	Ground Truth		Total
	B	NB	
B	3929	165	4094
NB	71	3835	3906
Total	4000	4000	8000
PA	98.22	95.88	
UA	95.97	98.18	
OA	97.05		
KC	0.9410		

Data-Set 10	Ground Truth		Total
	B	NB	
B	3900	128	4028
NB	100	3872	3972
Total	4000	4000	8000
PA	97.50	96.80	
UA	96.82	97.48	
OA	97.15		
KC	0.9430		

Data-Set 11	Ground Truth		Total
	B	NB	
B	3920	166	4086
NB	80	3834	3914
Total	4000	4000	8000
PA	98.00	95.85	
UA	95.94	97.96	
OA	96.93		
KC	0.9385		

Data-Set 12	Ground Truth		Total
	B	NB	
B	3885	158	4043
NB	115	3842	3957
Total	4000	4000	8000
PA	97.13	96.05	
UA	96.09	97.09	
OA	96.59		
KC	0.9317		

Data-Set 13	Ground Truth		Total
	B	NB	
B	3908	227	4135
NB	92	3773	3865
Total	4000	4000	8000
PA	97.70	94.33	
UA	94.51	97.62	
OA	96.01		
KC	0.9203		

Data-Set 14	Ground Truth		Total
	B	NB	
B	3681	91	3772
NB	319	3909	4228
Total	4000	4000	8000
PA	92.03	97.72	
UA	97.59	92.46	
OA	94.88		
KC	0.8975		

Table C. 7. For the data-sets (14 in total) of Sub-Area III, the SVM classification accuracies computed using 2000 test pixels.

Data-Set 1	Ground Truth		Total	Data-Set 2	Ground Truth		Total
	B	NB			B	NB	
B	874	73	947	B	949	18	967
NB	126	927	1053	NB	51	982	1033
Total	1000	1000	2000	Total	1000	1000	2000
PA	87.40	92.70		PA	94.90	98.20	
UA	92.29	88.03		UA	98.14	95.06	
OA	90.05			OA	96.55		
KC	0.8010			KC	0.9310		

Data-Set 3	Ground Truth		Total	Data-Set 4	Ground Truth		Total
	B	NB			B	NB	
B	882	80	962	B	876	82	958
NB	118	920	1038	NB	124	918	1042
Total	1000	1000	2000	Total	1000	1000	2000
PA	88.20	92.00		PA	87.60	91.80	
UA	91.68	88.63		UA	91.44	88.10	
OA	90.10			OA	89.70		
KC	0.8020			KC	0.7940		

Data-Set 5	Ground Truth		Total	Data-Set 6	Ground Truth		Total
	B	NB			B	NB	
B	893	35	928	B	922	54	976
NB	107	965	1072	NB	78	946	1024
Total	1000	1000	2000	Total	1000	1000	2000
PA	89.30	96.50		PA	92.20	94.60	
UA	96.23	90.02		UA	94.47	92.38	
OA	92.90			OA	93.40		
KC	0.8580			KC	0.8680		

Data-Set 7	Ground Truth		Total	Data-Set 8	Ground Truth		Total
	B	NB			B	NB	
B	900	86	986	B	954	17	971
NB	100	914	1014	NB	46	983	1029
Total	1000	1000	2000	Total	1000	1000	2000
PA	90.00	91.40		PA	95.40	98.30	
UA	91.28	90.14		UA	98.25	95.53	
OA	90.70			OA	96.85		
KC	0.8140			KC	0.9370		

Table C. 7. Continued

Data-Set 9	Ground Truth		Total
	B	NB	
B	921	17	938
NB	79	983	1062
Total	1000	1000	2000
PA	92.10	98.30	
UA	98.19	92.56	
OA	95.20		
KC	0.9040		

Data-Set 10	Ground Truth		Total
	B	NB	
B	944	27	971
NB	56	973	1029
Total	1000	1000	2000
PA	94.40	97.30	
UA	97.22	94.56	
OA	95.85		
KC	0.9170		

Data-Set 11	Ground Truth		Total
	B	NB	
B	927	14	941
NB	73	986	1059
Total	1000	1000	2000
PA	92.70	98.60	
UA	98.51	93.11	
OA	95.65		
KC	0.9130		

Data-Set 12	Ground Truth		Total
	B	NB	
B	942	21	963
NB	58	979	1037
Total	1000	1000	2000
PA	94.20	97.90	
UA	97.82	94.41	
OA	96.05		
KC	0.9210		

Data-Set 13	Ground Truth		Total
	B	NB	
B	928	34	962
NB	72	966	1038
Total	1000	1000	2000
PA	92.80	96.60	
UA	96.47	93.06	
OA	94.70		
KC	0.8940		

Data-Set 14	Ground Truth		Total
	B	NB	
B	946	20	966
NB	54	980	1034
Total	1000	1000	2000
PA	94.60	98.00	
UA	97.93	94.78	
OA	96.30		
KC	0.9260		

Table C. 8. For the data-sets (14 in total) of Sub-Area III, the SVM classification accuracies computed using 4000 test pixels.

Data-Set 1	Ground Truth		Total	Data-Set 2	Ground Truth		Total
	B	NB			B	NB	
B	1787	109	1896	B	1942	50	1992
NB	213	1891	2104	NB	58	1950	2008
Total	2000	2000	4000	Total	2000	2000	4000
PA	89.35	94.55		PA	97.10	97.50	
UA	94.25	89.88		UA	97.49	97.11	
OA	91.95			OA	97.30		
KC	0.8390			KC	0.9460		

Data-Set 3	Ground Truth		Total	Data-Set 4	Ground Truth		Total
	B	NB			B	NB	
B	1793	128	1921	B	1790	124	1914
NB	207	1872	2079	NB	210	1876	2086
Total	2000	2000	4000	Total	2000	2000	4000
PA	89.65	93.60		PA	89.50	93.80	
UA	93.34	90.04		UA	93.52	89.93	
OA	91.63			OA	91.65		
KC	0.8325			KC	0.8330		

Data-Set 5	Ground Truth		Total	Data-Set 6	Ground Truth		Total
	B	NB			B	NB	
B	1792	61	1853	B	1866	97	1963
NB	208	1939	2147	NB	134	1903	2037
Total	2000	2000	4000	Total	2000	2000	4000
PA	89.60	96.95		PA	93.30	95.15	
UA	96.71	90.31		UA	95.06	93.42	
OA	93.28			OA	94.23		
KC	0.8655			KC	0.8845		

Data-Set 7	Ground Truth		Total	Data-Set 8	Ground Truth		Total
	B	NB			B	NB	
B	1796	117	1913	B	1942	46	1988
NB	204	1883	2087	NB	58	1954	2012
Total	2000	2000	4000	Total	2000	2000	4000
PA	89.80	94.15		PA	97.10	97.70	
UA	93.88	90.23		UA	97.69	97.12	
OA	91.98			OA	97.40		
KC	0.8395			KC	0.9480		

Table C. 8. Continued

Data-Set 9	Ground Truth		Total
	B	NB	
B	1947	56	2003
NB	53	1944	1997
Total	2000	2000	4000
PA	97.35	97.20	
UA	97.20	97.35	
OA	97.28		
KC	0.9455		

Data-Set 10	Ground Truth		Total
	B	NB	
B	1893	45	1938
NB	107	1955	2062
Total	2000	2000	4000
PA	94.66	97.75	
UA	97.68	94.81	
OA	96.20		
KC	0.9240		

Data-Set 11	Ground Truth		Total
	B	NB	
B	1949	34	1983
NB	51	1966	2017
Total	2000	2000	4000
PA	97.45	98.30	
UA	98.29	97.47	
OA	97.88		
KC	0.9575		

Data-Set 12	Ground Truth		Total
	B	NB	
B	1893	35	1928
NB	107	1965	2072
Total	2000	2000	4000
PA	94.65	98.25	
UA	98.18	94.84	
OA	96.45		
KC	0.9290		

Data-Set 13	Ground Truth		Total
	B	NB	
B	1874	70	1944
NB	126	1930	2056
Total	2000	2000	4000
PA	93.70	96.50	
UA	96.40	93.87	
OA	95.10		
KC	0.9020		

Data-Set 14	Ground Truth		Total
	B	NB	
B	1905	27	1932
NB	95	1973	2068
Total	2000	2000	4000
PA	95.25	98.65	
UA	98.60	95.41	
OA	96.95		
KC	0.9390		

Table C. 9. For the data-sets (14 in total) of Sub-Area III, the SVM classification accuracies computed using 8000 test pixels.

Data-Set 1	Ground Truth		Total	Data-Set 2	Ground Truth		Total
	B	NB			B	NB	
B	3595	184	3779	B	3894	102	3996
NB	405	3816	4221	NB	106	3898	4004
Total	4000	4000	8000	Total	4000	4000	8000
PA	89.88	95.40		PA	97.35	97.45	
UA	95.13	90.41		UA	97.45	97.35	
OA	92.64			OA	97.40		
KC	0.8528			KC	0.9480		

Data-Set 3	Ground Truth		Total	Data-Set 4	Ground Truth		Total
	B	NB			B	NB	
B	3591	228	3819	B	3590	229	3819
NB	409	3772	4181	NB	410	3771	4181
Total	4000	4000	8000	Total	4000	4000	8000
PA	89.78	94.30		PA	89.75	94.28	
UA	94.03	90.22		UA	94.00	90.19	
OA	92.04			OA	92.01		
KC	0.8408			KC	0.8403		

Data-Set 5	Ground Truth		Total	Data-Set 6	Ground Truth		Total
	B	NB			B	NB	
B	3600	123	3723	B	3736	211	3947
NB	400	3877	4277	NB	264	3789	4053
Total	4000	4000	8000	Total	4000	4000	8000
PA	90.00	96.92		PA	93.40	94.72	
UA	96.70	90.65		UA	94.65	93.49	
OA	93.46			OA	94.06		
KC	0.8692			KC	0.8812		

Data-Set 7	Ground Truth		Total	Data-Set 8	Ground Truth		Total
	B	NB			B	NB	
B	3615	189	3804	B	3894	96	3990
NB	385	3811	4196	NB	106	3904	4010
Total	4000	4000	8000	Total	4000	4000	8000
PA	90.38	95.28		PA	97.35	97.60	
UA	95.03	90.82		UA	97.59	97.36	
OA	92.83			OA	97.48		
KC	0.8565			KC	0.9495		



Table C. 9. Continued

Data-Set 9	Ground Truth		Total
	B	NB	
B	3896	111	4007
NB	104	3889	3993
Total	4000	4000	8000
PA	97.40	97.22	
UA	97.23	97.40	
OA	97.31		
KC	0.9463		

Data-Set 10	Ground Truth		Total
	B	NB	
B	3846	115	3961
NB	154	3885	4039
Total	4000	4000	8000
PA	96.15	97.13	
UA	97.10	96.19	
OA	96.64		
KC	0.9327		

Data-Set 11	Ground Truth		Total
	B	NB	
B	3898	70	3968
NB	102	3930	4032
Total	4000	4000	8000
PA	97.45	98.25	
UA	98.24	97.47	
OA	97.85		
KC	0.9570		

Data-Set 12	Ground Truth		Total
	B	NB	
B	3884	82	3966
NB	116	3918	4034
Total	4000	4000	8000
PA	97.10	97.95	
UA	97.93	97.12	
OA	97.53		
KC	0.9505		

Data-Set 13	Ground Truth		Total
	B	NB	
B	3759	147	3906
NB	241	3853	4094
Total	4000	4000	8000
PA	93.97	96.33	
UA	96.24	94.11	
OA	95.15		
KC	0.9030		

Data-Set 14	Ground Truth		Total
	B	NB	
B	3889	73	3962
NB	111	3927	4038
Total	4000	4000	8000
PA	97.22	98.17	
UA	98.16	97.25	
OA	97.70		
KC	0.9540		

## APPENDIX D

### THE RESULTS OF THE SVM CLASSIFICATION

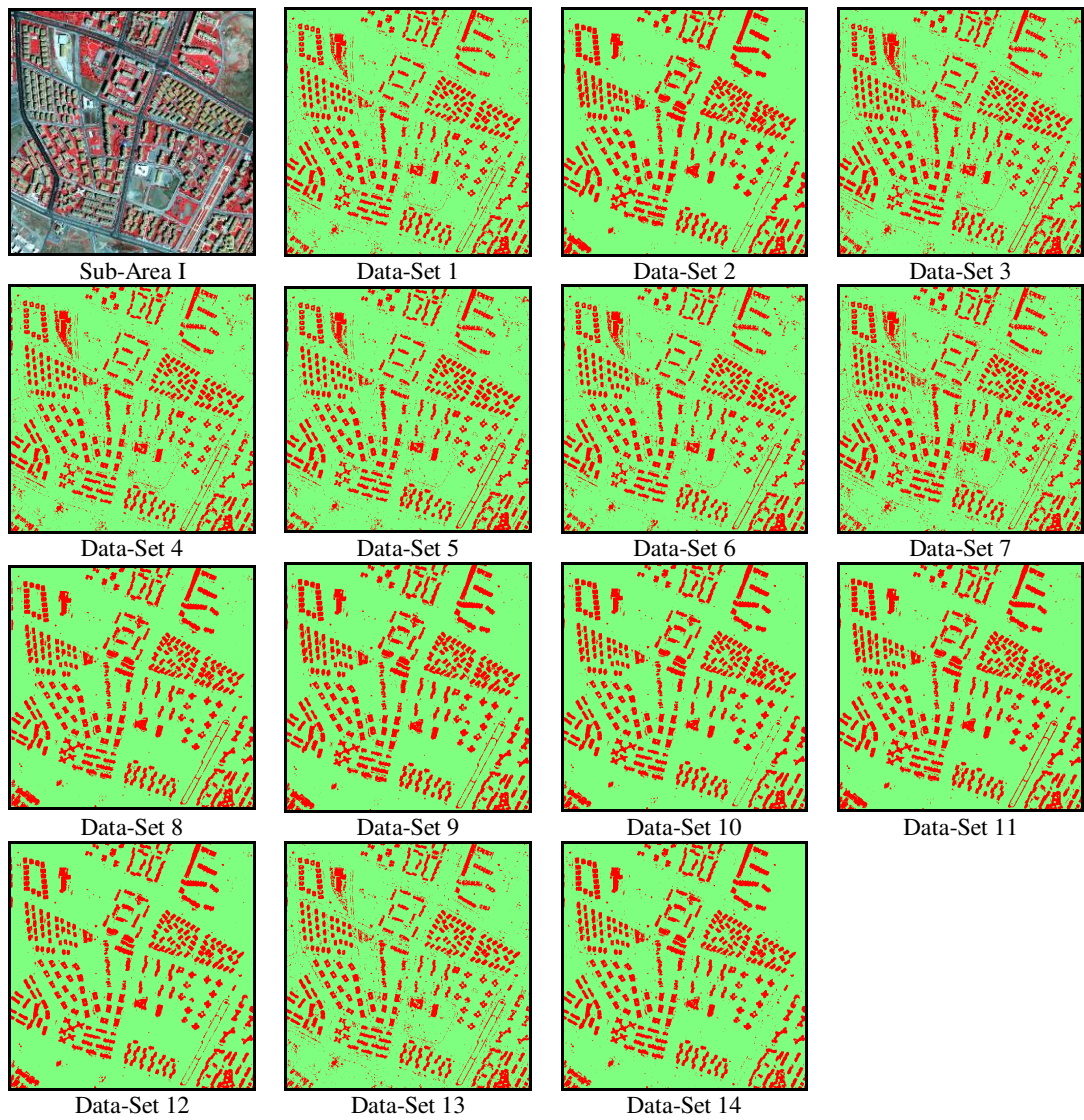


Figure D. 1. For Sub-Area I, the results of SVM classification performed using 14 Data-Sets and 1000 samples

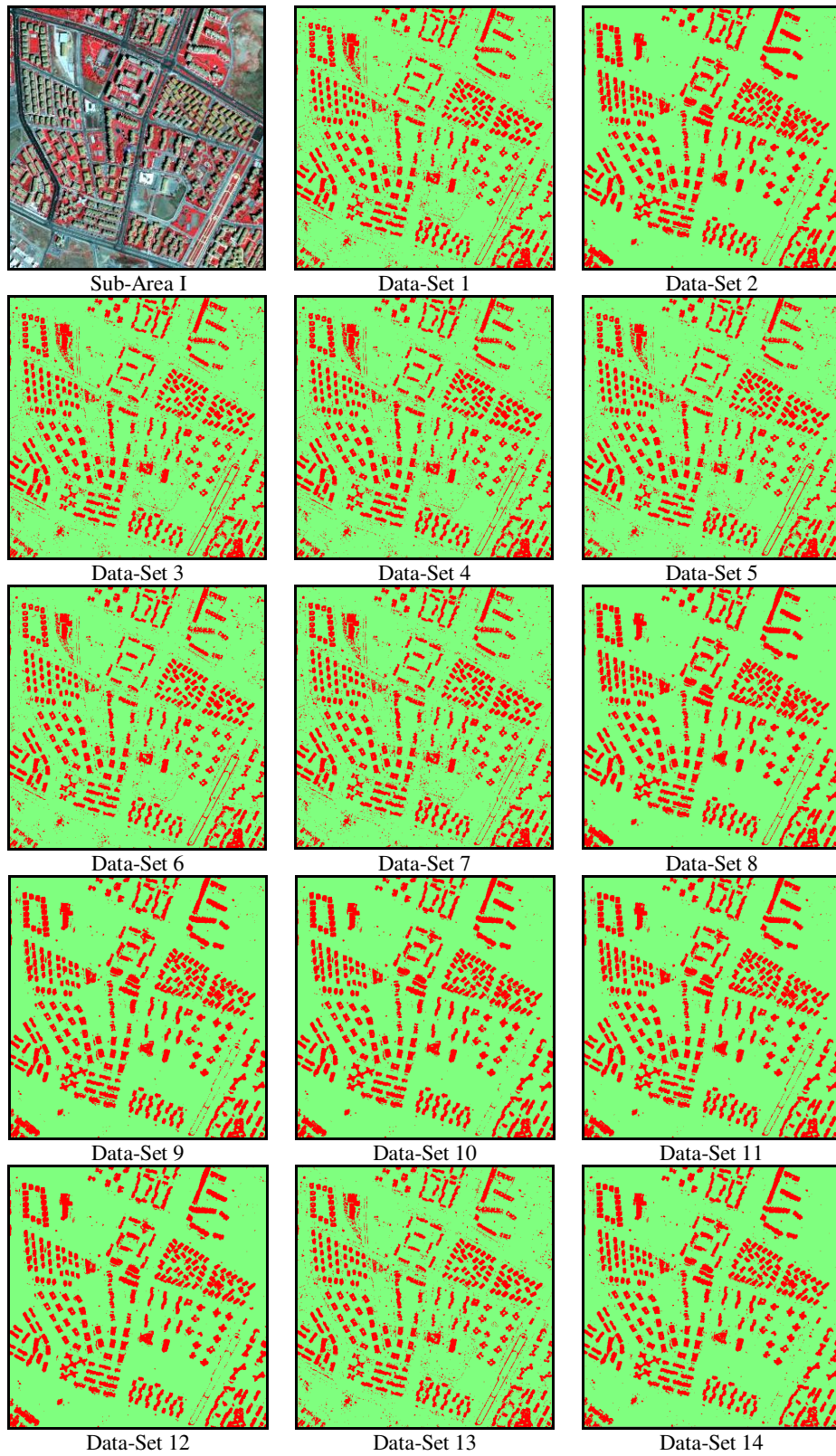


Figure D. 2. For Sub-Area I, the results of SVM classification performed using 14 Data-Sets and 2000 samples



Figure D. 3. For Sub-Area II, the results of SVM classification performed using 14 Data-Sets and 1000 samples



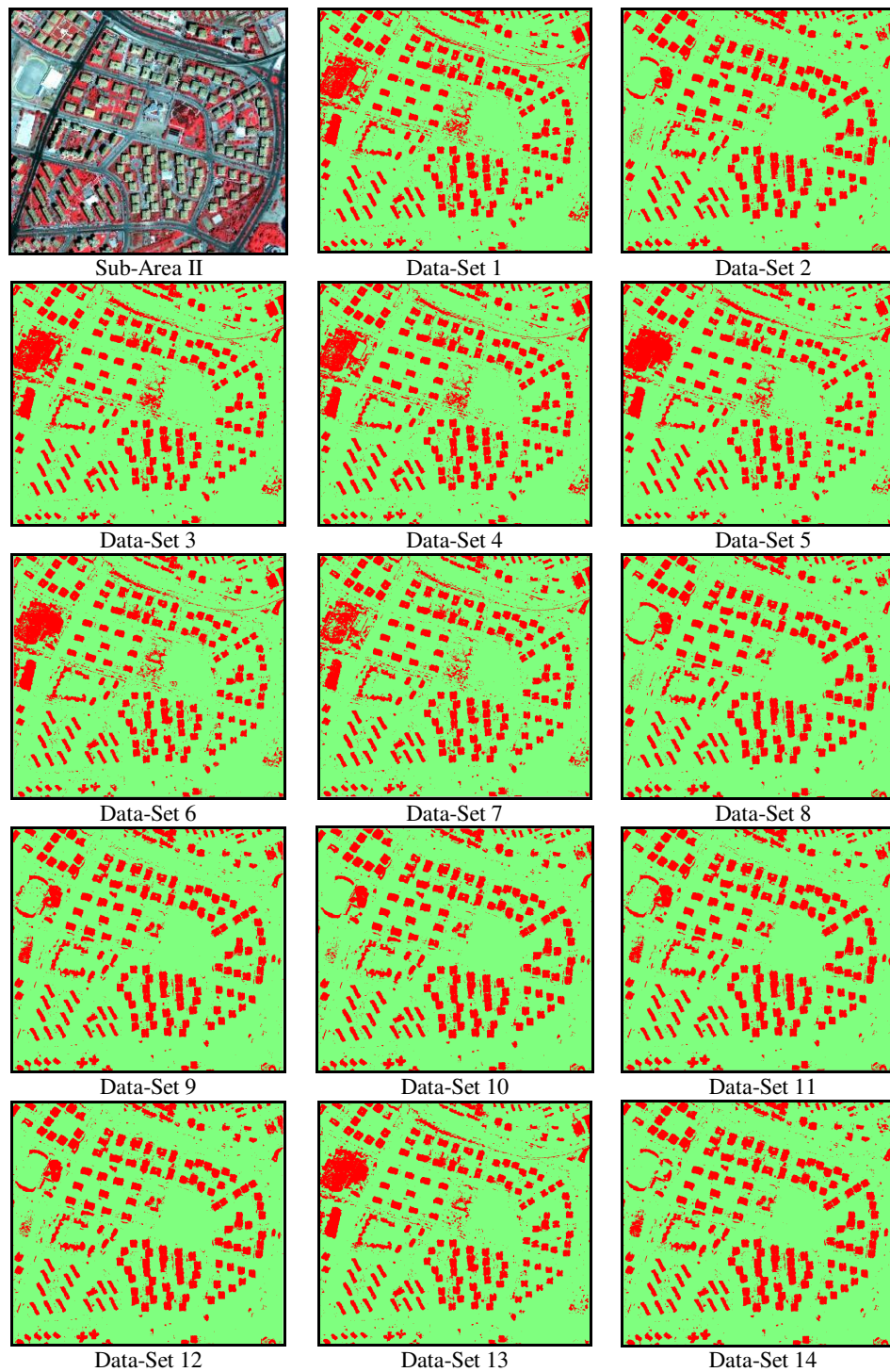


Figure D. 4. For Sub-Area II, the results of SVM classification performed using 14 Data-Sets and 2000 samples

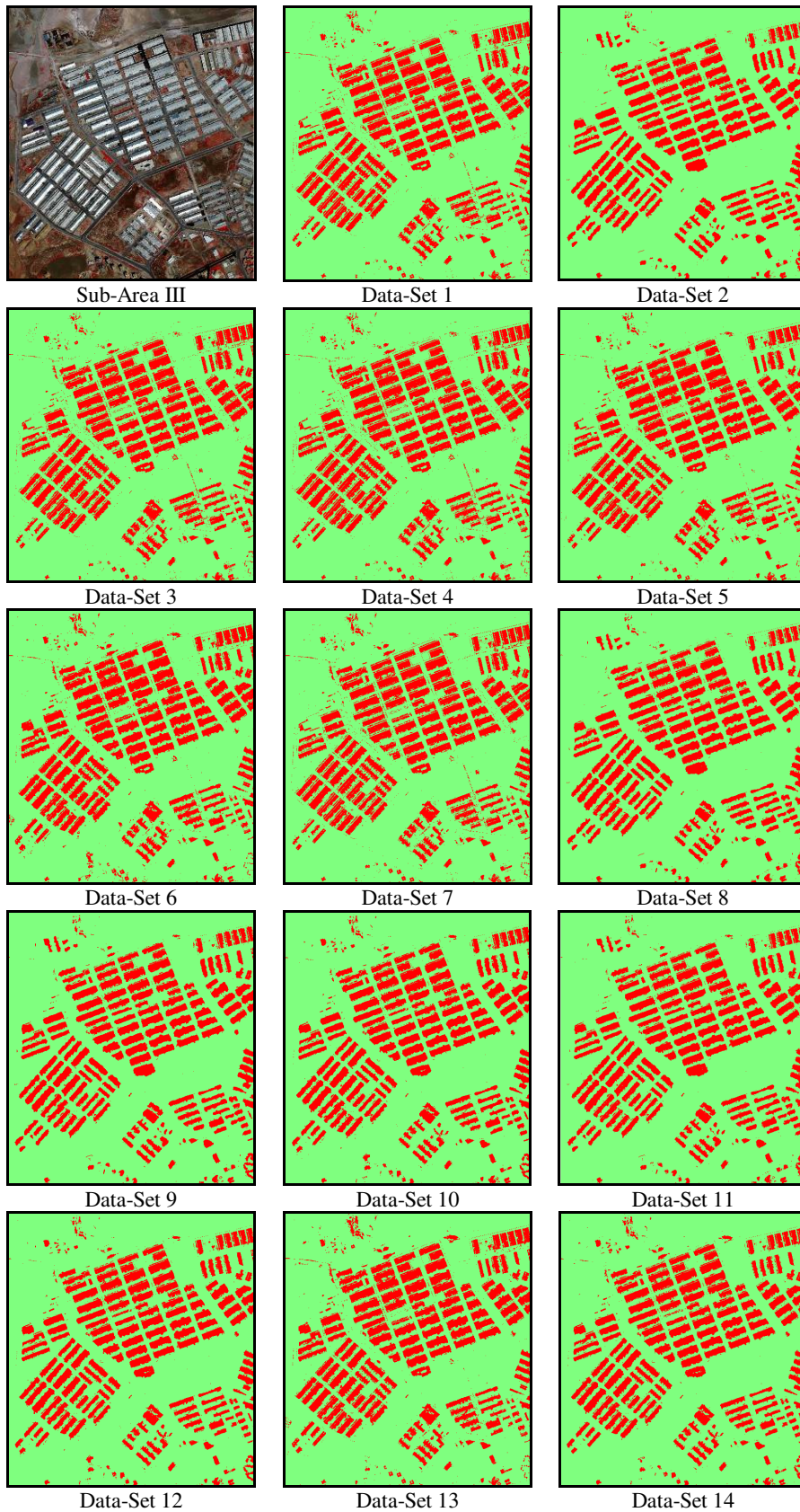


Figure D. 5. For Sub-Area III, the results of SVM classification performed using 14 Data-Sets and 1000 samples

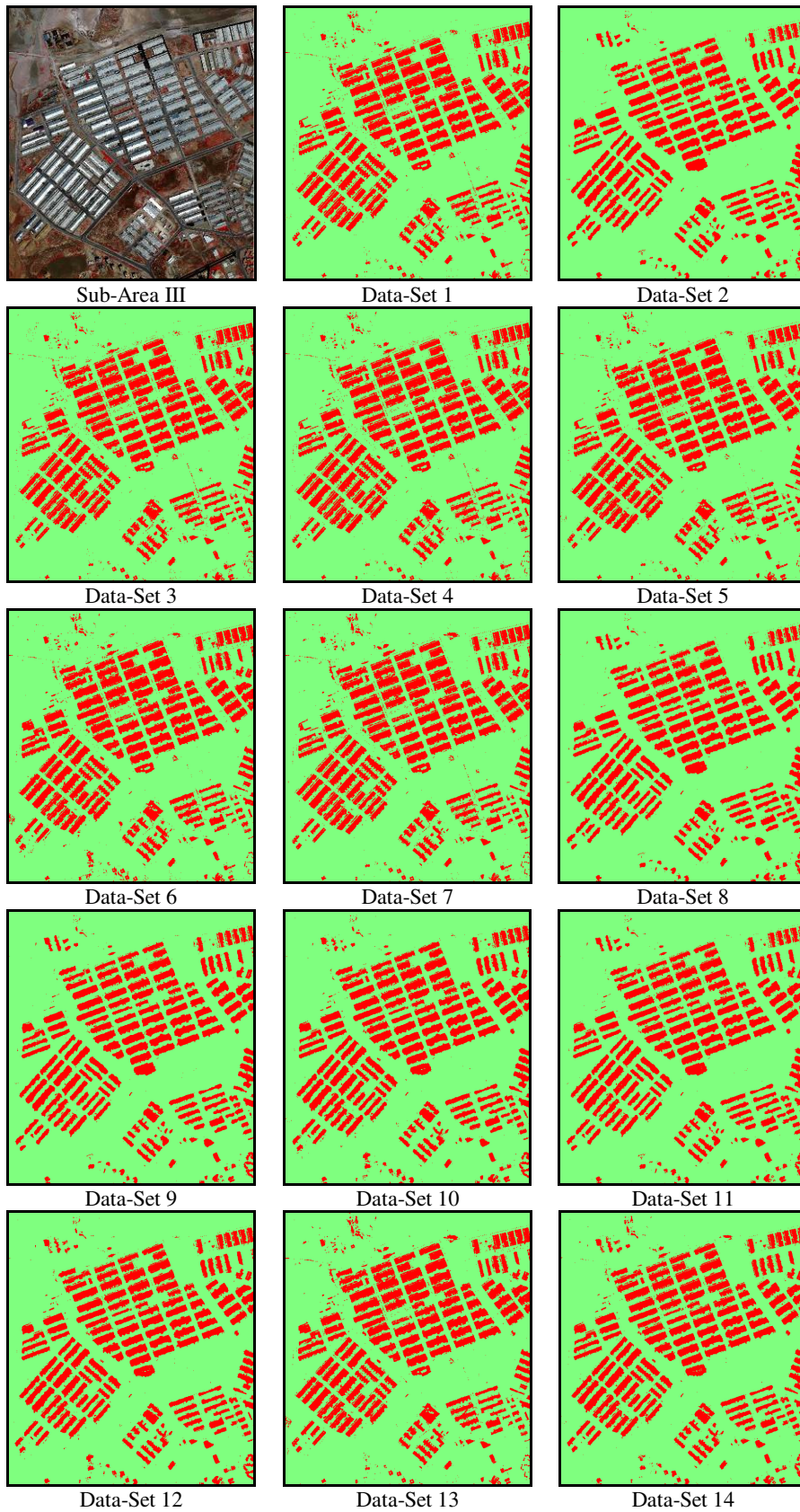


Figure D. 6. For Sub-Area III, the results of SVM classification performed using 14 Data-Sets and 2000 samples

## APPENDIX E

### SOURCE CODE FOR BUILDING MODEL SELECTION

*% For each building patch, the differences of the shape parameters between the building patch and all of the existing building boundaries are calculated as follows:*

```
area_dif(e)= abs (area_eb (l,e) - area_bp);  
per_dif(e)= abs(per_eb (l,e) - per_bp);  
major_dif(e)= abs(major_eb (l,e) - major_bp);  
minor_dif(e)= abs(minor_eb (l,e) - minor_bp);  
elong_dif(e)= abs(elongation_eb (l,e) - elongation_bp);  
comp_dif(e)= abs(comp_eb (l,e) - comp_bp);  
solid_dif(e)= abs(solid_eb (l,e) - solid_bp);
```

*% The minimum and maximum values of these differences are found as follows:*

```
area_dif_min = min(area_dif(l,:));  
area_dif_max = max(area_dif(l,:));  
  
per_dif_min = min(per_dif(l,:));  
per_dif_max = max(per_dif(l,:));  
  
major_dif_min = min(major_dif(l,:));  
major_dif_max = max(major_dif(l,:));  
  
minor_dif_min = min(minor_dif(l,:));  
minor_dif_max = max(minor_dif(l,:));  
  
elong_dif_min = min(elongation_dif(l,:));  
elong_dif_max = max(elongation_dif(l,:));  
  
comp_dif_min = min(comp_dif(l,:));  
comp_dif_max = max(comp_dif(l,:));  
  
solid_dif_min = min(solid_dif(l,:));  
solid_dif_max = max(solid_dif(l,:));
```



```

% These differences are rescaled between 0 and 1;
area_delta = area_dif_max - area_dif_min;
area_sc(e) = (area_dif(e) - area_dif_min)/area_delta;

per_delta = per_dif_max - per_dif_min;
per_sc(e) = (per_dif(e) - per_dif_min)/per_delta;

major_delta = major_dif_max - major_dif_min;
major_sc(e) = (major_dif(e) - major_dif_min)/major_delta;

minor_delta = minor_dif_max - minor_dif_min;
minor_sc(e) = (minor_dif(e) - minor_dif_min)/minor_delta;

elong_delta = elongation_dif_max - elongation_dif_min;
elong_sc(e) = (elongation_dif(e) - elongation_dif_min)/elongation_delta;

comp_delta = comp_dif_max - comp_dif_min;
comp_sc(e) = (comp_dif(e) - comp_dif_min)/comp_delta;

solid_delta = solid_dif_max - solid_dif_min;
solid_sc(e) = (solid_dif(e) - solid_dif_min)/solid_delta;

% The total differences are calculated by adding all shape parameter differences;
total_dif(e) = area_sc(e) + per_sc(e) + major_sc(e) + minor_sc(e) + comp_sc(e) + ...
... + solid_sc(e) + elongation_sc(e);

% To select the optimum building model for each candidate building patch, the
minimum total difference value between the shape parameters of candidate building
patch and the existing building boundaries is determined
MIN_DIFF = min(total_dif(1,:));

% To select the optimum building model the below given query is performed:
b = size(E);
for a = 1:b
    if MIN_DIFF == total_dif(1,a)
        BM = shaperead('exist_build.shp', 'Selector', {@(v1) (v1 == E(a,1).BuildID),
            'BuildID'});
        shapewrite(BM, 'selected_building.shp')
    end
end
end

```

## CURRICULUM VITAE

### PERSONAL INFORMATION

Surname, Name: Koç San, Dilek  
Nationality: Turkish (TC)  
Date and Place of Birth: 30 June 1978, Trabzon  
Marital Status: Married  
Phone: +90 312 210 5471  
e-mail: dilekoc@gmail.com

### EDUCATION

Degree	Institution	Year of Graduation
PhD on BS	METU, Geodetic and Geographic Information Technologies Dept.	2009
BS	Gazi Univ., City and Regional Planning Dept.	2000
High School	Çankaya High School	1996

### WORK EXPERIENCE

Year	Place	Enrollment
2002 – Present	METU, Geodetic and Geographic Information Technologies Dept.	Research Assistant

### PUBLICATIONS

1. Koç San, D. and Türker, M., (2009), Binaların Yüksek Çözünürlüklü Uydu Görüntülerinden Otomatik Güncellenmesi için Modele Dayalı Yaklaşım, Bakanlıklararası Harita İşlerini Koordinasyon ve Planlama Kurulu (BHİKPK) I. Sempozyumu, ODTU, Kültür Kongre Merkezi, Ankara, Türkiye, 23 – 25 Şubat.
2. Koç San, D. and Türker, M., (2009), Mevcut Bina Veri Tabanlarının Yüksek Çözünürlüklü Uydu Görüntülerinden Otomatik Güncellenmesi, Türkiye Ulusal Fotogrametri ve Uzaktan Algılama Birliği (TUFUAB) V. Teknik Sempozyumu, MTA Genel Müdürlüğü, Ankara, Türkiye, 4 – 6 Şubat.
3. Koç San, D. and Türker, M., (2008), Destek Vektör Makineleri ile Yüksek Çözünürlüklü Görüntülerden Binaların Belirlenmesi, CBS Günleri Sempozyumu, Ankara, Türkiye, 19 – 21 Kasım.

4. Koç San, D. and Türker, M., (2008), Binaların Yüksek Çözünürlüklü Uydu Görüntülerinden Destek Vektör Makineleri Sınıflandırma Tekniği Kullanılarak Belirlenmesi, 2. Uzaktan Algılama ve Coğrafi Bilgi Sistemleri Kongresi, Kayseri, Türkiye, 13 – 15 Ekim.
5. Koc San, D. and Turker, M., (2007), Automatic Building Extraction from High Resolution Satellite Images for Map Updating: A Model Based Approach, Urban Data Management Symposium (UDMS), Stuttgart, Germany, October 10-12. *Published in:* Urban and Regional Data Management – UDMS Annual 2007. V. Coors, M. Rumor, E.M. Fendel and S. Zlatanova. (eds)., Taylor & Francis/Balkema. The Netherlands, pp.3-13.
6. Koç San, D. and Türker, M., (2007), Binaların Yüksek Çözünürlüklü Uydu Görüntülerinden Belirlenebilme Potansiyeli, TMMOB Harita ve Kadastro Mühendisleri Odası, Ulusal Coğrafi Bilgi Sistemleri Kongresi, KTÜ, Trabzon, Türkiye, 30 Ekim– 3 Kasım.
7. Ertuğay K., Kemeç S., Koç San D., and Özdarıcı A., (2007), Fiziksel Erişebilirlik Analizlerine Eğimin Etkisi: ODTÜ Yerleşkesi Bisiklet Erişebilirliği Örneği, TMMOB Harita ve Kadastro Mühendisleri Odası, Ulusal Coğrafi Bilgi Sistemleri Kongresi, KTÜ, Trabzon, Türkiye, 30 Ekim– 3 Kasım.
8. Koc San, D. and Turker, M., (2007), Automatic Building Extraction from High Resolution Stereo Satellite Images, WG VII/2+7 joint Conference on Information Extraction from SAR & Optical Data with Emphasis on Developing Countries, Band XXXVI-7 Part C46 (ISBN No: 1682-1750), Istanbul, Turkey, May 16-18.
9. Koç San, D. and Türker, M., (2007), Binaların Yüksek Çözünürlüklü Uydu Görüntülerinden Modele Dayalı Yaklaşım Kullanılarak Belirlenmesi, TUFUAB IV. Teknik Sempozyumu, İstanbul, Türkiye, 5-7 Haziran.
10. Koc San, D. and Turker, M. (2006)., Automatic Building Detection and Delineation from High Resolution Space Images Using Model Based Approach, ISPRS Workshop on Topographic Mapping from Space (with Special Emphasis on Small Satellites), Band XXXVI-1/W41, Ankara, Turkey, February 14-16.
11. Koc San, D. and Turker, M. (2005). “An Approach for Automatic Building Detection from High Resolution Images” ISPRS Workshop on Spatial/Spatio-Temporal Data Mining, Ankara, Turkey, November 24-25.
12. Koç, D. and Türker, M. (2005)., IKONOS Pankromatik Uydu Görüntülerinden Sayısal Yükseklik Modeli Oluşturulması (Digital Elevation Model Generation from IKONOS Panchromatic Images), Harita Dergisi, Sayı: 134, 31-43.
13. Koc, D. and Turker, M. (2005)., Automatic Building Detection from High Resolution Satellite Images, Proceedings of the 2nd International Conference on Recent Advances in Space Technologies, Istanbul, Turkey, June 09-11, pp. 633-640.

14. Koç, D. and Türker, M. (2005), Yüksek Çözünürlüklü Uydu Görüntülerinden Binaların Otomatik Bulunması İçin Bir Yaklaşım, Ege Coğrafi Bilgi Sistemleri Sempozyumu Bildiri Kitabı, pp. 217-228, İzmir, Türkiye, 27-29 Nisan.